UNIVERSITA' DEGLI STUDI ROMA TRE

PhD's thesis XXXI Cycle

Probing the AGN/galaxy co-evolution in the widest luminosity range ever

Supervisors:
Prof. Fabio La Franca

Dr. Angela Bongiorno

Author:
Federica Duras

PhD Coordinator:
Prof. Giuseppe Degrassi

Al mio Nonnino.

Riesco a vedere i tuoi occhi lucidi di orgoglio anche da qui.

Preface

As Active Galactic Nuclei (AGN) began to be discovered less than a century ago, it was clear that they would play an important role in many aspects of modern astrophysics. In the past decade, studies of the local Universe have established the presence of Supermassive Black Holes (SMBHs) in the nuclei of virtually all galaxies with a bulge/spheroidal component (Kormendy and Richstone, 1995), and one of the first queries people raised up was whether and how the SMBH and its host galaxy could be interconnected. The comparison between the shape of the Stellar Mass Function, and the Halo Mass Function and the discovery that they do not follow the same behavior at the lowest and at the highest mass regimes, gave birth to the idea that some mechanisms are necessary to explain the different efficiency of the dark matter halos in turning gas into stars (see e.g., Behroozi et al., 2013). At low masses the most accepted scenarios deal with either the action of feedback from Supernovae (which regulates the formation of stars into galaxies by heating the inter-galactic medium) or the so-called gas starvation or strangulation (recently proposed by Peng et al., 2015, and which assumes that for some reasons the gas inflow into the SMBH is halted, so the star formation can continue for a limited period of time depending on the gas reservoirs still present within the galaxy). On the contrary, at the high mass end there is the need for more disruptive phenomena, able to quench the star formation and not simply to slow it down. Since feedback from AGN has been proposed as the major channel for the BH-galaxy interplay, efforts have been made to understand where and how it works. There is now a direct evidence for AGN-driven outflows being able to remove large amounts of gas from the galaxy central region, and so for being regarded as a viable feedback mechanism. Nevertheless, both observations and theory suggest that the mass outflows' rate is proportional to the AGN luminosity; therefore, the best places where to hunt for feedback mechanisms are the sources which lie at the high extreme of the AGN Luminosity Function (LF).

The characterization of the AGN evolution through the study of the AGN LF is mandatory if we want to constrain the theories of galaxy and SMBH formation and growth. It is therefore obvious that the luminosity emitted from the AGN begins a key parameter not only to describe the single source itself, but within a wider context of galaxy-BH evolution. Even the famous argument by Soltan (1982), who predicted that the cosmological growth of SMBHs is mostly because of the accretion of matter during their active phases, is based on some assumptions on the AGN luminosity and accretion efficiency. The same goes for several theories which have been developed to describe physical processes possibly responsible of a common formation scenario for galaxies and their central black hole (Volonteri et al., 2003; Springel et al., 2005; Vittorini et al., 2005). However, the bolometric luminosity (i.e., the luminosity integrated over the whole electromagnetic spectrum) is not the simplest observable to measure, because it requires a complete and reliable knowledge of the AGN spectral energy distribution (SED), and a good treatment of the contamination by the galaxy. Hence the need to calibrate affordable methods to estimate the AGN luminosity when only a narrow region of their spectrum is available. There is a further point which raises problems in our current knowledge of the SMBH-galaxy connection paradigm: all the scaling relations between the SMBH mass and some properties of the galaxy (i.e., mass and luminosity of the bulge, stellar velocity dispersion) have been found using local quiescent galaxies. Shankar et al. (2016) showed that using Monte Carlo simulations, resolution-related selection effects have the potential to increase the normalization of the M_{BH} - σ relation by a factor of a few, and the M_{BH} - M_* by at least an order of magnitude. The presence of these biases is confirmed when the scaling relations are measured using type 1 AGN where the BLR structure and dynamics have been modelled directly (Pancoast et al., 2014; Grier et al., 2017; Williams et al., 2018). Even more: what about the role of type 2 sources in these scaling relations? Due to the difficulty in measuring their BH mass, we have no strict constraints on the way they move on the local scaling relations. Being however the most predominant fraction of the AGN population, they are fundamental to puzzle the co-evolutionary scenario.

The work performed in this thesis is inserted in this scientific framework. We have studied two main AGN samples showing complementary properties. The first one belongs to a wide project which consists in the broad-band analysis of an infrared-selected (WISSH, standing for **WIS**E-**S**DSS **S**elected **H**yper-luminous) sample of the $\sim$ 90 type 1 most luminous AGN known in the redshift range 2<z<4. Given their extreme luminosities ($L_{BOL} > 2 \times 10^{47}$ erg/s), they represent the perfect place to look for feedback mechanisms in place. Thanks to the multi-wavelength coverage available, studies focused in different bands of their SED have been performed, leading to the characterization of their X-ray properties (Martocchia et al., 2017) and to the discovery of very powerful outflows

(Bischetti et al., 2017; Vietri et al., 2018). For this specific work we analyzed the 16 WISSH sources with *Herschel* data available in the three SPIRE bands (250, 350 and 500 μm), deriving their main physical properties (i.e., bolometric and monochromatic luminosities, star formation rate and dust masses). We focused on their infrared properties, finding extreme (up to thousands of solar masses per year) values of star formation rate (SFR) even properly accounting for the not negligible AGN contribution to the FIR fluxes, estimated to be about the 50%. Their unusual properties make them as witnesses of a very precise phase in the galaxy life cycle, in between the hot dust-obscured galaxies (hot DOGs) and the optically luminous sources. Within this framework we have carried out the analysis of a Compton thick hyper-luminous AGN at $z \sim 2$ observed by NuSTAR, and whose X-ray emission and SED-derived physical properties confirm the dust-enshrouded transitional phase which eventually leads to an optically bright AGN.
The second sample of type 1 and type 2 sources, extracted from the SWIFT/BAT 70-month catalog, shows complementary properties both in redshift (being local, at $z < 0.1$) and luminosity ($L_{BOL} \sim 10^{43} - 10^{44}$ erg/s) if compared with the WISSH one. For a sub-sample of 15 type 2 sources, estimates of the BH mass are available via deep NIR spectroscopy (Onori et al., 2017b). Together with the derivation of the physical properties via SED-fitting, the knowledge of the BH masses allowed us to characterize the $M_{BH} - M_*$ plane adding the information about the type 2 population, which was not investigated so far.
The combination of the high luminosity WISSH sample and of the low luminosity SWIFT/BAT sample, results in a collection of type 1 and type 2 AGN sources which spans a wide range of AGN luminosity (from 10^{41} erg/s to 10^{48} erg/s). We were therefore able to build up a new bolometric correction relation, statistically representative for the whole AGN population, and valid over the most extended luminosity range (~ 7 decades) ever sampled.

A general overview of our theoretical understanding (or lack thereof) of the AGN phenomenon, their physical and observational features and their classification in the unified model framework are summarized in Chapter 1, while Chapter 2 is focused on our current knowledge about the AGN-galaxy co-evolution. In Chapter 3 we describe the SED-fitting method we used to disentangle the different emission components. Chapter 4 is devoted to the analysis of the high-luminosity WISSH AGN sample, the characterization of their SED, the derivation of the main physical properties of both AGN and galaxy and the focus on the BH accretion-star formation activity relation. In Chapter 5 we analyze the particular case of the hyper-luminous hot DOG source W1835+4355, describing the data reduction process and the optical-to-IR SED modelling with the derivation of both its bolometric luminosity and SFR. In Chapter 6 the low-luminosity SWIFT/BAT sample

is described, with a focus on the SED-fitting procedure adopted to gain the best from the X-ray data, and the main physical properties we were able to derive. Moreover, we present a new bolometric correction in the hard X-ray regime, obtained by using the WISSH AGN with X-ray data available and the SWIFT/BAT sample, and which allowed to extend the range of luminosities at the high and at the low tails of the $K_{BOL} - L_{BOL}$ relation.

The work described in this Thesis was undertaken between January 2016 and October 2018, while I was a PhD student under the supervision of Prof. Fabio La Franca at Università degli studi Roma Tre, and in collaboration with Dr. Angela Bongiorno of the astronomical observatory of Rome in Monte Porzio Catone. I have been also visiting student (3 May - 3 August 2018) at Kavli IPMU (Kashiwanoha, Tokyo, Japan) where I worked in collaboration with John Silverman.

Portions of this Thesis have appeared in the following papers:

Chapter 4:
F. Duras, A. Bongiorno, E. Piconcelli, S. Bianchi, C. Pappalardo, R. Valiante, M. Bischetti, C. Feruglio, S. Martocchia, R. Schneider, G. Vietri, C. Vignali, L. Zappacosta, F. La Franca, F. Fiore. **2017A&A...604A..67D**, *The WISSH quasars project. II. Giant star nurseries in hyper-luminous quasars*;

M.Bischetti, E.Piconcelli, C.Feruglio, **F. Duras**, A.Bongiorno, S.Carniani, A.Marconi, C.Pappalardo, R.Schneider, A.Travascio, R.Valiante, G.Vietri, L.Zappacosta, and F.Fiore. **2018A&A...617A..82B** *The WISSH quasars project. V. ALMA reveals the assembly of a giant galaxy around a z = 4.4 hyper-luminous QSO.*

Chapter 5:
L. Zappacosta, E.Piconcelli, **F. Duras**, C.Vignali, R.Valiante, S.Bianchi, A.Bongiorno, F.Fiore, C.Feruglio, G.Lanzuisi, R.Maiolino, S.Mathur, G.Miniutti, C.Ricci. **2018A&A...618A..28Z** *The hyperluminous Compton-thick $z \sim 2$ quasar nucleus of the hot DOG W1835+4355 observed by NuSTAR.*

Moreover, the WISSH program in which I have been involved in during my PhD has led to the publication of other refereed papers:

- G. Vietri, E. Piconcelli, M. Bischetti, **F. Duras**, S. Martocchia, A. Bongiorno, A. Marconi, L. Zappacosta, S. Bisogni, G. Bruni, M. Brusa, A. Comastri, G. Cresci,

C. Feruglio, E. Giallongo, F. La Franca, V. Mainieri, F. Mannucci, F. Ricci, E. Sani, V. Testa, F. Tombesi, C. Vignali, and F. Fiore. **2018A&A...617A..81V** *The WISSH Quasars Project IV. BLR versus kpc-scale winds*

- S. Martocchia, E. Piconcelli, L. Zappacosta, **F. Duras**, G. Vietri, C. Vignali, S. Bianchi, M. Bischetti, A. Bongiorno, M. Brusa, G. Lanzuisi, A. Marconi, S. Mathur, G. Miniutti, F. Nicastro, G. Bruni, F. Fiore. **2017A&A...608A..51M**, *The WISSH Quasars Project III. X-ray properties of hyper-luminous quasars*

- M. Bischetti, E. Piconcelli, G. Vietri, A. Bongiorno, F. Fiore, E. Sani, A. Marconi, **F. Duras**, L. Zappacosta, M. Brusa, A. Comastri, G. Cresci, C. Feruglio, E. Giallongo, F. La Franca, V. Mainieri, F. Mannucci, S. Martocchia, F.Ricci, R. Schneider, V. Testa, C. Vignali. **2017A&A...598A.122B**, *The WISSH quasars project. I. Powerful ionised outflows in hyper-luminous quasars*

Moreover, I also gave my contribution to the following refereed papers:

- M. Brusa, G. Cresci, E. Daddi, R. Paladino, M. Perna, A. Bongiorno, E. Lusso, M.T.Sargent, V. Casasola, C. Feruglio, F. Fraternali, I. Georgiev, V. Mainieri, S. Carniani, A. Comastri, **F. Duras**, F. Fiore, F. Mannucci, A. Marconi, E. Piconcelli, G. Zamorani, R. Gilli, F. La Franca, G. Lanzuisi, D. Lutz, P. Santini, N.Z. Scoville, C. Vignali, F. Vito, S. Rabien, L. Busoni, M. Bonaglia. **2018A&A...612A..29B**, *Molecular outflow and feedback in the obscured Quasar XID2028 revealed by ALMA*

- F. Fiore, C. Feruglio, C. Shankar, M. Bischetti, A. Bongiorno, M. Brusa, S. Carniani, C. Cicone, **F. Duras**, A. Lamastra, V. Mainieri, A. Marconi, N. Menci, R. Maiolino, E. Piconcelli, G. Vietri, L. Zappacosta. **2017A&A...601A.143F**, *AGN wind scaling relations and the co-evolution of black holes and galaxies*

The work I have carried out during my PhD has been presented by myself as a speaker in the following international conferences:

- October 8-12 2018, at Milano (MI): Conference "AGN13. Beauty and the beast: when the Supermassive Black Hole has a crush on the galaxy";
  Talk: "Probing the AGN/galaxy coevolution in the widest dynamical range ever"

- September 3-7 2018, at Favignana (TP): Conference "Birth, life and fate of massive galaxies and their central beating heart";
  Talk: "AGN/galaxy coevolution in the widest dynamical range ever"

- June 25-29 2018, at IAP-Paris: "Conference Massive black holes in evolving galaxies, from quasars to quiescence";
  Talk: "Comparing the interplay between SMBH accretion and SF at the bright and the faint end of the AGN luminosity function"

- November 15-17 2017, at Firenze (FI): Conference "Galaxy Evolution and Environment 5":
  Talk: "Looking for the feedback in place:studies on the relationship between star formation and nuclear activity in galaxies"

- September 26 2016, at Napoli (NA): Conference "AGN12. A multi-messenger perspective";
  Talk: "The WISSH Project: Broad-band SED of Hyper-luminous WISE-selected Quasars at z 3."

- June 15 2016, at Mykonos Island: Conference "Hot spots in the XMM sky: Cosmology from X-ray to Radio";
  Talk: The WISSH Quasars project. Probing the AGN/galaxy co - evolution in the most luminous quasars.

- June 13 2016, at Mykonos Island: "XXL consortium meeting";
  Talk: Probing the AGN/galaxy co-evolution through multi-component SED fitting."

Contents

CHAPTER 1

Active Galactic Nuclei

This chapter aims at providing a brief introduction on the physics of Active Galactic Nuclei (AGN).

1.1 Basic concepts

With the name Active Galactic Nuclei, or AGN, one refers to energetic astrophysical sources powered by accretion onto supermassive black holes (SMBHs) in galaxies, which present unique observational signatures that cover the full electromagnetic spectrum over more than twenty orders of magnitude in frequency (Padovani et al., 2017). They are stronger emitters than the nuclei of normal galaxies, and this “adjoint” component cannot be attributed directly to stars. Active Galactic Nuclei have been known since 1943, when Seyfert (1943) discovered six spiral nebulae with bright nuclei whose spectra showed broad permitted emission lines, produced by atoms in a wide range of ionization states. Carl Seyfert was the first to notice that these emission lines were emitted from point-like sources at the center of the galaxies, which contributed to a huge fraction of the total light of the entire system. These objects are today known as "Seyfert galaxies". With the advances in radio astronomy in the 1950s, a lot of energetic phenomena were discovered, leading to the observation of the first quasars. The distinction between the two subclasses of AGN (Seyfert and quasars) is to some degree a matter of semantics. The fundamental difference relies in the amount of radiation emitted by the compact

central source; in the case of a typical Seyfert galaxy, the total energy emitted by the nuclear source at visible wavelengths is comparable to the energy emitted by all the stars in the galaxy (i.e. $\sim 10^{11} L_{\odot}$), but in a typical quasar the nuclear source is brighter than the stars by a factor of 100 or more.
Historically, the early failure to realize that Seyferts and quasars are probably related has probably to do with the different methods by which these two types of objects were first isolated, which left a large gap in luminosity between them. The appearance of quasars did not initially suggest identification with galaxies, which is a consequence of the basic fact that high-luminosity objects, like bright quasars, are rare. One is likely to find rare objects only at great distances, which is of course what happens with quasars. At very large distances, only the star-like nuclear source is seen in a quasar, and the light from the surrounding galaxy, because of its small angular size and relative faintness, is lost in the glare of the nucleus. Hence, the source looks “quasi-stellar".

However, the main peculiar features that one can ascribe to an AGN source, although not necessary present at the same time, are :

- small/unresolved angular size
- broad-band emission from the nucleus
- strong nuclear emission lines (mainly in the UV/optical and IR part of the spectrum)
- variability both in the continuum and emission lines and especially in the X-rays
- higher degree of polarization (0.5-2%) with respect to normal galaxies

1.2 AGN Taxonomy

From an observational point of view the classification of AGN can be rather complex and confusing, and the past years have seen a proliferation of AGN classes. However, the reality is simpler, as differences in the various classes of AGN can be ascribed to small changes in a few number of parameters (the orientation, the accretion rate, the presence of jets, and so on). A simple taxonomy of the main types of AGN (see e.g., Peterson, 1997) is the following:

- **Seyfert galaxies:** originally classified by Seyfert (1943). They are composed of AGN with moderate bolometric luminosity ($L_{bol} \sim 10^{41} - 10^{44}$ erg s^{-1}). These are radio-quiet object and have high central surface brightness, although the host

galaxy is still clearly detectable; they tend to be spirals, with massive galactic bulges and the presence of an interstellar medium. Since their original discovery, the classification has evolved such that they are also spectroscopically identificable by the presence of high-ionization emission lines. Seyfert galaxies are, themselves, divided into two groups: Seyfert 1 and Seyfert 2 sources (Sy1s and Sy2s), as was first realized by Khachikian and Weedman (1974).

- Type-1 Seyfert galaxies: are those with highly ionized, broad permitted lines, together with narrow forbidden lines. The narrow lines come from low-density, low-ionization gas, in the so-called Narrow-Line Region (NLR, see Section 1.3.3), and have full width at half maximum (FWHM) of a few hundred km s^{-1} (i.e. still broader than those lines observed in non-active galaxies). Because the density in the NLR is low, transitions are not collisionally de-excited, and so the radiative transitions (and, hence, the forbidden lines) are observed. The broad lines have widths Doppler-broadened up to 10^4 km s^{-1}. The Broad Line Region (BLR, see Section 1.3.3) is located closer in to the black hole, shown by both the increased width of the lines, and the higher ionization state; since only permitted lines are seen, the BLR is thought to be the densest between the two regions, with $n_e \gtrsim 10^9 \mathrm{cm}^{-3}$, compared to $\sim 10^3 - 10^6 \mathrm{cm}^{-3}$ for the NLR. There are certain objects, known as Narrow Line Seyfert 1 galaxies, which do show the broad lines (c.f. type-2 galaxies; see below), but they are narrower than in the typical broad-line Seyfert 1s. NLS1s are thought to have high accretion rates and, very probably, small black hole masses (see, e.g., Bian and Zhao, 2003). This will be discussed below.
- Type-2 Seyfert galaxies: differ from the type-1 objects by showing only the narrow lines. They have an [OIII] λ5007 to H_β ratio of < 3 (Shuder and Osterbrock, 1981); Seyfert 2s also tend to show weaker [FeII] (or higher ionization iron) emission lines than their Seyfert 1 counterparts. The difference between Seyfert 1 and 2 type galaxies, as discussed in Section 1.5, it is likely to be mainly due to an orientation effect.

- **Quasars:** or QSOs (Schmidt 1963) are the most luminous of the AGN family with a bolometric luminosity $L_{bol} \sim 10^{44} - 10^{47}$ erg s^{-1}. Their spectra are similar to those of Seyferts. However they are usually found at higher redshift ($z > 0.1$) and the host galaxy is hardly, if not at all, resolved. They can have a significant radio emission, in which case this radiation can be related to relativistic jets or extended emission lobes.

- **Radio Galaxies:** are moderate or bright AGN ($L_{bol} \sim 10^{42} - 10^{46}$ erg s^{-1}) and their peculiarity is their powerful emission in the radio-mm band. Although radio

galaxies are considered, in some senses, to be radio-loud Seyferts, they typically occur in elliptical galaxies, rather than spirals. The radio lobes in these galaxies are powered by a jet of particles and emit non-thermal, synchrotron radiation (e.g., Blandford, 1974). They can be classified as Broad Line radio Galaxies (BLRGs) or Narrow Line radio Galaxies (NLRGs) depending on the presence of broad or narrow emission lines in their optical-UV spectra.

- **OVV & Blazars:** the Optically Violent Variables (OVV) show the highest variability among all the AGN, from the radio up to the X-ray bans. Their optically emission is also strongly polarized.
  Blazars or BL Lacs (named after the first object in the class, identified in the direction of the constellation of Lacerta, the lizard) do not have visible radio lobes and do not show emission/absorption lines. Blazar spectra are purely power-law continua, with no thermal component.

- **LINERs:** Low Ionisation Nuclear Emission-Line Region galaxies are the least luminous of the classifications. They were first identified by Heckman (1980) and are, in fact, very common, possibly existing in nearly half of all spiral galaxies (Ho et al., 1994). LINERS show only weak nuclear activity, with most of their emission coming from starlight. The emission line spectra indicate the existence of a non-stellar continuum, although this has yet to be observed directly (Netzer and Maoz, 1990). The observational difference, in the optical region, between LINERS and Seyfert 2 type galaxies lies in the relative strength of certain low-ionization lines, with Heckman's definitions being that the [OII] $\lambda\lambda$ 3727, 3729 lines are stronger than the [OIII] λ5007 line, [OI] λ 6300/[OIII]λ5007 $\lesssim$ 0.33 and [NII] λ 6584/H_α $\gtrsim$ 0.6.

As a final note to this section, Starburst galaxies should be mentioned. These are galaxies in which the star-formation rate is much higher than average. They contain many young stars and are more energetic than normal galaxies, although not as luminous as AGN. They show strong IR emission, due to the heating of dust by UV emission from the young stellar population. Starbursts may be formed through the merger of galaxies. Although there are not AGN as such, much work has been done on the connection between the groups.

1.3 AGN structure

It is widely accepted that the central engine of AGN consists of a supermassive black hole surrounded by an accretion disc where the material in gravitational infall dissipates

its kinetic energy. This accretion disc is heated to high temperatures and it is thus responsible of most of the observed radiation.

1.3.1 The central engine

The nature of the central engine is in turn related to the conversion of the mass into radiant energy, which can be defined as:

$$E = \eta M c^2 \tag{1.1}$$

Here, η is the mass-energy efficiency conversion.

The rate at which the energy is emitted is simply:

$$L = \frac{dE}{dt} = \eta \dot{M} c^2 \tag{1.2}$$

where $\dot{M} = dM/dt$ is the mass accretion rate and c is the speed of light.
Using observations of the variability time-scale Δt (of the order of hours) together with the assumption of the casuality principle, the size of the central emitting source is recognized to be (as an upper limit) $R \leq c\Delta t \sim 10^{-4} pc$.

One of the most important astronomical discoveries of the last 10-20 years is the finding that massive galaxies in the local Universe host a central massive black hole ($M_{BH} \sim 10^5 - 10^{10} M_\odot$) with a mass proportional to that of the galaxy spheroid (e.g., Magorrian et al., 1998; Tremaine et al., 2002). The tightness of this BH-spheroid mass relationship suggests a symbiotic connection between the formation and growth of galaxy spheroids and BHs, which might be expected since both processes are predominantly driven by a cold-gas supply, provided by the host galaxy or the larger-scale extragalactic environment. The big difference in physical size between the BH and the galaxy spheroid ($\sim$ 9 orders of magnitude) means that the gas has to be driven down to $\sim$ 10 pc before it will come under the gravitational influence of the BH. The gas has to lose $\sim$ 99.9% of its angular momentum to go from a stable orbit at $r = 10kpc$ to $r = 10pc$ (e.g., Jorge, 2006).
The potential energy of a mass m at a distance r from a central source of mass M is:

$$\Omega = \frac{GMm}{r} \tag{1.3}$$

with G Gravitational constant.
The rate at which the potential energy of the infalling material is converted to radiation

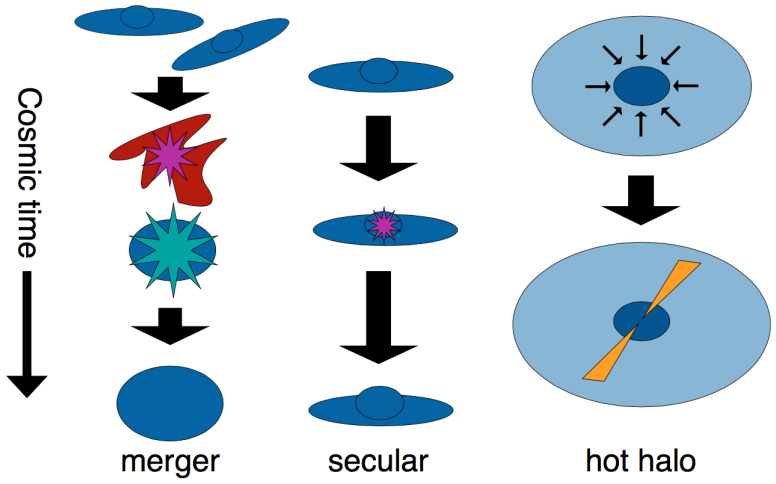

FIGURE 1.1: Schematic diagrams from Alexander and Hickox (2012a) to illustrate the large-scale processes that are thought to be responsible for triggering AGN activity: major mergers of gas-rich galaxies, secular evolution (which includes both internal secular evolution and external secular evolution, the latter of which is driven by galaxy interactions), and hot halo accretion, which is presumed to be the dominate BH growth mode for low-excitation radio-loud AGNs.

is:

$$L \sim \frac{d\Omega}{dt} = \frac{GM}{r}\frac{dM}{dt} = \frac{GM\dot{M}}{r}. \tag{1.4}$$

The comparison between the equations gives the accretion efficiency:

$$\eta_{accr} \sim \frac{GM}{rc^2} = \frac{R_S}{2r} \tag{1.5}$$

R_S is the Schwarzschild radius : $R_S = 2GM/c^2$.
The efficiency for a Schwarzschild black hole is typically estimated to be ~ 0.057 (e.g., Marconi et al., 2004; Merloni, 2004) while considering a maximally rotating Kerr SMBH it can reach values of ~ 0.42. Large-scale gravitational instabilities such as those produced by galaxy bars, mergers and interactions between galaxies, are expected to remove significant amounts of angular momentum and to drive the gas into the central regions of galaxies, as shown in Figure 1.1.
However, the gravitational torques exerted on the gas by these large-scale processes have a limited effect on sub-Kpc scales, and smaller-scale processes are predicted to drive the gas down to $\sim$ 10-100 pc.

The accretion onto a SMBH is limited by the effects of the radiation pressure experienced by the infalling matter. As first pointed by Arthur Eddington in the 1920s, this limit

depends on the mass of the central source and by the opacity of the infalling material. A SMBH accreting at the critical mass accretion rate emits at the so called Eddington luminosity: this critical value is obtained by imposing the balance between radiation pressure acting on electrons (neglecting radiation pressure on protons) and the gravitational force acting on protons (neglecting that acting on electrons), being electrons and protons coupled by the electromagnetic interaction. The outward radiation force acting on a single electron at a distance r from a source of luminosity L is given by:

$$F_{rad} = \frac{L}{4\pi r^2 c} \cdot \sigma_T \tag{1.6}$$

where the first term is the outward momentum flux and the second the Thomson scattering section [1]. The modulus of the gravitational force experienced by a proton with mass m_p at a distance r due to the central mass M is given by:

$$F_{grav} = \frac{GMm_p}{r^2} \tag{1.7}$$

Equating the two relations one gets the Eddington luminosity:

$$L_{Edd} = \frac{4\pi G m_p c}{\sigma_T} \simeq 1.26 \cdot 10^{38} \frac{M}{M_\odot} erg/s \tag{1.8}$$

Luminosities and accretion rates higher than the Eddington limit in so-called Super-Eddington accretion are possible: if the luminosity exceeds the Eddington luminosity, the gas is expelled. The ratio of the observed accretion luminosity over the Eddington luminosity is called the Eddington ratio ($\lambda_{Edd} = L_{acc}/L_{Edd}$) and it is a useful quantity to compare BH accretion rates over a wide range of BH masses.

1.3.2 The Accretion Disc

The power house behind AGN activity is mass accretion onto the BH on $\ll 1pc$ scales. The basic theory of the accretion disc (the so-called α disc) has been around for almost 40 years (e.g., Shakura and Sunyaev, 1973). In the case of optically thick accretion, viscosity causes the gas to lose angular momentum and fall towards the BH, transporting the angular momentum outwards. The optically thick accretion disc is geometrically thin and the energy spectrum is comprised of multi-temperature components which reach their peak temperature at the centre. According to the virial theorem, half of the potential gravitational energy released heats the gas, while the other half is radiated away:

$$\frac{GM\dot{M}}{2r} = 2\pi r^2 \sigma T^4 \tag{1.9}$$

[1] $\sigma_T = \frac{8\pi}{3}\langle\frac{e^2}{m_e c^2}\rangle^2 = 6.65 \cdot 10^{-25} cm^2$.

where σT^4 is the energy emitted per unit area and time by a black body with temperature T and $2\pi r^2$ is the disk area.
The temperature at a distance r is then:

$$T \propto (M\dot{M})^{1/4} r^{-3/4} \tag{1.10}$$

which can be rewritten in terms of the Eddington accretion rate $M_{Edd} = L_{Edd}/\eta c^2$ as follows:

$$T(r) = 6.3 \cdot 10^5 \langle \frac{\dot{M}}{\dot{M}_{Edd}} \rangle^{1/4} \qquad \langle \frac{M}{10^8 M_\odot} \rangle^{-1/4} \langle \frac{r}{r_S} \rangle^{-3/4} K. \tag{1.11}$$

Thermal emission from an AGN accretion disk is expected to be prominent in the large UV spectrum with a temperature peak T $\sim 10^5$ K.

Depending on the accretion disc viscosity and the mass accretion rate, the accretion disc is predicted to change between an optically thick and an optically thin state. The transition from optically thin to optically thick is likely to correspond to an Eddington ratio of $10^{-3} - 10^{-2}$ (e.g., Esin et al., 1997; Gallo et al., 2003). The alternative solution to the accretion-disc equations is therefore the optically thin accretion disc, a state achieved at low mass accretion rates and generically referred to as Radiatively Inefficient Accretion Flows (RIAFs; e.g., Narayan and Yi, 1994; Blandford and Begelman, 1999). The optically thin accretion disc is unable to cool efficiently (the cooling time exceeds the accretion time) and the energy is lost through non-radiative processes such as convective transport of energy and angular momentum to large radii or an outflowing wind. Magnetic fields are likely to dominate viscosity and the transport of angular momentum in accretion discs.

1.3.3 Narrow and Broad-Line regions

One of the most important observational features of AGN is the presence of redshifted, time variable emission lines with Doppler widths of order of 10^3 to a few 10^4 km s^{-1}. The most prominent of these lines are the hydrogen Balmer lines Hα λ6563, Hβ λ4861, Hγ λ4340 and Lyα λ1216. Moreover, also forbidden or semi-forbidden lines as MgII λ2798, [CIII] λ1909 and CIV λ1549. The narrower widths (a few hundred km s^{-1}) and the lack of variability led to the conclusion that these lines originate from a region that was much larger and kinematically distinguished from that of the broad lines. The Broad Line Region (BLR) has a size of 10-100 light days in Seyfert 1 galaxies, and up to a few light years in bright quasars. The electron density in this region is at least $10^8 cm^{-3}$ and the gas velocity 3000-10000 km s^{-1}. On the contrary, in the Narrow Line Region the density is about $10^3 - 10^6$ cm^{-3} with a velocity of the gas of 300-1000 km s^{-1}. It is resolved by ground-based observations in several nearby Seyfert galaxies, showing dimension of 100

- 300 pc. Low density hot (T $\simeq$100-1500 K) gas in this extended region is ionized by high energy photons from the inner AGN regions.

1.3.4 The dusty torus

The dusty molecular torus surrounding the central engine of AGN is expected to consist of molecular gas of warm and hot dust (T $\simeq$100-1500 K). The simplest torus is made of a smooth distribution, while observations prefer more elaborated structures, made of clumps and inter-clump material. The inner radius of the torus is set by the dust sublimation temperature.

1.4 Spectral Energy Distribution

Active Galactic Nuclei show a detectable emission covering the whole electromagnetic spectrum: this means that they are being discovered in all spectral bands and, most importantly, that the different wavelength regimes open different windows on the physics of AGN. They emit roughly equal amounts of energy throughout the major part of the electromagnetic spectrum, extending from $> 100\mu$m in the FIR to > 10 keV in the hard X-ray. The 10% also emit strongly at radio wavelengths and a significant fraction of these are strong gamma-ray sources. Their emission can be described by means of the Spectral Energy Distribution (SED), generally a $log(\nu F_\nu)$ vs $log\nu$ or $log(\lambda F_\lambda)$ vs $log\lambda$ plot showing the energy emitted per decade of frequency (or wavelength).
Thus, to obtain a complete picture of these powerful sources, observations must be made at all wavelengths. In many parts of the spectrum these objects are sufficiently faint to push the limits of current technology. Given that many of them are variable on fairly short timescales, obtaining a single snapshot of a AGN SED is a daunting task and one that has not been completed for many AGN to date. The number of compiled AGN SEDs in the literature has increased rapidly in the past decade, including many for individual objects and larger compilations at both low and high redshift.
While many of these incorporate data observed over many years and often by many different groups in order to produce an SED, the majority are partially contemporaneous and provide a reasonable approximation to an instantaneous SED for relatively non-variable objects in at least the near-IR-optical range. When multiple epochs are available, it is also possible to estimate the level of variability and thus the uncertainty in the final SED.

The notable features in quasar SEDs are labelled in Figure 1.2. Both radio-loud (RLQs) and radio-quiet quasars (RQQs) typically show bumps in the optical-UV and in the

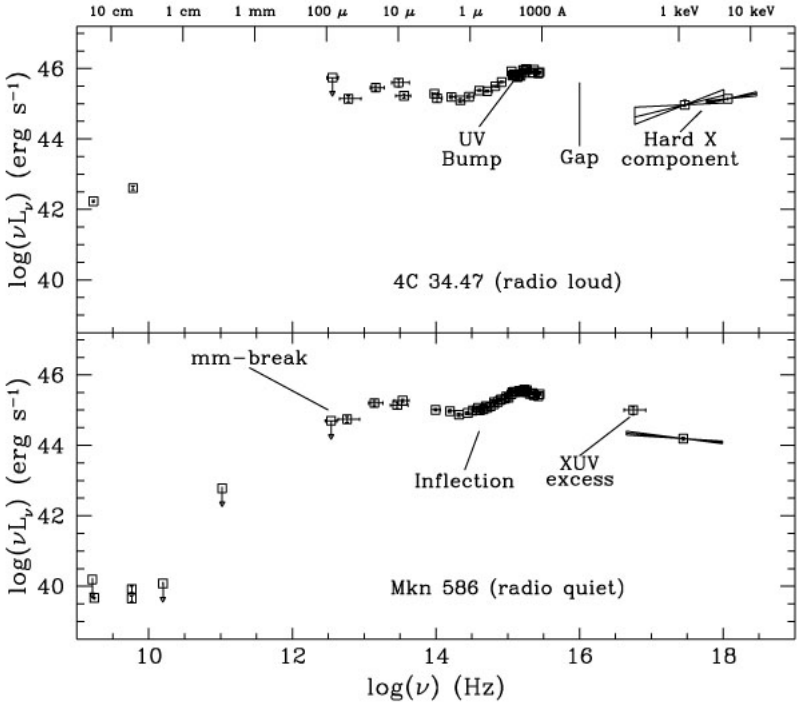

FIGURE 1.2: Rest-frame radio-X-ray spectral energy distributions (SEDs) from Elvis et al. (1994), for low-redshift radio-loud (upper panel) and radio-quiet (lower panel) QSOs.

IR with an inflection point at ~ 1 μm between the two. This inflection point, which represents a minimum in the energy output of the quasar, lines up with the peak in the starlight contribution from the host galaxy. In the lower luminosity Seyfert galaxies the host galaxy contribution becomes comparable to the emission from the active nucleus, flattening the optical-IR SED and resulting in an apparent decrease in the strength of the optical and IR bumps.

1.4.0.1 Infrared and Radio

The near-IR bump generally peaks at ~ 25 - 60 μm, and the emission is due to cold dust heated by star formation in the host galaxy. Temperature ranges from 10 to 1800 K (Phinney, 1989). The spectrum is broad, decreasing slowly to wavelengths $> 100\mu$m. For RQQs, those objects with sub-mm or mm data are those which are brightest in the FIR and are mostly at low redshift. Typically very sharp cut-offs are seen between 100 μm and 1 mm (Chini et al., 1989; Barvainis et al., 1992; Hughes et al., 1993).
RLQs fall into two distinct groups generally believed to be distinguished by the orientation of the source to our line-of-sight. Core-dominated (CD) RLQs are those in which relativistically beamed, synchrotron emission is pointed directly at us and so is boosted. In these sources, the radio-IR SED tends to be smooth, suggesting that the IR is a higher-energy extension of the synchrotron emission in the radio. The SED extrapolates

smoothly from the radio into the IR and it is argued to be probably due to non-thermal emission. In the near-IR, $\sim 3\mu$m, there is a narrow peak of emission which does not vary in the same way and is believed to originate in hot dust (Courvoisier, 1989). Even in this well-established, non-thermal source, dust emission is an important contributor.
Lobe-dominated (LD) RLQs are dominated by extended emission on either side of the central AGN, powered by the relativistic jets which, in these sources, are not close to our line-of-sight. Studies of the radio-FIR SEDs of the core emission have revealed a discontinuity in the mm region which implies that emission in the FIR is unrelated to the non-thermal radio emission (Antonucci et al., 1990) and so favors a thermal origin for the FIR.
The typical steepness of the FIR cut-off, $\alpha_{FIR} \sim 3.75 \pm 0.48$ (Hughes et al., 1993) in RQQs, provides a convincing argument for thermal emission from cool dust to dominate the FIR SEDs. Detailed modelling of the dust reverberation deduces that the clouds are $\sim$ 0.3 - 1.3 light years from the central source with dust sublimation temperatures 1300-2000 K (Barvainis et al., 1992). In addition the first large compilations of AGN SEDs demonstrated the universal presence of the inflection mentioned above. In a dust scenario, the corresponding decrease in the NIR emission coincides with the sublimation temperature. This mounting evidence for thermal dust emission led to the development of pure dust models to explain the IR continuum of AGN. These models generally include some combination of cool dust from the host galaxy, warm dust in star formation regions and hot dust, for example in a dusty torus, heated by the central ionizing continuum. The remaining emission at 1 μm is assumed to originate in starlight from the host galaxy and perhaps a nuclear starburst in the higher luminosity objects. Problems with these models include: the lack of observed silicate features in the NIR spectra of AGN which results in the need to minimize their strength in models (Roche et al., 1984), the fine tuning required to explain the strong IR-X-ray correlation, and the similarity of the IR continua in RLQs and RQQs which, in this scenario, originate in different mechanisms.

1.4.0.2 Optical and ultra-violet

There is a second "bump" in typical quasar SEDs, the big blue bump (BBB), which dominates the optical-UV emission and often their total energy output. Since the X-ray emission is generally below an extrapolation of this BBB, it is generally thought to peak in the EUV region. The detection of a peak is a major step forward as it allows constraints to be placed on the EUV emission, which is the source of most of the ionizing photons, and on the relation between the UV and soft X-ray emission. At high redshift a similar measurement is difficult due to the affects of intervening absorption on the continuum shortward of the Ly - α emission line. The origin of the BBB in AGN has

been the subject of some debate in the literature over the past decade or so. Thermal emission from an optically thick, geometrically thin accretion disk (AD) is favored by many. When combined with a corona, it is able to explain the ultra-soft X-ray excess as well. Theoretically, since AGN are generally believed to be powered by a central massive black hole, an AD is very likely to be present in an AGN core and to be a substantial contributor to its energy output. However problems with this model occur when detailed predictions are compared with the observations. In particular, AD models generally predict that the emission is polarized and has Lyman edge absorption due to the large optical depths. Neither of these properties is universally present in AGN SEDs and there is an on-going debate concerning the importance of these discrepancies.
The main alternative model for the BBB is free-free emission. This model can produce an OUV continuum with roughly the correct shape, but it is unable to explain the observed range of slopes. It is also inconsistent with the lack of observed, strong X-ray emission lines.

In conclusion, despite the continuing debate, the AD plus corona model remains the most viable model for the OUV-soft-X-ray BBB in AGN SEDs.

1.4.0.3 X - ray and γ - ray

There are several components to the X-ray emission from AGN and their relative contributions differ depending on the type of object and energy range.
In RQQs and Sy1 galaxies, the mid-X-ray region $\sim$ 1 - 5 keV) is dominated by a power law with a slope $\alpha_X \sim 1$ ($F_\nu \propto \nu^{-\alpha_X}$, (Wilkes and Elvis, 1987; Reeves et al., 1997). The simplest, non-thermal models include a power-law distribution of electrons which Thomson scatter off soft seed photons. These models match the observed spectral slope but do not produce the observed $\sim$ 200 keV, high-energy cut-off. Currently the best models include repeated Compton scattering, either combined with a non-thermal plasma having power law electron distribution or thermal Comptonization of soft seed photons.
In the same spectral region, CDRLQs tend to have stronger emission (Zamorani 1981) and flatter slopes, $\alpha_X \sim 0.5$; this is thought to be due to a radio-linked, synchrotron self-Compton (SSC) component. LDRLQs are intermediate between the two classes.
At harder X-ray energies, > 5 keV, the spectrum flattens, particularly in low-luminosity objects. This flattening is generally weak or absent in higher luminosity quasars. The flattening is widely accepted to originate in Compton reflection of the primary X-ray continuum in cool ($\sim 10^4$ K) optically thick material at the surface of the AD. Reflection from neutral and ionized material, probably located in the molecular torus and/or the AD has been observed in a large number of Sy1 galaxies and dominates the X-ray spectrum up to $\sim$ 300 keV, where the material becomes optically thick to Compton scattering.A

fluorescent, Fe Kα emission line is commonly observed, again tending to be stronger in low luminosity sources. This line is often broad, and sometimes double-peaked, consistent with its origin in an accretion disk.
At soft energies, < 1 keV, the X-ray spectra of $\sim 50\%$ of both radio-loud and radio-quiet AGN steepens significantly to form the soft excess (Masnou et al., 1992). This component generally dominates their spectra leading to systematically steeper slopes at these energies (Fiore et al., 1994; Buehler et al., 1995). The soft excess can be extremely steep and is often called the ultra-soft excess. Given the general increase of both the BBB on the low energy and the ultra-soft excess on the high energy side of the EUV region, it is tempting to identify both as part of the same, BBB component. There is little direct evidence to this effect, for example observations of coordinated variability, but circumstantial evidence includes the anti-correlation of optical and soft X-ray slopes (Puchnarewicz et al., 1996) and the extrapolation of the soft X-ray into the UV region (Laor et al., 1997).

Another key component of X-ray spectra of quasars and Sy galaxies is absorption by cold and/or warm material. Sy1 galaxies and quasars typically show low absorption column densities ($N_H \sim 1020$ - 21 cm^{-2}) often including ionized absorption edges indicating the presence of warm material originating in the same material as that responsible for the narrow associated UV absorption lines common in many types of AGN.

There is a well-established correlation between X-ray and optical emission in AGN, such that higher luminosity sources have relatively weak X-ray emission. Similar evidence is found when comparing low and high luminosity quasar SEDs. The relation as determined by Just et al. (2007) and investigated by several authors later on (e.g., Lusso et al., 2010; Martocchia et al., 2017), is:

$$\alpha_{OX} = \frac{log(f_{2keV}/f_{2500\text{Å}})}{log(\nu_{2keV}/\nu_{2500\text{Å}})} = 0.3838\ log(f_{2keV}/f_{2500\text{Å}}) \tag{1.12}$$

where α_{OX} is the effective optical-to-X-ray slope.

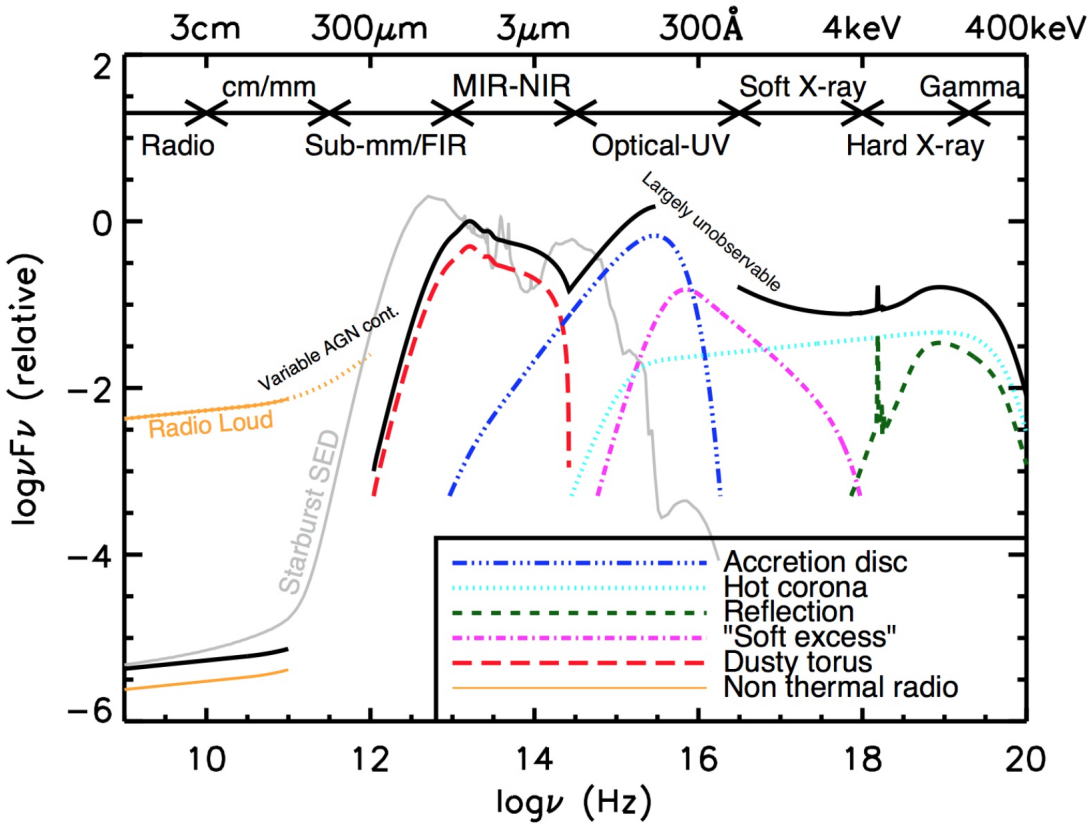

FIGURE 1.3: A schematic representation of an AGN SED (Padovani et al., 2017), based on the observed SED of radio-quiet AGN (Elvis et al., 1994; Richards et al., 2006). As comparison, the grey curve shows an example of radio-UV SED of the starburst galaxy M82 (Silva et al., 1998).

1.5 Unified Model

In the last twenty years a lot of unification schemes have been proposed to explain the wide range of spectral properties of AGN. They try to explain the most important differences between type 1 and type 2 AGN, making very few assumptions. The simplest hypothesis to explain much of AGN phenomenology is that the differences among various types of AGN arise from orientation dependence; the so called "unification model" tries to unify various AGN types in terms of a single basic source structure whose appearance to the observer depends strongly on the viewing angle. In such unification schemes it is therefore postulated that the different appearance of one class compared with a second is the result of viewing the same type of object at a different angle. Properties that may depend on the viewing angle and may so contribute to intrinsic anisotropy in these sources include absorption by dust or optically thick gas in any non-spherically symmetric distribution and relativistic motion, leading to Doppler boosting of the emission which peaks in the direction of this motion.

The current AGN paradigm is built around an axisymmetric central engine that consists of an accretion disk surrounding (up to a distance $R < 0.01$ pc) a Supermassive ($\geq 10^6 M_\odot$) black hole (SMBH). The UV–optical continuum emission is supposed to arise primarily in the accretion disk. Bi-directional relativistic jets emerge from this system along the disk axis, emitting Doppler-boosted radiation via synchrotron and inverse Compton mechanism. Both the jets and the accretion disk structure are thought to contribute to the X-ray emission. The broad emission lines that are so prominent in the UV - optical spectra of AGN are produced in the relatively dense ($n_e \sim 10^{11}$ cm^{-3}) gas clouds at distances of $R \sim 0.01 - 0.1$ pc, with a covering factor [2] around $1 - 3\%$. On parsec scales, this entire system is embedded in a dusty torus that is opaque over most of the electromagnetic spectrum; this torus plays a key role in AGN unification models, since it shields both the accretion disk, the BLR and inner jet structure from the direct view of external observers in the torus plane. The torus absorbs radiation from the central source and re-emits this energy in the infrared.

Probably the best known unification scheme is that between the two types of Seyfert galaxies. Seyfert galaxies are AGN whose luminosity ranges from 0.1 to 10 times that of the host galaxy, while QSOs have luminosity 10-10^5 times greater than the galaxy luminosity. In the mid-1970s, Khachikian and Weedman (1974) found that Seyfert galaxies fell into two spectroscopic classes, those with both narrow and broad emission lines (Sy1) and those with narrow lines only (Sy2). The narrow-line spectra of types 1 and 2 are statistically indistinguishable from one another, so Sy2s seem to be Sy1s without the broad lines. Moreover, Sy2s are typically less luminous than Sy1s by about 1 magnitude

[2] The covering factor indicates the fraction of photons occulted by the absorbing clouds.

in the optical part of the spectrum. This led to unification hypotheses in which Sy2s are intrinsically Sy1s whose continuum and broad-line emission is attenuated in the direction of the observer. In the early 1980s Antonucci et al. (1990) found that the polarization spectra of some Sy2 galaxies contained broad emission lines like those seen in Sy1 spectra. At least some Sy2 galaxies contain broad emission lines, but with their strength greatly reduced such that they are dominated by the continuum and narrow lines except when viewed in polarized light. Since the most common cause of polarization is scattering of light by either dust or electrons, this observation led to an interpretation of Sy2 galaxies as edge-on Sy1 galaxies where optically thick material in a flattened, disk-like geometry obscures our direct view of the broad emission-line region. The broad lines are visible in polarized light when they are scattered into our line of sight by dust or electrons above and/or below this material. If the line of sight is along the system axis or under a small offset angle the observer sees a greater luminosity coming from a small angular region because he intercepts the direction of the jets. In this case the observed object is a QSO or a quasar.
Although the Unified Model has allowed to explain much of the complex AGN phenomenology, it appears to be in conflict with recent set of observations (Bianchi et al., 2012), requiring additional effects to explain the difference between type 1 and type 2 AGN (e.g., the discovery of type 2 sources without broad optical lines in the polarized spectrum).

The radio unification scheme combines the torus with a relativistic jet observed in approximately 10% of all high-ionization AGNs, aligned with the symmetry axis of the system. Radio unification can be used to make specific predictions about the observed properties of compact and extended radio-loud AGNs.

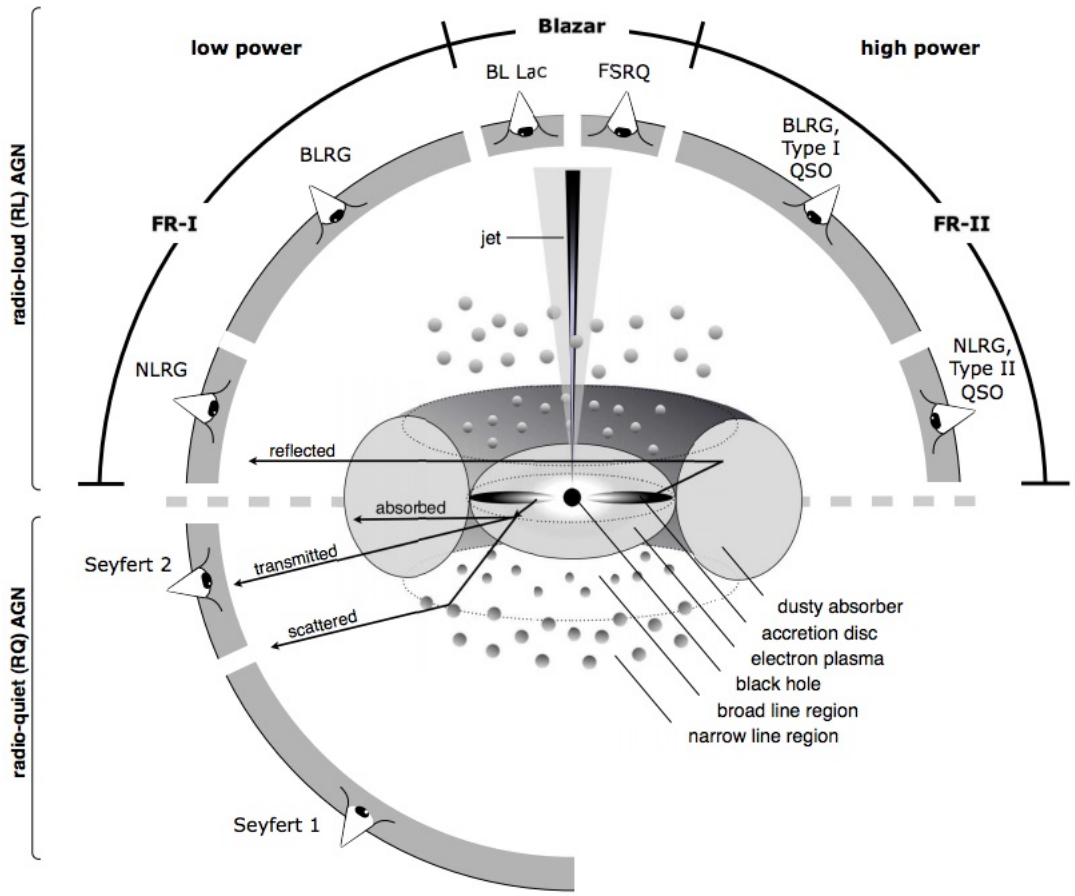

FIGURE 1.4: A schematic representation of an AGN according to the unified model, from Singh (2013).

CHAPTER 2

Evolution of Active Galactic Nuclei and AGN-galaxy co-evolution

Over the last few years there has been a lot of interest in the cosmic "co-evolution" of Supermassive black holes and the stellar populations of the galaxies that they reside in. Beginning at about the turn of the 21st century, black hole astrophysicists have acknowledged the relevance of their subject of study for a broader community of cosmologists and extragalactic astronomers, thanks to the multiple lines of evidence pointing towards a fundamental role played by black holes in galaxy evolution.
It is now understood that SMBH black hole growth is due mainly to radiatively efficient accretion over cosmological times, taking place during their active phases. This, together with the understanding of a near universal presence of black holes in galactic centers has led to the suggestion that most, if not all, galaxies went through a phase of nuclear activity in the past, during which a strong physical coupling (generally termed "feedback") might have established a long-lasting link between host and black hole properties.

2.1 Evolution of AGN

From the point of view of AGN, the most basic description of the evolving population lies in the luminosity function (i.e. AGN Luminosity Function, LF) $\phi(L, z)$, defined as the number of sources per unit volume and luminosity in the range between L and L+dL.

$$\Phi(L) = \frac{dN}{dV dL} \tag{2.1}$$

Let us assume that the local universe is Euclidean and filled with sources with LF $\Phi(L)$. Sources with luminosity L can be observed out to a distance $r = (L/4\pi S)^{1/2}$, being S the limiting flux of the observations. The number counts of sources over the solid angle Ω are then:

$$N(>S) = \int_{L_{min}}^{\infty} \frac{1}{3}\Omega r^3 \Phi(L) dL = \frac{1}{3}\frac{\Omega}{(4\pi)^{3/2}} S^{-3/2} \int_{L_{min}}^{\infty} L^{3/2}\Phi(L) dL \tag{2.2}$$

where $L_{min}(r)$ is the faintest luminosity that can be observed over a flux limit S out to a distance r_{max}. Therefore, the slope of the cumulative number counts of a (non-evolving) class of objects in an Euclidean universe is fixed to $-3/2$.
In a more general case, the correct relativistic expression for number counts differs from Equation 2.2, due to cosmological effects. Radiation emitted at frequency ν' is observed at a redshifted frequency $\nu = \nu'/(1+z)$, and therefore the observed flux density depends on the shape of the spectrum of the source. Moreover, curvature effects modify the volume element per unit redshift, making it smaller at increasing z.
The simplest general approach to describe the evolution of a LF is by defining two functions $f_d(z)$ and $f_l(z)$ that take into account the evolution of the number density and luminosity, respectively:

$$\Phi(L, z) = f_d(z)\Phi\left(\frac{L}{f_l(z)}, z = 0\right). \tag{2.3}$$

In the *pure luminosity evolution* (PLE, Mathez, 1976) scenario, the comoving number density of sources is constant (so $f_d = cost$), but luminosity varies with cosmic time. In the *pure density evolution* (PDE, Schmidt, 1968) case the shape of the LF and the source luminosity are fixed ($f_l = cost$), while the comoving density of sources of any luminosity varies (Merloni and Heinz, 2013).
Both the PLE and PDE should be basically considered as mathematical descriptions of the evolution of the LF. There is no clear reason why the LF should behave only in one of these two simple pictures, and indeed as wider and deeper surveys has been completed, larger samples have been collected and hence more complex models have been developed throughout the years.

Probably the most accurate description of the overall evolution of the LF comes from deep X-ray surveys. Thanks to the advent of deep surveys in the optical and in the X-ray bands, the LF of both optically and X-ray selected AGN are nowadays usually described by the *luminosity dependent density evolution* (LDDE) model (for the X-rays see e.g. Ueda et al. (2003), Hasinger et al. (2005) and see Bongiorno et al. (2007) for the first optical LF which has been successfully modelled with the LDDE).

As in the PDE model, the redshift evolution of the LF is described as

$$\frac{d\Phi(L_X, z)}{dlog(L_X)} = \frac{d\Phi(L_x, z=0)}{dlogL_X} e(L_X, z), \tag{2.4}$$

where the local LF is usually represented with a power-law with two different indexes, for low and high luminosities:

$$\frac{d\Phi(L_X, z=0)}{dL_X} = \begin{cases} AL_\star^{\gamma_1-\gamma_2} L_X^{-\gamma_1} & L_X \leq L_\star \\ AL_X^{\gamma_2} & L_X > L_\star \end{cases} \tag{2.5}$$

and the evolution factor $e(z)$ is defined as:

$$e(z) = \begin{cases} (1+z)^{p_1} & z \leq z_c(L_X) \\ e(z_c)[(1+z)/(1+z_c(L_X))]^{p_2} & z > z_c. \end{cases} \tag{2.6}$$

The z_c parameter represents the redshift at which the evolution stops. The parameters p_1 and p_2 characterize the rate of the evolution and the rate of counterevolution for $z > z_c$ respectively.
The LDDE model is obtained by introducing a luminosity dependence of z_c, assumed to be a power-law (La Franca et al., 2005):

$$z_c(L_X) = \begin{cases} z_c^\star & L_X \geq L_a \\ z_c^\star (L_X/L_a)^\alpha & L_X < L_a. \end{cases} \tag{2.7}$$

In the last decade, hard X–ray surveys have allowed to select almost complete AGN samples (including both type-1 and type-2 objects). Thanks to these studies, the evolution of the whole AGN population has been derived up to $z \sim 5$ by many authors, all achieving fairly consistent results (Ueda et al., 2003; La Franca et al., 2005; Brusa et al., 2009; Civano et al., 2011; Ueda et al., 2014; Kalfountzou et al., 2014; Vito et al., 2014; Aird et al., 2015b,a). It has been shown that (a) the peak of the AGN space density moves to smaller redshift with decreasing luminosity, and (b) the rate of evolution from the local Universe to the peak redshift is slower for less luminous AGN. It appears that SMBH generally grow in an anti-hierarchical fashion, i.e. while more massive SMBH ($10^{7.5}$–$10^9 M_\odot$) in rare, luminous AGN could grow efficiently at $z = 1-3$, smaller SMBH in more common, less luminous AGN had to wait longer to grow ($z < 1.5$). The differential evolution of bright and faint AGN with redshift has been described as *downsizing* (Barger and Cowie, 2005; Hasinger et al., 2005), see Figure 2.1. This implies that AGN activity in the low-z universe is dominated by either high-mass BHs accreting at low rates

or low-mass BHs growing rapidly. Hopkins et al. (2005) proposed that the faint end of the LF is composed of high mass BHs experiencing quiescent accretion. The bright end, on the other hand, in this picture corresponds to BHs accreting near their Eddington limit. In this model, QSO activity is short-lived and it is assumed to be driven by galaxy mergers.

There is also strong evidence on the redshift and luminosity dependence of the fraction of obscured ($N_H > 10^{22}$ cm^{-2}) AGN, indeed it has been shown that this fraction increases with decreasing luminosity (Lawrence and Elvis, 1982; La Franca et al., 2005; Treister et al., 2005; Ueda et al., 2014; Aird et al., 2015b, see also Sazonov et al. 2015 for a discussion of selection biases), and increasing redshift (La Franca et al., 2005; Treister and Urry, 2006; Hasinger, 2008; Ueda et al., 2014; Vito et al., 2014, but see also Gilli et al. 2010).
Attempts to constrain models for galaxy formation and evolution from the optical and X-ray luminosity functions were made in the last decade by several authors (see e.g. Granato et al., 2001, 2004; Di Matteo et al., 2005; Menci et al., 2005). The predictions of these models are in good agreement with some of the observations, like the downsizing trend; however, they overestimate by a factor of ~ 2 the space density of low-luminosity Seyfert-like AGN at $z = 1.5 - 2.5$.

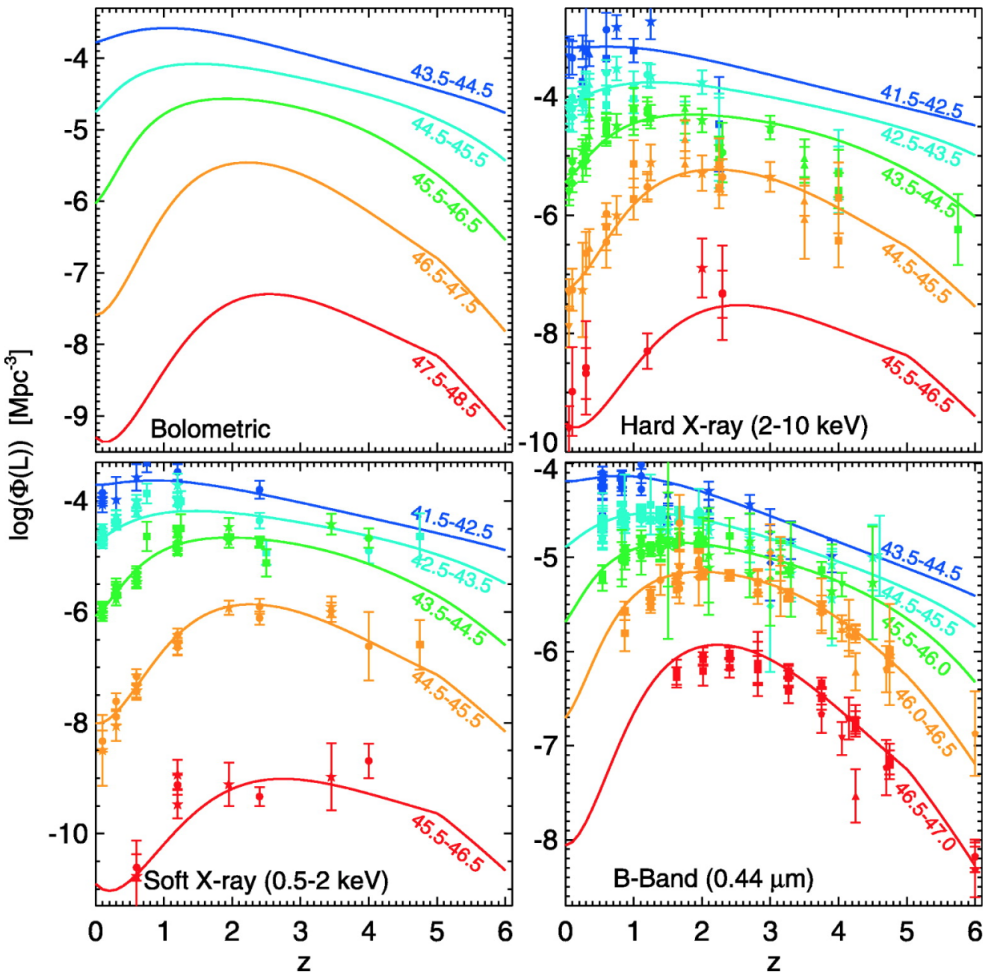

FIGURE 2.1: Total number density of QSOs in different luminosity intervals (colors) reported in $\log(L_{band}/\mathrm{erg\ s^{-1}})$ as a function of redshift, from the data best-fit double power law model; in bolometric luminosity, B band, soft X-rays (0.5 - 2 keV) and hard X - rays (2 - 10 keV). Figure from Hopkins et al. (2007).

2.2 X-ray surveys and the X-ray background

AGN are powerful X-ray emitters. The discovery of the cosmic X-ray background (CXRB, Giacconi et al., 1962) opened up a privileged window for the study of the energetic phenomena associated with accretion onto black holes.
The X-ray sky is almost dominated by the AGN population, due to the relative weakness of the other X-ray emitters (mostly X-ray binaries, but also magnetically active stars and cataclysmic variables), at least down to the faintest fluxes probed by current X-ray telescopes. The goal of reaching a complete census of evolving AGN has therefore been intertwined with that of fully resolving the CXRB into individual sources.
In the last decade, the launch of modern X-ray telescopes like *Chandra* (NASA) and *XMM-Newton* (ESA) has enabled strong observational progress. Sensitive imaging spectroscopy in the $0.5-10$ keV band with up to $50-250$ times the sensitivity of previous missions, as well as high quality positional accuracies (up to $\sim 0.3-1$" for Chandra) were made available for X-ray astronomy studies. Deep extra-galactic surveys have probed the X-ray sky down to extremely faint fluxes (as low as $\sim 10^{-17}$ erg s^{-1} cm^{-2} in the $0.5-2$ keV band and $\sim 10^{-16}$ erg s^{-1} cm^{-2} in the $2-8$ keV band), thus making available large source samples for statistical X-ray source population studies.
With these deeper and larger X-ray surveys that have been performed, a new generation of synthesis model for the CXRB has been developed (see Gilli et al., 2007; Treister et al., 2009). These new models have progressively reduced the uncertainties in the N_H absorption distribution, providing an almost complete census of the unobscured and moderately obscured AGN populations. These sources dominate the X-ray counts in the lower energy band, where almost all the CXRB radiation has been resolved into individual sources.
However, at the peak energy of the CXRB (around ~ 30 keV), only a small fraction ($\sim 5\%$) of the emission has been resolved into individual sources (Merloni and Heinz, 2013). CXRB synthesis models ascribe a substantial fraction of this unresolved emission to Compton-thick AGN. Gilli et al. (2007) model requires a population of Compton-thick AGN as large as that of Compton thin AGN to fit the residual background emission. Still, the redshift and luminosity distribution of these sources is essentially unknown, due to their faintness even at hard X-ray energies. The quest for the physical characterization of this missing AGN population represents one of the last current frontiers of the study of AGN evolution.

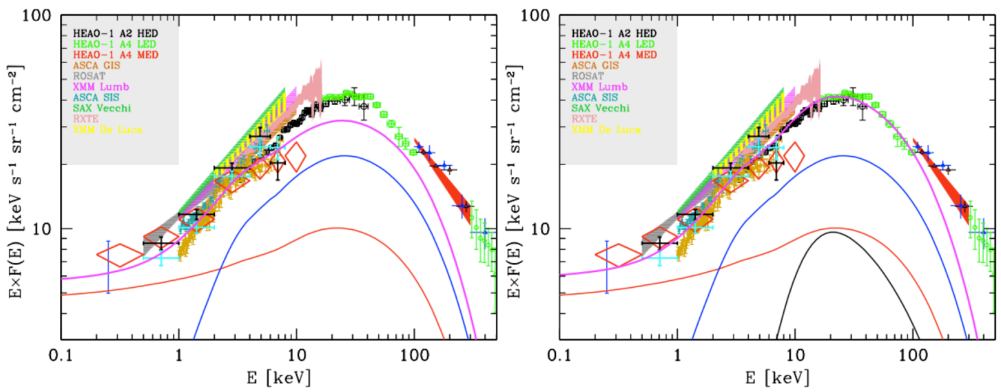

FIGURE 2.2: Observed spectrum of the extra-galactic CXRB from several X-ray satellites data. The solid magenta line shows the prediction of the Gilli et al. (2007) model for AGN and galaxy clusters; red and blue solid lines represent the contribution from unobscured and Compton-thin AGN respectively. These contributions, shown in the left panel, are not enough to fully describe the data. In the right panel, the black line marks the Compton-thick AGN contribution required to match the CXRB intensity above 30 keV. Adopted from Gilli et al. (2007).

2.3 BH evolution

In the early 1990s, deep optical surveys of star-forming galaxies began to probe the cosmological evolution of the rate at which stars are formed within galaxies, thus providing robust constraints for models of galaxy formation and evolution (see Madau et al., 1996). It was soon clear that the QSO (optical) luminosity density and the *Star Formation Rate* (SFR) density evolved in a similar fashion, being much higher in the past, with a broad peak around z∼2 (Boyle and Terlevich, 1998).

Therefore, studying the mass function of SMBHs and its evolution with redshift is of great significance not only for understanding their cosmological evolution of mass and spin but also for addressing many issues in galaxy formation (e.g., Di Matteo et al., 2005; Shankar et al., 2009).

The most usual approach to investigate the SMBH mass function stems from the pioneering work of Soltan (1982) and it is based on the argument that black hole growth is mainly driven by mass accretion and assumes two parameters: the radiative efficiency for energy conversion of accretion and the Eddington ratio of AGN. With an appropriate mass-to-energy conversion efficiency is then possible account for the the mass of black holes in local AGN by integrating the overall energy density released by AGN themselves. A much larger amount of information can be found in the differential mass and luminosity functions. Assuming that a continuity equation governs the SMBH mass evolution, the mass function at any given time can be used to predict the mass function at any other time, if the distribution of accretion rates as a function of black hole mass is known.

The continuity equation can be written in the form:

$$\frac{\partial \psi(\mu,t)}{\partial \mu} + \frac{\partial}{\partial \mu}(\psi(\mu,t) < \dot{M}_{BH}(\mu,t) >) = 0 \tag{2.8}$$

where $\mu = log(M_{BH})$, $\psi(\mu,t)$ is the SMBH mass function at a time t, and $< \dot{M}_{BH}(\mu,t) >$ is the avarage accretion rate of SMBH of mass M_{BH} and can be defined through a *fueling* function $F(\dot{\mu},\mu,t)$ describing the distribution of accretion rates for objects with mass M_{BH} at a time t:

$$< \dot{M}_{BH}(\mu,t) >= \int \dot{M}_{BH} F(\dot{\mu},\mu,t) d\dot{\mu} \tag{2.9}$$

The last function can be derived by inverting the integral that relates the luminosity function of the population with the relative mass function:

$$\phi(l,t) = \int F(l-\epsilon,\mu,t)\psi(\mu,t)d\mu \tag{2.10}$$

with $l = log(L_{BOL})$ and $\epsilon = log(\epsilon_{rad}c^2)$, being ϵ_{rad} the radiation efficiency, assumed to be constant.

The continuity equation can then be integrated backwards from z = 0 where both the luminosity function and the mass function are known.

This computation has been performed either using the CXRB as a "bolometer" to derive the total energy density released by the accretion process (Fabian and Iwasawa, 1999), or by considering evolving AGN luminosity functions (Yu and Tremaine, 2002; Marconi et al., 2004; Merloni and Heinz, 2008). This approach represents a major success of the standard paradigm of accreting black holes as AGN power-sources, as the radiative efficiencies requested in order to explain the local relic population are within the range ϵ= 0.06−0.20, predicted by standard relativistic accretion disc theory. These evidences suggest that a tight link should exist between SMBH growth and host galaxy evolution.

The specific instantaneous ratio of black hole mass to accretion rate as a function of SMBH mass defines a timescale, the so-called *growth time*, or *mass doubling time* (see Figure 2.3a and 2.3b). The redshift evolution of the growth time distribution can be used to identify the epochs when black holes of different sizes grew the largest fraction of their mass: black holes with growth times longer than the age of the universe are not experiencing a major growth phase, which must have necessarily happened at earlier times (see Merloni and Heinz, 2013).

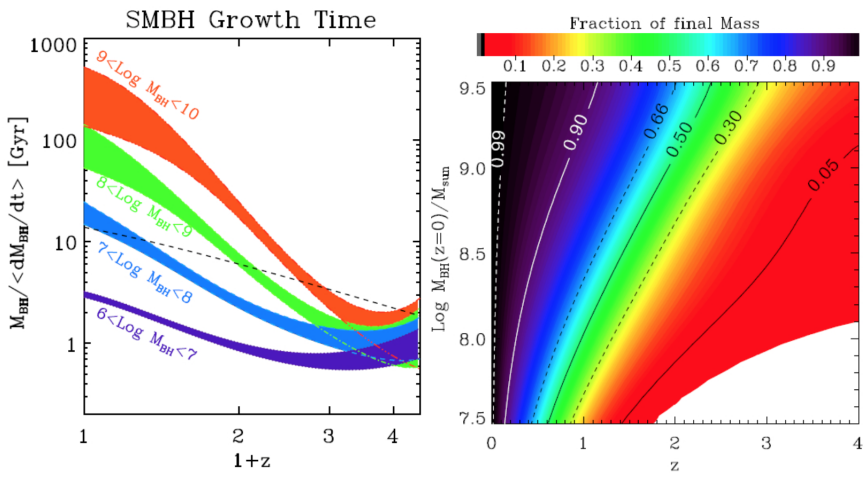

(A) (B)

FIGURE 2.3: In Figure 2.3a the average Growth time of SMBH (in years) as a function of redshift for different black hole mass ranges. The dashed line marks the age of the universe; only black holes with instantaneous growth time smaller than the age of the universe at any particular redshift can be said to be effectively growing. In Figure 2.3b the fraction of the final black hole mass accumulated as a function of redshift and final mass is plotted as contours. Figure from Merloni and Heinz (2013).

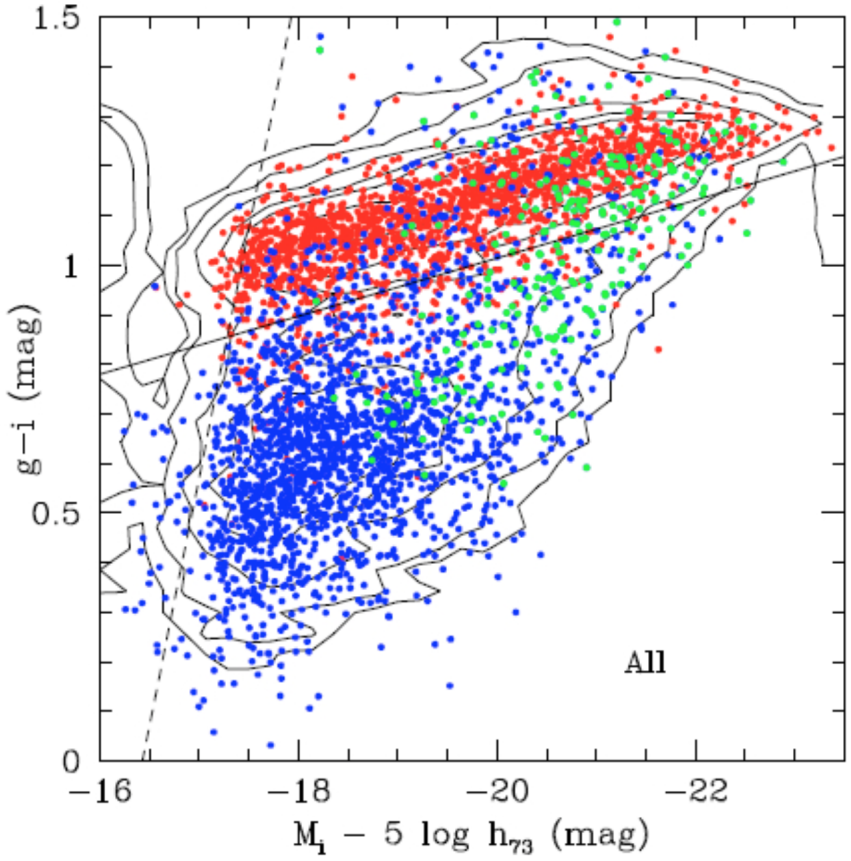

FIGURE 2.4: g-i color versus i-band absolute magnitude relation of all galaxies in the Coma cluster from Gavazzi et al. (2010). Early-type galaxies are shown in red, disk galaxies are shown in blue and bulge galaxies in green. The continuum line $g - i = 0.0585 \cdot (M_i + 16) + 0.78$ represents the empirical separation between the red-sequence and the remaining galaxies. The dashed line illustrates the effect of the limiting magnitude r=17.77 of the spectroscopic SDSS database, combined with the color of the faintest E galaxies $g - r \sim 0.70$ mag.

2.4 AGN - Galaxy co-evolution

In the local Universe the observed galaxy population presents a bimodality between:

Blue galaxies (Hubble late - type): galaxies characterized by recent or on-going star formation and low stellar surface density.

Red galaxies (Hubble early - type): galaxies characterized by little or absent star formation, large stellar mass and high surface density.

In Figure 2.4 the g-i color versus the absolute magnitude in the i-band relation for galaxies in the Coma cluster (Gavazzi et al., 2010). Early-type galaxies are on a *red sequence* (RS) while late-type galaxies show a greater dispersion and form a *blue cloud* (BC). An intermediate population of bulge galaxies in the so called *green valley* places between the RS and the BC.

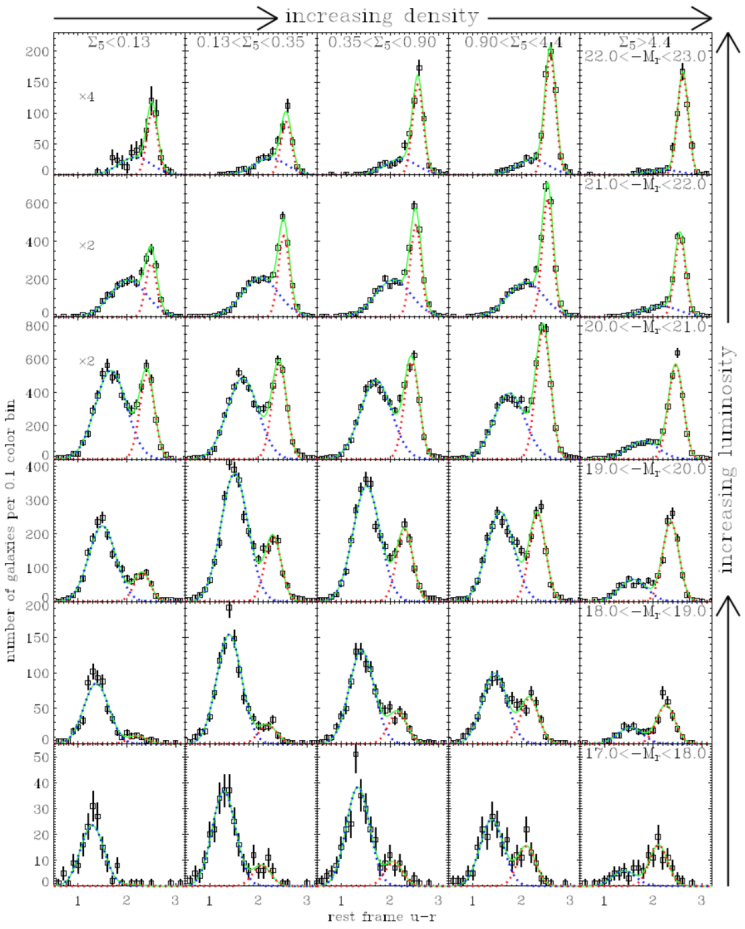

FIGURE 2.5: u-r color galaxies distribution in bins of absolute magnitude in the r-band and projected environmental density from Baldry et al. (2004). The projected two dimensional density is $\xi_5 = 5/\pi r^2$ in units of Mpc^{-2}, where r is the projected distance to the fifth-nearest-spectroscopically confirmed neighbor with $M_r \leq -20$.

The most luminous galaxies (with $M_i < -22$) are on the red sequence, while both sequences become redder with increasing luminosity: it means that the most massive galaxies are red and passive.

There is another factor which can influence the color distribution: the environmental density. Fitting the distribution of galaxies in color after dividing the sample into magnitude and environmental density bins one obtains the Figure 2.5 from Baldry et al. (2004). It confirms that galaxies become redder at higher luminosity and, in addition to that, the fraction of galaxies in the red sequence appears to rise with increasing environmental density. It is also evident that masses and environmental conditions of galaxies influence their star formation rate and dust content: the reddening of galaxy colors can in fact be related to a decreasing star formation and to an aging of the stellar population, or due to an increase in dust content.

Studies of the evolution of the galaxy color distribution up to z $\sim$ 1 (Bell et al., 2004) revealed that colors tend to become bluer and that the luminosity function shifts to higher luminosities for both RC and BC. The number density of blue galaxies has remained almost constant from z $\sim$ 1 to the present day, while the number of red galaxies has increased.

The bimodality seems to be a characteristic of the galaxy population at least up to z $\geq$ 2 (Whitaker, 2013), so it is possible to consider this kind of distribution in an evolutionary context in which AGN seems to be the main responsible of the transition from blu galaxie to red ones.

Classical semi-analytic models not taking into account AGN activity, succeed in matching the global behavior of galaxy evolution, but fail in reproducing the bi-modality shown in the color-magnitude diagram, especially the observed ratio between massive red and blue galaxies.

In order to understand how the Active Galactic Nuclei can influence the host galaxy it is useful to compare the energy released by the accretion of matter onto a SMBH and the binding energy of the gas into the host galaxy. The binding energy can be simply expressed as:

$$E_{bind} = M_{gal}\sigma^2 \tag{2.11}$$

M_{gal} and σ are the mass and the velocity dispersion of the host galaxy, respectively.

Usually the SMBH mass is about a thousandth of the galaxy mass and the velocity dispersions are lesser than a few hundred km s^{-1}, so the ratio E_{BH}/E_{bind} can exceed 80.

The majority of the mass accretion onto black holes occurred at z $>$ 1 (Merloni and Heinz, 2008; Delvecchio et al., 2014), with a rise from z = 0 to z = 1 and a maximum at z $\sim$ 2 - 3 followed by a steep decline. A similar trend has been found for star formation (Hopkins and Beacom, 2006).

The evolution at low redshift is probably due to a decrease in the cold gas, used as fuel for both processes, in the central regions of galaxies, but the amount of cold gas required to fuel these processes is different. For the accretion process only a small fraction of the gas needed for star formation is required, thus producing a time delay between the shut down of star formation and AGN activity of about 0.1 Gyr (Hopkins et al., 2012), and also between the peak of star formation activity and the maximum of accretion onto the SMBH of about 0.5 Gyr (Schawinski, 2009).

The typical size of a SMBH is in the range from 0.001 to 100 AU, while the host galaxy can extend over a few kpc up to a few ten kpc; the connection is thus not obvious. As discussed in the previous chapter, it is necessary that mechanism as galaxy interactions, galaxy bars, major mergers remove the gas angular momentum and allow it to inflow.

Nowadays, the most evolutionary scenario from blue cloud galaxies to red sequence galaxies can be summarized in three main phases:

- The growth and interaction between galaxies
- The galaxies coalescence and their nuclear activity
- The passive evolution towards red elliptical / spheroidal galaxies.

Looking at Figure 2.6, the first phase (a-c) is characterized by young gas-rich and star forming galaxies, growing and assembling in groups. Minor and major mergers and galaxies encounters are expected to drive nuclear inflows of gas, enhancing star formation (starburst activity) and leading to an obscured black hole growth: this is the phase associated to heavily obscured QSOs.
The second phase (d-f) begins with the coalescence of galaxies. At the beginning of this phase the starburst luminosity dominates and black holes accreted in buried AGN; the accretion rate increase and QSOs expell gas from the host galaxies by means of strong winds originated by the accretion energy release into the ISM. Gas is also consumed by AGN triggered starburst activity and dispersed by supernovae explosions.
When no substantial amount of gas remains, galaxies enter the last phase (g-h) in which both star formation and nuclear activity rapidly fades out. Mergers become inefficient to drive gas toward the galaxy center, and galaxies evolve into dead elliptical or spheroidal ones.

2.4.1 Scaling relation for SMBH

The connection between SMBH and bulge properties has been evident since the first attempts to measure the masses of the black holes (Kormendy and Richstone, 1995), while a correlation seems to lack between SMBH and disk properties. The launch of the Hubble Space Telescope nearly twenty years ago made easier the search for local QSO relics and the study of their dynamical influence on the surrounding stars and gas. The discovery of correlations between local SMBH and galaxy bulges have changed the way we conceive the physical link between galaxy and AGN evolution. If one thinks that the SMBH growth is now known to be due mainly to radiatively efficient accretion over cosmological times, this suggests that most, if not all, galaxies went through a phase of nuclear activity in the past, during which a strong physical coupling (which is generally assigned the term "feedback") must have established a long-lasting link between host's and black hole's properties.
Both semi-analytic models and hydrodynamical simulations have tried to assess the role of AGN in galaxy evolution, using the local relations to constrain the model parameters. Concerning the observational point of view, the current situation is far from being clear.

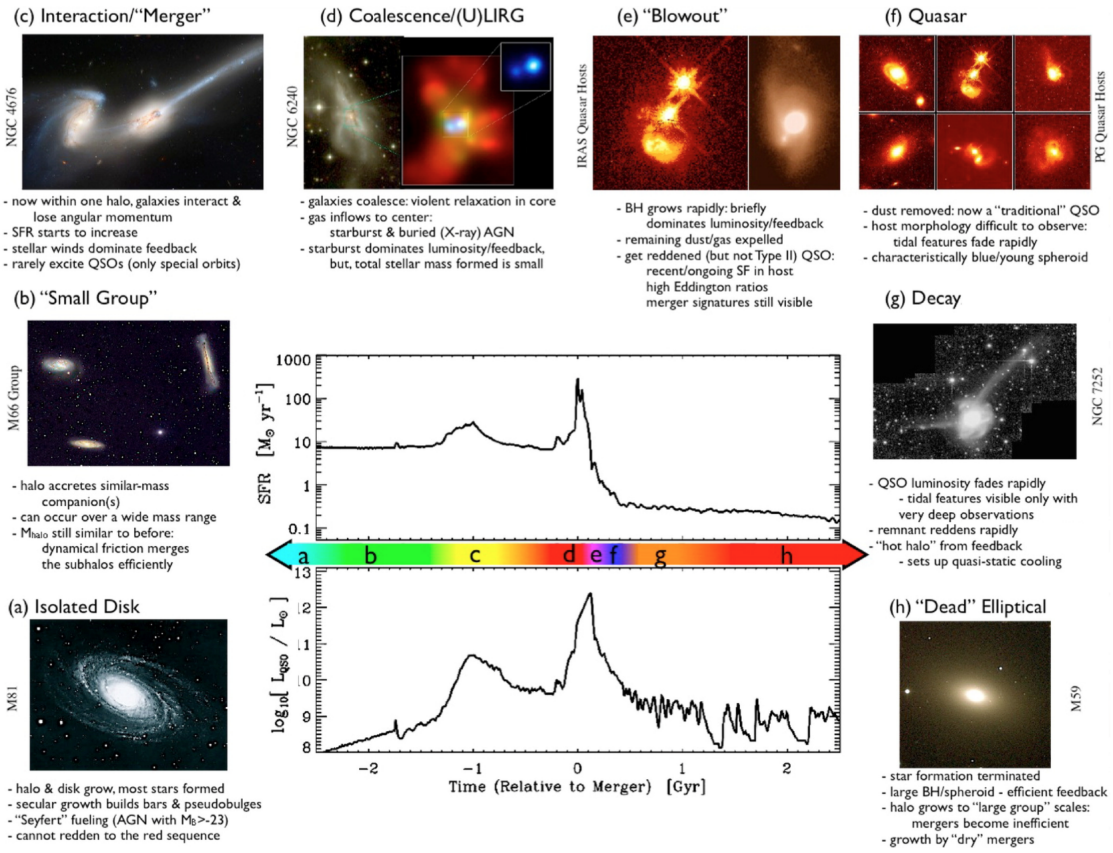

FIGURE 2.6: Schematic outline of the phases of growth in a galaxy undergoing a gas-rich major merger from Hopkins et al. 2005.

The earliest BH demographic result was the correlation between M_{BH} and the luminosity of the bulge component of the host galaxy (see Figure 2.7). Dressler (1989) was the first to propose such a correlation, basing just on five objects. Further elaboration of the $M_{BH} - L_{bulge}$ relation were made in the last decades, (see e.g., Kormendy and Ho, 2013). This correlation implicitly include a correlation with the bulge mass.

The first attempts to explicitate the relation in terms of the bulge masses were done by deriving the masses both from dynamical modelling (Magorrian et al., 1998) and using the virial theorem (Marconi and Hunt, 2003). Many studies are consistent with a linear relation, but others have found hints (Häring and Rix, 2004) of a steeper relationship, $M_{BH} \propto M_{bulge}^{1.54\pm0.15}$. In most cases, comparing these studies is far from simple, because some include BH masses from AGN emission-line widths (Laor, 2001) and others do not.

Probably the most famous relation is the one between the BH mass and the velocity dispersion of the bulge (see Figure 2.8), announced at the Spring 2000 meeting of the American Astronomical Society. Many papers have then expanded on this result with

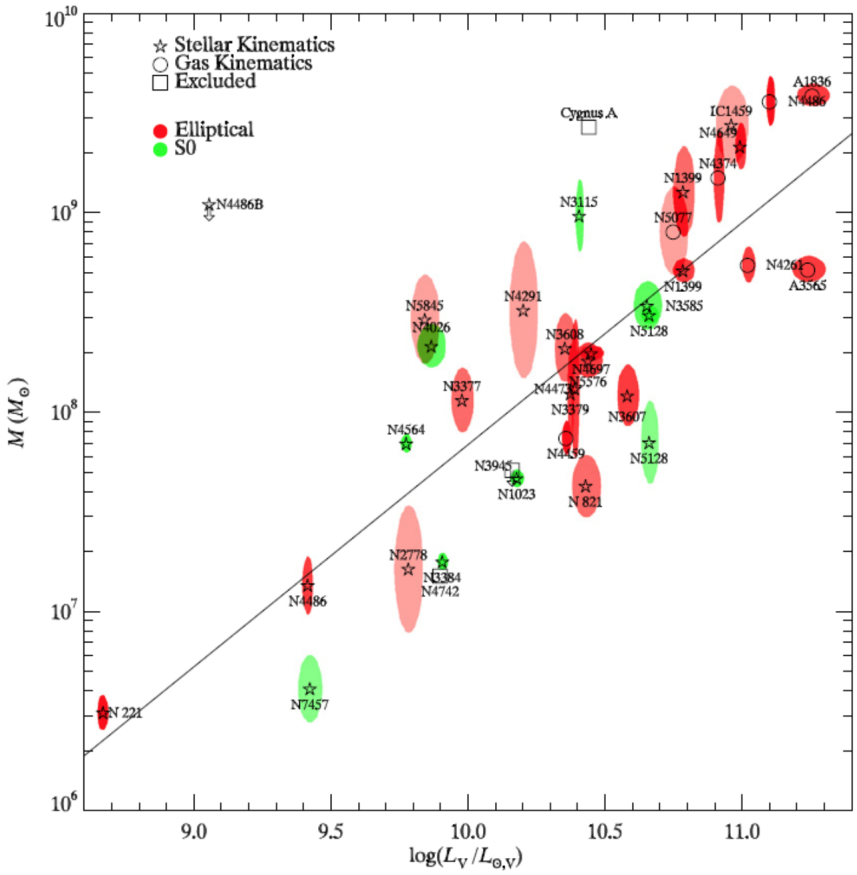

FIGURE 2.7: $M_{BH} - L_{bulge}$ plot from Gultekin (2009). The best fit relation for the sample in which upper limits BH masses have been excluded is $log(M/M_\odot) = (8.95 \pm 0.11) + (1.11 \pm 0.18) \cdot log(L_V/10^{11} L_{V,\odot})$.

bigger samples and have explored its applicability to AGNs, other kinds of objects and to the distant Universe (see e.g., Gultekin, 2009; Graham et al., 2011; McConnell and Ma, 2013). It is worth noticing that the $M_{BH} - \sigma$ and the $M_{BH} - M_{bulge}$ relation (as pointed out by Kormendy and Ho (2013)) have the same intrinsic scatter, $\sim 0.3dex$.

A key question is if these scaling relations are dependent or not dependent on redshift because BH masses estimation techniques are limited to galaxies in the local Universe. Testing their dependence on redshift is quite challenging, because the high-z SMBH is biased towards higher masses and reverbaration mapping, which is the main technique for BH mass measurements at high-z, is calibrated on the local $M_{BH} - \sigma$ relation.
In AGN the central emission can dominate the emission of galaxy, so measurements of velocity dispersion and luminosity in the host may be not reliable values.
All the empirical correlations described point toward a global physical link between the SMBH and the properties of the hosting galactic bulge and indicate that AGN play a significant role in the evolution of galaxies.

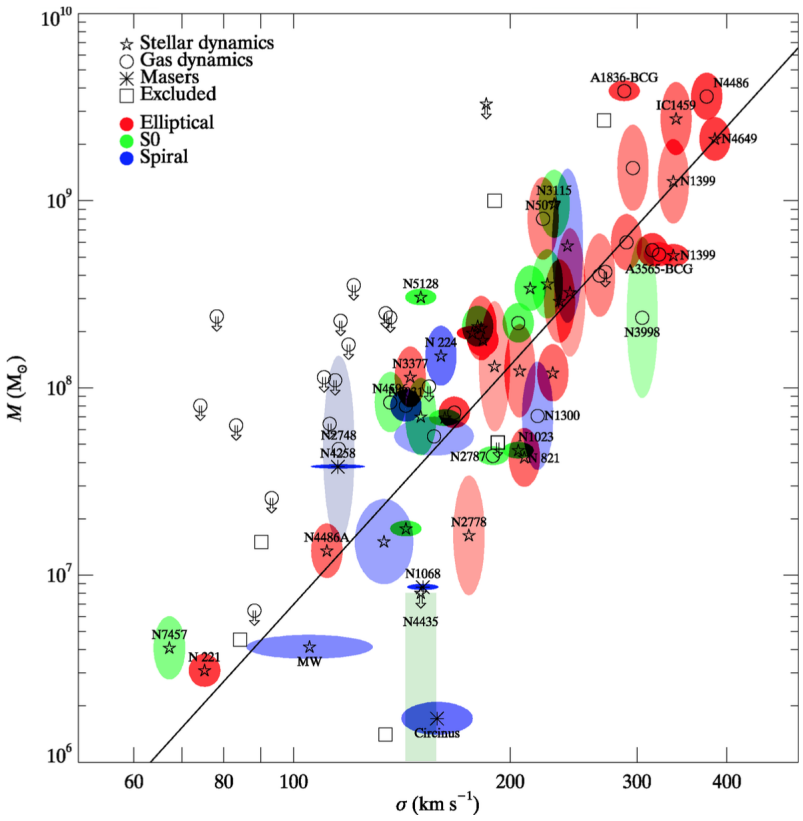

FIGURE 2.8: $M_{BH} - \sigma$ plot from Gultekin (2009) for galaxies with direct dynamical measurements from different estimation methods as indicate by symbols. Arrows indicate upper limits to BH mass, colors refer to the Hubble type of the host galaxy and squares indicate galaxies excluded from the fit. Data have been fitted using the relation $log(M/M_\odot) = \alpha + \beta log(\sigma/200kms^{-1})$; best fit parameters are: $\alpha = 8.12 \pm 0.08$ and $\beta = 4.24 \pm 0.41$. The measured cosmic scatter evaluated as r.m.s. deviation in $log(M/M_\odot)$ is $\epsilon_0 = 0.44 \pm 0.06$.

2.4.2 The role of feedback

The discovery of SMBH in local bulges, the need for a mechanism able to deplete galaxies of their gas content to explain the bi-modality of the population, the observed correlations between the SMBH masses and the bulge properties, they all suggest that nuclear activity might have a prominent role in galaxies evolution.

Active Galactic Nuclei seem to exert a *feedback* mechanism on the host galaxy (and in particular on its star formation activity), which in principle can be a positive or negative feedback (see e.g., Harrison, 2017; Cresci and Maiolino, 2018). In the case of a negative feedback, AGN might be able to heat, ionize and eventually expel cold gas from the central regions of the host galaxy. An AGN can be thus responsible of the creation of the local red massive galaxies observed.

All the theoretical works which have investigated the impact of AGN feedback on galaxy formation agree in assuming that black holes seeds, initially residing in the nucleus of each

galactic halo, grow both by merging with other black holes and through gas accretion episodes, triggered by galaxy interactions.
It is possible to distinguish between two feedback modes:

- Quasar mode : it is associated with accretion at high rates onto SMBH triggered by mergers and galaxy encounters. The typical time scale of this transient phase is $\sim 10^7$ years and during it powerful winds evacuate cold gas quenching star formation in the host galaxy. The same gas feeding the AGN can obscure the central source, so the best candidates for quasar mode feedback are bright obscured QSOs at redshift around z$\sim$2 (Menci et al., 2008).
- Radio mode : it is a quiescent feedback mode associated with the accretion of hot gas onto an already formed SMBH from a surrounding hot halo at low accretion rate. This process depends only on the hot gas and SMBH masses, being more efficient at lower redshift and for massive objects in rich environments. Mechanical energy is pushed into the ISM through radio jets traversing the galaxy.

As it is shown in Figure 2.9, during the quasar-mode phase wide angle, sub-relativistic outflows are produced, driven by the radiative output of the AGN. During the radio-mode phase, radio jets consisting of relativistic electrons with narrow opening angle are launched from the nuclear region.

Radio jets have been copiously observed in local massive radio galaxies, while direct observations of the quasar-mode feedback have become available just in the last years.
AGN outflows trace in fact the action of winds on nuclear scale, but they are not able to prove that the influence can reach kiloparsec scales. Feruglio et al. (2010) and Rupke and Veilleux (2011) provided the first direct observations of massive molecular outflows on galactic scales, which is the signature of the quasar-mode feedback on the host galaxy.

2.4.3 Two-Phase expansion mechanism

A theoretical model of quasar-mode feedback from accreting SMBH has been developed by Andrew King, in order to explain the detection by Pounds et al. (2003) of a highly ionized intrinsic outflow in the source PG 1211+143, characterized by a high column density and velocity ($N_H \sim 5 \cdot 10^{23}$ cm^{-2} and $v \sim 0.08$ c respectively).
The model consists of a simple theory of optically thick winds driven by the continuum radiation pressure from an highly accreting SMBH (King and Pounds, 2003).It is considered a radial wind propagating in a double cone of a solid angle $d\Omega = 4\pi b$, with b

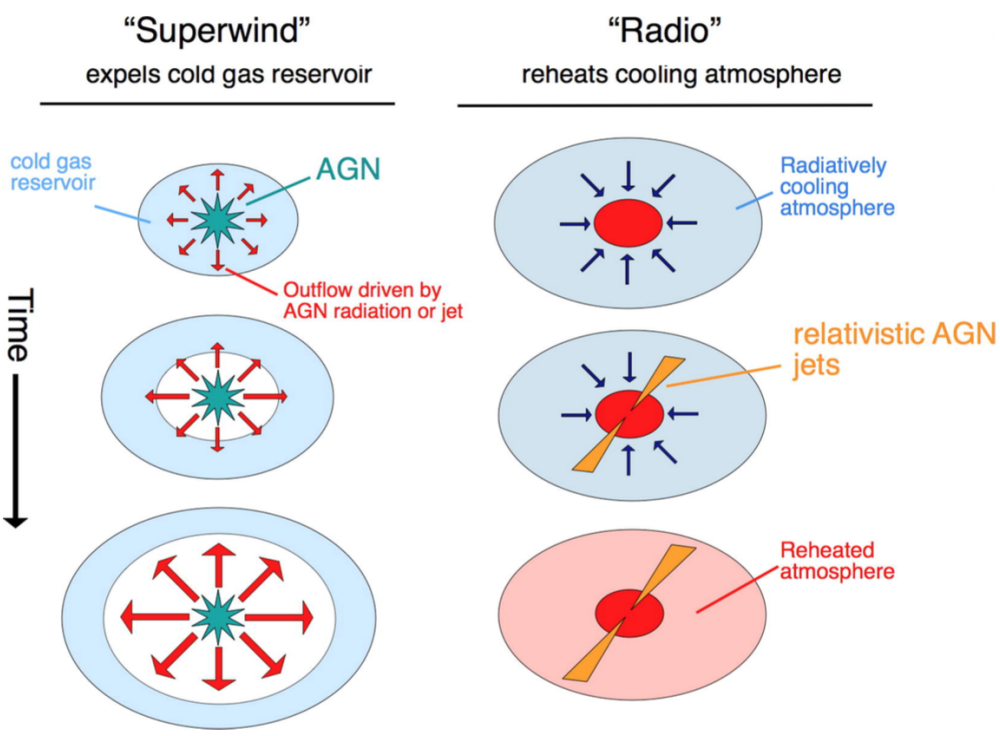

FIGURE 2.9: Schematic diagrams of the two main modes of AGN outflows: quasar-mode and radio-mode. Adapted from Alexander and Hickox (2012b).

covering factor of the outflow, assumed to be ~ 1. The mass conservation at distance r from the SMBH is given by:

$$\frac{d}{dt}\langle\frac{4}{3}\pi b r^3 \rho\rangle = \dot{M}_{out} \tag{2.12}$$

where $\dot{M}_{out} = dM_{out}/dt$ is the outflowing mass rate.
The wind density ρ is thus:

$$\rho = \frac{\dot{M}_{out}}{4\pi b v r^2} \tag{2.13}$$

where v is the wind velocity assumed to be constant at large distances r.
The optical depth of the flow from electron scattering is:

$$\tau = \int_R^\infty k\rho dr = \frac{k\dot{M}_{out}}{4\pi v b R} \tag{2.14}$$

$k = \sigma_T/m_p$ is the electron scattering opacity.
The mass accretion rate necessary to produce the Eddington luminosity L_{EDD} is the Eddington accretion rate:

$$\dot{M}_{Edd} = \frac{dM_{Edd}}{dt} = \frac{L_{Edd}}{\eta c^2} = \frac{4\pi G M m_p}{\sigma_T \eta c} = \frac{4\pi G M}{\eta k c} \tag{2.15}$$

Substituting Eq. 2.15 in Eq. 2.14 and defining the photospheric radius as the distance from the SMBH at which the electron scattering optical depth through the flow is unitary,

$R_{ph} = R(\tau = 1)$, gives:

$$\frac{R_{ph}}{R_S} = \frac{1}{2\eta b v}\frac{c}{v}\frac{\dot{M}_{out}}{\dot{M}_{Edd}} \tag{2.16}$$

where the accretion efficiency η is assumed to be ~ 0.1 and R_S is the Schwarzschild radius. From Eq. 2.16 it is evident that for a covering factor around 1 and an accretion rate close to the Eddington rate the wind is optically thick at larger radii than Schwarzschild radius. In this optically thick flow photons have scattered and on average transferred their momentum to the flow.

At larger radii than R_{ph} matter and photons decouple with resulting no more acceleration so the previous assumption of $v \sim const$ is justified.

The flow can reach the escape velocity from the photosphere if R_{ph} lies close to the escape radius deined as $R_{esc} = \langle\frac{c}{v}\rangle^2 R_S$. Imposing $R_{ph} = R_S$ one obtains the relation:

$$\frac{v}{c} = \frac{2\eta b\dot{M}_{Edd}}{\dot{M}_{out}} = \frac{2bL_{Edd}}{\dot{M}_{out}c^2} \tag{2.17}$$

The momentum flux of the wind is given by:

$$\dot{P}_w = \dot{M}_{out}v \simeq \frac{L_{Edd}}{c} \tag{2.18}$$

while the kinetic energy flux:

$$\dot{E}_w = \frac{1}{2}\dot{M}_{out}v^2 \simeq \frac{1}{2}v\frac{L_Edd}{c} = \epsilon_{AGN}L_{Edd} \tag{2.19}$$

where the AGN driven wind with velocity $v \sim 0.1c$ has an efficiency of about $\epsilon_{AGN} \sim 0.05$.

The momentum flux of these thick winds arising from supercritical accretion onto the SMBH is thus comparable to the momentum flux of an Eddington limited radiation field; the energy is a few percent lower than the energy of an Eddington limited radiation field.

Zubovas and King (2012) proposed a two phase mechanism in which the wind, colliding with the galactic gas, is firstly slowed in an inner strong shock; the shocked gas is cooled by inverse Compton effect from the QSO radiation field and then compressed in a radial extent. The thin cooled gas shell exerts the pre-shock ram pressure ($P_{ram} = \rho v^2$) on the galactic ISM and sweeps it into a dense shell of increasing mass.

Its velocity depends on whether the shocked gas is able to cool down or not: in the first case the wind gives rise to a momentum driven outflow, valid out to a radius R_C at which the Compton cooling time becomes comparable with the expansion time of the ouflow, otherwise to an energy driven outflow.

In the MD case the cooled shocked wind gas is compressed to high density and radiates

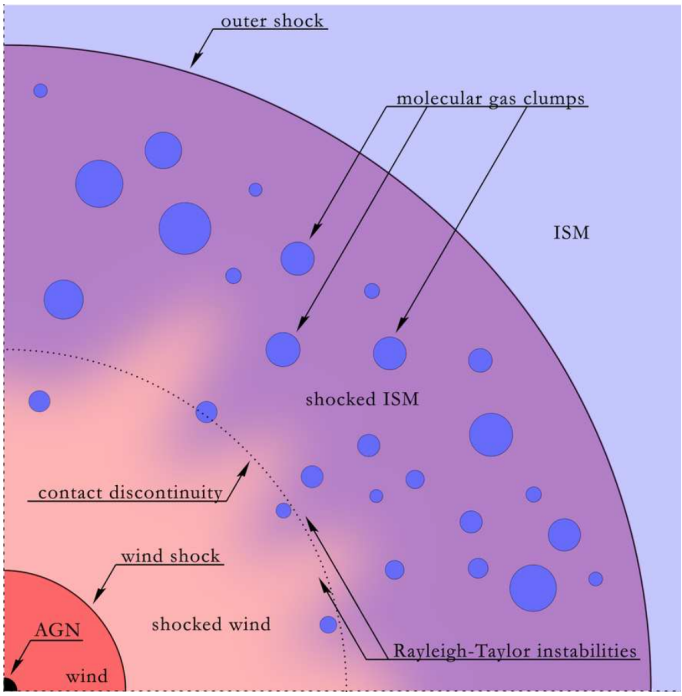

FIGURE 2.10: Zubovas & King two-phase model.

away almost all of its original kinetic energy, retaining only its pressure. For a SMBH accreting close to the Eddington rate the momentum flow rate is comparable with the radiative momentum output:

$$\dot{P}_w \simeq \frac{L_{Edd}}{c} \tag{2.20}$$

In an energy driven outflow the shocked regions are much wider and do not cool: they expand adiabatically communicating most of the kinetic energy of the wind to the outflow, with:

$$\dot{P}_{out} \simeq 20\sigma_{200}^{-2/3} l^{1/6} \frac{L_E dd}{c} \tag{2.21}$$

where σ_{200} is the velocity dispersion in unit of 200 km s^{-1} and $l = L/L_{Edd}$ is the Eddington ratio, i.e. the ratio between the observed luminosity of the AGN and the corresponding Eddington luminosity.

It is possible to note from the equations given above that in both energy-driven and momentum-driven outflows, the strength increases proportionally with the bolometric luminosity of the AGN; however, in MD case the momentum flow rate is expected to be a few ten greater than in ED one.

Recent observations from Cicone et al. (2014) support both the AGN energy-drive nature of the outflows and the AGN feedback two-phase mechanism model, in which a fast and highly ionized wind, arising from the nuclear regions of the AGN, creates a shock wave that propagates into the ISM of the galaxy.

In Figure 2.11 it is visible the momentum boost, which represents the ratio of $\dot{P}_{out}$ ($\dot{M}_{H_2} v$ in Figure 2.11) and the AGN radiative momentum output ranges from 10 - 50 in

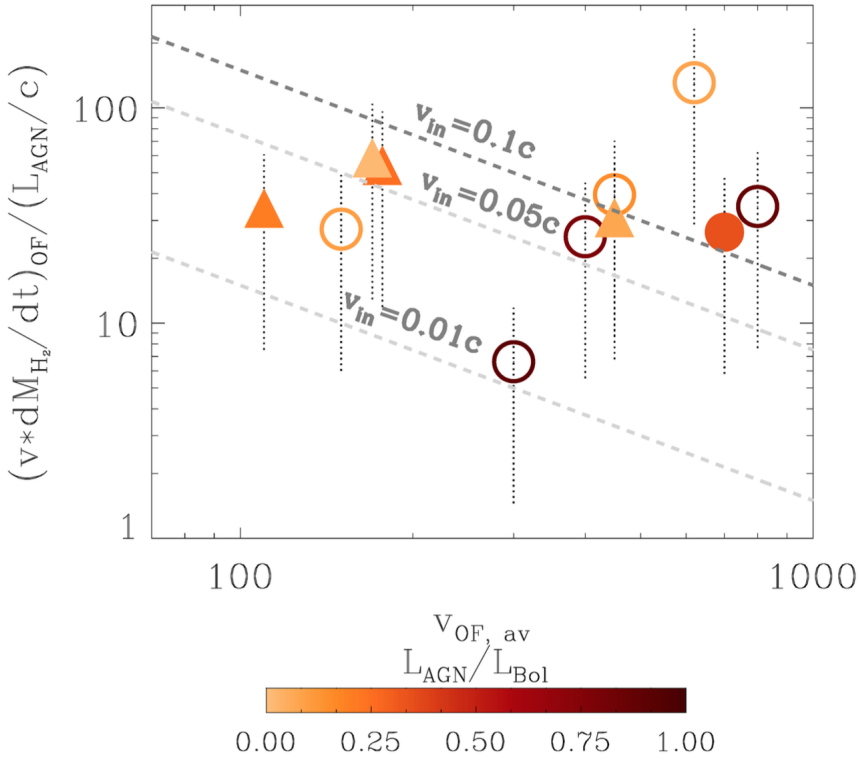

FIGURE 2.11: Outflow momentum boost with respect to the AGN radiative momentum output as a function of the outflow velocity for a sample of AGN. Colors refer to different AGN luminosities respect to the total AGN-galaxy bolometric emission (Cicone et al., 2014).

galaxies where the AGN contributes more than 10% to the total AGN-galaxy bolometric luminosity.

CHAPTER 3

Modeling multi-wavelength Data

Multi-band datasets from large surveys provide a lot of information on the complex physics of galaxy SEDs and are the primary source of our knowledge of galaxies themselves. Accurate modelling and analysis should be, in principle, able to provide robust measurements of the fundamental properties of galaxies, such as stellar mass (M_*), Star Formation Rate (SFR), gas and dust content. Indeed, all the emission processes coming into play leave characteristic imprints at different wavelengths on the global SED of extragalactic sources. The analysis of the spectral energy distribution of galaxies allows the investigation of the different physical processes taking place during their life-time. When considering multi-wavelength data, more than one emission component needs to be taken into account to get a complete view of the physical mechanisms taking place in active galaxies and their hosts.

This chapter is dedicated to the description of the different physical emission mechanisms that need to be considered when modelling the AGN + galaxy SEDs.

3.1 AGN emission

The contribution of the AGN to the total emission over the whole electromagnetic spectrum cannot be neglected. In type 1 AGN the accretion disc contributes to most of the emission at X-ray, optical and UV wavelengths, often overwhelming that of the host galaxy. Moreover, the hot dust emission attributed to the AGN torus emits in the IR.

The bulk of its energy interests MIR wavelengths, where silicate features at 9.7 and 18 μm, related to the presence of silicate dust grains, are also observed.

3.2 Galaxy emission

Stars populating the galaxy emit stellar emission mostly in the optical/UV regime. This same radiation is reprocessed by the gas and dust composing the Inter Stellar Medium. This re-radiation is observed in emission/absorption lines due to gas photoionization/excitation at various wavelengths as well as in the continuum emission and PAH features in the IR regime.

3.3 The interstellar medium around stars

To reproduce the entire SED of a galaxy the stellar spectra is not sufficient because the radiation from stars is absorbed and processed by the gas and dust that lie between them, in turn the ISM. This reprocessed radiation contributes to the observed continuum emission and special absorption and emission features, e.g. emission and absorptions lines associated with the presence of gas and PAH features due to the dust.
While gas and dust are intermingled within the ISM, in practice they are often treated as separate components because their absorption properties have a different wavelength dependence.

3.3.1 Principle of Radiative Transfer

The radiation coming from a source, being it a star, an AGN nucleus or a galaxy, passes through the surrounding medium before arriving at the observer. When dealing with a material emitting both thermal and scattered radiation, these two components are described by the absorption (α_ν) and the coherent isotropic scattering (σ_ν) coefficients, respectively. The radiative transfer equation will be then written as follows (see Rybicki and Lightman, 1979):

$$dI_\nu = -\alpha_\nu(I_\nu - B_\nu) - \sigma_\nu\,(I_\nu - J_\nu) = -(\alpha_\nu + \sigma_\nu)\cdot(I_\nu - S_\nu) \tag{3.1}$$

where I_ν is the specific intensity, B_ν is the Planck function and J_ν is the isotropic intensity. S_ν is the source function, also written as: $S_\nu = \frac{\alpha_\nu B_\nu + \sigma_\nu J_\nu}{\alpha_\nu + \sigma_\nu}$, in turn a weighted (by their

respective absorption coefficients) average of the two separate source functions. When scattering is present the solution of Eq. 3.1 needs to be partially solved with numerical techniques as it does not have an analytical solution. The detailed treatment of the solution of the radiative transfer problem depends on the exact setup of the dust grains, e.g. single or composite grain and the size of the cells in which the model space is divided.

3.4 Interstellar Dust

3.4.1 Attenuation by dust

The presence of interstellar dust was first inferred from obscuration, or "extinction", of the starlight (Trumpler, 1930). This attenuation of the radiation emitted by stars is strongly wavelength dependent and, at the same time, it varies from one line of sight to another. The intrinsic flux of the source, $F_{\lambda\, intr}$, would be attenuated by dust, with a dependence on the wavelength, resulting in an observed flux:

$$F_{\lambda\, obs} = F_{\lambda\, intr} 10^{-0.4\, E\,(B-V)\, k(\lambda)} \tag{3.2}$$

where E(B-V) is the color excess between the B and V band. This is a measure of the "reddening" of a source because of the wavelength dependence of attenuation, greater in the blue (short wavelengths) than in the red (longer wavelengths) part of the spectrum. k(λ) is the extinction curve, commonly parametrized as:

$$k(\lambda) = \frac{A_\lambda}{E(B-V)} \tag{3.3}$$

where $A_\lambda = 2.5\, log(F_\lambda / F_{\lambda intr})$ is the wavelength dependent extinction. It is a measure of the total light absorbed or scattered out of the line-of-sight by dust, either bolometrically or in a single band.

The dust extinction phenomena of a galaxy, referred to as "attenuation", is the result of the interplay between the geometry and the different optical depth characterizing the different regions of a galaxy. It applies to the whole stars and not to the single stars. A measure of the slope of the extinction curve is usually given with a dimensionless quantity:

$$R_V = \frac{A_V}{E(B-V)} \tag{3.4}$$

which varies from line of sight to line of sight, from values as low as 2.1 (Welty and Fowler, 1992) to value as large as 5.6-5.8 (Cardelli et al., 1989).
Attenuation laws have been obtained for the Milky Way, with $R_V = 3.1$ (Savage and Mathis, 1979; Cardelli et al., 1989), and for the Small and Large Magellanic Clouds (SMC and LMC, respectively). Calzetti et al. (1994) derived an empirical curve for starburst galaxies, with $R_V = 4.5$.

However, all the previous works still do not account for differential dust distribution, stellar geometries (such as bulges and discs) and the clumpiness of the ISM. Moreover, light is not only scattered out from the line of sight but it is also scattered into it. This anisotropic light scattering by dust is also not considered (Walcher et al., 2011). All of this need for a proper radiative transfer to be taken into account with iterative methods and Monte Carlo methods (Baes et al., 2010). In such approaches the emitted and scattered light is broken up into various components, the radiative transfer equation is solved for each one of these and the solution from the previous components is used for the subsequent until the convergence of the equation (see e.g., Kylafis and Bahcall, 1987; Xilouris et al., 1998; Tuffs et al., 2004). A simple extinction curve is still the most commonly used way to account for effects of dust on the optical/UV SED because radiative transfer codes require the introduction of several free parameters.
Note that the silicate dust grains also contribute to the absorption with two characteristic features at 9.7 and 18 μm. These features are observed in sources with high optical depth and, in general, in galaxies hosting a strong nuclear source.

3.4.2 Emission by dust

As already mentioned dust can give rise to some features in the MIR associated with PAH and silicate grains. But the presence of dust can also be observed as a continuum emission, associated with reprocessed optical/UV radiation, at IR and sub-mm wavelengths. The bulk of the contribution of the cold dust emission due to starburst heating is expected to be in the FIR and sub-mm regimes. At such wavelengths the cold dust emission can be modelled in a simplistic way with a black body emission or a emissivity modified black body under the assumption of thermal equilibrium. To model the MIR emission a simple black body is not enough because, at such wavelengths, the grains have smaller surfaces with a consequent reduction and randomization of the photon incidence, and as a result are statistically less- well represented by a black body (Draine, 2003). There is the need for a model in which the dust has a range of temperatures parametrized with the strength of the radiation field heating it. One possibility is to apply Monte Carlo techniques or a steady-state distribution to solve the radiative transfer equation or to solve, with a more simplistic approach, the steady-state distribution of

temperatures for given radiation field, dust size and composition (Draine and Li, 2007). PAH features, which also contribute to the emission at MIR wavelengths, are generally incorporated in starburst emission models. Realistic FIR models are, then, those taking into account the various range of temperatures. Once the radiation field and the dust properties have been chosen, the following step, to obtain the total FIR emission of a model is to calculate the emission from each grain and then to integrate over all the dust grains. In all these models, the temperature distribution depends on the dust-gas geometry of the ISM. This information cannot be obtained by optical/UV data alone. For this reason, empirical templates of FIR emission of galaxy are often used to reproduce the galaxy SEDs. These templates are, in general, realized taking the mentioned dust models and matching them with observations of sample of galaxies. The use of such empirical templates (Chary and Elbaz, 2001; Dale and Helou, 2002; Lagache et al., 2004; Rieke et al., 2009) allows for investigation of the galaxy-wide properties.

3.5 The Inter Galactic Medium

It is well known that radiation from cosmological sources is absorbed by neutral hydrogen left in the intergalactic medium (IGM) even after the cosmic reionization. The characteristics of this absorption reflect the density distribution, ionization state and temperature of the intergalactic gas. The gas, in turn, closely traces the underlying distribution of dark matter, albeit with significant deviations arising from hydrodynamics coupled to the radiative and mechanical feedback from galaxies and active galactic nucleus (Becker et al., 2013).
Along the observer's line of sight there appear to be numerous discrete systems composed of the integralactic neutral hydrogen which produce a number of absorption lines in the spectra of distant sources. These systems are divided into the Lyα forest, Lyman limit systems and damped Lyα systems depending on the column density of the neutral hydrogen along the line of sight. It is so necessary to correct the spectra of cosmological sources for this intergalactic absorption in order to know the intrinsic ones.The spectrum between Lyα (at a wavelength of $\lambda_\alpha = 1215.67$ Å) and Lyβ ($\lambda_\beta = 1026$ Å) lines in the source rest-frame is absorbed by the Lyα transition of the neutral hydrogen in the IGM: it is the so called Lyα depression.

3.5.1 The code for treating the Ly-α absorption in the spectra

The most known theoretical model for the treatment of the Inter Galactic Medium absorption has been developed by Madau et al. (2001) and it is still the starting point for all the other developments. Recently, Inoue et al. (2014) have presented a new version

of the Madau model, deriving the updated analytic formulae for the attenuation due to the intergalactic neutral hydrogen. In this model, the Lyman series (LS) optical depths are given as:

$$\tau^i_{\rm LS}(\lambda_{\rm obs}, z_{\rm S}) = \sum_j \tau^i_j(\lambda_{\rm obs}, z_{\rm S}) = \sum_j \int_0^{z_{\rm S}} f_i(z) I_{i,j}(z) dz\,, \tag{3.5}$$

where τ^i_j is the optical depth of jth line of Lyman series of i (LAF or DLA) component and $I_{i,j}$ is the integration of the column density function g_i for the jth line.Likewise, the Lyman continuum (LC) optical depths are given as:

$$\tau^i_{\rm LC}(\lambda_{\rm obs}, z_{\rm S}) = \int_0^{z_{\rm S}} f_i(z) I_{i,{\rm LC}}(z) dz\,, \tag{3.6}$$

where $I_{i,{\rm LC}}(z)$ is the column density integral.
For the Lyman series absorption, it is assumed a narrow rectangular shape of the cross section of the Lyman series lines. The optical depth for the Lyα absorption at the observed wavelength $\lambda_{\rm obs} = \lambda_\alpha(1+z_\alpha)$ is produced by absorbers within a narrow redshift range $(1+z_\alpha) \pm \Delta(1+z_\alpha)/2$, where $\Delta(1+z_\alpha) \approx (1+z_\alpha)(\delta b/c)$. Then, the Ly$\alpha$ optical depth is independent of the source redshift $z_{\rm S}$ but just depends on the absorbers' redshift z_α: $\tau_\alpha(z_\alpha)$. So it is possible to write:

$$\tau_\alpha(z_\alpha) \approx f_{\rm LAF}(z_\alpha)(1+z_\alpha)\left(\frac{\delta b}{c}\right)\int_0^\infty g_{\rm LAF}(N_{\rm HI})(1-e^{-\sigma_{\alpha,0}N_{\rm HI}})dN_{\rm HI}\,. \tag{3.7}$$

For other Lyman series lines $\sigma_{\alpha,0}$ is replaced with $\sigma_{j,0}$ for the jth line, and then, the optical depth function for the jth line has the same functional shape as that of Lyα:

$$\tau^{\rm LAF}_j(z_j) \propto f_{\rm LAF}(z_j)(1+z_j)\,, \tag{3.8}$$

where $1+z_j = \lambda_{\rm obs}/\lambda_j$ with the wavelength of the jth line λ_j.
Given the functional shape of $f_{\rm LAF}$ with the fiducial set of the parameters, one obtains, for $\lambda_j < \lambda_{\rm obs} < \lambda_j(1+z_{\rm S})$,

$$\tau^{\rm LAF}_j(\lambda_{\rm obs}) = \begin{cases} A^{\rm LAF}_{j,1}\left(\frac{\lambda_{\rm obs}}{\lambda_j}\right)^{1.2} & (\lambda_{\rm obs} < 2.2\lambda_j) \\ A^{\rm LAF}_{j,2}\left(\frac{\lambda_{\rm obs}}{\lambda_j}\right)^{3.7} & (2.2\lambda_j \le \lambda_{\rm obs} < 5.7\lambda_j) \\ A^{\rm LAF}_{j,3}\left(\frac{\lambda_{\rm obs}}{\lambda_j}\right)^{5.5} & (5.7\lambda_j \le \lambda_{\rm obs}) \end{cases} \tag{3.9}$$

otherwise $\tau^{\rm LAF}_j(\lambda_{\rm obs}) = 0$.
For the exact value of the coefficients $A^{\rm LAF}_{j,k}$ (k = 1, 2, and 3) calculated with $\delta = \sqrt{\pi}$ see Table 2 of Inoue et al. (2014).

The optical depths for the components are:

$$\tau_{\rm LC}^{\rm LAF}(\lambda_{\rm obs}, z_{\rm S}) \approx \Gamma(2-\beta_{\rm LAF})(N_{\rm l}\sigma_{\rm L})^{\beta_{\rm LAF}-1} \int_0^{z_{\rm S}} f_{\rm LAF}(z) \left(\frac{1+z_{\rm L}}{1+z}\right)^{\alpha(\beta_{\rm LAF}-1)} dz\,, \tag{3.10}$$

and

$$\tau_{\rm LC}^{\rm DLA}(\lambda_{\rm obs}, z_{\rm S}) \approx \frac{\Gamma(1-\beta_{\rm DLA})}{\Gamma(1-\beta_{\rm DLA}, N_{\rm l}/N_{\rm c})} \int_0^{z_{\rm S}} f_{\rm DLA}(z) \left\{1-(N_{\rm c}\sigma_{\rm L})^{\beta_{\rm DLA}-1}\left(\frac{1+z_{\rm L}}{1+z}\right)^{\alpha(\beta_{\rm DLA}-1)}\right\} dz\,, \tag{3.11}$$

For the LAF component, when $z_{\rm S} < 1.2$,

$$\tau_{\rm LC}^{\rm LAF}(\lambda_{\rm obs}, z_{\rm S}) \approx \begin{cases} 0.325\left[\left(\frac{\lambda_{\rm obs}}{\lambda_{\rm L}}\right)^{1.2} - (1+z_{\rm S})^{-0.9}\left(\frac{\lambda_{\rm obs}}{\lambda_{\rm L}}\right)^{2.1}\right] & (\lambda_{\rm obs} < \lambda_{\rm L}(1+z_{\rm S})) \\ 0 & (\lambda_{\rm obs} \geq \lambda_{\rm L}(1+z_{\rm S})) \end{cases} \tag{3.12}$$

when $1.2 \leq z_{\rm S} < 4.7$,

$$\tau_{\rm LC}^{\rm LAF}(\lambda_{\rm obs}, z_{\rm S}) \approx \begin{cases} 2.55\times10^{-2}(1+z_{\rm S})^{1.6}\left(\frac{\lambda_{\rm obs}}{\lambda_{\rm L}}\right)^{2.1} + 0.325\left(\frac{\lambda_{\rm obs}}{\lambda_{\rm L}}\right)^{1.2} - 0.250\left(\frac{\lambda_{\rm obs}}{\lambda_{\rm L}}\right)^{2.1} & (\lambda_{\rm obs} < 2.2\lambda_{\rm L}) \\ 2.55\times10^{-2}\left[(1+z_{\rm S})^{1.6}\left(\frac{\lambda_{\rm obs}}{\lambda_{\rm L}}\right)^{2.1} - \left(\frac{\lambda_{\rm obs}}{\lambda_{\rm L}}\right)^{3.7}\right] & (2.2\lambda_{\rm L} \leq \lambda_{\rm obs} < \lambda_{\rm L}(1+z_{\rm S})) \\ 0 & (\lambda_{\rm obs} \geq \lambda_{\rm L}(1+z_{\rm S}) \end{cases} \tag{3.13}$$

and when $z_{\rm S} \geq 4.7$,

$$\tau_{\rm LC}^{\rm LAF}(\lambda_{\rm obs}, z_{\rm S}) \approx \begin{cases} 5.22\times10^{-4}(1+z_{\rm S})^{3.4}\left(\frac{\lambda_{\rm obs}}{\lambda_{\rm L}}\right)^{2.1} + 0.325\left(\frac{\lambda_{\rm obs}}{\lambda_{\rm L}}\right)^{1.2} - 3.14\times10^{-2}\left(\frac{\lambda_{\rm obs}}{\lambda_{\rm L}}\right)^{2.1} & (\lambda_{\rm obs} < 2.2\lambda_{\rm L}) \\ 5.22\times10^{-4}(1+z_{\rm S})^{3.4}\left(\frac{\lambda_{\rm obs}}{\lambda_{\rm L}}\right)^{2.1} + 0.218\left(\frac{\lambda_{\rm obs}}{\lambda_{\rm L}}\right)^{2.1} - 2.55\times10^{-2}\left(\frac{\lambda_{\rm obs}}{\lambda_{\rm L}}\right)^{3.7} & (2.2\lambda_{\rm L} \leq \lambda_{\rm obs} < 5.7\lambda_{\rm L}) \\ 5.22\times10^{-4}\left[(1+z_{\rm S})^{3.4}\left(\frac{\lambda_{\rm obs}}{\lambda_{\rm L}}\right)^{2.1} - \left(\frac{\lambda_{\rm obs}}{\lambda_{\rm L}}\right)^{5.5}\right] & (5.7\lambda_{\rm L} \leq \lambda_{\rm obs} < \lambda_{\rm L}(1+z_{\rm S})) \\ 0 & (\lambda_{\rm obs} \geq \lambda_{\rm L}(1+z_{\rm S})) \end{cases} \tag{3.14}$$

For the DLA component, when $z_{\rm S} < 2.0$,

$$\tau_{\rm LC}^{\rm DLA}(\lambda_{\rm obs}, z_{\rm S}) \approx \begin{cases} 0.211(1+z_{\rm S})^{2.0} - 7.66\times10^{-2}(1+z_{\rm S})^{2.3}\left(\frac{\lambda_{\rm obs}}{\lambda_{\rm L}}\right)^{-0.3} - 0.135\left(\frac{\lambda_{\rm obs}}{\lambda_{\rm L}}\right)^{2.0} & (\lambda_{\rm obs} < \lambda_{\rm L}(1+z_{\rm S})) \\ 0 & (\lambda_{\rm obs} \geq \lambda_{\rm L}(1+z_{\rm S})) \end{cases} \tag{3.15}$$

and when $z_{\rm S} \geq 2.0$,

$$\tau_{\rm LC}^{\rm DLA}(\lambda_{\rm obs}, z_{\rm S}) \approx \begin{cases} 0.634 + 4.70\times10^{-2}(1+z_{\rm S})^{3.0} - 1.78\times10^{-2}(1+z_{\rm S})^{3.3}\left(\frac{\lambda_{\rm obs}}{\lambda_{\rm L}}\right)^{-0.3} & \\ -0.135\left(\frac{\lambda_{\rm obs}}{\lambda_{\rm L}}\right)^{2.0} - 0.291\left(\frac{\lambda_{\rm obs}}{\lambda_{\rm L}}\right)^{-0.3} & (\lambda_{\rm obs} < 3.0\lambda_{\rm L}) \\ 4.70\times10^{-2}(1+z_{\rm S})^{3.0} - 1.78\times10^{-2}(1+z_{\rm S})^{3.3}\left(\frac{\lambda_{\rm obs}}{\lambda_{\rm L}}\right)^{-0.3} & \\ -2.92\times10^{-2}\left(\frac{\lambda_{\rm obs}}{\lambda_{\rm L}}\right)^{3.0} & (3.0\lambda_{\rm L} \leq \lambda_{\rm obs} < \lambda_{\rm L}(1+z_{\rm S})) \\ 0 & (\lambda_{\rm obs} \geq \lambda_{\rm L}(1+z_{\rm S})) \end{cases} \tag{3.16}$$

Using the relations shown above I have developed a Fortran code and I have used it to extinguish the original templates, before running the main code.

3.6 SED-fitting procedure

The major observational challenge in any study of the AGN-galaxy co-evolution lies in the accurate separation of the AGN and galaxy emission components, at all optical-IR wavelengths. This is a fundamental step to be done because, depending on the intrinsic spectral energy distribution of the nuclear and of the stellar light, and of their

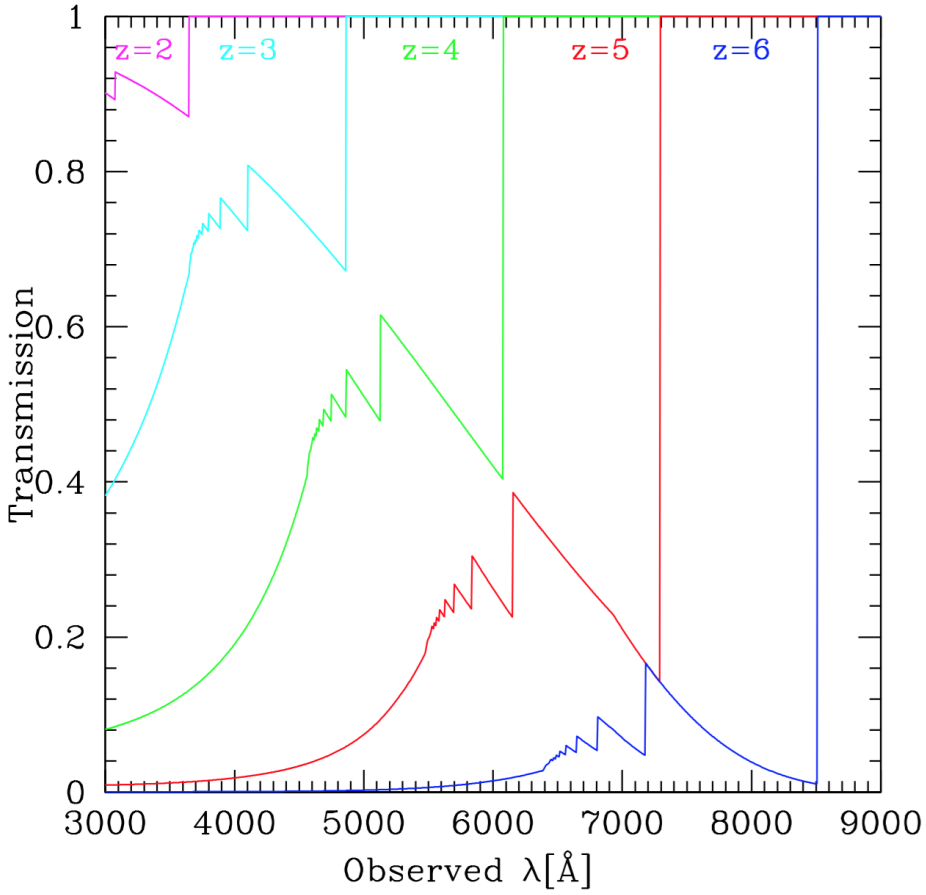

FIGURE 3.1: Mean transmission function at different redshifts, as from Inoue et al. 2014.

respective level of extinction, inaccurate de-blending might not only hamper any precise determination of the galaxies' physical properties, but also mask AGN signatures and bias our view of the SMBH growth. Since the relative contribution in the SED of the different components (AGN/host galaxy) varies with wavelength, a proper decomposition can be obtained by an SED-fitting approach. The main tool used to investigate galaxy SED is to apply appropriate SED-fitting techniques with sophisticated models. In recent years tools for SED-fitting have progressed significantly, with the introduction of procedures to fit data from the UV to the FIR.

The approach I have followed consists in considering each observed SED in the sample as the result of the superposition of the nuclear AGN emission and of the galactic light, the last usually modeled as due to the integrated light of the stellar populations of the galaxy which are generated by different star-formation histories. I remind that galaxy SEDs peak typically at around 1 μm for a very wide range of SFR histories.

The strength of the SED fitting method is that, given sufficiently wide photometric coverage, it is applicable to all AGN, obscured and unobscured, independent of their

luminosity. In particular, once a comprehensive set of templates for the SED components is chosen, the method can be applied almost blindly to any detected object in a multi-wavelength survey, reaching an accuracy that depends on the number of bands and depth of the available photometric catalogs. In general, both components significantly contribute and the global SED is the result of the combination of the central QSO's and the host galaxy's SED (see e.g. Hao et al., 2009; Merloni et al., 2010; Lusso et al., 2012; Bongiorno et al., 2012). How much these two components contribute to the global SED depends on a number of factors, the most important ones being their relative luminosity and the level of obscuration affecting each of them. In type-1 unobscured AGN, the AGN component typically dominates in the optical and IR bands with some degree of contribution from the host galaxy; on the contrary, the optical continuum of type-2 obscured AGN is dominated by the host galaxy emission with the AGN component rising mainly at IR wavelength. Obviously, not both components are always detectable. Solutions in which the SED is a pure QSO (in case of type-1 AGN) or a galaxy with a negligible contribution from the central AGN (in case of type-2 AGN), are both possible.

For the work presented in this Thesis I have used a SED-fitting code which I developed on the basis of the one by Bongiorno et al. (2012). It has been written to be as flexible as possible: various input information can be set up by the user to configure the fitting methodology (e.g. cosmology and fitting options), the input photometry (i.e. number of photometric points and available bands) and the library templates (for both AGN and galaxy templates) to be used. Once that all the files required have been settled, the code runs generating some output files, containing useful information for the analysis of the SED. The code takes as input files the AB magnitudes of each object, converting them in the relative flux density, according to the relation:

$$F_\lambda = 10^{-0.4\,mag_{AB}\,+48.60} \cdot \frac{c}{\lambda_{eff}^2} \tag{3.17}$$

where λ_{eff} are the effective wavelengths of the band-filters. Missing magnitudes are recognized by assigning to them a negative value, e.g. in the form -99.00. The observed SED is fitted with a multi-component model. In particular:

$$F_{obs} = A\ F_1 + B\ F_2 + C\ F_3 + ... \tag{3.18}$$

where F_{obs} is the total observed flux of a given source, F_i is the i-th emission component; A, B, C are the relative normalization parameters. From the match among the AGN and galaxies' templates the code returns the best choice of the model and the values of the normalization parameters reproducing the data. In details, the code reads the input data file described in Appendix A, considering one object at the time. Then it calculates

the luminosity distance for each object, assuming a ΛCDM cosmology with $H_0 = 67.90$, $\Omega_m = 0.3065$, $\Omega_\lambda = 0.6935$, as from Planck mission's latest results. These parameters can however be modified in the setup file (see Appendix A). Then it proceeds with the SED fitting. The determination of the combination of the models that better reproduce the set of the observed data points is performed by weighted least square, better known as the standard reduced χ^2 minimization, where the reduced χ^2 is in the form:

$$\chi^2_\nu = \frac{1}{n-p} \sum_{i=1}^{n} \left(\frac{F_i^M - F_i^O}{\sigma_i} \right)^2 \tag{3.19}$$

where n is the number of observed data points, p the number of free model parameters, F_i^O and F_i^M the observed and model fluxes in the i-band, respectively, and σ_i the errors in the observed fluxes.

CHAPTER 4

Giant star nurseries in hyper-luminous quasars

The AGN efficiency in driving powerful outflows is expected to increase with the bolometric luminosity of the AGN. Therefore, one would expect that AGN feedback could reach its maximum of efficiency at the brightest end of the AGN luminosity function. Accordingly, this Chapter aims at investigating the AGN-galaxy co-evolution in the most luminous AGN, which are therefore potentially the best places where we can hunt for feedback phenomena.

4.1 Introduction

Since the co-evolution of BHs and galaxies is directly linked to the SFR and consumption of gas, one of the key parameters to study is the SF activity of the quasar host galaxies. This has benefitted from progressively larger numbers of quasars being identified in wide, systematic infrared galaxy surveys. The problem in this type of analysis is that the quasar may bias the SF estimate in the host by contaminating the UV and optical range of the spectrum. A possible solution might be to use the far-infrared (FIR) emission, through UV light that is reprocessed by the dust grains. The quasar contamination drops towards the FIR band (see, however, Schneider et al., 2015) and the effect of dust extinction is almost negligible.

The first investigations of the FIR emission in quasars was carried out with the Infrared Astronomical Satellite (IRAS) and the Infrared Space Observatory (ISO) combined with

data from SCUBA and IRAM which extended the observational range at longer wavelengths. The launch of the *Herschel* Space Observatory in 2009 (Pilbratt et al., 2010) allowed us to observe the galaxy rest-frame emission as never before. Thanks to *Herschel* observations, several studies have been made in the past years to understand whether the presence of a quasar in the centre of the galaxy has any influence on the host SFR. The results have been contradictory, however. Most of these studies have found evidence for enhanced SFR in quasars hosts, compared to non-active galaxies of the same stellar mass, and argued that the bulk of moderate-luminosity X-ray selected quasars are hosted in galaxies that trace the normal star-forming main-sequence (MS) galaxies (e.g., Harrison et al., 2012; Mullaney et al., 2012b; Rosario et al., 2013; Santini et al., 2012; Stanley et al., 2015). Conversely, Bongiorno et al. (2012), Azadi et al. (2015) and Mullaney et al. (2015) reported a broad specific SFR (sSFR) distribution for X-ray selected quasars that peak below the MS.

In addition, a further analysis is required to understand whether quasars are more likely to reside in quiescent or in star-forming host galaxies, that is, to search for an overall correlation between the SF and the nuclear activity in individual galaxies. Hatziminaoglou et al. (2010), studying a sample of *Herschel* Multi-tiered Extragalactic Survey (HerMES) high-redshift quasars, found a correlation between the quasar and the SF luminosities for both high- and low-luminosity sources. Shao et al. (2010), alternatively, showed a slight dependence on quasar luminosity for the SF in the latter class, in accordance with the results of Mullaney et al. (2012b) for moderate- luminous quasars and results of Rosario et al. (2012) who used a larger sample, including the COSMOS sample. Conversely, Mullaney et al. (2012a) did find hints of coeval growth of the super-massive BH and host galaxy, suggesting a causal connection, which was also found by Delvecchio et al. (2015) in their analysis of about 8500 sources with *Herschel* observations up to $z = 2.5$. A possible reason for such discrepant results resides in the fact that an additional question needs to be kept in mind, which is the strength of the quasar contamination in the FIR. Symeonidis (2017) argued that in their sample of the most powerful quasars collected from Tsai et al. (2015) and Netzer et al. (2016), the total infrared luminosity was dominated by the quasar emission and there was no need for a star-forming component. On the contrary, Hatziminaoglou et al. (2010) showed that a starburst was always needed to reproduce the FIR emission of their sample. The truth is probably in between these two scenarios: Haas et al. (2003) proposed that objects hosting the highest FIR luminosities ($L_{FIR} > 10^{13} - 10^{14} L_{\odot}$) have a strong star-forming component but the quasar contribution in the FIR is not negligible. Similarly, Dai et al. (2012) and Schneider et al. (2015) concluded that the radiation emitted by the central nucleus can provide an important source of heating for the dust in the galaxy.

In order to understand the discrepant results of the aforementioned works, it is important to constrain any correlation between the quasars and their host galaxy parameters. Models and observations have both confirmed that the efficiency in driving energetic winds and the momentum fluxes of galaxy-scale outflows increases with the quasar bolometric luminosity (see e.g., Menci et al., 2008; Hopkins et al., 2016; Fiore et al., 2017). Hence, we would expect that feedback could reach its maximum efficiency at the brightest end of the quasar luminosity function. For this reason, understanding the coupling between the nuclear energy output and the host galaxy is an open issue that is particularly relevant for the most luminous quasars, especially at 1<z<3, the golden epoch for galaxy-quasar co-evolution.

The Chapter is organized as follows: In Section 4.2 we describe the sample and the data, with the focus on the *Herschel* data extraction procedure. Section 4.4 provides a detailed explanation of the method we used to separate the different emission components, and we describe the templates we adopted to model the whole spectral energy distribution. The result of the fitting procedure is shown in Section 4.5, where we report bolometric and monochromatic luminosities and a study of the infrared properties (host infrared luminosity and SFR, cold and hot dust masses) of the sources. In the same section we also thoroughly study the possible contribution of the quasar to the FIR fluxes, from which we gain a statistical result that can be be applied to the entire sample. Finally, Section 4.6 presents the conclusions of our work.

In what follows, we adopt a ΛCDM cosmology with $H_0 = 67.90\,\mathrm{km/s/Mpc}$, $\Omega_m = 0.3065$, $\Omega_\Lambda = 0.6935$ (Planck Collaboration et al., 2016).

4.2 The WISSH sample

Weedman et al. (2012) presented a list of ~ 100 hyper-luminous AGN with the highest $7.8\,\mu m$ luminosities, i.e. $\nu L_\nu(7.8\,\mu m) \geq 10^{47}$ erg s^{-1}, selected by cross-correlating the sources detected at $22\,\mu m$ from the Wide-field Infrared Survey Explorer (WISE) with the Sloan Digital Sky Survey (SDSS) optically discovered type 1 AGN, in the redshift range $1.5 < z < 5$. The selection has been made in the mid-IR band, with these major advantages: (1) we are not biased against dust obscured sources, since the absorbed optical emission is re-emitted at IR wavelengths; (2) all AGN can be compared consistently without the uncertainties due to extinction correction affecting the luminosity measurements at shorter wavelengths; and (3) in this way, we tend to select red AGN which are ideal targets as they likely represent an intermediate population emerging from the merger-driven, heavily-obscured phase and preceding the blue quasar phase in which the

gas/dust content in the host galaxy may be already swept away. Banerji et al. (2012) found that the obscured phase of a quasar is probably associated with its most intrinsically luminous stage as it corresponds to a time when the black-hole is accreting mass very quickly.

Most of the sources in the catalog by Weedman et al. (2012) are at z $\sim 2-3$, the golden epoch of AGN and galaxy evolution, since it is the epoch when SMBHs of the most powerful AGN have accreted most of their mass, and the nearby massive elliptical galaxies formed the bulk ($\sim$ 90%) of their stars. The sample of SDSS/WISE AGN was created starting from the 105 783 objects in data release 7 of the SDSS quasar catalog, choosing only all sources with z$>$ 1.5. The redshift criterion results in 52 761 AGN from the SDSS. Of these, the most luminous 100 as measured by $\nu L_\nu(7.8\,\mu m)$, were selected. The sources analyzed in this chapter belong to the WISSH (**WI**SE-**S**DSS **s**elected **h**yper-luminous) sample, which consists of 87 AGN obtained from the Weedman sample by removing the lensed objects and those with a contaminated WISE photometry (leading to an overestimation of the $\nu L_\nu(7.8\,\mu m)$).
Among the WISSH sources, this work focuses on the 16 quasars for which *Herschel* observations are available on the archive. The lack of a unique preselection in the observational campaigns from which the data have been extracted shall ensure no bias. Moreover, as shown in Figure 4.1, these sources seem to be randomly distributed both in redshift and luminosity: they are therefore representative of the total WISSH sample. In Table 4.1 we list the 16 sources studied here, reporting the numeric ID associated to each source, their SDSS ID, and their redshift. Most of the objects have redshift taken from the seventh or the tenth release of the SDSS, but for 5 sources out of 16, we can rely on more accurate z estimates performed by Vietri et al. (2018) on LBT/LUCI spectra using the Hβ line.

4.3 Multi-walength data

For the 16 sources analyzed here, we have collected data from four different surveys, for a total of 15 bands: SDSS covering the optical bands u, g, r, i and z [1]; 2MASS in the NIR J-, H- and K-bands [2], WISE at 3 μm, 4.5 μm, 12 μm and 22 μm and finally SPIRE in the FIR, at 250 μm, 350 μm and 500 μm. All the photometric data have been corrected for Galactic extinction following Schlegel et al. (1998). While for the UV-to-MIR data we have collected the data from published catalogs, the photometry in the FIR bands has been extracted from archival data.

[1] http://skyserver.sdss.org/dr10/en/home.aspx
[2] http://irsa.ipac.caltech.edu/frontpage/

N	SDSS name	z
1	SDSSJ012403.77+004432.6	3.840
2	SDSSJ020950.71-000506.4	2.856
3	SDSSJ073502.30+265911.5	1.982
4	SDSSJ074521.78+473436.1	3.225 *
5	SDSSJ080117.79+521034.5	3.263 *
6	SDSSJ081855.77+095848.0	3.694
7	SDSSJ090033.50+421547.0	3.294 *
8	SDSSJ092819.29+534024.1	4.390
9	SDSSJ101549.00+002020.0	4.400
10	SDSSJ121549.81-003432.1	2.707
11	SDSSJ123714.60+064759.5	2.781
12	SDSSJ125005.72+263107.5	2.044
13	SDSSJ143352.20+022713.9	4.620
14	SDSSJ170100.60+641209.3	2.737
15	SDSSJ212329.46-005052.9	2.283 *
16	SDSSJ234625.66-001600.4	3.512 *

Table 4.1: Sample of the 16 WISSH AGN here studied: source number, SDSS ID, SDSS redshift (* sources have z obtained by Vietri et al. (2018), from LBT NIR spectroscopy or SINFONI spectroscopy).

Survey/Instrument	Filter	$\lambda_{\rm eff}$
SDSS	u	3543 Å
	g	4770 Å
	r	6231 Å
	i	7625 Å
	z	9134 Å
2MASS	J	12350 Å
	H	16620 Å
	K	21590 Å
WISE	W1	3.35 μm
	W2	4.60 μm
	W3	11.56 μm
	W4	22.08 μm
Herschel	SPIRE1	243 μm
	SPIRE2	340 μm
	SPIRE3	482 μm

Table 4.2: Summary of the photometric surveys properties.

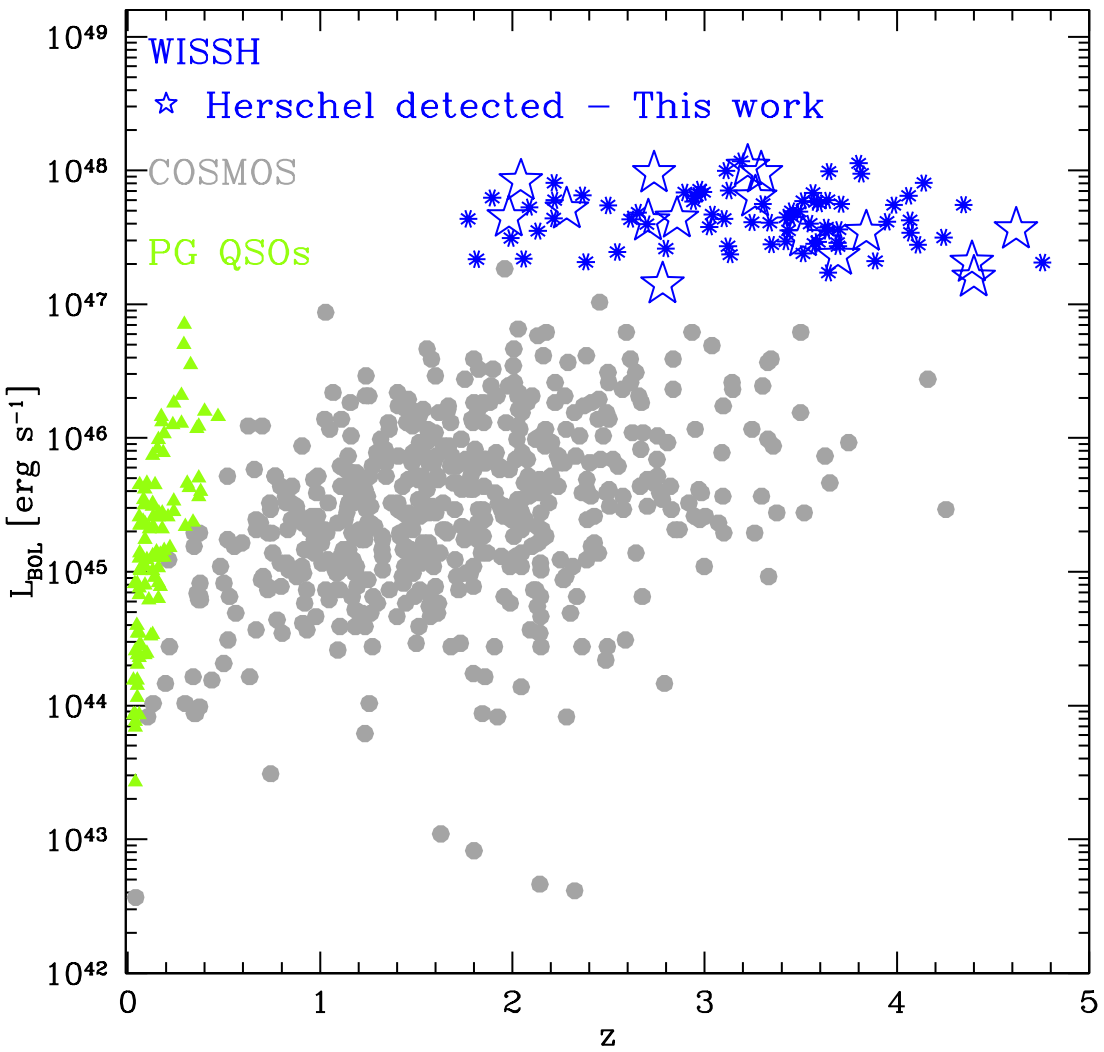

FIGURE 4.1: Bolometric luminosity versus redshift of the total WISSH sample (in blue). The large stars are the 16 sources with *Herschel* data. For comparison, the COSMOS survey by (Bongiorno et al., 2012) and the PG QSOs by Veilleux et al. (2009) and Petric et al. (2015) are shown in grey and green, respectively.

4.3.1 *Herschel* SPIRE data: source extraction

For the FIR photometry we used *Herschel* archival data. For each source we estimated the *Herschel* flux densities at SPIRE wavelengths using the `sourceExtractorTimeline` (Bendo et al., 2013), a fitting method implemented in HIPE (Ott, 2010), which is widely used for point-like sources (see e.g., Pappalardo et al., 2016; Ciesla et al., 2012). *Herschel* observations are performed by orthogonally scanning each target with the SPIRE bolometers, measuring the fluxes at regular time intervals. The measurement set of the bolometers for each cross-scan is called "timeline" data. The `sourceExtractorTimeline` fits these timeline data from all bolometers within an individual array with a two-dimensional Gaussian function. The input is the source position, a radius containing

the source, and an aperture identifying the background annulus. Following the prescriptions of Pappalardo et al. (2015), we set a search radius for the target of 22", 30", and 42", at 250 μm, 350 μm, and 500 μm, respectively. For the background annulus we define a set of different apertures between 140" and 220", and we estimate the background from the median of all the values recovered. Two fits were performed to the timeline data. The first fit was performed using a circular Gaussian function in which the FWHM was allowed to vary. Then the FWHM was used to determine whether the source is resolved or unresolved and to reject sources that are either too narrow (which may be unremoved glitches) or too broad (which are probably extended sources). To test at which distance two sources are distinguishable, point-like objects with the same flux density and an increasing distance from each other were injected in the timeline data. We found that two sources are resolved only if they are at a distance above $\sim$ 22", 30", and 46" at 250, 350, and 500 μm, respectively. Fixing the distance between the sources to these values, as a second step, we injected point-like objects at different flux densities in the timeline data to investigate the FWHM recovered by sourceExtractorTimeline. These tests demonstrate that artificial sources with FWHM corresponding to the telescope beam (17.5", 23.9", and 35.1" at 250, 350, and 500 μm, respectively) added to timeline data may have an FWHM between 10" and 30" at 250 μm, 13.3" and 40" at 350 μm, and 20" and 60" at 500 μm. Therefore, sources, whose FWHM was determined via sourceExtractorTimeline and were outside these values were excluded from the analysis. Although other software packages have been developed for source extraction within complex extragalactic fields (including software developed specifically for *Herschel*), we prefer to use the timeline fitter because the SPIRE data are flux calibrated at the timeline level using timeline-based point-spread function-fitting techniques, so that the method we used is consistent with the flux calibration measurements themselves and it is therefore expected to be more accurate.
In Table 4.3 we report the photometric flux densities obtained from the images.

4.4 UV-to-FIR Spectral Energy Distribution

This section is intended to describe the tool developed to study the SED of our sources. As described in Chapter 3, the approach is based on the idea that the overall observed SED of each AGN is the result of the combination of different emission components that can be properly disentangled. In particular, we used a fitting procedure that in turn is based on the weighted least-square method, better known as the standard reduced χ^2 minimization, where the reduced χ^2 is in the form :

N	$f_{250\,\mu m}$[mJy]	$f_{350\,\mu m}$[mJy]	$f_{500\,\mu m}$[mJy]
1	< 48	< 44	< 40
2	71 ± 18	61 ± 10	31 ± 10
3	91 ± 7.2	53 ± 7.3	33 ± 9.2
4	55 ± 7.4	58 ± 7.3	52 ± 9.5
5	93 ± 7.3	80 ± 8.1	57 ± 10
6	48 ± 7.2	49 ± 7.3	< 56
7	29 ± 7.7	19 ± 7.4	< 27
8	65 ± 7.7	75 ± 8.2	66 ± 9.8
9	20 ± 5.2	23 ± 5.1	19 ± 6.6
10	75 ± 12	58 ± 12	51 ± 8.3
11	93 ± 5.1	94 ± 5.1	62 ± 6.4
12	< 45	< 31	< 65
13	28 ± 2.9	23 ± 2.9	16 ± 3.6
14	81 ± 3.0	56 ± 2.9	< 40
15	36 ± 3.7	28 ± 3.6	18 ± 4.5
16	41 ± 14	38 ± 9.9	< 35

TABLE 4.3: FIR flux densities in the three *Herschel*-SPIRE bands for the WISSH quasars.

$$\chi^2_\nu = \frac{1}{n-p} \sum_{i=1}^{n} \left(\frac{f_i^{obs} - f_i^{model}}{\sigma_i} \right)^2 \tag{4.1}$$

with n the observed data points, f_i^{obs} and σ_i the observed fluxes and associated errors of the photometric bands, f_i^{model} the total flux of the chosen model with p free parameters, and $\nu = n - p$ the degrees of freedom.
Our model (f_{model}) includes three emission components:

$$f_{model} = A\ f_{AD+T} + B\ f_{CD} + C\ f_{ME} \tag{4.2}$$

where f_{AD+T} represents the emission coming from the accretion disc (both direct and reprocessed by the dusty torus), f_{CD} accounts for the FIR emission due to the reprocessed flux by cold dust and is modelled as a modified blackbody, f_{ME} is any possible MIR emission excess modelled with a simple blackbody. Finally, A, B, and C are the relative normalization. For each component we have created a library of templates described below. The fitting procedure, through χ^2 minimization, allows us to determine the combination of templates that best describes the observed SED and their relative contribution.
The lack of a galaxy emission component in the fitting procedure is due to the fact that, in such extremely bright and unobscured sources, the UV galactic emission is completely

overwhelmed by the AGN light. Indeed, the need for such galactic emission has been rejected by the minimization procedure.

4.4.1 Library templates

The data were fitted with three main emission components (see previous section). For each component, a number of templates spanning a large grid of physical parameters were created. In the next sections we describe them in detail.

4.4.1.1 AGN emission

The first component of the SED-fitting tool includes the direct emission from the central engine and the light absorbed and re-emitted by the dusty torus.

(i) Nuclear emission

The shape of the SED of the primary source is commonly described by power laws of different spectral indices that vary considerably from one work to another, however. In order to evaluate the best shape to describe the observed emission of a generic quasar, we analysed different models of UV emission that are used in literature.

Fritz et al. (2006) modelled the primary source of emission, which was updated by Stalevski et al. (2012, 2016), as a composition of power laws with indices from Granato and Danese (1994) and Nenkova et al. (2002),

$$\lambda L_\lambda = \begin{cases} \lambda^{1.2} & 0.001 \leq \lambda \leq 0.030 \ [\mu m] \\ \lambda^{0} & 0.030 < \lambda \leq 0.125 \ [\mu m] \\ \lambda^{-0.5} & 0.125 < \lambda \leq 20.0 \ [\mu m] \, . \end{cases} \tag{4.3}$$

Feltre et al. (2012) proposed an updated version of this model, changing the spectral indices of the power laws according to Schartmann et al. (2005), making them steeper at short wavelengths:

$$\lambda L_\lambda = \begin{cases} \lambda^{2} & 0.001 \leq \lambda \leq 0.050 \ [\mu m] \\ \lambda^{1.8} & 0.050 < \lambda \leq 0.125 \ [\mu m] \\ \lambda^{-0.5} & 0.125 < \lambda \leq 10.0 \ [\mu m] \\ \lambda^{-3} & \lambda > 10.0 \ [\mu m] \, . \end{cases} \tag{4.4}$$

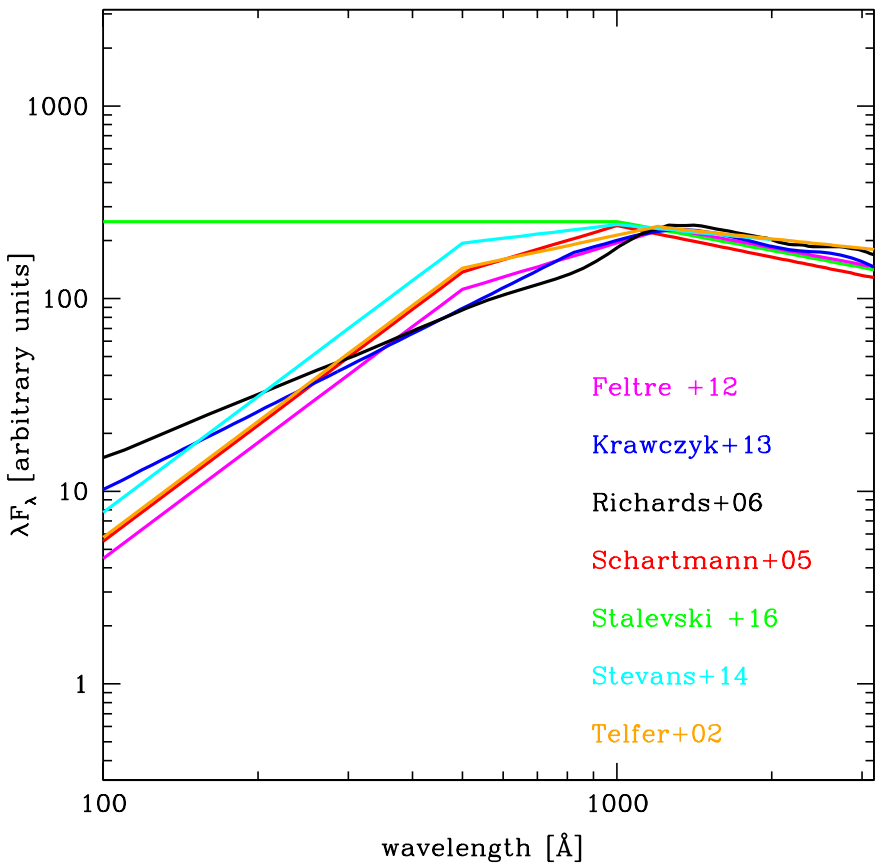

FIGURE 4.2: Comparison of the SED for different emission models of the quasar primary source.

Figure 4.2 shows the aforementioned models from Stalevski et al. (2012) and Feltre et al. (2012) compared to the models derived from the composite quasar spectra by Telfer et al. (2002) and Stevans et al. (2014) based on HST quasars spectra and compared to the empirical SDSS quasar mean spectra from Richards et al. (2006) and Krawczyk et al. (2013). As visible in Figure 4.2, the slope of Stalevski's power law at short wavelengths ($\lambda < 0.125$ μm) seems to be at odds with all the other emission models, both empirical and theoretical ones. In our library of templates, we therefore chose to model the accretion disc emission using the recipe by Feltre et al. (2012).

(ii) Torus emission

Several models for the radiation that is emitted by the dusty torus surrounding the accretion disc are available in the literature, and they often result in very different solutions when fitted to the data. Feltre et al. (2012) studied the differences between a smooth and clumpy dusty torus by comparing the works by Fritz et al. (2006) and Nenkova et al. (2008). They concluded that the models with only a smooth grain distribution are not a

realistic description of the torus, since they imply a large number of collisions that would raise the temperature so high that it would destroy the dust grains (see also Krolik and Begelman, 1988). However, as a result of the difficulties in handling clumpy media and the lack of computational power, smooth models were used at first. Using a Monte Carlo radiative transfer code (SKIRT), Stalevski et al. (2012, 2016) simulated a dusty torus as a three-dimensional two-phase medium made of a combination of high-density clumps and low-density medium filling the space between the clumps. The models have been obtained starting from the smooth models by Fritz et al. (2006) and applying the algorithm described by Witt and Gordon (1996) to generate a two-phase clumpy medium, according to which each individual cell in the grid is assigned randomly, by a Monte Carlo process, to either a high- or a low-density state. In these models, the dust is a mixture of silicate and graphite grains (as in Mathis et al., 1977) with optical properties from Laor and Draine (1993) and Li and Draine (2001). Its distribution is described by a flared disc whose geometry is defined by the inner (R_{in}) and the outer (R_{out}) radii, and by the half-opening angle OA, which measures the dust-filled zone, from the equator to the edge of the torus, which is linked to the covering factor. Of the other models of dusty tori, we considered the model by Hönig and Kishimoto (2010), which is similar to Stalevski's in that it uses a three-dimensional transfer code based on a Monte Carlo approach. However, the model proposed by Stalevski et al. (2012, 2016) provides the best description of the reprocessed emission by the torus, being both smooth and clumpy, and therefore it represents the best choice to constrain the IR part of the spectrum of our sources with high accuracy.

Of the available empirical infrared quasar SEDs, we compared our choice of the torus emission with the SEDs proposed by Netzer et al. (2007), Mor and Netzer (2012), Netzer et al. (2016) (an extended version of Mor and Netzer (2012) template at longer wavelenghts), and Symeonidis et al. (2016); these are shown in Figure 4.3 in cyan, red, black and magenta respectively. Except for the SED proposed by Symeonidis et al. (2016), our torus model (in green) is in good agreement with all models. As described in more detail in Sect. 4.5.3, we found SFR values consistent with those published by Netzer et al. (2016) for three sources in common between the two samples, although different tori templates have been adopted. Focusing on the longest wavelengths, the empirical SED by Symeonidis et al. (2016) shows a much higher contribution (lower temperature) than the others. The reason probably is that in Symeonidis et al. (2016) the torus extent is larger than in the other cases. From a theoretical point of view, a huge radius of the torus (as the one described by Symeonidis et al. (2016)) should predict a height of the torus itself that is difficult to support. Moreover, as recently pointed out by Lani et al. (2017), the discrepancy found between the mean SED by Symeonidis et al. (2016) and the other tori templates shown, might be due to the fact that the first has been obtained

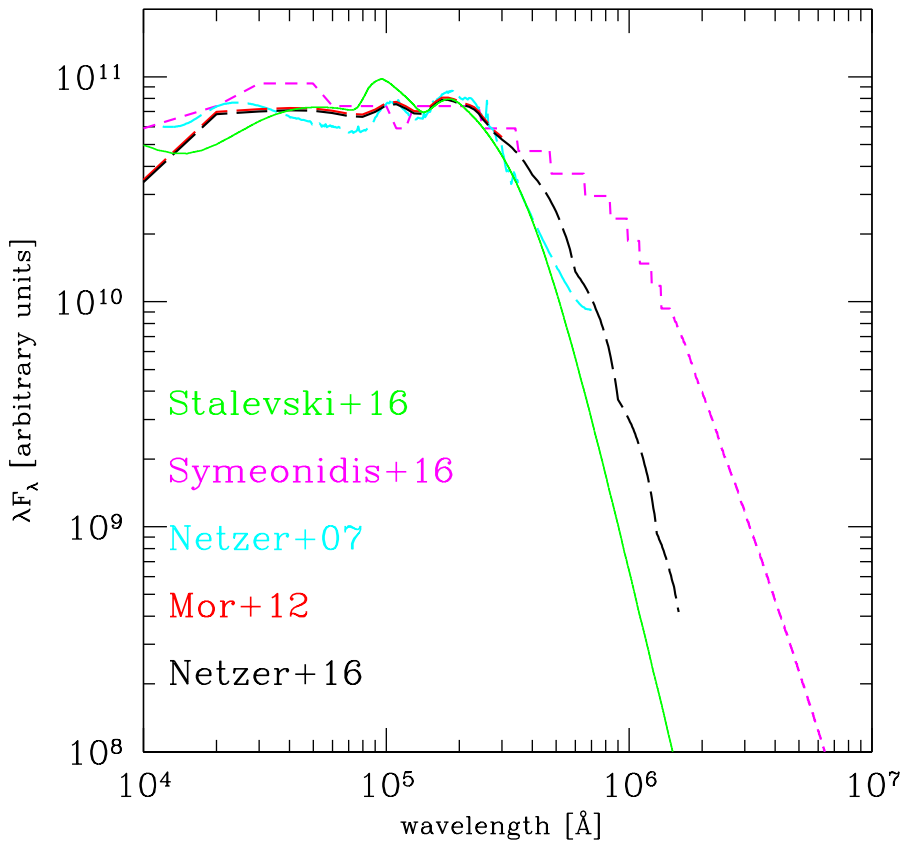

FIGURE 4.3: Infrared torus model by Stalevski et al. (2016) compared with the empirical SEDs by Netzer et al. (2007),Mor and Netzer (2012), Netzer et al. (2016), and Symeonidis et al. (2016).

without normalising the individual SEDs at a given wavelength and, above all, that it does not represent the entire quasar population but rather the extremely IR-luminous ones.

In view of the above, for this work we created new templates accounting for the accretion disc plus torus emission, made by the combination of the quasar torus emission from Stalevski et al. (2016) and the nuclear emission from Feltre et al. (2012), appropriately normalized to preserve the energy balance between the UV and the IR bands. This library is made of 1920 templates with different values of optical depth τ at 9.7 μm, half-opening angle OA, and dust distribution. In addition, each of them has ten different lines of sight θ, from face-on (0°, for typical unobscured type 1 AGN) to edge-on (90°, obscured type 2 AGN) view, for a total of 19200 templates (in Figure 4.4 torus templates for different varying parameters are shown). However, in order to reduce the computational time, we used only those with inclination angle 0°, which is a reasonable assumption considering that we study type 1 AGN and that the inclination angle i and the optical depth τ are

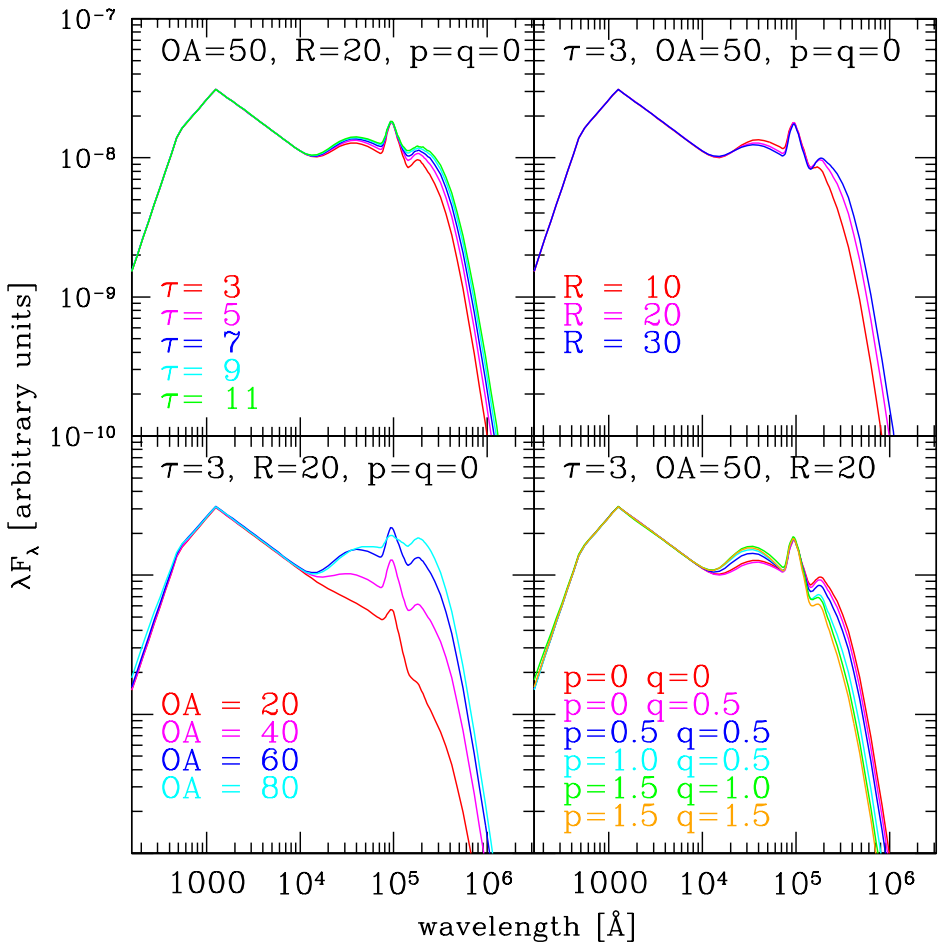

FIGURE 4.4: Examples of templates at inclination angle i = 0° used to describe the AD plus T emission. Different panels show how the torus emission changes when the physical parameters are varied, i.e. optical depth τ, ratio of outer to inner radius $R = R_{out}/R_{in}$, half-opening angle OA, and the p and q parameters related to the density gradient along the radial direction and with polar angle $\rho(r,\theta) \propto r^{-p}e^{-q|\cos\theta|}$ (Granato and Danese, 1994).

strongly degenerate. In this way, we obtained a reduced library of 1920 templates of accretion disc plus torus.

4.4.1.2 Cold dust emission

The second component of the SED-fitting procedure is a modified blackbody accounting for the emission powered by SF, which is absorbed by dust grains and re-emitted in the MIR and FIR. We know that the stellar light is emitted in the UV-to-NIR bands of the spectrum, with the NIR dominated by the older stars, while the UV is dominated by the massive short-lived stars. The young stars are responsible for polluting the ISM with metals and dust, producing grains that absorb the stellar light and re-radiate it in the IR and sub-millimiter domains, while the oldest stars ($\sim 10^9$ years) get dust into the

ISM during their AGB phase (Calura et al., 2008).

In the far-infrared, this dust emits thermal emission that is characterized by a blackbody spectrum with an additional $\lambda^{-\beta}$ term that accounts for the emissivity of the dust (Hildebrand, 1983). It must be stressed that since the FIR emission is produced by a mixture of grains of different shapes and sizes, this results in a distribution of temperatures. For simplicity, we can assume a single-temperature modified blackbody emission even if the SEDs of real galaxies are obviously more complex. Following Blain et al. (2002), the rest-frame emission of this cold dust is modeled as:

$$MBB(T_{CD}, \lambda) = \lambda^{-\beta}\, BB(T_{CD}, \lambda) \tag{4.5}$$

where $\mathrm{BB}(\mathrm{T_{CD}}, \lambda)$ is the Planck function for a dust temperature $\mathrm{T_{CD}}$ and β is the emissivity index. The temperature of the modified blackbody and the normalization are free parameters.

The emissivity of dust grains is generally taken to be a power law at these long wavelengths, with models and laboratory data suggesting indices in the range $1 \leq \beta \leq 2$. One of the main sources of uncertainty lies in the exact determination of this value: different values of β produce a systematic change in the best-model value of $\mathrm{T_{CD}}$ since a smaller β implies a higher cold dust temperature. Following Beelen et al. (2006), we fixed β to 1.6, which seems to be the most appropriate value for high-z AGN. Recently, works based on Planck and *Herschel* data have shown that the value of $\beta = 1.6$ (instead of $\beta = 2.0$ used in the past) might be the most correct to describe also the dust in local galaxies (see for example the studies on the Milky Way by Bianchi et al. 2017 and Sect. 4.3 of Planck Collaboration et al. 2014).

The cold dust library consists of about 50 BB templates, with temperatures in the range $20\,\mathrm{K} < \mathrm{T_{CD}} < 70\,\mathrm{K}$.

4.4.1.3 MIR emission excess

As outlined by several authors in the past, and shown in Figure 4.7, an additional component in the mid-infrared is often required to fit the MIR part of the SED of luminous quasars (see e.g., Barvainis, 1987; Mor et al., 2009; Leipski et al., 2013).
In the works mentioned above, the authors speculated that the dust grains are probably made of pure graphite since they are able to survive to temperatures higher than the silicate temperatures present in the torus (Minezaki et al., 2004; Suganuma et al., 2006). The physical scale of this hot dust is delimited by the sublimation radius of "typical" dust

composed of both silicate and graphite grains (torus inner radius) and the sublimation radius of pure graphite grains (which has a sublimation temperature of $\sim 1500\,\mathrm{K}$).

To describe the NIR emission excess, we generated about 650 templates using blackbodies of different temperatures, from $\mathrm{T_{NE}} = 190\,\mathrm{K}$ to $\mathrm{T_{NE}} = 1800\,\mathrm{K}$.

4.5 Results of the SED fitting

Given the wide multi-wavelength coverage, the fitting technique described above allows us to decompose the entire spectral energy distribution into the different emission components and to derive robust measurements of both the AGN and the host galaxy properties. In Figures 4.5 and 4.6 we show the best-fit SED model for the 16 sources. Black circles are the rest-frame photometric points corresponding to the observed bands we used to constrain the SED. Data below 1216 Å corresponding to the Lyman-α emission line, are plotted as open circles and are not taken into account in the fit. At these wavelengths, the flux is expected to be weakened due to the Lyman α absorption forest, which is not included in our model. Data points above 1216 Å were fitted with a combination of the components described above. In detail: (i) accretion disc plus torus emission (AD+T, blue line with cyan shaded area); (ii) cold dust emission in the IR band (CD, red line with orange shaded area); and (iii) NIR excess when necessary (NE, green line with shaded area). The shaded areas describe the range of values corresponding to the solutions for which $\Delta\chi^2 = \chi^2(\mathrm{sol}) - \chi^2(\mathrm{best}) \leq 1.0$, 1σ in the case of one parameter of interest (see Avni, 1976).

As a first step, we considered a standard combination of AD+T and CD components in the fit. However, in a few cases we found that these models are not enough to reproduce the whole SED, which shows an excess of emission in the MIR bands. For these cases, we therefore added as a third component, the additional MIR excess template, while fixing the AD+T and CD best-emission models found in the first run. To quantify whether such a component really does improve the fit, we performed the F-test, which measures the goodness of two nested models through the comparison of the χ^2 and degrees of freedom obtained in the two cases.

Figure 4.7 shows as an example, one of the sources for which the additional component was added (SDSSJ123714.60+064759.5). As visible even by eye, the inclusion of the MIR excess component improves the fit: the WISE 3 photometric point shows that including the MIR excess component brings the fit a factor of $\sim$5 closer to the observed point. For SDSSJ123714.60+064759.5, the result of the F-test is F=16.67, meaning that the

FIGURE 4.5: Resulting rest-frame SED decompositions for half of the sources (continues in Figure 4.6). Black circles are the rest-frame photometric points corresponding to the observed bands used to constrain the SED. Black open circles represent the photometric points not included in the fits (at $\lambda < 1216$ Å due to Ly-α absorption, see the text for more details), while the black arrows correspond to upper limits on the observed flux densities at 1σ. Lines (and shaded areas) correspond to the model templates (and the 1σ error) found as best-fit solution to describe the photometric points through the χ^2 minimization: blue is the accretion disc plus torus template (AD+T), red is the cold dust component (CD) while dark green is the NIR excess (NE) when present. Finally, the black line shows the sum of all these contributions. Blue, orange, and light green shaded areas correspond to the accretion disc plus torus, the cold dust, and the NIR excess templates within 1σ of the best-fit template, and light grey shaded area to their sum.

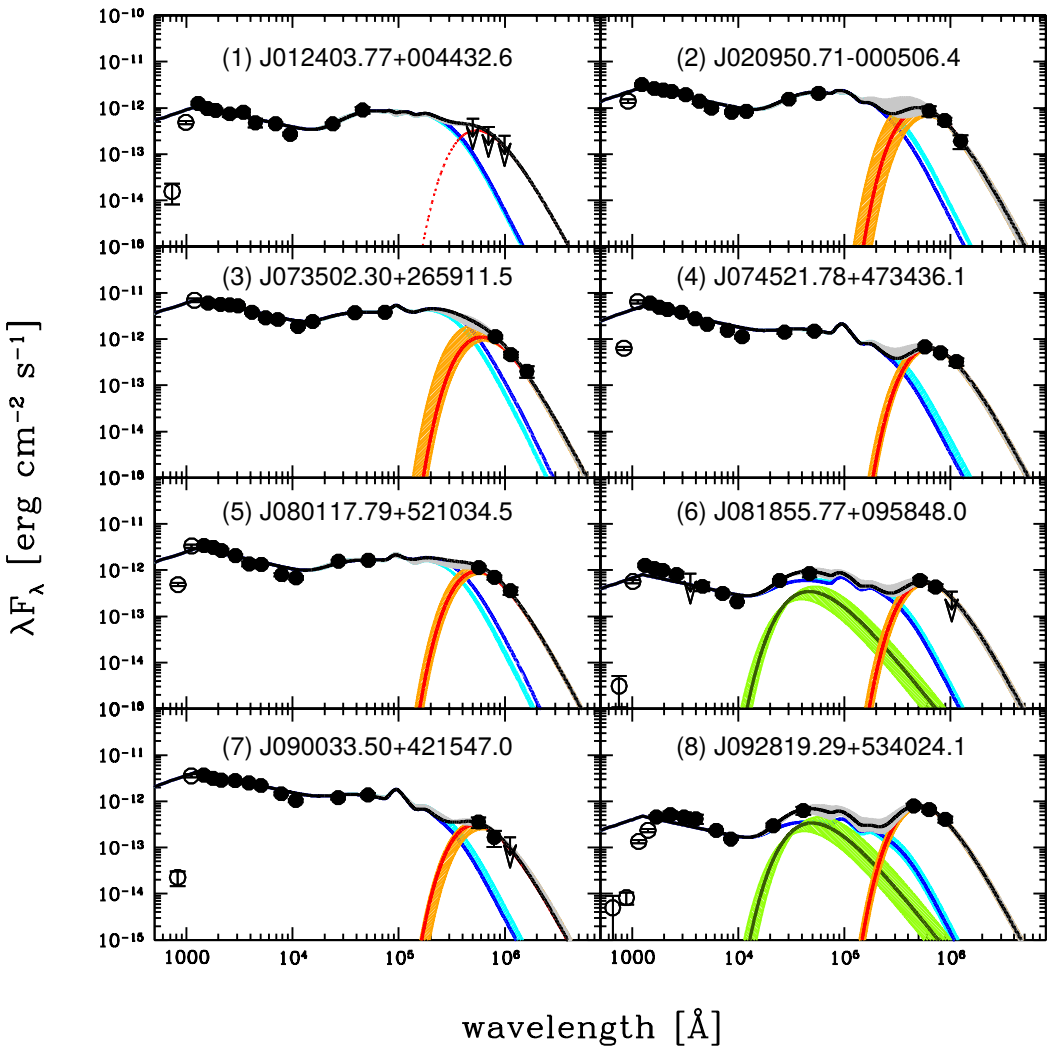

FIGURE 4.6: Same as in Figure 4.5 for the remaining 8 sources.

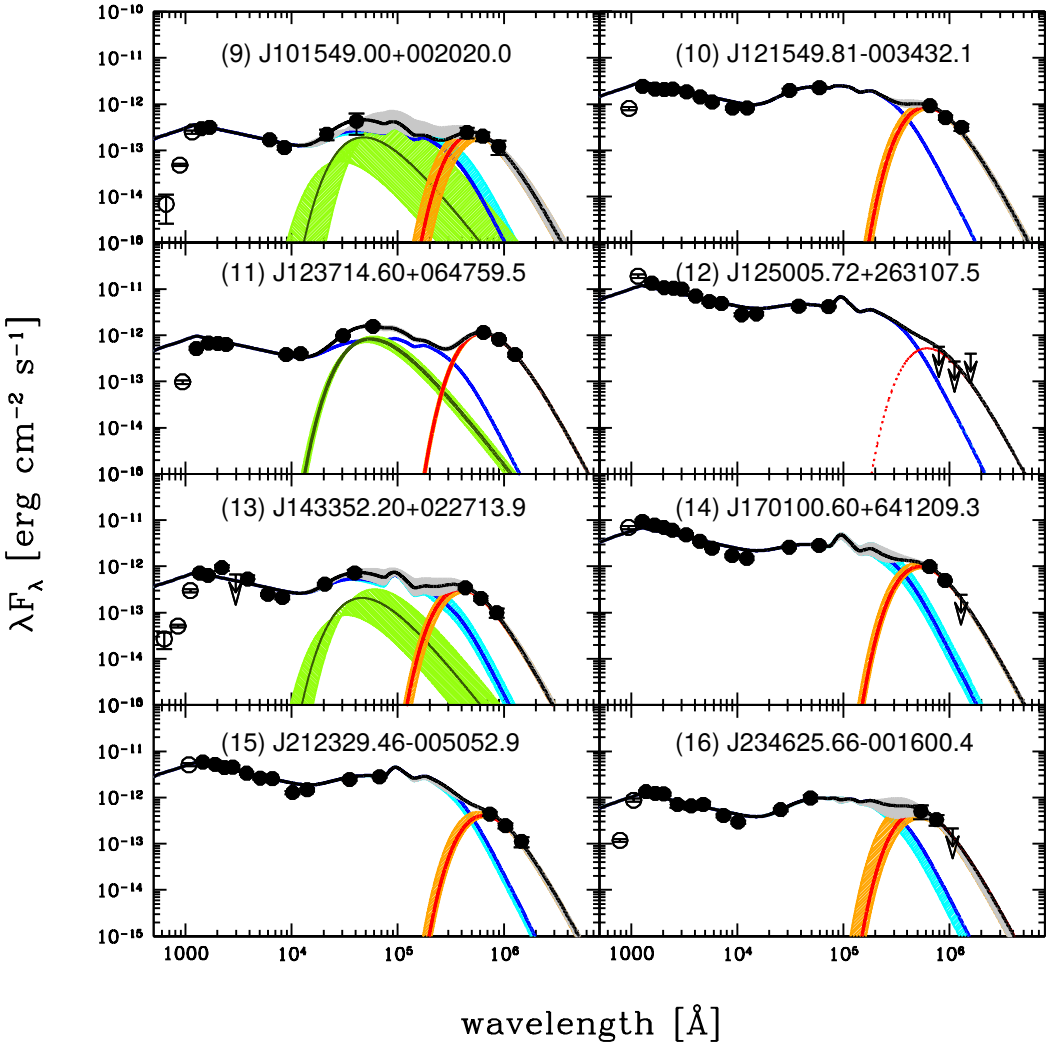

addition of the third component produces an improvement in the resulting fit statistic that is significant at a confidence level $\geq 99\,\%$. In the whole sample, we found that the MIR excess blackbody component is required in 5 out of the 16 sources ($\sim 31\%$).

4.5.1 Bolometric and monochromatic luminosities

From the final SED best-fit, we derived several physical quantities of both the host galaxy and the nuclear source. The intrinsic AGN bolometric luminosity was computed for each source by integrating the accretion disc emission in the range $60\,\text{Å} - 1\,\mu\text{m}$ (although Figure 4.5 and 4.6 only show wavelengths above $\sim 500\,\text{Å}$).
In particular,

$$L_{bol} = 4\pi d_L^2 \int_{60\,\text{Å}}^{1\,\mu m} A\, f_{AD} \;\; [erg/s] \tag{4.6}$$

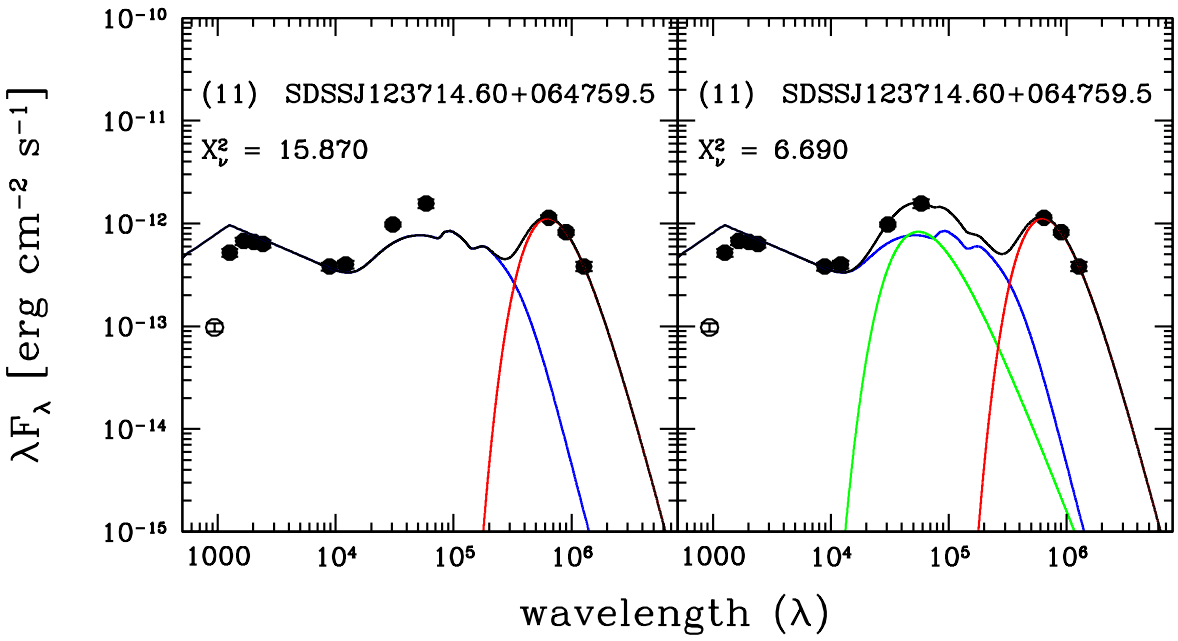

FIGURE 4.7: Example of a fit in which an additional component (ME) has been added to fully describe the MIR emission. The left panel shows the standard fit with two components, while the right panel shows a fit in which the MIR excess blackbody is included. The F-test on this source shows that this component improves the fit at a $\geq$99% confidence level.

where d_L is the luminosity distance and f_{AD} is the accretion disc emission component with A relative normalization. In the computation of the bolometric luminosity, we do not account for the soft X-ray emission, which has been demonstrated to be negligible. In fact, the bolometric correction, that is, the ratio between the bolometric luminosity and the luminosity at a specific wavelength, found in the soft X-ray band are quite large, of the order of 20-30, as in Marconi et al. (2004) and Lusso et al. (2012), for instance. Similarly, the AGN monochromatic luminosities at 2500 Å, 4500 Å and 6 μm and the luminosity at 158 μm (which corresponds to CII emission line), were computed as:

$$\lambda L_\lambda = 4\pi d_L^2 \, \lambda \, f(\lambda) \;\; [erg/s] \tag{4.7}$$

where f(λ) was obtained by interpolating the best-fit model accretion disc plus torus template (for $L_{2500\,\text{Å}}$, $L_{4500\,\text{Å}}$ and $L_{6\,\mu\text{m}}$) and the total template (for $L_{158\,\mu\text{m}}$), and properly correcting for dust absorption, considering the value of the corresponding intrinsic template.

The AGN bolometric and the monochromatic luminosities computed as described above are reported in Table 4.4. As expected, these sources show very high bolometric luminosities (in the range $10^{47} - 10^{48}$ erg s^{-1}) and they therefore populate the brightest end of the luminosity function.

N	$\log(L_{bol})$ [erg/s]	$\log(L_{2500Å})$ [erg/s]	$\log(L_{4500Å})$ [erg/s]	$\log(L_{6\,\mu m})$ [erg/s]	$\log(L_{158\,\mu m})$ [erg/s]
1	47.54	47.05	46.93	47.10	45.73
2	47.64	47.15	47.03	47.19	45.84
3	47.65	47.16	47.04	47.05	45.77
4	48.03	47.54	47.41	47.15	46.05
5	47.80	47.31	47.18	47.22	46.05
6	47.36	46.87	46.75	46.87	46.00
7	47.98	47.49	47.36	47.10	45.52
8	47.31	46.82	46.70	46.83	46.15
9	47.20	46.71	46.58	46.71	45.65
10	47.62	47.13	47.00	47.17	45.94
11	47.15	46.66	46.53	46.71	46.15
12	47.92	47.43	47.30	47.15	45.45
13	47.56	47.07	46.94	47.03	45.42
14	47.98	47.49	47.36	47.27	45.83
15	47.71	47.22	47.10	47.09	45.54
16	47.50	47.01	46.88	47.06	45.69

TABLE 4.4: Quasar bolometric luminosity and monochromatic luminosities at 2500 Å, 4500 Å, 6 μm, and 158 μm

It is well known that the optical continuum luminosity can be used as a proxy of the AGN luminosity, while the MIR flux is directly linked to the circumnuclear hot dust emission. Moreover, the dust-covering factor for type 1 AGN can be obtained from the ratio between the thermal MIR emission and the primary AGN radiation. Under these assumptions, a plot such as that in Figure 4.8 has been shown by Maiolino et al. (2007) to recognize a mild trend of the covering factor with the AGN luminosity, that is, it decreases with optical luminosity. A strong trend with luminosity also emerges from our sources (blue stars in Figure 4.8), which lie slightly above (by ~ 0.2 dex) the relation derived by Maiolino et al. (2007), however. This is not surprising since the WISSH quasars have been selected to be the most luminous in the 22 μm band, which corresponds to about $\sim 6\,\mu$m rest-frame given their redshift.

4.5.2 Infrared luminosities and star formation rates

An interesting parameter to derive is the IR luminosity of the host galaxy component, which is due to the reprocessed UV stellar emission by dust and indeed depends on both the physical properties of the dust (i.e. mass) and of the incident radiation (i.e. SF and the AGN, see discussion in Section 4.5.2.1).

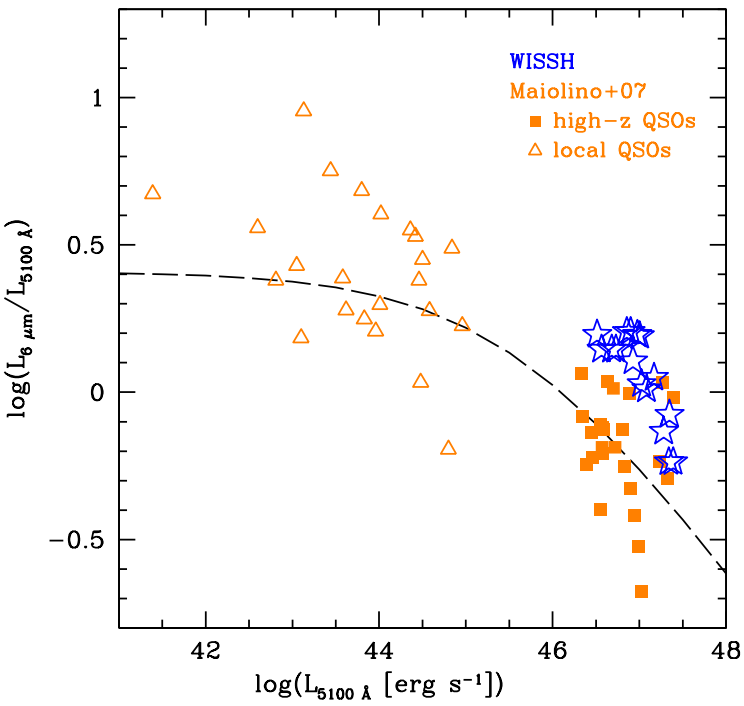

FIGURE 4.8: MIR-to-optical continuum luminosity versus optical continuum luminosity. The WISSH quasars are the blue stars in the plot, while we plot in orange the sample from Maiolino et al. (2007) of high-z (squares) and local (triangles) sources. The dashed black line is the relation derived by Maiolino et al. (2007).

We computed the SFR using the relation by Kennicutt (1998) scaled to a Chabrier IMF:

$$SFR(M_\odot/yr) = 10^{-10} L^{Host}_{IR\,8-1000\,\mu m}\ (L_\odot) \tag{4.8}$$

where the IR host galaxy luminosity (L^{Host}_{IR}) was obtained by integrating the best-fit modified blackbody in the range $8 - 1000\,\mu$m:

$$L^{Host}_{IR\,8-1000\,\mu m} = 4\pi d_L^2 \int_{8\,\mu m}^{1000\,\mu m} B\, f_{CD}\ \ [erg/s] \tag{4.9}$$

Both $L^{Host}_{IR\,8-1000\,\mu m}$ and SFR are given in Table 4.5, while B is the normalization related to the CD template. The values of SFR found for these sources are extremely high ($> 400\,M_\odot$/yr and up to $\sim 4500\,M_\odot$/yr). These derived SFR values assume that all the FIR emission comes from young stars. However, we know that this is not completely true since the AGN emission might contribute to it (Schneider et al., 2015; Symeonidis, 2017). For this reason, the SFR values reported in the table have to be considered as upper limits. A more detailed discussion on this can be found in Section 4.5.2.1, where the AGN contribution to the FIR radiation is accounted for in a statistical way.

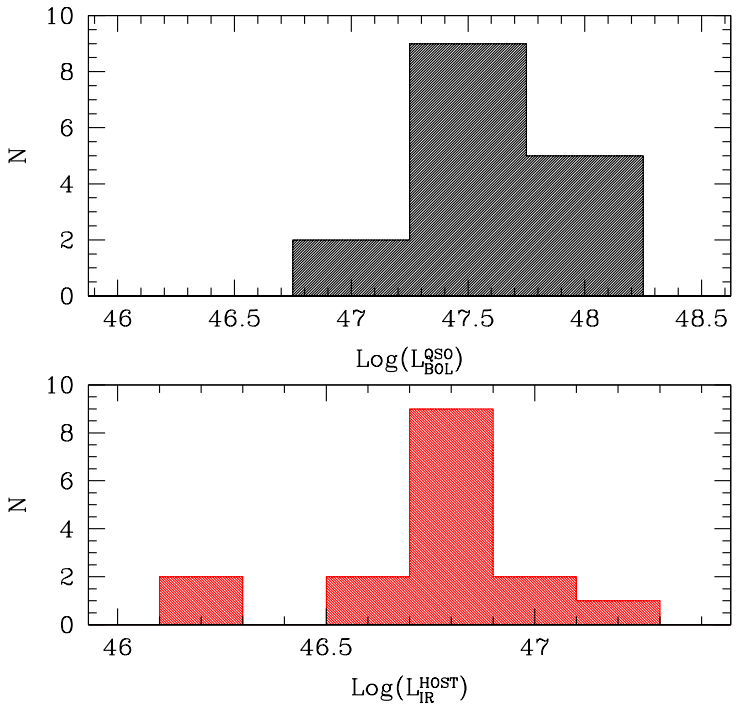

FIGURE 4.9: Distribution of the bolometric luminosities (upper panel) and of the host IR luminosities (lower panel) of the sample.

N	$\log(L^{Host}_{IR\,8-1000\,\mu m})$ [erg/s]	SFR [$M_\odot$/yr]	$\log(L^{Host}_{FIR\,40-120\,\mu m})$ [erg/s]
1	< 46.72	< 1400	< 46.59
2	46.87	2000	46.73
3	46.55	930	46.44
4	46.83	1800	46.72
5	47.01	2700	46.88
6	46.90	2100	46.78
7	46.54	910	46.41
8	47.24	4500	47.09
9	46.70	1300	46.56
10	46.77	1600	46.66
11	46.92	2200	46.81
12	< 46.21	< 410	< 46.10
13	46.90	2000	46.61
14	46.85	1800	46.71
15	46.27	490	46.17
16	46.79	1600	46.64

TABLE 4.5: Infrared luminosity computed by integrating the host emission from 8 μm to 1000 μm, related SFRs from Kennicutt (1998), and FIR luminosity of the host component from 40 μm to 120 μm.

4.5.2.1 Quasar contribution to the FIR emission

While there is broad consensus that the strong NIR emission observed in quasars is due to the central source, the debate is still on whether the FIR emission is mainly powered by the starburst, or if quasars are required as an additional energy source.
We estimated the possible contribution of the AGN to the heating of the dust in the host galaxy using the same approach as in Schneider et al. (2015). For the z=6.4 quasar SDSS J1148+5251, they modelled the dust in the host with a spheroidal inhomogeneous distribution extending from just outside the quasar dusty torus up to a few kpc. A central source was included, with a bolometric luminosity sufficient to match the observed optical data; the AGN SED was chosen from a few templates including the contribution of the dusty torus in the MIR. The heating of the dust in the host by the central source (and by an additional contribution from stars in the galaxy) was computed using the radiative transfer code TRADING (Bianchi, 2008), assuming the typical properties of dust in the Milky Way (Draine and Li, 2007). From their simulations, Schneider et al. (2015) concluded that dust in the host galaxy, heated by the IR radiation from the dusty torus, can contribute significantly (at least for 30% and up to 70%) to the FIR SED of the AGN-host system.

We repeated the same procedure here for two extreme sources in our sample: the least (SDSS J123714.60+064759.5) and the most (SDSS J074521.78+473436.1) luminous ones. Given the importance of such an estimate, we will apply the same procedure for the whole sample in the future. For the two sources in this work, we produced TRADING radiative transfer simulations, choosing as the central source the nuclear and torus emission best-fit templates obtained from the optical/NIR data. We adopted the same dust distribution and mass as in Schneider et al. (2015): as we show in the next section, the dust masses in our sample are of the same order of the mass for SDSS J1148+5251, studied by Schneider et al. (2015). By comparing the modelled and observed SED, we found that the AGN contribution to the FIR fluxes is about 43% in the least luminous source, which increases to 60% for the most luminous source. This points towards a mild trend with luminosity. However, considering that the bolometric luminosities are homogeneously distributed, as visible in Figure 4.9, we can assume an average AGN contribution of ∼50% to the total FIR luminosity, which also accounts for the uncertainties in the radiative transfer model. The AGN-corrected infrared luminosities and SFR can therefore be derived by simply dividing the values given in Table 4.5 by a factor of 2.

4.5.3 Star formation rate vs black hole accretion

Figure 4.10 shows the IR luminosity that is due to SF (hereafter SF luminosity) versus the AGN bolometric luminosity. As expected, the WISSH sources populate an extreme region of this plane. In the same figure we also show the SF luminosity values statistically corrected for the AGN contribution. Such extreme values are in perfect agreement with the results found for AGN at high z with similar properties, such as the two samples presented by Netzer et al. (2014) and Netzer et al. (2016), and the hot dust obscured galaxies (from the work by Fan et al., 2016b). For three objects in our sample in common with Netzer et al. (2016), we can directly compare the values of SFR. These are SDSS J020950.71-000506.4 (2) with an SFR of 1700 $M_\odot$/yr from Netzer et al. (2016) and of 2000 $M_\odot$/yr from our analysis, SDSS J123714.60+064759.5 (11), which has 2700 $M_\odot$/yr and 2200 $M_\odot$/yr in the two works, and SDSS J212329.46-005052.9 (15), with 300 $M_\odot$/yr and 490 $M_\odot$/yr, respectively.

Previous studies about a possible correlation between the SF activity and the quasar luminosity led to discrepant results. Several works based on X-ray data revealed the presence of a robust correlation at high redshift and quasar luminosity, which weakens or disappears for sources at lower redshift and luminosity. In particular, Stanley et al. (2015), Harrison et al. (2012), and Rosario et al. (2012), who examined data obtained via stacked photometry, found a flat distribution of $L_{SF} - L_{QSO}$. However, Dai et al. (2016), for a sample of FIR-detected quasars at $0.2 < z < 2.5$, found a significant trend between these two parameters over four orders of magnitude in luminosity. As noted in several previous works (see e.g., Netzer et al., 2016), these discrepancies might be attributed to different selection criteria and/or methods of analysis. In particular, Dai et al. (2016) have been able to reconcile their results with those obtained by Stanley et al. (2015), by considering stacked IR values.

Given the limited luminosity range spanned by our sample, we are not able to determine any possible $L_{SF} - L_{AGN}$ trend. In Figure 4.10 we report the local sample of IR-selected galaxies from Gruppioni et al. (2016) and the AGN sample from the COSMOS survey (Bongiorno et al., 2012). The combination of these samples allows us to span a wide range of luminosity and redshift. Very high L_{QSO} objects are indeed missing from studies based on small fields, like COSMOS, which do not properly sample the bright end of the AGN luminosity function. The plot clearly shows that at high luminosities (both bolometric and SF luminosity), there is a smaller dispersion in luminosity than what is found for less luminous samples. Quantitatively, the highly luminous sources have a dispersion that is 2.15 times smaller than the lowly luminous ones. However, it is worth noting that all the aforementioned samples are *Herschel*-detected, except for COSMOS.

We investigated whether there is an hidden redshift dependence in the relation $L_{SF} - L_{AGN}$. Figure4.11 shows the ratio between the SF and the AGN bolometric luminosity versus z, for the same samples of Figure 4.10. Black points represent the median values in bins of redshift with associated errors, which were computed considering the differences between the first and third quartiles and the median value (or second quartile) of the set of data. As clearly visible, there is no sign of strong trend with redshift, which allows us to use samples at different redshifts to derive a relation between the SF and the AGN activity for the IR sources. Here we concentrate on the *Herschel*-detected samples, that is, the local sample from Gruppioni et al. (2016), the $z > 2$ samples from Netzer et al. (2014) and Netzer et al. (2016), the Hot DOGs from Fan et al. (2016b) and the WISSH sample at $1.9 < z < 4.6$. For these samples we have obtained a fit that is reported as a green solid line in Figure 4.10, for which we assumed the same correction for the AGN contamination to the FIR (50%) as for the measurements belonging to the samples from Netzer et al. (2014) and Netzer et al. (2016) and from Fan et al. (2016b), which have similar properties. In contrast, we cannot make the same assumption for the objects by Gruppioni et al. (2016): these are local sources at lower luminosity, therefore the AGN contribution to the FIR may be different compared to high-luminous sources. To be more accurate, we calculated the bisector of the two regression lines by first treating L_{AGN} (dashed green line) as the independent variable and then considering the SF luminosity L_{SF} as the independent variable (dot-dashed green line). The bisector, the green straight line in the plot, has a dispersion of 0.39 dex and presents the following form:

$$\log\left(\frac{L_{SF}}{10^{44}\mathrm{erg/s}}\right) = \log\left(\frac{L_{QSO}}{1.82\times10^{44}\mathrm{erg\,s^{-1}}}\right)^{0.73} \tag{4.10}$$

and it can be directly compared with the relation found by Delvecchio et al. (2015) ($L_{SF} \propto L_{BOL}^{0.85}$) for their SF-dominated sources (i.e. those with $L_{SF} > L_{QSO}$) at $1.5 < z < 2.3$ and with the relation obtained by Netzer (2009) for quasar-dominated sources ($L_{SF} \propto L_{BOL}^{0.78}$).

As expected, this relation differs significantly from the relation of Delvecchio et al. (2015), while it is in much better agreement with the relation derived by Netzer (2009), especially at the high-luminosity end. At lower luminosities, in contrast, the newly derived relation is flatter than the relation reported by Netzer (2009) one, with a slope of 0.73 instead of 0.78. The difference can be attributed to the fact that our relation has been derived considering only *Herschel*-detected sources, while the relation published by Netzer (2009) is mainly based on optically selected SDSS sources.

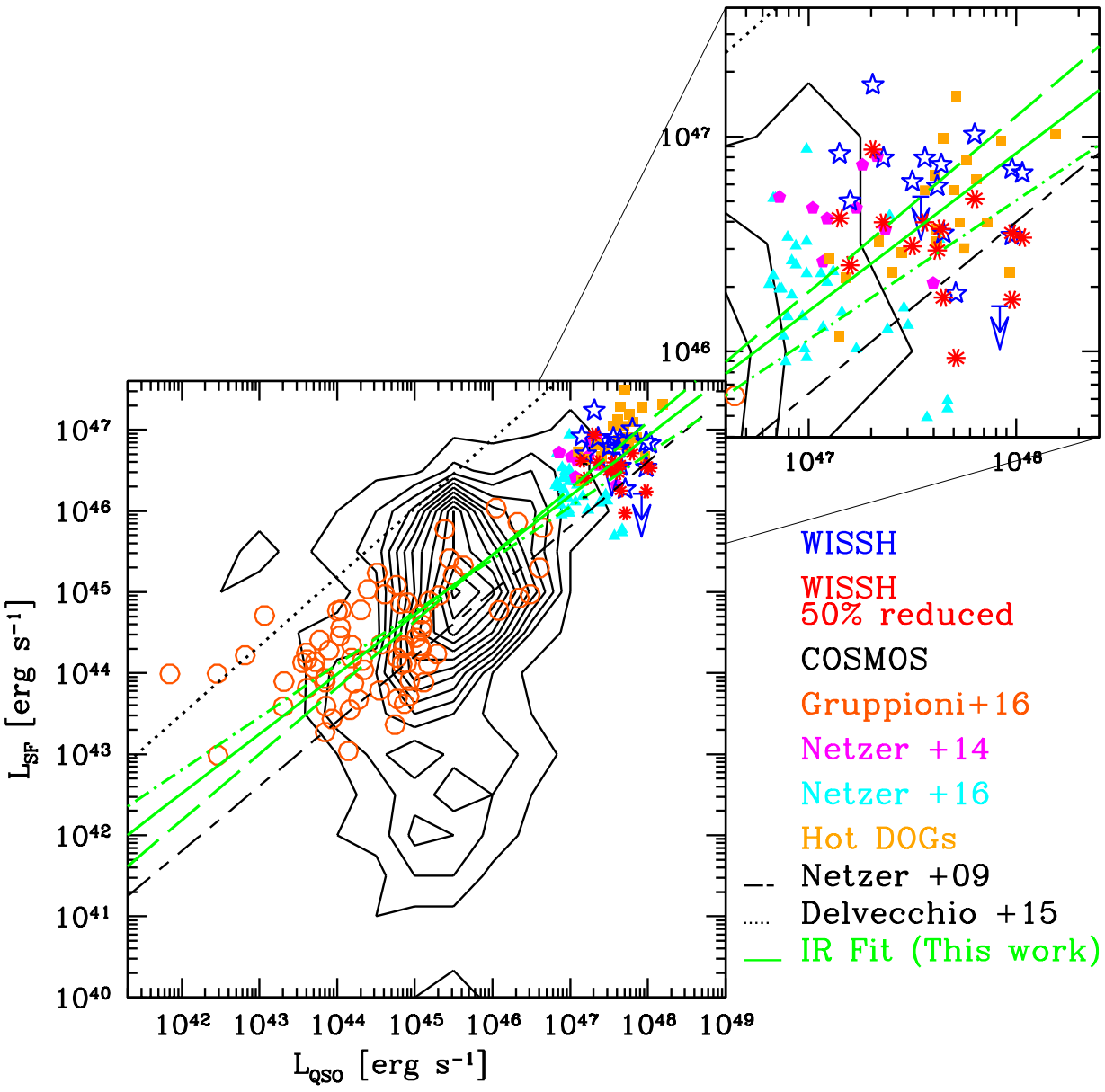

FIGURE 4.10: SF luminosity vs AGN bolometric luminosity for the WISSH quasars in comparison with other samples. The 16 WISSH sources are shown as blue stars in the plot, while the red asterisks show SF luminosity values reduced by a factor of about 2 to account for the quasar contribution to the FIR. The same correction has been applied to the samples from Netzer et al. (2014) and Netzer et al. (2016) and Fan et al. (2016b), which are of the same luminosity range.

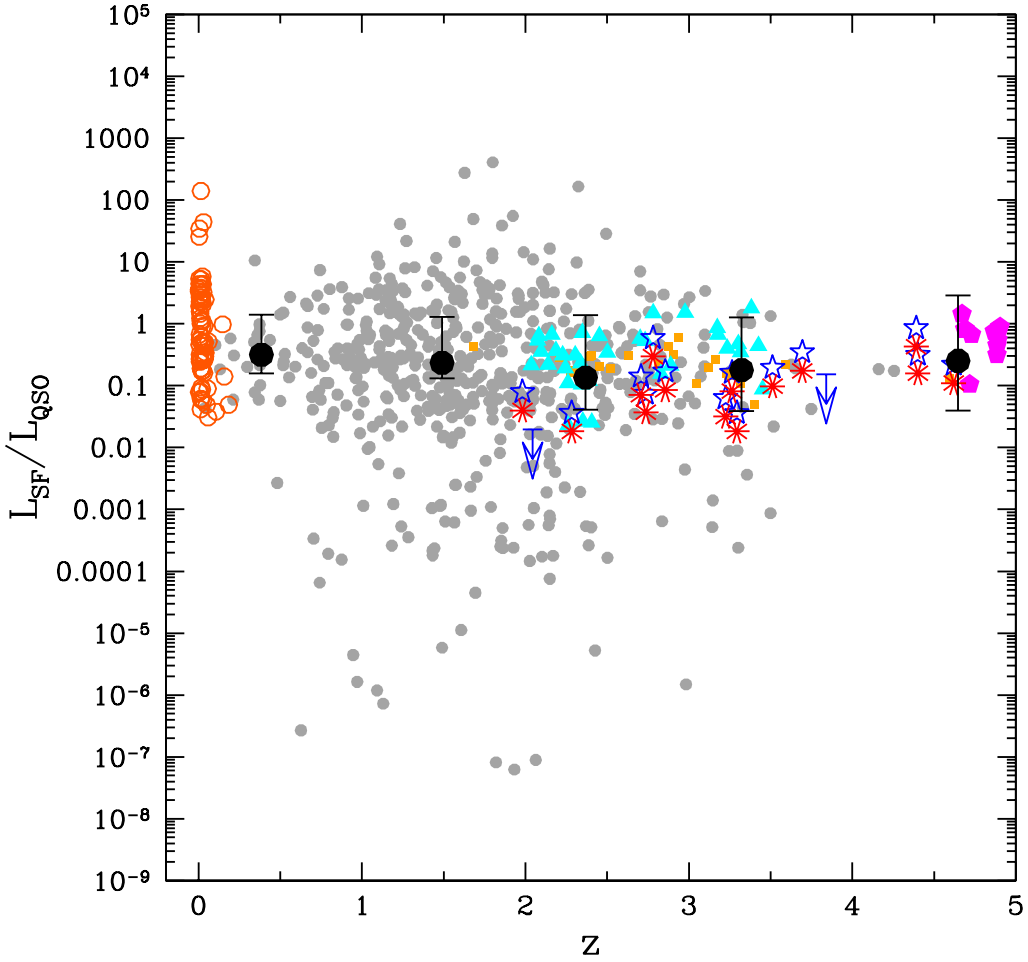

FIGURE 4.11: Ratio between SF and AGN bolometric luminosities as a function of redshift for the same sources as presented in Figure 4.10. Black points represent the median value in a redshift bin.

4.5.4 Dust temperatures and masses

(i) Cold dust

Under the assumption that the dust emissivity can be described as a simple frequency power-law, and assuming that dust is in thermal equilibrium, we can also derive some dust properties from the result of the SED fitting, in particular its mass and temperature. More specifically, the FIR emission is linked to the cold dust component that is present on the galaxy scale while the NIR emission is related to the hot dust component close to the nucleus in the torus. Following Wien's displacement law, we know that the peak of the blackbody component is strictly connected to the temperature of the emitting dust grains. We have underlined the fact that the real SEDs of galaxies cannot be described by a single-temperature modified blackbody because grains of different sizes and shapes give birth to a non-trivial distribution of temperatures. However, for simplicity, a blackbody

(or a modified blackbody) component or a grid of templates (as in Chary and Elbaz, 2001; Dale et al., 2014) that is also characterized by a single-temperature emission, is commonly used to describe the IR radiation (see e.g., Leipski et al., 2013; Netzer et al., 2016).

Figure 4.12 shows the distribution (normalized for the maximum value) of the temperatures of the cold dust component found for our objects, ranging from about T = 40 K to T = 50 K, in good agreement with the results of previous studies of high-redshift, IR luminous AGN (Beelen et al., 2006; Leipski et al., 2014; Valiante et al., 2011), as visible in the upper panel. The central and lower panels show as a comparison the distribution of cold dust temperatures found for different classes of objects. It is important to note that all these works have assumed different values of both the coefficient of the modified blackbody β and the dust absorption coefficient k_0. In the central panel we report the WISSH sources compared to the local (z < 0.5) PG sources from Petric et al. (2015) and the SDSS optically selected AGN at z < 4.7 from Ma and Yan (2015). The different IR luminosity ranges directly translate into a different dust temperature distribution, meaning that while the less luminous PG quasars have lower temperatures (in the range 20 K - 50 K) than the WISSH sample, the SDSS objects show a wider distribution, with the bulk peaking at higher value ($\sim$ 40 K) than the PG quasars, and with the warmer tail of the distribution comparable to ours. For the same reason, WISSH AGN show dust temperatures that are much higher than the bulk of the galaxy population, as clearly shown in the lower panel of Figure 4.12, where they are compared to normal galaxies, that is, to the sample of main sequence galaxies from Magdis et al. (2012) and Santini et al. (2014), the dust obscured galaxies (DOGs) from Melbourne et al. (2012) and the submillimiter galaxies (SMGs) from Chapman et al. (2005), Magnelli et al. (2014), and Miettinen et al. (2015).

With the previously derived $L^{\rm Host}_{\rm IR8-1000\,\mu m}$, it is also possible to obtain a measure of the mass associated with the cold dust component (cold M_d) using the formula derived by Hughes et al. (1997) (for a detailed derivation see also Berta et al., 2016):

$$M_d = \frac{L^{Host}_{IR\,8-1000\,\mu m}}{4\pi \int k_d(\nu)\, B(\nu, T_d)\, d\nu} \tag{4.11}$$

which is valid under the assumption that the emission is optically thin with optical depth $\tau << 1$.

In the above formula, $B(\nu, T_d)$ is the Planck function for dust with a temperature T_d, determined by the best-fit, and $k_d(\nu) = k_0\,(\nu/\nu_0)^{\beta}$ with k_0 the absorption coefficient and

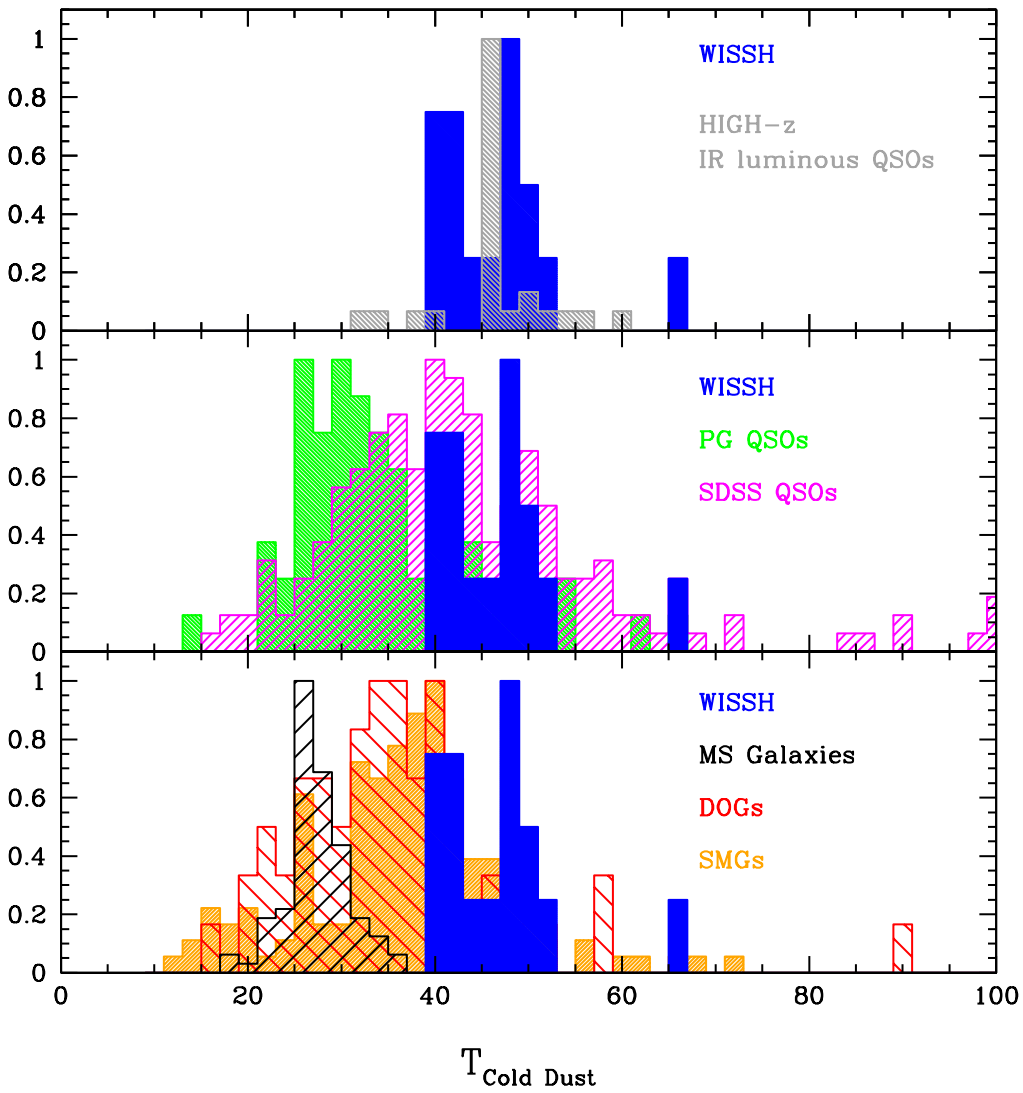

FIGURE 4.12: Temperature distribution of the cold dust for the WISSH quasars (blue) compared to: high-z IR luminous quasars from Beelen et al. (2006); Leipski et al. (2014); Valiante et al. (2011) (upper panel); local PG quasars from Petric et al. (2015) and SDSS quasars at z<4.7 from Ma and Yan (2015) (central panel); and galaxies from Magdis et al. (2012); Santini et al. (2014); Melbourne et al. (2012); Chapman et al. (2005); Magnelli et al. (2014); Miettinen et al. (2015) (lower panel). Note that all these works have assumed different values of both the coefficient of the modified blackbody β and the dust absorption coefficient k_0.

ν_0 the frequency at which τ=1. Following Beelen et al. (2006), here we assume k_0 = 0.4 [cm^2/g] and ν_0 = 1200 μm. The dust mass therefore depends on the IR luminosity (SFR) of the source and the temperature of the dust grains, meaning that for a given temperature, there is a linear relation between dust mass and SFR.

The derived masses, reported in Table 4.6, are of the order of 10^8 $M_\odot$, in agreement with previous studies on high-z IR luminous sources (e.g., Beelen et al., 2006; Wang et al., 2008; Banerji et al., 2017; Valiante et al., 2011; Ma and Yan, 2015).

As we mentioned before, temperatures and dust masses are sensitive to the adopted dust absorption coefficient and spectral index; in particular, we estimated that, for the WISSH sources, T_d might change for a factor $< 10\%$ and M_d even for $\sim 25\%$ - 30% depending on the assumption on β and k_0.

(ii) Hot dust

As we mentioned in Sect. 4.4.1.3, some of our sources (31%) show a MIR excess in their SED that requires a component in addition to the classical torus models (Stalevski et al., 2012, 2016). The presence of such component has been noted in several previous works on luminous AGN, but the physical origin of this component is not yet clear. Edelson and Malkan (1986) were the first to note the need of an additional component that peaks at about 5 μm, corresponding to a dust temperature of about 600 K. More recently, Mor et al. (2009), analyzed a sample of Spitzer-selected low-z AGN with luminosities ranging from $44.6 < \log(\mathrm{L_{bol}}) < 46.8$. They found that their objects require two additional dust components to fit the MIR emission. The first component (very hot dust component) has temperatures ranging from 900 K to 1800 K, and the second (warm dust component) has 200 K. Similarly, Hernán-Caballero et al. (2016) found a peak in the distribution of the very hot dust temperatures at about 1180 K and of the warm temperatures at 400 K for a sample of luminous AGN at $z < 3$. While the warm component has been interpreted as dusty clouds in the narrow line region, the very hot dust emission might be related to graphite clouds located at the edge of the dusty torus, thus inside the sublimation radius of silicate (whose sublimation temperature is lower than for pure graphite grains), but outside the broad line region. However, as the MIR SED of the total AGN emission (disc plus dust) is strictly connected to the spectral shape assumed for the MIR spectrum of the disc, the resulting excess components are somewhat model dependent.

As shown in Table 4.6, we found a MIR excess for the WISSH sample corresponding to dust with temperatures ranging from T = 650 K to T = 850 K. Such values are in agreement with the result from Edelson and Malkan (1986), but in between the results found by Mor et al. (2009) and Hernán-Caballero et al. (2016).
It is worth noting that this further component peaks at about 22 μm rest-frame, where the sources in the sample have been selected to be the brightest. This excess is a sign of the fact that our sources show more hot dust than that is present in the torus models. Moreover, they may have a large covering factor, allowing clouds to intercept more continuum radiation.

N	Cold T_d [K]	Cold M_d [$10^8 M_\odot$]	Hot T_d^{Ex} [K]	Hot M_d^{Ex} [$M_\odot$]	Hot M_d^{TOT} [$M_\odot$]
1	48	1.9	-	-	130
2	49	2.5	-	-	190
3	43	2.5	-	-	240
4	41	6.1	-	-	72
5	47	4.3	-	-	90
6	45	4.3	790	57	85
7	49	1.2	-	-	84
8	51	4.6	742	106	210
9	50	1.5	786	51	51
10	43	4.1	-	-	156
11	41	7.5	664	134	170
12	42	1.4	-	-	237
13	66	0.5	814	54	69
14	49	2.3	-	-	169
15	41	1.9	-	-	196
16	52	1.5	-	-	145

TABLE 4.6: Cold and hot dust masses computed as described in Sect. 4.5.4. We report both the total hot dust mass and the excess found for our sources alone. The 11 sources with no additional MIR BB component have no estimates of the hot dust mass excess.

Furthermore, from the MIR excess emission component, we also estimated the mass of the additional hot dust found. Differently from the cold dust component, which is described as a greybody, the hot dust emission excess was fitted with a single-temperature blackbody. Therefore it is in principle not possible to compute the hot dust mass using the previous relation. However, following Jiang et al. (2006), we approximated the hot dust emission as a greybody with $k_0 = 2.06 \times 10^3 [cm^2/g]$. Since in a greybody the emissivity α is below 1, these values have to be considered as lower limits and are in agreement with the values found in the aforementioned work.

Finally, we also computed the total hot dust mass for all sources (hot M_d^{TOT}) by fitting the photometric points from the UV to the MIR with a combination of pure accretion disc (Feltre et al., 2012) and single-temperature black body templates to describe the whole MIR emission.

The values of the total hot dust masses, ranging from tens to hundreds of solar masses, are given in Table 4.6 together with the masses associated with the excess for the five sources that require this component.

4.6 Conclusions

We studied a sample of hyper-luminous quasars, selected by cross-correlating data from the SDSS and the WISE All-Sky Survey, and we focused on 16 sources with *Herschel*/SPIRE data coverage.

Thanks to the multi-wavelength coverage, we were able to analyse in detail the source SEDs, fitting the observed fluxes with a multi-component model, based on a combination of quasar and host-galaxy emission emerging in the IR (where the reprocessed stellar light is re-emitted by the dust). The quasar emission was described using a combination of power laws for the primary source (Feltre et al., 2012) and the model by Stalevski et al. (2016) for the smooth and clumpy dusty torus, while the galaxy cold dust emission in the infrared bands was modeled as a modified blackbody. However, we found that in some cases, our sources show peculiar features in their SED that cannot be described by the standard modelization. In other words, a further component, in the form of a pure blackbody, is necessary to reproduce their NIR emission. Through the SED multi-components fitting method we were able to derive robust measurements of both the quasar (i.e. bolometric and monochromatic luminosities) and the host galaxy properties (i.e. dust mass, SFRs).

Our main findings can be summarized as follows:

- The WISSH quasars populate the brigthest end of the luminosity function with very high bolometric luminosities, $L_{BOL} > 10^{47}$ erg s^{-1}. They are hosted in galaxies with extremely high SFRs of up to 4500 $M_\odot$/yr. Since the quasar light might contaminate the FIR emission, following Schneider et al. (2015), we estimated its possible contribution to the heating of the dust in the host galaxy, taking as test cases the least and the most luminous sources of the sample. We found that the quasar contribution to the FIR fluxes is about 43% in the least luminous source, which increases to 60% for the most luminous source. Considering that the bolometric luminosities are homogeneously distributed, we therefore assumed an average quasar contribution of ∼50% to the total FIR luminosity. Even accounting for this correction, the SFRs of the sources still remain of the order of thousands $M_\odot$/yr.

- By combining our sample with both high-z hyper-luminous quasars (Netzer et al., 2014, 2016) and local quasars from Gruppioni et al. (2016) and the quasar sample

from the COSMOS survey (Bongiorno et al., 2012), from the $L_{SF} - L_{QSO}$ plane a narrower (2.15 times smaller) dispersion at high quasar and SF luminosities emerges than what was found for lower values of both bolometric and SF luminosities. Using only the *Herschel*-detected samples we derived a log-linear relation between the SF and the quasar luminosities, $L_{SF} \propto L_{QSO}^{0.73}$, which is flatter than the relation derived for optically selected type II AGN by Netzer (2009).

- While most of the WISSH quasars are well described by a standard combination of accretion disc plus torus and cold dust emission, for $\sim 31\%$ of them, an additional hotter component is required to reproduce the observed fluxes. The peak of this emission falls roughly at about $22\,\mu$m rest-frame, where the sources in the sample have been selected to be the brightest, and it has temperatures ranging from $T = 650\,K$ to $T = 850\,K$.

- The temperature of the cold dust component has a peak at about $50\,K$, in agreement with previous studies of high-z IR luminous quasars (Beelen et al., 2006; Leipski et al., 2014; Valiante et al., 2011) and much higher than main-sequence galaxies. The thermal emission of the cold dust component is associated with a dust mass of the order of 10^8 $M_\odot$, which is in good agreement with previous works on high-z quasars (e.g., Beelen et al., 2006; Wang et al., 2008; Banerji et al., 2017; Valiante et al., 2011; Ma and Yan, 2015).

The WISSH quasars lie in the most extreme region of the plane $L_{SF} - L_{QSO}$. It is worth noting that the same locus is occupied by other hyper-luminous ($L_{BOL} > 10^{47}$ erg s^{-1}) quasars collected according to the level of extinction. We can place the WISSH quasars in between the heavily dust enshrouded sources such as the WISE-selected hot dust obscured galaxies by Fan et al. (2016b), Piconcelli et al. (2015) and Wu et al. (2012), the NIR-selected heavily reddened quasars by Banerji et al. (2015) and Glikman et al. (2015), and finally the blue optically selected luminous quasars (e.g., Netzer et al., 2016). However, we should keep in mind that, while both the bolometric luminosity and the extinction are instant observables, the infrared-derived SF luminosity is the result of the integration of bursts of SF that occurred over billions of years, assuming that the SF remains constant over the lifetime of the burst (Leitherer and Heckman, 1995). Hence, it is difficult to gain information from the SF luminosity about the ongoing SF in the host galaxy. On the other hand, the extinction of a single galaxy is strictly linked to its merger-induced evolutionary sequence. Through the WISSH quasars we therefore witness a very peculiar phase in the quasar life, during which the dust in the host has not yet been fully cleared up.

This suggests that the typical evolution timescales of the quasar feedback are much shorter than those of the host galaxy SF activity. Signatures of ionized outflows are ubiquitously detected in WISSH quasars (see e.g., Bischetti et al., 2017; Vietri et al., 2018). It is worth to stress the importance to get higher resolution data in the sub-mm bands to constrain the SFR of the sources which much higher accuracy. For the specific case of the source SDSS J101549.00+002020 (see Bischetti et al., 2018), in the last months we have analyzed ALMA high-resolution (0.1800 x 0.2100) observations of the 840 μ m continuum and [CII] λ 174.4 μm emission line, which have revealed an exceptional overdensity of [CII]-emitting companions with a very small (<150 kms^1) velocity shift with respect to the redshift of the AGN. The new SED is obtained by quantifying and removing the contribution to the 250–840 mu m fluxes from the two companion sources characterized by a continuum flux density comparable to that of the QSO. We derived a corrected SFR which is a factor of 6 smaller than the previous estimation, being although still so high to confirm the extreme SF activity of these hyper-luminous sources. On the contrary, for the source SDSS J143352.20+022713.9, ALMA data have confirmed the SFR estimate obtained listed in Table 4.5. Further ALMA data are therefore mandatory to understand source by source if the SFR estimates obtained with *Herschel* might be overestimated or not. Moreover, data from NOEMA will help to quantify the gas reservoir in the WISSH quasars and to reveal possible massive molecular outflows, allowing us to obtain a comprehensive view of the outflow phenomenology in these hyper-luminous quasars, and test the impact of the quasar output on the host gas ISM and its SF efficiency.

An alternative scenario suggests that the action of the quasar outflow and the host SF might not be geometrically connected. In this sense, future spatially resolved observations will be useful to perform an accurate investigation of the ongoing SF (via spectral analysis of the narrow Hα emission line, as in Carniani et al. 2015 and Cano-Díaz et al. 2012).

These quasars are also unique laboratories for studying the properties of the interstellar medium at high redshift, as the metals and dust content of their host galaxies can provide insights into both the galaxy evolution process (e.g., SFH) and the quasar feedback effects (e.g., Valiante et al., 2011, 2014).

Portions of the work presented in this Chapter have been published in the following papers:

- **F.Duras**, A.Bongiorno, E.Piconcelli, S.Bianchi, C.Pappalardo, R.Valiante, M.Bischetti, C.Feruglio, S.Martocchia, R.Schneider, G.Vietri, C.Vignali, L.Zappacosta, F.La

Franca and F.Fiore. **2017A&A...604A..67D** *The WISSH quasars project. II. Giant star nurseries in hyper-luminous quasars*

- M.Bischetti, E.Piconcelli, C.Feruglio, **F. Duras**, A.Bongiorno, S.Carniani, A.Marconi, C.Pappalardo, R.Schneider, A.Travascio, R.Valiante, G.Vietri, L.Zappacosta, and F.Fiore. **2018A&A...617A..82B** *The WISSH quasars project. V. ALMA reveals the assembly of a giant galaxy around a $z = 4.4$ hyper-luminous QSO*

CHAPTER 5

The hyper-luminous Compton-thick $z \sim 2$ quasar nucleus of the hot DOG W1835+4355 observed by NuSTAR

This chapter focuses on the analysis of the hot DOG source W1835+4355, as a particular case of hyper-luminous AGN which, contrary to the WISSH sources described in the previous Chapter, shows heavy obscuration. For this object I performed a dedicate SED-fitting analysis, obtaining its main physical properties, e to be compared with those found for the WISSH AGN. At the end of the Chapter, we will try to insert these results in a wide evolutionary scenario.

5.1 Introduction

Recent sensitive wide-area mid-infrared ($\sim 3-30$ μm; MIR) surveys allowed an almost obscuration-independent selection of rare populations of distant ($z = 2-4$) quasars that are characterized by their huge infrared (IR) output ($L_{\rm IR} \gtrsim 10^{14} L_{\odot}$), which gave them the name hyper-luminous infrared galaxies. Using the all-sky survey performed by the Wide-field Infrared Survey Explorer (*WISE*; Wright et al., 2010), samples of ∼100-1000 high-redshift ($z \approx 2-4$) MIR-bright[1] type 1 and type 2 hyper-luminous sources have been selected according to specific selection criteria (e.g., Weedman et al., 2012; Eisenhardt et al., 2012; Wu et al., 2012). These rare systems are important as they may provide the clearest view of quasars at the peak epoch of AGN activity ($z \approx 2-3$; Richards

[1]Specifically at observed wavelengths $\gtrsim 10$ μm.

et al., 2006; Hopkins et al., 2007; Merloni and Heinz, 2008; Delvecchio et al., 2014) and in that they may be a low-redshift analog of the most luminous and massive highest-redshift quasars known (e.g., Fan et al., 2001, 2003; Willott et al., 2010; Bañados et al., 2016) .They therefore provide an important tested to models of SMBH formation and popular AGN/galaxy co-evolution scenarios (Silk and Rees, 1998; Fabian and Iwasawa, 1999; King and Pounds, 2003; Volonteri et al., 2006; Hopkins et al., 2008; Kormendy and Ho, 2013; Heckman and Best, 2014). They may indeed represent different evolutionary phases of popular merger-driven quasar formation scenarios in which the loss of angular momentum of large cold gas reservoirs as a consequence of multiple major galaxy encounters causes rapid SMBH growth through infall of chaotic nuclear matter. This triggers powerful AGN activity and generates strong bursts of star formation (Sanders et al., 1988; Di Matteo et al., 2005; Hopkins et al., 2008; Menci et al., 2008; Narayanan et al., 2010; Treister et al., 2012). A key transitional stage of this process predicts that the dense concentrations of infalling matter will eventually isotropically enshroud the active nucleus, heavily obscuring the sightline to the AGN and causing it to appear red and heavily absorbed at shorter than near-infrared wavelengths (Hopkins and Beacom, 2006; Urrutia et al., 2008; Glikman et al., 2012).

Alternative scenarios involving stochastic short transitional phases of high-matter nuclear accretion flows have also been considered for obscured quasars. They are not connected to major mergers, but are rather linked to minor mergers and episodic cold-gas accretion episodes (flickering AGN scenario; Schawinski et al., 2012, 2015; Farrah et al., 2017).

Observationally obscured AGN are better suited for studying the AGN/galaxy coevolution because they allow the best view of the host galaxy. The most promising $z = 2 - 4$ AGN candidates for the transitional dust-enshrouded phase are the so-called "hot dust-obscured galaxies" (hot DOGs; Eisenhardt et al., 2012; Wu et al., 2012), that is, sources selected to be bright in the *WISE* 12 μm (W3) and/or 22 μm (W4) bands and faint or undetected in the 3.4 μm (W1) / 4.6 μm (W2) bands (hence called W1W2 drop-out; Eisenhardt et al., 2012). These sources are hyper-luminous with $L_{\rm bol} > 10^{47}$ erg s^{-1}, and they are rare ($\sim$ 1000 across the sky; Eisenhardt et al., 2012). They exhibit a peculiar spectral energy distribution (SED) that peaks in the MIR, which suggests that the main source powering these objects is the central AGN and not a powerful starburst. The temperatures derived for their dust reservoir are indeed on the order of $T = 60 - 100$ K (Wu et al., 2012; Fan et al., 2016c), which is higher than the typical dust temperatures of $T = 30 - 40$ K in other more common MIR-selected sources such as the normal submillimeter galaxies (e.g., Magnelli et al., 2012) and dust-obscured galaxies (DOGs; Dey et al., 2008). For this reason, they have been dubbed hot DOGs. These sources have been found in regions populated on arcminute scales ($\sim 500 - 700$ kpc) by overdense concentrations of submillimeter galaxies, suggesting that they are indeed

possible signposts of protocluster regions (Jones et al., 2014). As expected, the few X-ray observations of hot DOGs performed so far showed remarkably clearly that they are luminous and heavily obscured quasars (Stern et al., 2014; Piconcelli et al., 2015; Assef et al., 2016; Ricci et al., 2017c; Vito et al., 2018). In particular, Piconcelli et al. (2015, hereafter P15) found from studying the *XMM-Newton* X-ray spectrum of the hot DOG WISE J183533.71+435549.1 (z=2.298; Wu et al., 2012, hereafter W1835) that the source is reflection dominated and hence obscured by Compton-thick[2] (CT) column densities. This provides further evidence that the source may be in the transitional heavily obscured phase.

We here report on the ∼150 ks *NuSTAR* observation of the hot DOG W1835, which provides the first and most obscured *NuSTAR* detection of a $z > 2$ AGN. We perform a broadband ∼0.5-20 keV joint *XMM-Newton-NuSTAR* spectral analysis and updated SED modeling.

Throughout the Chapter we assume a cosmology with $\Omega_\Lambda = 0.73$ and $H_0 = 70\,\mathrm{km\,s^{-1}Mpc^{-1}}$. Errors are quoted at 1σ and upper and lower limits at 90% confidence level, unless otherwise stated.

5.2 NuSTAR data reduction

The source W1835 was observed with *NuSTAR* (Harrison et al., 2013) for 155 ks (OBSID 60101040002, PI: L. Zappacosta) on 19 November 2015. We removed periods of high 3-20 keV background. The remaining cleaned event files consist of 140 and 143 ks for detectors FPMA and FPMB, respectively. Because the source is expected to be weak and *NuSTAR* has a spatially dependent background (at energies <15-20 keV) given by cosmic unfocused straylight striking the detector through the open design of the telescopes, we chose to completely model the background in the whole detector areas. We employed the *nuskybdg* procedure (Wik et al., 2014). We sampled the background by extracting from each of the four chips in each detector spectra from circular regions of 3-4 arcmin radius. We excluded from these regions the hot DOG position, the chip gaps, and all the point sources detected in the *XMM-Newton*-PN and *XMM-Newton*-MOS images, adopting circular regions with an aperture of radius ∼ 30 arcsec. We then performed a joint modeling of the instrumental FPMA/FPMB and cosmic focused and unfocused (i.e. straylight) backgrounds. From the best fit we reconstructed the background image and checked visually for residual spatial variations in the background-subtracted images. The source is detected in both images at a significance of $\sim 2.5 - 2.7\sigma$ within 20 arcsec

[2]The Compton-thick obscuration is formally defined as absorption due to material with a column density of $N_\mathrm{H} \geq 1.5 \times 10^{24}$ cm^{-2}.

radius. The combined significance is 3.3σ. In Figure 5.1 we report the combined 3-24 keV FPMA and FPMB images in order to highlight the significance of the hot DOG (blue circle) above the field and compare the *XMM-Newton*-detected point sources in the field (dashed red circles). We then chose the source spectral extraction radius for each detector by simultaneously maximizing the signal-to-noise ratio and the net-source counts within increasing apertures (for details, see Zappacosta et al., 2018) centered on the *XMM-Newton*-detected source position (P15). The chosen extraction radii are 30 and 20 arcsec for FPMA and FPMB, respectively. We extracted the spectra from these circular regions using the *nuproduct* task in NuSTARDAS v. 1.4.1 with calibration database (CALDB) v. 20150123. The background spectra within the source spectral extraction regions were simulated from the best-fit model with 100 times the exposure time in order to ensure good statistics for background subtraction.

5.3 X-ray spectral analysis

The 3-24 keV FPMA and FPMB spectra consist of 40^{+7}_{-6} and 21^{+7}_{-5} background-subtracted counts (which are 24.5% and 24.8% of the total number of counts) whose 1σ uncertainties were estimated assuming Poissonian statistics (Gehrels, 1986). The apparent discrepancy between the collected counts in the two detectors is due to the different adopted spectral extraction radii as the *NuSTAR* PSF encloses in its 30 arcsec aperture (the FPMA extraction region) $\sim$ 1.5 times more flux than in its 20 arcsec aperture (the FPMB extraction region). We used them jointly with the XMM-PN and the coadded XMM-MOS spectra extracted and produced by P15 from a 42 ks *XMM-Newton* observation (OBSID 0720610101) performed on 18 August 2013. The addition of PN and MOS spectra (106 and 71 net-counts in the 0.5-8 keV band, respectively) allowed us to perform spectral modeling in the broad 0.5-24 keV band. All four spectra were grouped to a minimum of one net-count (i.e. background-subtracted) per bin. We note that *NuSTAR* has 26^{+6}_{-5} (FPMA+FPMB) net-counts compared to 31 ± 0.6 for the XMM-PN and 27^{+6}_{-5} for the XMM-MOS in the common 3-8 keV energy band, and it expands the spectral coverage above the unexplored $\sim$ 8 keV spectral region (i.e. $\sim$ 25 keV rest-frame) with another 35 source counts up to $\sim$24 keV. We used the Cash statistic (C-stat) as implemented in XSPEC v. 12.8.2 with direct background subtraction (Cash, 1979; Wachter et al., 1979).

5.3.1 Empirical models

In P15 the *XMM-Newton* data alone suggested a best-fit parametrization consisting of a reflection-dominated model. The source was modeled by a cold Compton reflection component model empirically parametrized by a reflector with an infinite plane geometry

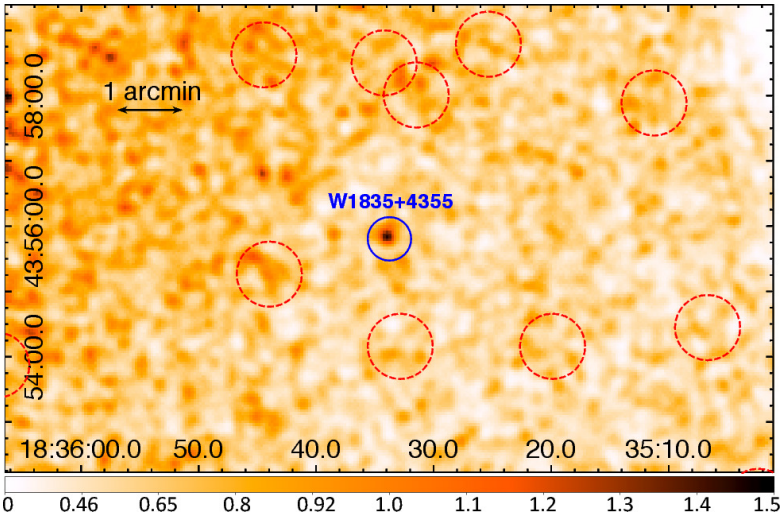

FIGURE 5.1: *NuSTAR* image in equatorial coordinates of the W1835 field in the energy range 3-24 keV (FPMA and FPMB were coadded in order to increase the signal-to-noise ratio). The blue solid 20 arcsec radius circular aperture reports the position of the hot DOG. Red dashed circles report the regions (30 arcsec radius) centered at the position of all the *XMM-Newton*- detected sources in the field (except for W1835) that were removed during the background-modeling procedure. The image was smoothed with a Gaussian kernel of 4 pixels (i.e. 10 arcsec) for better visualization. The color bar reports count/pixel values.

and infinite optical depth, which also includes the most pronounced fluorescent lines from Fe and Ni K-shell transitions. To this model a soft component consisting of a power law with fixed photon index $\Gamma_{sc} = 2.5$ was added. It accounts for the soft excess over the simple reflection model, which might originate from the primary component that leaked unaltered from the absorber or from photoionized or collisionally ionized or shocked gas (e.g., Guainazzi and Bianchi, 2007; Teng and Veilleux, 2010; Feruglio et al., 2013). We refer to it as the "scattered component". A further Gaussian component parametrizing the presence of a unresolved ionized Fe transition at 6.7 keV was added in order to account for residuals in the high-energy part of the Fe Kα line at 6.4 keV. This may indicate a possible presence of an ionized reflector or a high-temperature collisionally ionized plasma surrounding the active nucleus. The addition of the *NuSTAR* data allows an energy coverage up to observed $\sim$20 keV. This enables us to cover rest-frame energies in the range $\sim$1.6-70 keV and therefore obtain better global constraints on the high-energy part of the spectrum and further shed light on the obscuration state of this quasar. Because of the heavily obscured nature of the source, we properly account for Compton scattering and geometric effects through our modeling. These effects are more pronounced at the highest column densities.

5.3.1.1 Power-law-based models

We first tried simple models and checked the consistency of the broadband parameterization by comparing it with the parameterization obtained by P15 using *XMM-Newton* data alone. In our models we always accounted for a multiplicative factor for the possible difference in the calibration between *XMM-Newton* and *NuSTAR* (which has been measured to be no more than 10%; Madsen et al., 2015) and source flux variability that may have occurred between observations. We started with an unabsorbed power-law model. This resulted in a poor fit (C-stat/dof=174/157) with a photon index $\Gamma = 0.9 \pm 0.1$ that is consistent with the slope obtained by modeling *XMM-Newton*-only data (P15). The addition of a cold intrinsic absorber (ZWABS model in XSPEC) gave $\Gamma \approx 1$ and $N_{\rm H} \sim 10^{23}{\rm cm}^{-2}$, but did not improve the modeling much (C-stat/dof=173/156) over the previous parameterization. Strong residuals at the position of the Fe K lines are present. These were interpreted by P15 as due to a prominent neutral Fe Kα line at 6.4 keV with an equivalent width (EW) larger than 1-2 keV, and also due to a ionized Fe line at ~6.67 keV. By fixing $\Gamma = 1.9$, we also obtained high residuals at low energies (1-2 keV). Hence we added a low-energy scattered power-law component whose photon index was tied to that of the primary component. We found a best-fit (C-stat/dof=169/156) with $N_{\rm H} \approx 6 \times 10^{23}$ cm^{-2} and a soft scattered component flux compared to that of the unabsorbed primary (called scattered fraction[3], hereafter $f_{\rm sc}$), which is in the 1σ range $f_{\rm sc} \approx 10 - 20\%$. This is significantly higher than normally found for heavily absorbed AGN (e.g., Brightman et al., 2014; Lanzuisi et al., 2015). Leaving Γ free to vary did not improve our modeling significantly. The addition of two unresolved Gaussian lines to account for the neutral and ionized Fe lines further improved our fit (C-stat/dof=147/154), giving a column density $N_{\rm H} = 1.4^{+0.7}_{-0.5} \times 10^{24}$ cm^{-2}that is compatible with CT absorption. We further modified the absorber by accounting for Compton scattering of X-ray photons using the multiplicative CABS model. This model accounts for scattering of photons outside of the line of sight (therefore neglecting photons that scatter into the line of sight). Compton scattering at the highest column densities is a non-negligible effect and further suppresses the level of the primary continuum at a fixed column density. This leads to an almost unaltered best-fit parameterization that we refer to as model CAbsPow with the exception of the scattered fraction, which resulted in a more reasonable $f_{\rm sc} = 5^{+4}_{-3}\%$. The 2-10 keV and 10-40 keV unabsorbed luminosities are $L_{2-10} = 2.9 \times 10^{45}$ erg s^{-1}and $L_{10-40} = 1.9 \times 10^{45}$ erg s^{-1}. A summary of the parameters derived by our spectral analysis is given in Table 5.1.

[3]Given the Γ tied between the scattered and primary power-law components, we calculated it as the ratio between the model normalizations.

5.3.1.2 Modeling scattering and reflection from dense medium

The presence of the neutral Fe line suggests the existence of an additional reflection component that still must be accounted for. In addition to a primary power-law component modified by photoelectric absorption and Compton scattering, we therefore modeled the spectrum by employing a reflection component including spectral features from neutral Fe and Ni at 6-7 keV parametrized by the PEXMON model (Nandra et al., 2007) and a 6.65 keV (best fit from *XMM-Newton* spectra alone, see P15) line for the ionized Fe line at ∼6.67 keV. The reflection model assumes an infinite planar geometry with infinite optical depth illuminated by the primary continuum and subtending for an isotropic source an angle of $\Omega = 2\pi \times R$, where R is the reflection parameter. In the model we assumed solar abundance, an exponential energy cutoff for the incident primary power-law $\mathrm{E_c} = 200$ keV (Fabian et al., 2015), and a reflector inclination angle of 60 deg (default in *XSPEC*). We further added a soft-excess component parametrized as a power law with photon index tied to that of the primary component. In order to decrease the number of free parameters, we set its flux to be 2% of the primary flux, as is commonly found in heavily obscured ($N_\mathrm{H} \gtrsim 10^{23}\mathrm{cm}^{-2}$) AGN (e.g., Lanzuisi et al., 2015). We obtain a best fit with a primary component completely suppressed by $N_\mathrm{H} \gg 10^{25}\mathrm{cm}^{-2}$ and in which only the scattered and reflection components effectively contribute to the modeling[4]. A more accurate treatment of scattering and reflection in high dense medium is performed by exploiting physically motivated toroidal models in Section 5.3.2.

The primary component is heavily obscured, therefore we tried to model the spectrum assuming a reflection-dominated scenario in which the coronal component is completely absorbed. Hence we removed the absorbed power-law component from our model. In our parametrization we linked the power-law slope and normalization of the PEXMON and scattered power-law. We therefore assumed that the scattered component is composed of coronal flux leaking through the obscurer unabsorbed (i.e. assuming a patchy obscurer distribution). We furthermore assumed that the scattered flux is 2% of the primary, giving rise to the reflected component. The resulting best-fit parametrization (model REFLDOM) constitutes an equally good yet simpler parametrization to the data with C-stat/dof=149/156. This confirms that the primary absorbed component is not required to parametrize our data. Leaving Γ free to vary does not significantly improve the parametrization (C-stat/dof=148/155). The observed 2-10 keV and 10-40 keV luminosities from the reflected component are $L_{2-10} = 2.4 \times 10^{44}$ erg s^{-1} and $L_{10-40} = 5.7 \times 10^{44}$ erg s^{-1}, respectively. When we assume a column density $N_\mathrm{H} \approx 10^{25}\mathrm{cm}^{-2}$ of the obscuring material, the unobscured X-ray luminosity is a factor of ~ 100 and ~ 10 higher, respectively.

[4]We verified that the derived column density is insensitive to the particular choice of inclination angle.

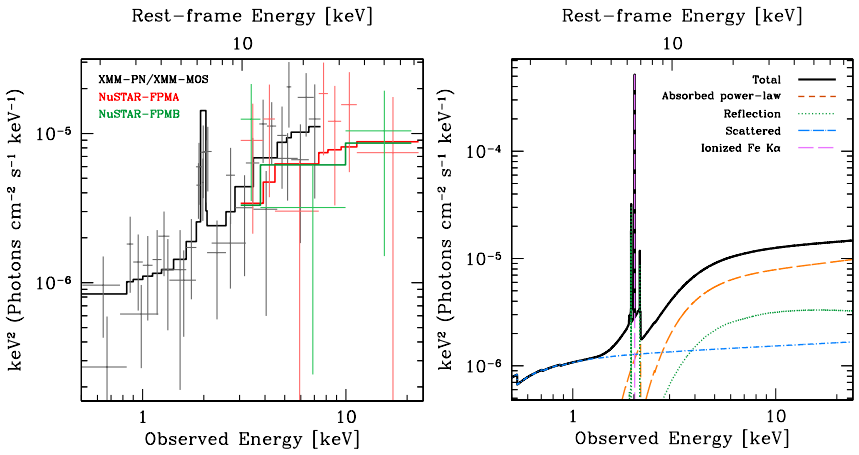

FIGURE 5.2: Left panel: *XMM-Newton* and *NuSTAR* broadband 0.5-24 keV unfolded spectrum of W1835 grouped at a minimum of five net-counts per bin for better visual representation. The black, red, and green thick solid lines are the best-fit MYTOR unfolded model (as reported in Table 5.1 and discussed in Section 5.3.2) for *XMM-Newton*-PN, *NuSTAR*-FPMA, and *NuSTAR*-FPMB, respectively. Data are reported in lighter colors. At low energy we omit the *XMM-Newton*-MOS best-fit model for clarity and report MOS and PN spectra with the same color. Right panel: Corresponding best-fit theoretical model (thick solid black line) and sub-components (discontinuous lines). The absorbed primary power-law, the reflection, and the scattered components are reported with dashed orange, dotted green, and dash-dotted blue lines. The magenta dashed line indicates the ionized Fe line.

TABLE 5.1: X-ray spectral fitting: derived parameters

Model[a]	C-stat/*dof*	Γ	$N_{\rm H}$ (10^{24} cm^{-2})	Γ_{sc}	f_{sc} (%)	L_{2-10} (10^{45} erg s^{-1})	L_{10-40} (10^{45} erg s^{-1})
CABSPOW[b]	147/154	(1.9)	$1.4^{+0.7}_{-0.5}$	$(=\Gamma)$	5^{+4}_{-3}	$2.9^{+3.6}_{-1.3}$	$1.9^{+2.4}_{-0.9}$
REFLDOM[c]	149/156	(1.9)	-	$(=\Gamma_{pexmon})$	(2)	0.2^{f}	0.6^{f}
MYTOR[d]	149/155	(1.9)	$1.1^{+0.5}_{-0.3}$	$(=\Gamma)$	9^{+5}_{-3}	$1.6^{+0.9}_{-0.5}$	$1.0^{+0.6}_{-0.6}$
BNSPHERE[e]	149/155	(1.9)	$0.9^{+0.3}_{-0.2}$	$(=\Gamma)$	15^{+6}_{-4}	$0.9^{+0.3}_{-0.2}$	$0.6^{+0.2}_{-0.2}$

(a) see Sect. 5.3.1, 5.3.1.1 and 5.3.2
(b) WABS(ZPOWERLW$_{sc}$+ZWABS*CABS*ZPOWERLW+ZGAUSS$^{neut}_{FeK\alpha}$+ZGAUSS$^{ion}_{FeK\alpha}$), where ZGAUSS$^{neut}_{FeK\alpha}$, ZGAUSS$^{ion}_{FeK\alpha}$ are Gaussian lines to parametrize the neutral and ionized Fe Kα line;
(c) WABS(ZPOWERLW$_{sc}$+ZGAUSS$^{ion}_{FeK\alpha}$+PEXMON);
(d) WABS(ZPOWERLW$_{sc}$+ZPOWERLW*MYTZ+MYTS+MYTL);
(e) WABS(ZPOWERLW$_{sc}$+BNTORUS);
(f) Observed luminosity not corrected for absorption.

5.3.2 Geometry-dependent models

In order to obtain more accurate and physically motivated constraints, we used MYTorus (Murphy and Yaqoob, 2009; Yaqoob, 2012), which is a Monte Carlo model based on a toroidal circumnuclear structure that absorbs and reprocesses the primary radiation self-consistently and accounts for geometric effects, Compton scattering for radiation propagating toward high column density medium, and reflection and fluorescent line emission in the reprocessed radiation. The torus has a half-opening angle of 60 deg and is composed of uniform and neutral material. An input power-law incident primary radiation is assumed. Its implementation in *XSPEC* consists of three different table model components: (1) one for the attenuation of the line-of-sight radiation due to photoelectric and Compton-scattering effects (MYTZ); (2) one to reprocess the radiation due to reflected radiation into the line of sight (MYTS); (3) and one that calculates the contribution from scattered line emission (MYTL). We combined all the three components by linking the column density and setting the relative normalization constants of each component to unity. We furthermore added a power law to account for the scattered flux at soft energies and for the ionized Fe line.

Because of the high column density and in order to comply with the geometrical requirements invoked by the standard unification schemes in which type 2 sources are seen at high inclinations, an almost edge-on view of the torus of 85 deg was assumed (Brightman et al., 2014; Lanzuisi et al., 2015; Zappacosta et al., 2018). We also fixed $\Gamma = 1.9$ and tied to it the photon index for the scattered component. We fixed the normalizations of MYTS (A_S) and MYTL (A_L) relative to (MYTZ) to unity and linked all the components to the same equatorial column density $N_{\rm H}^{\rm eq}$. The latter is related to the line-of-sight column density $N_{\rm H}$ according to the inclination angle assumed and in this almost edge-on case follows the relation: $N_{\rm H} \simeq 0.98\, N_{\rm H}^{\rm eq}$.

The best fit (C-stat/dof=149/155) with this model (model MYTor) is reported in Figure 5.2. In the left panel we report *XMM-Newton* and *NuSTAR* unfolded spectra along with the best-fit model. The right panel shows the different subcomponents contributing to the incident model. The column density estimated with this model is $N_{\rm H} = 1.1^{+0.5}_{-0.3} \times 10^{24}$ cm^{-2}. The scattered fraction is measured to be $f_{sc} = 9^{+5}_{-3}\%$, which, although slightly on the high side, is consistent within the errors with the typical fractions for highly absorbed ($N_{\rm H} > 10^{23}$ cm^{-2}) AGN. This fraction in our parametrization is highly degenerate with the column density. This is shown by the confidence contours reported in Figure 5.3 for the two interesting parameters[5]. Given this parametrization,

[5]We note that the assumed high-inclination angle is conservative in terms of $N_{\rm H}$ as it gives lower values than lower inclination angles. Furthermore, it does not affect the maximum allowed value of the scattered fractions, but it affects its constraints at the lower-end values. For instance, assuming an inclination angle of 70 deg, we obtain a 90% lower limit of $N_{\rm H} \sim 7 \times 10^{23}$ cm^{-2} and $f_s = 0.7 - 22\%$ (1σ

the 2-10 keV and 10-40 keV unabsorbed luminosities are $L_{2-10} = 1.6 \times 10^{45}$ erg s^{-1} and $L_{10-40} = 1.0 \times 10^{45}$ erg s^{-1}, respectively.

This model was not previously evaluated in P15 for the *XMM-Newton* data alone. The inclusion of the *NuSTAR* data allows us to confirm the *XMM-Newton* estimated values (which crucially depend on the level of the *XMM-Newton* higher energy bins, which, being in a regime of low signal-to-noise ratio, may suffer from systematics) and to better define the upper-end value on $N_{\rm H}$ as reported in Figure 5.3.

Hot DOGs are usually considered a transitional dust-enshrouded/highly star-forming phase in the merger-driven quasar formation scenario (Sanders et al., 1988; Hopkins et al., 2008; Wu et al., 2012). In this scenario, the accretion of matter proceeds through intense and chaotic accretion phases caused by the loss of angular momentum resulting from major mergers as opposed to more moderate accretion states typical of the secularly evolving planar geometries (disk-torus structure) invoked in unified models (e.g., Urry and Padovani, 1995). In this case, we expect that in the former the obscuring material is distributed more isotropically than in the toroidal structures that are typically invoked for more standard, Seyfert-like sources. If this is the true scenario for W1835, it is reasonable to evaluate a model in which the obscurer covers the entire sphere, regardless of its distance from the nucleus. We employed a specific table model derived from Monte Carlo based calculations for a homogeneous toroidal obscurer modeled as a sphere in which there is a biconical cavity with variable opening angle (hereafter BNTorus; Brightman and Nandra, 2011). We used the case with an opening angle of 0 deg (i.e. no biconical openings) and hence with a spherical obscurer distribution (i.e. isotropic obscuration; model BNSphere). This model, as well as MYTorus, assumes a homogeneous matter distribution, but this is a probably good approximation of the spherical high covering factor obscuration scenario, even if there may likely be inhomogeneities in the gas/dust distribution (possibly with some sightlines exhibiting Compton-thin column densities). This model is simpler than MYTor as it involves the same number of free parameters and does not need any inclination angle assumption. We obtain a best-fit (C-stat/dof=149/155) column density of $N_{\rm H} = 0.9^{+0.3}_{-0.2} \times 10^{24}$cm^{-2} with a slightly higher scattered fraction $f_{sc} = 15^{+6}_{-4}\%$ (assuming $\Gamma = 1.9$ and $Z = 1\,Z_{\odot}$). Confidence contours for this case are reported in red in Figure 5.3. The degeneracy of the two parameters is less pronounced than for the MYTor case, but the scattered fraction is rather high, as shown by the comparison with highly obscured/CT AGN candidates reported from the COSMOS survey in Lanzuisi et al. (2015). However, the increase in f_{sc} is expected

range). However, as for all inclinations angles $\lesssim$70-80 deg, the derived uncertainties are affected by the maximum tabulated $N_{\rm H} = 10^{25}$ cm^{-2} in the MYTorus model, which prevents an accurate and correct sampling of the entire parameter space of interest.

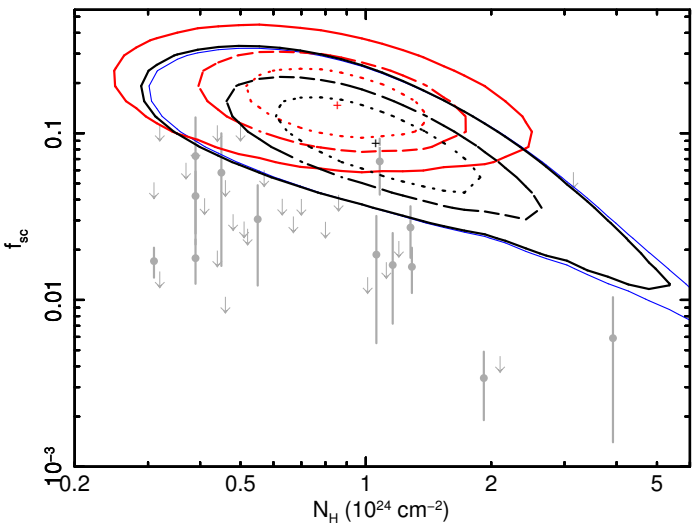

FIGURE 5.3: Confidence contours for f_{sc} and $N_{\rm H}$ in MYTOR modeling (black) and the BNSPHERE model (red). Dotted, dashed, and solid lines represent contours for 68%, 90%, and 99% confidence levels. Thick contours represent constraints from the joint *XMM-Newton-NuSTAR* modeling. The thin solid blue contour reports 99% constraints from *XMM-Newton*-only spectral analysis. Grey data indicate the scattered fractions for the heavily absorbed and CT AGN selected in the XMM-COSMOS field (Lanzuisi et al., 2015, errors and upper limits are 90% c.l.).

because in BNSPHERE the low-energy nuclear radiation can not escape or scatter outside of the nuclear region without being obscured. Therefore, if the source truly is dust enshrouded, the soft-excess emission must come from elsewhere. The derived parameters for both MYTOR and BNSPHERE modelings are reported in Table 5.1.

We expect that most of the CT absorption occurs in the innermost galactic regions around the AGN, as argued by Buchner and Bauer (2017). However, as stressed by these authors, their study is valid for the AGN population at large, and peculiar/rare sources such as hot DOGs are therefore not sampled. This means that we cannot make any strong conclusion on the location of the CT absorber in W1835.

5.4 Modeling the optical-to-infrared SED

In order to have the most complete view of W1835, P15 performed SED fitting based on ten photometric points covering the MIR to far-infrared (FIR) wavelength range collected from the literature. Their SED modeling included both a galactic starburst and nuclear emission components. In particular for the latter, they used a grid of smooth torus models with a flared-disk geometry (Fritz et al., 2006; Feltre et al., 2012). The galactic component at longer wavelengths was well parametrized with either the Arp 220 template or with a optically thin approximation of a modified blackbody with fixed emissivity index $\beta = 2$. From the latter, the authors obtained a temperature $T_{dust} \approx 40$ K for the dust

Table 5.2: Photometric points of W1835

Instrument	Band	Flux Density
HST/WFC3 F160W	1.6 μm	12.8 $\pm$ 0.9 μJy
Spitzer IRAC1	3.6 μm	51.5 $\pm$ 2.2 μJy
Spitzer IRAC2	4.5 μm	142.8 $\pm$ 3.0 μJy
WISE W3	12 μm	6790 $\pm$ 190 μJy
WISE W4	22 μm	24.6 $\pm$ 1.0 mJy
Herschel PACS	70 μm	53.6 $\pm$ 4.2 mJy
Herschel PACS	160 μm	92.8 $\pm$ 17.1 mJy
Herschel SPIRE	250 μm	81.0 $\pm$ 8.1 mJy
Herschel SPIRE	350 μm	72.0 $\pm$ 7.2 mJy
Herschel SPIRE	500 μm	33.0 $\pm$ 3.3 mJy
SCUBA-2	850 μm	8.0 $\pm$ 1.5 mJy

References: All photometric points are from P15, except for the *HST*/WFC3 point (Farrah et al., 2017) and the *Herschel* PACS points (IRSA)

Table 5.3: SED modelings: derived quantities

Model	χ^2_r	θ_{oa} (deg)	i (deg)	T^a_{dust} (K)	$L^b_{\rm IR}$ (erg s^{-1})	$L_{\rm bol}$ (erg s^{-1})	$L_{6\mu m}$ (erg s^{-1})	SFR ($M_\odot\, yr^{-1}$)	Dust mass^c ($10^8 M_\odot$)
Best fit	1.44	30	70	69	7.3×10^{46}	4.39×10^{47}	1.13×10^{47}	3300^{+100}_{-100}	3.9
MYTorus-like	2.06	(60)	70	63	6.0×10^{46}	4.71×10^{47}	1.07×10^{47}	2700^{+200}_{-150}	3.2
Sphere80	4.51	(10)	(80)	69	7.3×10^{46}	5.32×10^{47}	1.42×10^{47}	3300^{+200}_{-200}	3.9
Sphere90 (edge-on)	6.56	(10)	(90)	67	6.9×10^{46}	5.13×10^{47}	1.38×10^{47}	3100^{+100}_{-100}	3.7

Quantities reported in parentheses have been assumed fixed during the modeling.
(a) The typical uncertainty on the temperature is ± 5 K. (b) Relative to the dust emission component. (c) Calculated as in Beelen et al. (2006).

component. This temperature is lower than those estimated by Fan et al. (2016c) and Wu et al. (2012), that is, $T_{dust} \approx 70\ K$ and $T_{dust} \approx 90\ K$, respectively. Furthermore, it is lower than the typical hot DOG temperatures and compatible with the highest temperature for normal DOGs and with the maximum temperatures derived by dust heated by stellar processes (e.g., Magnelli et al., 2012; Wu et al., 2012). Here we perform an improved SED fitting using updated photometric points from the *Herschel* catalog in the NASA/IPAC Infrared Science Archive (IRSA) and adding *HST/WFC3* F160W band photometry at 1.6 μm with refined modeling that accounts for the clumpy circum-nuclear torus. Table 5.2 reports the photometric points considered for the SED modeling.

The approach we followed is based on a two-component fitting procedure recently developed and employed in type 1 hyper-luminous sources by Duras et al. (2017). In this procedure the SED is fit with a combination of quasar and host galaxy templates. The AGN component is described as the superposition of the accretion disk emission and of the radiation coming from the dusty torus. We built a library of templates for the quasar

emission using the broken power-law description by Feltre et al. (2012) for the accretion disk and the model by Stalevski et al. (2016) for a clumpy two-phase dusty torus characterized by high-density clumps embedded in a low-density and smooth medium. The two were appropriately normalized to preserve the energy balance between the ultraviolet and the IR bands. The library is composed of about 7200 templates with different values of the optical depth at 9.7 μm, the inclination along the line of sight (from 50 to 90 degrees, in order to force a type 2 configuration in which the direct view of the SMBH is blocked by the torus) and the dust geometry and distribution. The second component of the model is a modified blackbody that accounts for the emission powered by star formation that is absorbed and then re-emitted by the surrounding dust in the MIR and FIR bands. We parametrized it as

$$S_\lambda \propto (1 - e^{-\tau_\lambda}) B_\lambda(T_{dust}),$$

where $B_\lambda(T_{dust})$ is the blackbody model and $\tau_\lambda = (\lambda_0/\lambda)^\beta$, is the optical depth, which is assumed to have a power-law dependence, with λ_0 being the wavelength at which the optical depth reaches unity and β being the dust emissivity index. Because we only have a small number of photometric points, we fixed $\beta = 1.6$, which seems to be the most reliable value for both local and high-z quasars (Beelen et al., 2006; Bianchi et al., 2017) and $\lambda_0 = 125$ Å (Huang et al., 2014; Fan et al., 2016c). The cold-dust library consists of 70 templates with a range of temperatures from 30 to 100 K.

In Figure 5.4 we show the rest-frame optical-to-FIR SED with the best-fit model (solid line). The accretion disk plus torus emission is shown in blue and the cold-dust emission in red. The black line is the total best-fit model emission. From this best fit we were able to derive some physical quantities of both the host galaxy and the nuclear source. They are reported in Table 5.3. The intrinsic quasar bolometric luminosity was computed by integrating the emission coming from the AGN component from 1 up to 1000 μm and rescaling it by a factor ~ 1.7 to account for geometry and anisotropy of the radiation field caused by the obscurer geometry and its orientation (Pozzi et al., 2007). This correction is an average value computed for a sample of quasars characterized by a toroidal obscurer and moderate degree of obscuration ($\log[N_{\rm H}/{\rm cm}^{-2}] \approx 10^{22} - 10^{23.4}$ cm^{-2}). If the emitting dust is also responsible for the CT obscuration and if a spherical geometry is in place, we should expect larger corrections and therefore possibly higher bolometric luminosities. The IR luminosity (L_{IR}) of the host, a tracer of the reprocessed UV stellar light, is obtained by integrating the dust emission component in the range 8-1000 μm and is $L_{IR} = 7.3 \times 10^{46}$ erg s^{-1}. From this we computed the star formation rate (SFR) using the relation by Kennicutt (1998) scaled to a Salpeter initial mass function, gaining an extremely high value of SFR of about $SFR = 3300 \pm 100\ M_\odot\, yr^{-1}$. The best-fit dust emission shows a temperature of about $T_{dust} = 69$ K, in good agreement

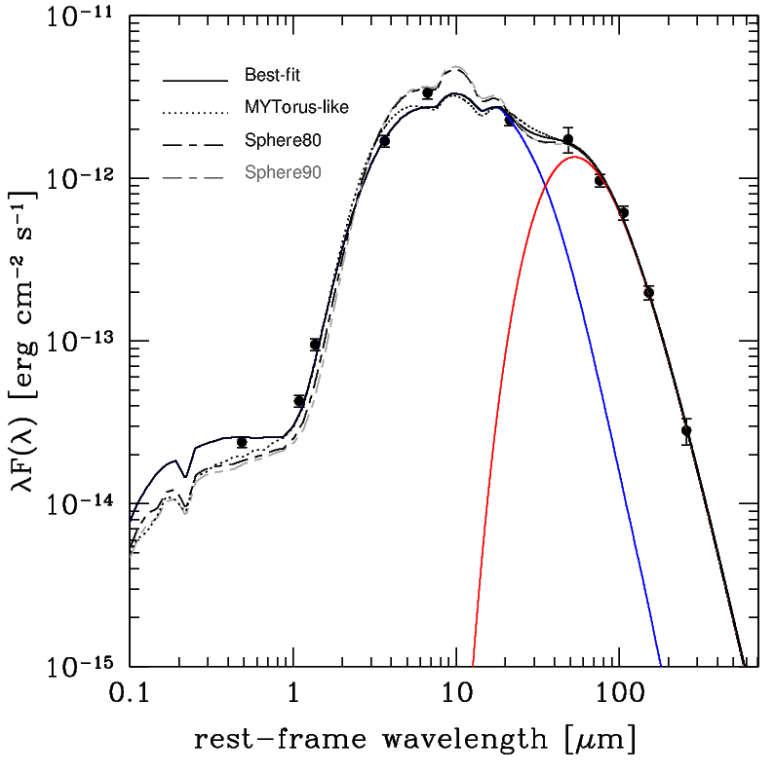

FIGURE 5.4: SED modeling for W1835. The solid line reports the best-fit model (black, red, and blue represent the total, AGN-only, and modified blackbody components). Dotted and dashed lines represent best-fit models assuming a toroidal geometry similar to the MYTOR and BNSPHERE (black and grey show 80 deg and 90 deg inclination angles) models used for the X-ray analysis (Sect. 5.3.2). See Sect. 5.4 and Table 5.3 for further details.

with the estimates by Fan et al. (2016c). Our estimates differ substantially from the $SFR \approx 2100\ M_{\odot}\, yr^{-1}$ and $T_{dust} \approx 40$ K reported by P15. We verified that this difference is mainly driven by the adoption of the modified blackbody model that in P15 was approximated assuming the optically thin regime and adopting $\beta = 2$. The inferred dust mass of $(3-4) \times 10^8 M_{\odot}$ (estimated as in Beelen et al., 2006, see Table 5.3) is consistent with typical abundances in other hot DOGs (Fan et al., 2016c) and in coeval and higher redshift type 1 analogs (e.g., Beelen et al., 2006; Valiante et al., 2014; Duras et al., 2017).

In order to be consistent with the toroidal models used in our X-ray analysis, we tried to model the SED by forcing similar torus parameters. To approximate the MYTORUS geometry (i.e. *MYTorus-like*), we fixed the same torus opening angle and allowed inclinations in the range 70-90 deg. We also tried an almost fully covered obscurer (i.e. *Sphere80*) by adopting the templates with only a polar cap of 10 degrees left open and a 80-degree inclination (almost edge-on)[6]. We obtained reasonable parametrizations although with a slightly worse χ^2. The very high obscuration of the quasar and the

[6]Compared to the smooth toroidal models used in our X-ray analysis, those used in the SED fitting are clumpy. Furthermore, the disk geometry for the latter is a conical torus (flared disk), while in MYTorus, a donut-shaped torus is assumed.

HST/WFC3 F160W image (Fan et al., 2016c; Farrah et al., 2017), which shows a somewhat extended and irregular host emission, means that the emission shortward of ~ 1 μm is very likely partially contributed by the host. In our models we tried to account for a maximum contribution from the AGN that does not include the host. Temperatures and derived SFRs are in the range $T_{dust} \approx 60 - 70$ K and around $SFR \approx 3000$ $M_{\odot}\, yr^{-1}$, respectively, hence not very dissimilar from the estimate from the best-fit parametrization (see Table 5.3 for detailed estimates). In Figure 5.4 we report the best-fit parametrizations for the *MYTorus-like* (dotted) and *Sphere80* (dashed) cases. We tried a fully covered (4π) obscurer (i.e. *Sphere90*) and report it as the grey dashed line in Figure 5.4. The spherical parametrizations slightly underestimate the photometric points around of 1 μm rest-frame. This is expected, and because of the extremely obscured nature of this source, these points can therefore be interpreted to be contributed by the stellar emission from the host, which is not accounted for in our modeling.

In the *HST/WFC3 F160W* image a low surface brightness contribution from the stellar host is visible (Fan et al., 2016c; Farrah et al., 2017). To infer its level, we included an additional component using ~ 900 galaxy templates from Bruzual and Charlot (2003), with different levels of extinction spanning the range $\Delta E(B-V) = 0-0.5$ and assuming a Chabrier (2003) initial mass function. We find a fractional contribution of $f_{host} \approx 58-75\%$ (90% confidence level interval) in the optical rest-frame band (i.e. in the Johnson B band). Despite this, the global AGN and dust properties remain remarkably consistent with the values reported in Table 3. However, the *HST/WFC3 F160W* photometric point is the only optical constraint to the host template in the SED modeling. At shorter wavelengths, the uncertainties at 90% level in f_{host} become much larger. In addition, systematics may likely be affecting the derived value. More data at bluer rest-frame wavelengths are required to remove possible systematics and reduce the uncertainty on the host contribution.

5.5 Discussion

5.5.1 Confirming high obscuration and high luminosity

Our analysis confirms that W1835 hosts a luminous and heavily obscured quasar. An empirical parameterization accounting separately for different primary and reflection components suggests mild to heavy CT obscuration. A model with a reflection-only component can already provide an excellent description of the data. Physically motivated models implementing a toroidal or spherical geometry for the obscurer and accounting for Compton-scattering effects give column densities at around $\sim 10^{24}$ cm^{-2}, that is,

somewhat lower than the formal threshold defining a source CT (i.e. $N_{\rm H} = 1.5 \times 10^{24}$ cm^{-2}). However, (i) they require scattered fractions of $f_{sc} \gtrsim 5-9\%$, which is slightly on the high side but still consistent within the errors, except for BNSphere ($f_{sc} \approx 15\%$), with the canonical observed few-percent values (see Sect. 5.5.2 for further details) and (ii) the scattered fractions and column density are anticorrelated. A CT obscuration with more moderate fractions is therefore very likely (i.e. at 1σ level, see Figure 5.3). To our knowledge, W1835 is the most obscured, most luminous high-redshift AGN detected by *NuSTAR*. Other known hot DOGs whose low-energy X-ray spectra were analyzed exhibit values of $N_{\rm H} \approx 6 - 7 \times 10^{23}$ cm^{-2} , although with large uncertainties (Assef et al., 2016; Ricci et al., 2017a). An exception is W0116–0505 (hereafter W0116), one of the X-ray brightest hot DOGs that has a column density similar to that of W1835 (Vito et al., 2018). Recently, Goulding et al. (2018) analyzed the X-ray emission of a sample of extremely red hyper-luminous quasars (ERQ) at $z = 1.5 - 3.2$, finding indication of heavy absorption ($N_{\rm H} \gtrsim 10^{23}$ cm^{-2}). Through spectral analysis of the stacked spectrum of the most weakly detected *Chandra* sources, they estimated column densities on the order of $N_{\rm H} \sim 10^{24}$ cm^{-2}.

The derived unabsorbed luminosities for W1835 are on the order of $L_X \approx 10^{45}$ erg s^{-1} (see Table 5.1). Based on this and on the estimated bolometric luminosities (Table 5.3), we can derive the bolometric corrections $k_{bol,X} = L_X/L_{bol}$ in the 2-10 keV and 10-40 keV bands. By assuming as fiducial models the MYTor X-ray parametrization and the best-fit SED modeling, we obtain $k_{bol,2-10} \approx 270$ and $k_{bol,10-40} \approx 440$. If we consistently (to the X-ray model) assume a MYTorus-like toroidal structure for the SED modeling, we obtain similar values, that is, a factor ~ 1.1 larger. These values are all in agreement with bolometric corrections found for X-WISSH sample of $z = 2 - 4$ type 1 hyper-luminous MIR/optically selected quasars (e.g., Martocchia et al., 2017) and with the extrapolated trend from less luminous type 2 AGN (e.g. Lusso et al., 2012).

Luminous optically bright quasars have been found to exhibit X-ray luminosities weaker than those inferred by a linear extrapolation from X-ray selected lower-luminosity AGN (Gandhi et al., 2009; Mateos et al., 2015) and are more in line, but still weaker, than extrapolations from dust-obscured galaxies at lower luminosities (Fiore et al., 2009; Lanzuisi et al., 2009). The X-WISSH quasars, which are the most luminous type 1 AGN in the universe, clearly show this X-ray weakness compared to their MIR radiative output (Martocchia et al., 2017). Recently revised nonlinear relations between X-ray and MIR intrinsic luminosities have been derived by Stern (2015) and Chen et al. (2017) in order to account for the observed X-ray weakness exhibited at the highest luminosities. Ricci et al. (2017a), considering a sample of X-ray detected hot DOGs for which spectroscopic analysis is possible (including W1835), reported L_{2-10} significantly lower than those reported by the X-WISSH sources that exhibit comparable $L_{6\mu m}$. This has been

considered as evidence of further intrinsic X-ray weakness or significant underestimation of the column density. A somewhat opposite behavior has been reported by Vito et al. (2018) for the hot DOG W0116, for which L_{2-10} appears to be comparatively higher than the extrapolated trends from hyper-luminous quasars (i.e. somewhat X-ray louder). As reported by Vito et al. (2018), $L_{6\mu m}$ for this source might be underestimated given that it has been computed under the assumption of isotropic emission (Tsai et al., 2015; Vito et al., 2018). In order to understand the level of underestimation and to consistently compare W0116 to our results for W1835, we performed SED fitting for W0116 using the photometric points provided by Tsai et al. (2015) (see their Table 2). From our best-fit model we obtain $L_{6\mu m} = 1.5 \times 10^{47}$ erg s^{-1}, that is, a factor > 4 higher than the values used by Vito et al. (2018). With this new estimate we found W0116 in line with the X-ray-to-MIR luminosity values reported for type 1 quasars. Similarly, the spectral analysis on the X-ray stacked spectrum of weak ERQs performed by Goulding et al. (2018) gives a value of the intrinsic X-ray luminosity that agrees with the expected $L_{6\mu m}$ for hyper-luminous type 1 AGN. Even in this case, anysotropic MIR emission could cause an underestimation of the true MIR luminosity. In this case, we would expect these sources to exhibit slightly lower X-ray radiative outputs (by a factor of a few) than the higher MIR luminosities, as suggested by Goulding et al. (2018) themselves.

In Figure 5.5 we report the X-ray-to-MIR luminosity for the W1835 (red circle), the Ricci et al. hot DOGs sample (blue filled triangles), W0116 (magenta squares empty and filled, the latter being plotted with our SED-derived $L_{6\mu m}$), the X-WISSH sources (stars), two reddened quasars (green empty triangles; Feruglio et al., 2014; Banerji et al., 2015; Martocchia et al., 2017), and the measure from the stacked ERQ spectrum by Goulding et al. (2018) (orange diamond). We also report X-ray-to-MIR relations obtained from MIR-selected AGN (Lanzuisi et al., 2009; Fiore et al., 2009), X-ray selected AGN (Mateos et al., 2015; Chen et al., 2017), and specifically tuned for the hyper-luminous regime (Stern, 2015). We note that W1835 lies higher than the average hot DOGs locus found by Ricci et al. (2017a) and close to W0116 and the heavily absorbed ERQs and is consistent with the lower portion of the type 1 quasars and the red quasars. Hence it exhibits a lower degree of X-ray weakness, at least similar to that inferred for type 1 luminous AGN.

5.5.2 Origin of the soft excess

In low-count spectra, the soft-excess component is usually reproduced by a single power-law component. If forced to have the same photon index as the primary intrinsic continuum, this component parametrizes an absorber in which the primary flux leaks (or Thomson scatters) unaltered through it. This parametrization is a convenient way to

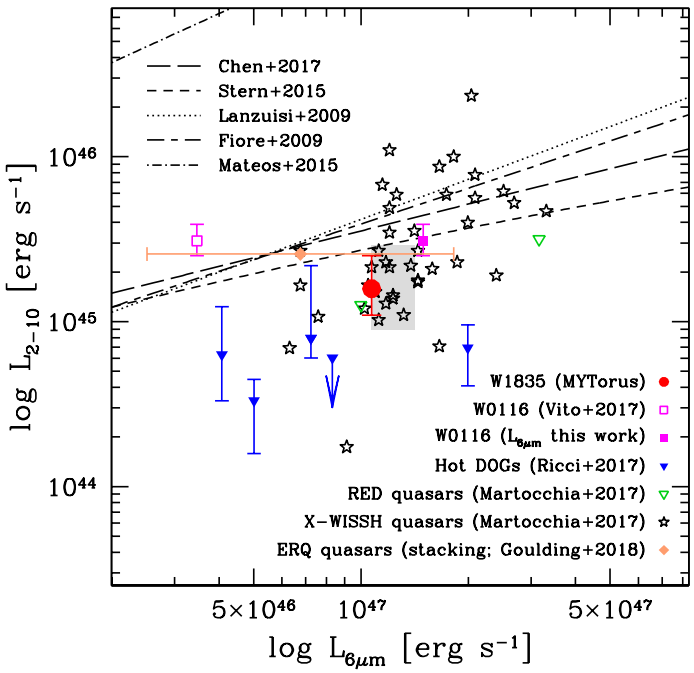

FIGURE 5.5: $L_{6\mu m}$ vs. L_{2-10} relation. The red circle represents W1835 for the MYTorus geometry (both in X-ray and SED analysis) with the range of systematic uncertainty due to different modelings (see Tables 5.1 and 5.3) reported as the grey shaded region. Blue triangles report a compilation of hot DOGs in Ricci et al. (2017a) except for W1835, which we update here. Magenta squares report W0116+0505 with $L_{6\mu m}$ reported by (Vito et al., 2018) (empty square) or estimated by our SED fitting (filled square; see Section 5.5.1). Black stars and green triangles represent the X-WISSH hyper-luminous type 1 quasar sample (Martocchia et al., 2017) and two reddened quasars (Martocchia et al., 2017). The orange diamond reports the best-fit L_{2-10} value obtained from X-ray spectral analysis performed on a stacked X-ray spectrum of a sample of ERQ sources observed in *Chandra* in Goulding et al. (2018). In the latter, the error bar represents the range of $L_{6\mu m}$ in the sample. We also report X-ray-to-MIR relations derived for different optical/MIR/X-ray selected AGN samples.

include a soft component by adding only one free parameter to the model and have a reference measure of f_{sc}. Given the highly obscured nature of W1835, the relatively high soft-excess emission may include additional components that are not directly linked to the quasar emission itself.

From our SED fitting we find that the host of this AGN harbors powerful stellar nurseries capable of producing stars at a rate of ~3000 $M_{\odot} yr^{-1}$. These levels of star formation are typical of other hyper-luminous high-redshift quasars (e.g., Fan et al., 2016c; Duras et al., 2017). The scattered flux may therefore be contributed by X-rays from powerful star-forming regions such as are found in local galaxies (Ranalli et al., 2003). If we

assume $SFR = 2000 - 3000\ M_{\odot}\, yr^{-1}$, we can estimate the expected 2-10 keV luminosity using the Ranalli et al. (2003) relation (updated by Kennicutt and Evans, 2012) and obtain $L^{SF}_{2-10} \approx 1.2 \times 10^{43}$ erg s^{-1} , which is ∼10% of the estimated scattered flux (Table 5.1). This does not significantly account for the soft excess, especially for the BNSphere model, whose estimated column density depends very little on f_{sc} (see Figure 5.3). Therefore the BNSphere model is not an adequate parametrization for the obscurer. This would imply either a patchy 4π obscurer with different properties from the more local sources (in terms of geometry, covering factor, and line-of-sight $N_{\rm H}$) or a more standard torus-like geometry. Alternatively, it would require a different soft X-ray contributor than is normally invoked for a more local source.

Other possible contributors to this emission are photoionized gas, which is typically observed in local AGN (Bianchi et al., 2006; Guainazzi and Bianchi, 2007), or galaxy-scale collisionally ionized halos, which are usually observed in local ultraluminous galaxies (Teng and Veilleux, 2010; Jia et al., 2012; Veilleux et al., 2014; Feruglio et al., 2015; Teng et al., 2015). Based on f_{sc} for local low-luminosity AGN, photoionized gas can account for the soft excess. However, this would require a photoionized gas phase emitting with a luminosity on the order of 10^{44} erg s^{-1} , which is a factor of five to one order of magnitude higher than any scattered or photoionized gas phase ever measured in local luminous quasars in the X-rays (Piconcelli et al., 2008; Tazaki et al., 2013; LaMassa et al., 2016). The recent stacking analysis carried out on high-z EQR by Goulding et al. (2018) reported a similarly high (10^{44} erg s^{-1}) scattered component. They used the same MYTor model as we did, with same assumptions on Γ and torus inclination angle. In order to understand whether these luminous scattered components are indeed associated with photoionized gas, a spectrum with a much higher signal-to-noise ratio is needed, hence it is not possible to make such a strong claim. However, there are indications that the photoionized [OIII]-emitting gas that is usually associated with the X-ray emitting gas tends to be lacking or weak in a large fraction (40-70%) of luminous AGN (Netzer et al., 2004; Shen and Ho, 2014; Vietri et al., 2018) and is generally more compact than suggested from low-luminosity AGN (Netzer et al., 2004; Bischetti et al., 2017). This has been interpreted as some kind of departure from the phenomenology reported for less luminous sources (Netzer et al., 2004) and may indicate that the photoionized gas origin is unlikely.

We also evaluated the possibility that the soft-excess emission is due to a collisionally ionized plasma halo. The presence of the ionized Fe line, if confirmed at higher significance than what has been found in P15, may be indicative of high-temperature plasma. If we use a thermal model (APEC in XSPEC) to parameterize the soft excess, we indeed estimate a plasma temperature of $kT \approx 4$ keV. Together with the high luminosity of the

soft excess, this may indicate intracluster-medium emission. This result may be tantalizing as hot DOGs have been claimed to be located in overdense galaxy regions (Jones et al., 2014). However, several caveats prevent us from making such a bold claim. The temperature may be driven by the presence of the low-significance putative ionized Fe line reported in P15, whose origin cannot be determined with the current data. Furthermore, as a first-order approximation, the cutoff of the thermal emission and the presence of L-shell Fe lines (a strong temperature indicator for < 2 keV plasma) cannot be determined for energies lower than $\sim$2 keV (as we cannot probe rest-frame energies much lower than this value). This means that our data are insensitive to lower temperatures, and we are not able to fully evaluate the parameter space down to lower temperatures.

5.5.3 Nature of W1835

Recently, Farrah et al. (2017) performed a morphological analysis on *HST/WFC3* images of a sample of $z = 2 - 3$ hot DOGs including W1835 in the optical rest-frame band (B band). They found W1835 to have an irregular light profile with no clear close companions. They employed several morphological indicators to quantify its appearance. They found that compared to all the other systems in their sample, the source is less likely to be in a clear merger state according to the boundaries in light concentration, asymmetry, and variance of the brightest 20% of the galaxy light (Conselice et al., 2003; Lotz et al., 2004, 2008). It is therefore possible that either the system is in a non-merger state or in an advanced merger state, showing a common envelope surrounding an unresolved sub-kiloparsec scale nuclear region. Farrah et al. (2017) concluded that there is no need to invoke a preferential link of hot DOGs with mergers, rather ascribing their phenomenology to brief and luminous nuclear accretion episodes in the evolutionary history of a massive star-forming $z \sim 2$ galaxy. A similar analysis carried on by Fan et al. (2016a) instead concluded on a different sample (with very little overlap and including W1835) that hot DOGs are likely a transitional obscured phase in the merger-driven evolutionary QSO formation sequence, leading to the unobscured quasar phase. Interestingly, Ricci et al. (2017b) found from analyzing the X-ray spectra of a sample of luminous and ultra-luminous infrared galaxies in different merging stages that CT AGN that are preferentially hosted in late-stage mergers, with the maximum obscuration reached when the galaxies have projected distances of 0.4-10.8 kpc. In the context of a merger-induced obscuration scenario, W1835 would therefore be interpreted as late-stage merger in which the nucleus is being obscured by infalling matter as a consequence of the loss of angular momentum of the ISM due to the merger phenomenon. However, unless there is a non-AGN-related prominent soft-excess contributor in our X-ray spectrum (i.e. photoionized or collisionally ionized copious amounts of gas), the obscuration

cannot be ascribed to an homogeneous 4π obscurer that completely enshrouds the nucleus, as implied by quasar-induced merger formation scenarios, because the scattered fraction for the spherical obscurer is too high compared to what is typically observed in AGN.

5.6 Conclusions

We presented a $\sim$ 155 ks *NuSTAR* observation of the hot DOG W1835. The source was detected with a significance of 3.3σ. We extracted *NuSTAR* spectra and jointly modeled them with the *XMM-Newton* spectra that were previously presented in P15. We used both phenomenological and physically motivated models. The latter includes an appropriate treatment of the Compton scattering and accounts for the geometry of the obscurer. We explored two scenarios: 1) an edge-on torus, and 2) a sphere isotropically covering the nucleus. We find that

- in all cases, a nearly CT ($\log[N_{\rm H}/{\rm cm}^{-2}] \sim 24$) to heavy CT ($\log[N_{\rm H}/{\rm cm}^{-2}] \gg 24$) obscuration is required. This makes W1835 the first and most obscured $z > 2$ AGN detected by *NuSTAR* so far;
- W1835 is very luminous and is a Compton-thick quasar, as indicated by the derived unobscured X-ray luminosity $L_{2-10} \approx 1 - 3 \times 10^{45}$ erg s^{-1}($L_{10-40} \approx 0.5 - 2 \times 10^{45}$ erg s^{-1});
- a soft excess at low energies (< 2 keV), which may amount to 5-15% of the emission of the primary continuum is also necessary. The uniform spherical model is disfavored because the soft excesses it produces is too high (i.e. $> 10\%$), unless a patchy obscurer distribution and/or an uncommon and powerful ($\sim 10^{44}$ erg s^{-1}) non-AGN-related component is invoked.

We further investigated W1835 by performing optical-to-FIR SED modeling with a clumpy two-phase dusty toroidal model accounting for the MIR reprocessed AGN primary emission with the addition of a modified blackbody to model the FIR dust emission primarily heated by stellar processes. In order to be as consistent as possible with the X-ray analysis, we employed similar toroidal and spherical geometrical configurations for the MIR emitter. We found that

- the source is hyper-luminous with a bolometric luminosity of $L_{\rm bol} \approx 3 - 5 \times 10^{47}$ erg s^{-1};

- the bolometric correction at 2-10 keV (10-40 keV) is on the order of ~ 300 ($\sim$500) and is consistent with those estimated in hyper-luminous type 1 AGN;
- it exhibits a powerful starburst with derived SFRs on the order of $\sim$3000 $M_{\odot} yr^{-1}$;
- the ratio of X-rays to MIR is higher than the average value for the hot DOGs and is consistent within the uncertainties and accounting for all the modelings with those inferred in type 1 hyper-luminous AGN at the same cosmic epoch.

Considering the heavy obscuration, the luminosity, the ratio of X-rays to MIR, the SFR, and its *HST* mildly disturbed morphology, this hot DOG can be interpreted as a late-stage merger in the context of the merger-induced quasar formation scenario. It exhibits relatively high values of soft excess, which, if confirmed, may indicate large reservoirs of photoionized or collisionally ionized gas.

Future deep imaging observations of W1835 at higher spatial/spectral resolution both in X-ray (i.e. *Chandra* and *ATHENA*) and at sub-millimeter wavelengths (*NOEMA*) may enable us to further shed light on the nature of W1835.

The work presented in this Chapter has been published in the following paper:
L. Zappacosta, E.Piconcelli, **F. Duras**, C.Vignali, R.Valiante, S.Bianchi, A.Bongiorno, F.Fiore, C.Feruglio, G.Lanzuisi, R.Maiolino, S.Mathur, G.Miniutti, C.Ricci. **2018A&A...618A..28Z**
The hyper-luminous Compton-thick $z \sim 2$ quasar nucleus of the hot DOG W1835+4355 observed by NuSTAR

CHAPTER 6

A universal X-ray bolometric correction for AGN: extending the $Kbol$ over 7 luminosity decades

This Chapter is devoted to the analysis of a low-luminosity sample extracted from the SWIFT/BAT 70-month catalog, which shows complementary features if compared to the hyper-luminous WISSH sample presented in Chapter 4. By combining the two samples, which lie at the extreme of the AGN luminosity function, it is possible to build up a new bolometric correction valid over the widest range of luminosity ever.

6.1 Introduction

To properly study AGN in a wide scenario and the eventual correlations with their host galaxies (whose existence is now well established at least in the local Universe, see e.g., Magorrian et al., 1998; Marconi and Hunt, 2003; Tremaine et al., 2002), an accurate knowledge of their internal mechanism and of their physical properties is mandatory. A fundamental question is how AGN produce the energy we detect as radiation, and given their broad-band nature, a multi-wavelength approach is binding to understand the physics hidden behind their emission. As a result, the bolometric luminosity, which is the integrated area under the full SED of the AGN, becomes one of the key parameters to know with as much high accuracy as possible. However, the characterization of the bolometric luminosity is a challenging issue for several reasons: first of all, we need to take into account the contamination from the host galaxy to the nuclear emission, which

adds a source of uncertainty to the calculations of the AGN bolometric luminosity. In addition, considering that the emission in different bands originates in different physical structures (a dusty parsec-scale torus in the infrared, kiloparsec-scale relativistic jets in the radio, a sub-parsec accretion disk in the UV-optical), different spectral regions are variable on different timescales. As a further problem, one should also consider the anisotropy of the AGN emission, which may depend on wavelength and which may be different from one source to another. Finally, given the multi-wavelength feature of the AGN emission, observations from different telescopes are necessary in order to build up a complete SED. What can be measured is usually a monochromatic luminosity, L_λ. For this reason, in the last decades several attempts have been made to accurately study the shape of AGN SED. Some authors have investigated the evolution of the α_{OX} index, defined as the ratio between the optical and the X-ray luminosity (see e.g., Kelly et al., 2008; Vasudevan et al., 2009; Lusso et al., 2010; Marchese et al., 2012) which should provide a hint about the nature of the energy generation mechanism in AGN. Others have focused on the characterization of a reliable bolometric correction $K_{BOL}(L_{band})$, which is defined as the ratio between the bolometric luminosity and the luminosity in a given band, (L_{BOL}/L_{band}). In their latest work, Lusso and Risaliti (2017) confirmed the existence of a non-linear relation between the X-ray and the UV/optical emission in AGN. On the contrary, the bolometric correction in the UV/optical bands seems to be constant with respect to the AGN bolometric luminosity.

Nevertheless, the bolometric luminosity and the deriving bolometric parameters (e.g., the K_{BOL} and the α_{OX} above mentioned), play an important role in a large number of theoretical models on AGN accretion and growth (see the works by Volonteri et al., 2003; Vittorini et al., 2005), starting from the outstanding argument by Soltan (1982) who demonstrated that the total mass density of SMBHs in the local universe could be inferred from counts of AGN. About this topic, both Shankar et al. (2004) Marconi et al. (2004) found that the mass function of local SMBHs can be well matched with the one expected from accreting AGN, if appropriate parameters (i.e. accretion efficiencies and Eddington ratios) are chosen.

Elvis et al. (1994) have estimated the bolometric corrections using a Mean Energy Distribution for a sample of 47 AGN, including the IR emission in the bolometric luminosity and therefore counting part of the emission twice. Both Marconi et al. (2004) and Hopkins et al. (2007) derived an estimate of the bolometric corrections in different bands (optical B-band, soft and hard X-ray in the first work, also in the IR at $15\mu m$ in the second one). Vasudevan and Fabian (2007) studied a sample of 54 X-ray bright ($L_X > 10^{43}$ erg s^{-1}) AGN, pointing out that particular classes of sources (as Radio-loud, X-ray weak or Narrow Line Seyferts 1) might have different bolometric correction relations if compared with the rest of the AGN population. Lusso et al. (2012) analyzed a sample of about 900 X-ray selected AGN deriving the bolometric corrections in the same bands as

Marconi, separately for type 1 and type 2 sources valid for approximately three orders of luminosity. Runnoe et al. (2012a) sampled the optical band giving the bolometric corrections at three different wavelengths (1450 Å, 3500 Å and 4000 Å), while IR bolometric corrections are provided in Runnoe et al. (2012b). More recently Krawczyk et al. (2013) focused on the characterization of the bolometric corrections of luminous broad-line AGN in a wide range of redshift ($0 < z < 6$).
All these works, although giving robust estimation of the bolometric corrections in different bands of the AGN emission, suffer from two fundamental points: the narrow range of luminosity sampled and the focus on luminous, unobscured sources (exception given to the sample by Lusso et al. 2012), whose bolometric luminosity is much more easily predictable, being their SED less affected by obscuration than type 2 sources' one.
According to these points, in this Chapter we focus on the characterization of the hard X-ray (2-10 keV) bolometric correction, which gives information about the fraction of emission coming from the accretion disk and scattered into the X-ray regime, and which becomes of fundamental importance for understanding the physics behind accretion. We aim at building up a hard X-ray bolometric correction valid using two samples of AGN (both type 1 and type 2 sources) with complementary properties which populate the two extremes of the AGN luminosity function, being the perfect collection to obtain a bolometric correction over the widest range sampled so far.

The Chapter is organized as follows: in Section 6.2 we present the data sample, while the Section 6.2.2 provides a detailed explanation of the method we used to disentangle the emission components of the low-luminosity sample. The results of the SED-fitting procedure are shown in Section 6.2.3, where we report bolometric luminosities, star formation rate and stellar masses of the sources. In Section 6.3 we go through the characterization of a new hard X-ray bolometric correction, presenting the result for the type 1 and the type 2 sample separately, and then a universal relation for the whole population. Finally, Section 6.4 presents the conclusions of the work.

6.2 The data sample

The analysis is based on two samples selected to cover the opposite extremes of the AGN luminosity function.
The first one (named SWIFT sample later on in the text) consists of a collection of 21 type 1 (2×10^{41} erg/s $< L_{2-10} < 8 \times 10^{45}$ erg/s) and 27 type 2 (3×10^{40} erg/s $< L_{2-10} < 3 \times 10^{44}$ erg/s) AGN at $z < 0.16$, randomly (see Onori et al., 2017a) extracted from the Swift/BAT 70-month catalogue, which is considered one of the most complete hard X-ray surveys containing about 1200 hard X-ray objects in the 14-195 keV band, of which

about 700 are classified as AGN sources (Baumgartner et al., 2013).
The SWIFT type 2 AGN[1] belong to an original sample of 41 AGN, for which our group obtained near-infrared spectroscopic observations using ISAAC and X-Shooter at VLT, and LUCI at LBT (Onori et al., 2017a). 6 additional sources with data from literature have been added in a second time. Among this total sample, a fraction of ∼30%, after deep NIR spectroscopy, showed faint broad emission lines that allowed to estimate their BH masses (see Onori et al., 2017b) using the BH mass virial estimator calibrated by Ricci et al. (2017d).
The SWIFT type 1 AGN belong to a control sample of 33 sources already presented in Onori et al. (2017b) included in the Swift/BAT 70-month catalogue, whose BH masses have been measured via reverberation mapping techniques, and for which reliable bulge classification is available (Ho and Kim, 2014)[2]. Both the local type 1 and the type 2 sources are randomly distributed in redshift and luminosity and can be considered as representative of the AGN populations of the entire Swift/BAT sample. In order to estimate the bolometric luminosity of the SWIFT AGN sample, a multi-wavelength photometric data-set has been collected, as better explained in the next section. Due to the lack of accurate photometric coverage, 20 type 2 sources out of 47, and 12 type 1 sources out of 33, were excluded from our analysis, thus the local sample of SWIFT AGN comprises 27 type 2 and 21 type 1 AGN.
The AGN sources of the second sample belong to the WIse Selected Hyperluminous quasars sample (WISSH sample, see Bischetti et al., 2017), composed of 87 hyperluminous ($L_{BOL} > 2 \times 10^{47}$ erg/s) type 1 AGN in the redshift range $2 < z < 4$, detected in the mid-IR by the WISE satellite. In this work we focused on a sub-sample of 35 WISSH AGN detected by XMM/Chandra (X-WISSH in the following) and whose X-ray properties have been studied by Martocchia et al. (2017, hereafter M17). For all of them, as explained in Chapter 4, a wide photometric coverage (from the X-ray to the MIR) is available.

In our analysis we have also included the XMM-COSMOS sample studied by Lusso et al. (2012, hereafter L12), composed of 380 type 1 and 540 type 2 sources in the redshift range $0.1 < z < 4$ with average hard X-ray luminosity of 10^{44} erg/s.

In Figure 6.1 the luminosity-redshift distribution of our total sample is shown.

[1] with type 2 AGN we are referring to those AGN where there is no (Seyfert 2) or weak (intermediate $1.8 - 1.9$) evidence of broad line region, or even no lines at all, in their optical spectra.
[2] This sample has been adopted by Ricci et al. (2017d) to calibrate a virial BH mass estimator that can be used to measure BH masses of low-luminosity and also obscured AGN.

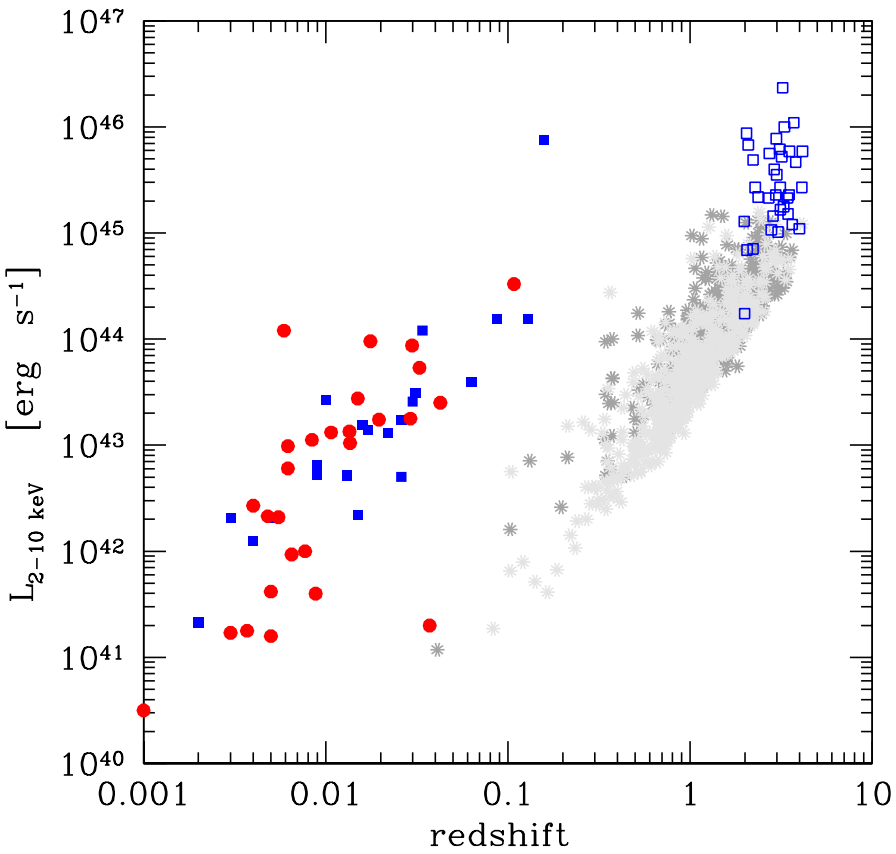

FIGURE 6.1: Intrinsic X-ray luminosity in the 2-10 keV band versus redshift of the low luminosity type 1 (blue filled squares) and type 2 (red filled circles) sample, the high-luminosity WISSH sample (blue open squares) and the COSMOS type 1 (grey) and type 2 (lightgrey) AGN.

6.2.1 Multi-wavelength data of the SWIFT sample

To study the SED of the SWIFT AGN sample, we have collected photometric data from public catalogues.

In order to build an homogeneous photometric data-set at the whole redshift range covered by this work, we have considered only those data whose photometric aperture was representative of the flux of the whole galaxy.

As an example, we report in Figure 6.2 an image of the source Mrk 348 with five photometric apertures showed in different colors.

We have collected photometric data for a total of 36 magnitudes, using both the NED database [3] and other public catalogs: far and near UV data are from GALEX observations (Gil de Paz et al. (2007)); U, B, V, R and I bands are taken from the atlas of galaxies by de Vaucouleurs et al. (1991) or from the SDSS DR12 [4]; the near-IR J,H and

[3] https://ned.ipac.caltech.edu/
[4] https://www.sdss.org/dr12/

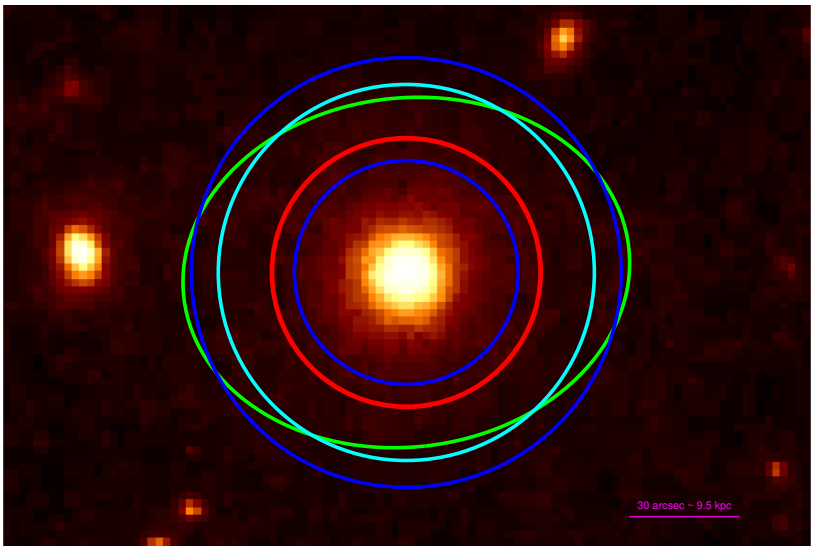

FIGURE 6.2: Optical image in the r-band of the source Mrk 348. North up, East left. The circles end ellipse show the apertures of the photometric bands in the different regions of the spectrum (UV bands in cyan, optical in blue, NIR in green and FIR in red). Magenta line represents 30 arcsec ($\sim$ 9.5 kpc)

K bands from 2MASS [5]; data at 3 μm, 4.5 μm, 12 μm and 22 μm are from WISE; data at 12 μm, 25 μm, 60 μm and 100 μm are from IRAS and from the IRAS Revised Bright Galaxy Sample by Sanders et al. (2003); data at 120 μm, 150 μm, 170 μm, 180 μm and 200 μm are from ISOPHOT (Spinoglio et al., 2002); finally, FIR data at 250 μm, 350 μm and 500 μm are from Herschel (Shimizu et al., 2016) or BLAST (Wiebe et al., 2009).

6.2.2 SED-fitting

The SED fitting procedure of the X-WISSH and the SWIFT samples (an example of which is shown in Figure 6.3 and in Figure 6.4 respectively) has been carried out using a modified version of the code described in Duras et al. (2017) (hereafter D17) and also adopted in the previous Chapters. As usual, the method is based on the model according to which the overall observed SED of each source is the result of the combination of different components produced by both the nuclear engine and the stellar light (e.g., Bongiorno et al., 2012; Berta et al., 2016; Calistro Rivera et al., 2016). The nuclear emission produces two bumps in the UV and NIR regimes which create a dip at around 1μm (Sanders et al., 1989; Elvis et al., 1994; Richards et al., 2006). The UV bump is due to thermal emission from the accretion disc (Czerny and Elvis, 1987), while the NIR bump is due to the intrinsic primary radiation absorbed by hot dusty clouds in the torus that is subsequently re-emitted at longer wavelengths. In the same way, the stellar light produces both a direct UV/optical emission (mainly due to hot stars) and a MIR-FIR

[5] https://irsa.ipac.caltech.edu/Missions/2mass.html

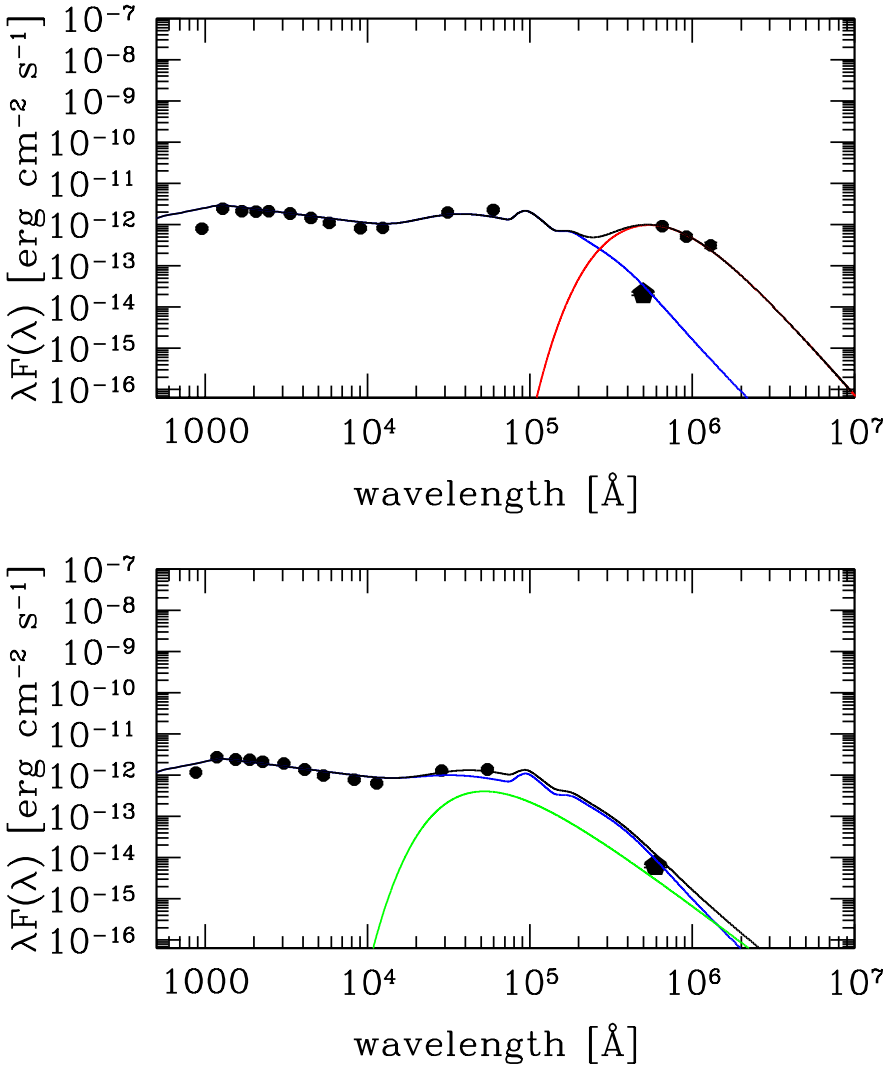

FIGURE 6.3: Example of SED fitting results for two sources (SDSSJ 1215 in the upper panel and SDSS J0947 in the lower panel) of the X-WISSH sample. Black circles are the photometric points of the sources. The virtual AGN pivotal photometric point at 50 μm, derived from the hard X-ray data, is shown as black pentagon (see text for details). In blue the AGN emission component is shown, green and red are the warm and the cold dust emission component respectively. Black line describes the total best-fit model.

component (caused by its reprocessing by the cold dust located on galactic scales). How much these two components contribute to the global SED depends on a number of factors, the most important ones being their relative luminosity and the level of obscuration affecting each of them.

In D17 the fit was performed with three emission components:

1. the accretion disk plus torus emission; (with a combination of the models by Feltre et al. 2012 and Stalevski et al., 2016)

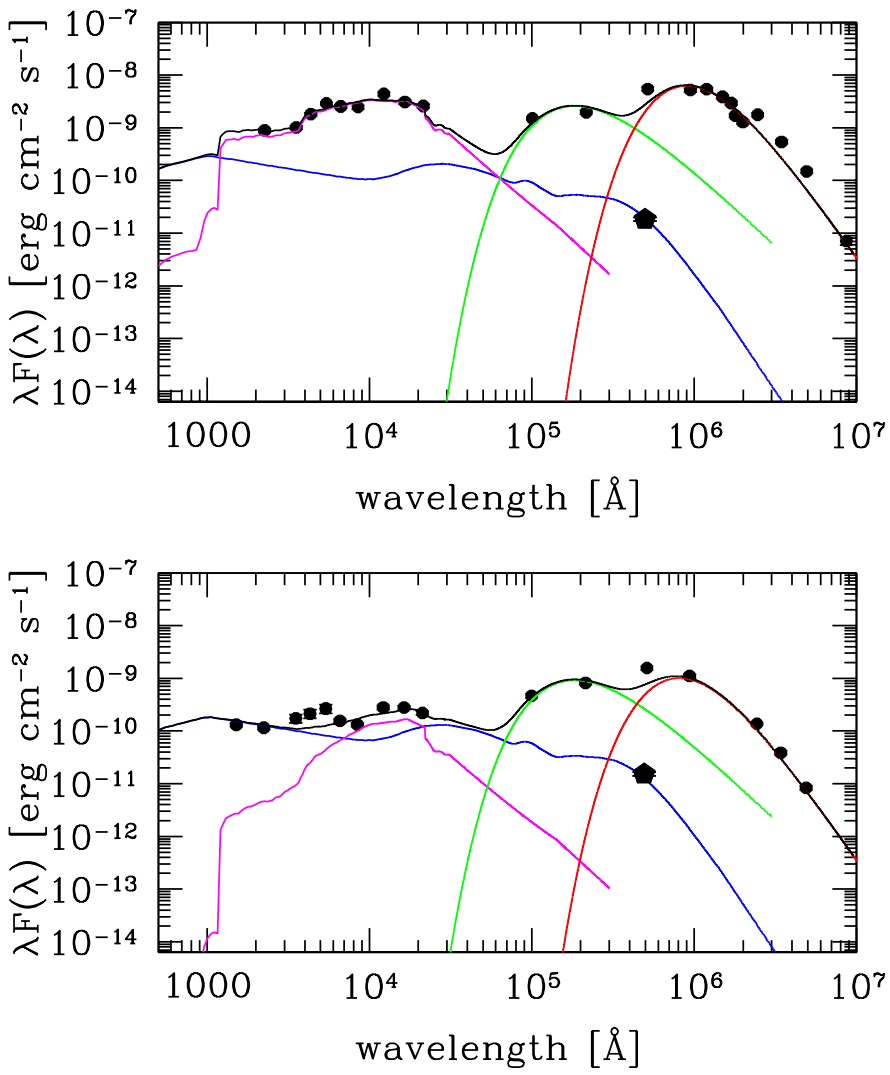

FIGURE 6.4: Example of SED fitting results for one type 2 (NGC1365, upper panel) and one type 1 (NGC7469, lower panel) SWIFT AGN. Points and lines as in the previous Figure 6.3. The galaxy emission component, not present in the X-WISSH modelling, is shown as magenta solid line.

2. the cold dust emission connected to the galactic star formation activity (modelled as a modified blackbody);

3. an additional component in the MIR, representing warmer dust in the vicinity of the nucleus (described by a simple blackbody).

For the present work we made two main changes with respect to D17: (a) we added an additional component, i.e. the UV-optical stellar emission from the host galaxy; (b) the optical-to-MIR AGN SED has been modelled by using the hard X-ray normalized templates by Silva et al. (2004).

(a) The galaxy emission component was not included in D17 for the study of type 1 WISSH AGN because for such bright unobscured sources the UV galactic light is completely over-shined by the AGN emission. For this work, dealing also with a sample of AGN at lower luminosities, we added a galaxy component to the three emission components already present in D17. The galaxy emission is produced by the integrated light of diverse stellar populations characterized by distinct star formation histories (SFHs). We have generated a library of synthetic spectra, using the models of stellar population synthesis of Bruzual and Charlot (2003). We have assumed a Chabrier (2003) initial mass function, building 10 declining SFHs as a function of the e-folding time and the age of the galaxy (see e.g., Bongiorno et al., 2012). For all the galactic templates we have taken into account the effect of dust extinction inside the galaxy itself, choosing as reddening curve the Calzetti's law (Calzetti et al., 2000). The final library of galaxy templates used consists of about 900 templates with extinction in the range $0 \leq \mathrm{E(B-V)} \leq 0.5$.

(b) In type 1 unobscured sources, the AGN component dominates in the optical and in the IR bands if compared with the host galaxy emission; on the other hand, in type 2 obscured AGN, the SED is characterized by an optical continuum dominated by the host galaxy emission while the AGN component is mainly relevant at IR wavelengths. To reproduce also the emission from type 2 AGN we have used the hard X-ray normalized AGN SEDs by Silva et al. (2004) which are derived from a sample of 33 Seyfert galaxies with no sign of non-stellar nuclear emission or properly corrected for any galaxy nuclear contribution, and are available in four intervals of X-ray absorption: $N_H < 10^{22} cm^{-2}$ for Seyfert 1 (Sy1), $10^{22} < N_H < 10^{23} cm^{-2}$, $10^{23} < N_H < 10^{24} cm^{-2}$ and $N_H > 10^{24} cm^{-2}$ for Seyfert 2 sources (Sy2). Indeed, these SEDs are able to properly provide the AGN optical-to-MIR component once good quality X-ray data (corrected for absorption, see Ricci et al., 2017c), as in our case, are available. As shown by Silva et al. (2004), all the AGN X-ray normalized SEDs can be considered quite identical above $40\mu m$ (see Figure 6.5). It was therefore possible, using the hard X-ray data, to compute a virtual pivotal photometric point at $50\mu m$, to be fitted only by the AGN templates (see Figure 6.4). To better reproduce the spectral emission of either very luminous type 1, we enriched the AGN library with all the models by Stalevski et al. (2016) used in D17.
Summarizing, our emission model (f_{model}) includes four emission components:

$$f_{model} = Af_{AGN} + Bf_{GAL} + Cf_{CD} + Df_{ME}, \tag{6.1}$$

where f_{AGN} represents the emission coming from the active nucleus, both direct and reprocessed by the dusty torus, f_{GAL} is the emission from the galactic stars, f_{CD} accounts for the FIR emission due to the reprocessed flux by cold dust and is modelled as a modified

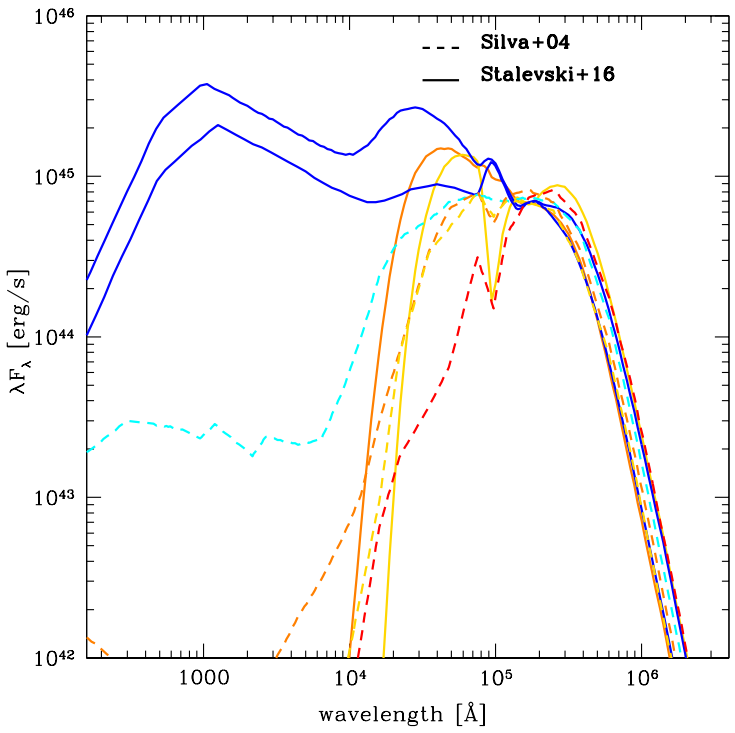

FIGURE 6.5: Examples of UV-to-IR AGN templates from Silva et al. (2004) and Stalevski et al. (2016). Models at different level of absorption are shown from blue (least absorbed one) to red (most absorbed one).

blackbody, f_{ME} is any eventual excess MIR component, modelled as a simple blackbody. Finally, A, B, C and D are the relative normalizations. The fitting procedure, through a χ^2 minimization, allows us to determine the combination of templates that best describes the observed SED and their relative contribution.

6.2.3 SED results

Based on the final SED best-fit models, we derived the main physical parameters of the host and the AGN for both the X-WISSH and the SWIFT samples.

X-WISSH derived physical parameters

The intrinsic AGN bolometric luminosity of the type 1 X-WISSH AGN (reported in Table 6.1) has been derived by integrating the AGN emission component in the range 60 Å - 1 μm. We neglected the IR emission in order to not count twice the UV/optical photons reprocessed by the dust. The values of the bolometric luminosity published in D17 for the 9 X-WISSH sources with *Herschel* coverage are in perfect agreement (within 5%) with those obtained with the modified version of the SED-fitting code, i.e., with the inclusion of the X-ray photometric information.
For the values of the SFR for the same sources we refer the reader to Table 6 in D17.

SWIFT derived physical parameters

Following Bongiorno et al. (2012), the total stellar mass of the SWIFT sample was derived by assuming a Chabrier (2003) IMF, and it is the result of a unique combination of the best-fit age and e-folding time of the galaxy (the obtained values are shown in Table 6.2).
Concerning the SFR, as the UV/optical bands are subject to large uncertainties due to either absorption, or poor photometric coverage, we decided to rely on the FIR-based measurements. We computed the SFR by using the relation by Kennicutt (1998), scaled to a Chabrier IMF. In those cases for which a reasonable FIR photometry is not available, the value of the SFR (always reported in Table 6.2) is not provided.

The intrinsic AGN bolometric luminosity of the sources of the SWIFT sample has been derived using two different estimation methods for the type 1 and type 2 samples. The bolometric luminosity of the type 1 sources has been computed, as for the X-WISSH, by integrating the AGN emission component in the range 60 Å - 1 μm. On the other hand, for type 2 sources, where the total SED emission in the UV/optical bands is affected by severe presence of the host galaxy, as pointed out by Pozzi et al. (2007) the bolometric luminosity can be estimated from the IR luminosity, by integrating the AGN template in the range 1 μm - 1000 μm and simply rescaling the result for the factor 1.7. We have verified that, applying this method to the type 1 sources, the resulting bolometric luminosities are consistent (within 8%) with the ones obtained by the integration of the

UV-to-NIR AGN emission. It is worth noting that the factor 1.7 found by Pozzi et al. (2007) accounts for two separate correction factors, taking into account either the geometry of the torus or its orientation. The first correction (~ 1.5) is related to the covering factor f (a key parameter in the description of the torus models and which represents the fraction of the primary optical-UV radiation intercepted by the torus itself); the second correction (in the range 1.8-2.0) is due to the anisotropy of the IR emission which is function of the viewing angle.

Also the values of the bolometric luminosity for the SWIFT sample are reported in Table 6.2.

Table 6.1: Properties of the X-WISSH sample.

Name (1)	z (2)	$\log L_{2-10}$ (3)	$\log L_{BOL}$ (4)	$\log(M_{BH}/M_{\odot})$ (5)
J0045+1438	1.992	44.24	47.38	-
J0209-0005	2.856	45.16	47.62	-
J0735+2659	1.982	45.11	47.65	-
J0745+4734	3.225 *	46.37	48.01	10.19
J0747+2739	4.11	45.43	47.44	-
J0801+5210	3.263 *	45.25	47.84	9.79
J0900+4215	3.294 *	46.00	47.93	9.32
J0904+1309	2.974	45.89	47.78	-
J0947+1421	3.040	45.01	47.67	-
J1014+4300	3.126	45.43	47.85	-
J1027+3543	3.112	45.79	48.00	-
J1057+4555	4.140	45.77	47.91	-
J1106+6400	2.220 *	45.69	47.78	10.00
J1110+4831	2.957	45.36	47.81	-
J1111+1336	3.492 *	45.36	47.69	9.93
J1159+1337	3.984	45.04	47.74	-
J1200+3126	2.993	45.55	47.84	-
J1201+1206	3.512 *	45.77	47.77	9.50
J1215-0034	2.707	45.33	47.62	-
J1236+6554	3.424 *	45.33	47.65	9.63
J1245+0105	2.798	45.03	47.25	-
J1249-0159	3.638	45.08	47.55	-
J1250+2631	2.044	45.94	47.91	-
J1328+5818	3.133	45.22	47.20	-
J1333+1649	2.089	45.83	47.73	-
J1421+4633	3.454 *	45.18	47.65	9.79
J1426+6025	3.189	45.72	48.07	-
J1441+0454	2.059	44.84	47.34	-
J1513+0855	2.897	45.60	47.67	-
J1521+5205	2.218 *	44.85	47.91	9.99
J1549+1245	2.365 *	45.34	47.81	10.10
J1621-0042	3.710	46.04	47.81	-
J1639+2824	3.801	45.67	48.05	-
J1701+6412	2.727	45.75	48.01	-
J2123-0050	2.281 *	45.43	47.72	9.63

(1) Source name; (2) redshift from SDSS or from Vietri et al. (2018) (marked with an asterisk); (3) intrinsic hard X-ray luminosity (2-10 keV) from Martocchia et al. (2017); (4) SED-fitting derived bolometric luminosity; (5) BH mass from Vietri et al. (2018).

TABLE 6.2: Properties of the SWIFT/BAT type 2 and type 1 sources: name and coordinates, redshift, intrinsic X-ray luminosity in 2-10 keV band as from Ricci et al. (2017c), bolometric luminosity, Black Hole mass, Stellar mass and Star Formation Rate

Name	z	$\log L_{2-10\ keV}$	$\log L_{BOL}$	$\log(M_{BH}/M_{\odot})$	$M_{\star}$	log(SFR)
(1)	(2)	(3)	(4)	(5)	(6)	(7)
			Type 2 sources			
ESO 234-G -050	0.0088	41.60	42.92	6.00	9.59	-0.72
MCG -01-24-12	0.0196	43.24	44.13	7.16	10.10	-0.32
Mrk 1210	0.0135	43.13	44.02	6.78	10.00	-1.29
NGC 1052	0.005	41.62	42.51	6.63	10.61	-1.52
NGC 1365	0.0055	42.32	43.67	6.65	10.78	1.11
NGC 2992	0.0077	42.00	42.70	6.72	10.33	0.31
NGC 4395	0.0013	40.50	41.38	5.14	7.53	-1.51
NGC 6221	0.0050	41.20	42.59	6.46	10.46	0.78
NGC 7314	0.0048	42.33	43.21	6.24	10.19	-0.07
IRAS F 05189-2524	0.0426	43.40	45.21	7.45	10.60	1.57
Mrk 348	0.0150	43.44	44.19	7.23	9.71	-0.25
NGC 1275	0.0176	43.98	44.69	7.46	10.69	0.45
NGC 7465	0.0065	41.97	43.36	6.54	9.93	-0.11
NGC 5506	0.0062	42.99	44.10	6.86	9.65	-0.15
2MASX J07595347+2323241	0.0292	43.25	43.90	7.78	10.71	0.91
3C403	0.0059	44.08	44.73	-	11.24	-
Mrk417	0.0327	43.73	44.61	-	10.21	-1.15

NGC3079	0.0372	41.30	42.70	-	12.18	2.67
NGC4138	0.003	41.23	42.44	-	9.84	-0.51
NGC4388	0.0084	43.05	43.93	-	10.77	0.42
ESO 005-G004	0.0062	42.78	43.90	-	10.41	0.05
NGC612	0.0298	43.94	44.71	-	11.07	0.92
NGC788	0.0136	43.02	43.71	-	10.91	-0.64
NGC3281	0.0107	43.12	44.18	-	10.98	0.01
PKS 0326-288	0.108	44.52	45.37	-	10.64	-
NGC4941	0.0037	41.25	42.14	-	9.85	-0.82
NGC5643	0.004	42.43	43.55	-	10.25	0.22
Type 1 sources						
3C 273	0.158	45.88	46.74	8.84	11.49	2.42
Mrk 79	0.022	43.11	44.18	7.92	9.72	0.27
Mrk 279	0.030	43.41	44.68	7.49	10.11	-1.05
Mrk 335	0.026	43.24	44.51	7.11	9.71	-0.30
Mrk 509	0.034	44.08	44.99	7.98	9.18	0.20
Mrk 590	0.026	42.70	43.76	7.50	10.90	0.43
Mrk 771	0.063	43.60	45.01	7.84	10.90	-
Mrk 817	0.031	43.49	44.60	7.80	10.34	-0.54
Mrk 876	0.129	44.19	45.34	8.34	12.00	-
Mrk 1383	0.087	44.19	45.42	9.21	10.36	-
NGC 3227	0.004	42.10	43.23	7.35	9.96	-0.08
NGC 3516	0.009	42.72	43.85	7.49	10.31	-2.14

NGC 3783	0.010	43.43	44.24	7.28	9.20	-0.07
NGC 4051	0.002	41.33	43.03	6.33	9.34	-0.43
NGC 4151	0.003	42.31	43.66	7.56	10.18	-0.72
NGC 4253	0.013	42.71	43.77	6.11	10.01	-0.70
NGC 4593	0.009	42.81	43.72	6.96	9.85	0.18
NGC 4748	0.015	42.34	43.72	6.48	10.57	-0.59
NGC 5548	0.017	43.14	44.21	7.77	10.58	-0.43
NGC 6814	0.005	42.31	43.64	7.20	10.36	-0.07
NGC 7469	0.016	43.19	44.42	7.32	10.79	1.27

(1) Source name; (2) redshift (Baumgartner et al., 2013); (3) intrinsic hard X-ray luminosity (2-10 keV) from Ricci et al. (2017c); (4) SED-fitting derived bolometric luminosity; (5) BH mass from Onori et al. (2017b) for the type 2 sources and from Ricci et al. (2017e) for the type 1 sources; (6) SED-fitting derived stellar mass; (7) SED-fitting derived SFR.

6.3 Hard X-ray bolometric correction as a function of the bolometric luminosity

The bolometric correction is by definition the ratio between the AGN bolometric luminosity and the luminosity computed in a specific band of the spectrum. It is a quantity of fundamental importance in astronomy, because it allows us to obtain an estimate of the AGN bolometric luminosity when a complete SED is not available. In this work we have studied the AGN hard (2-10 keV) X-ray bolometric correction as a function of the bolometric luminosity. The bolometric correction of the SWIFT sample has been computed by using the bolometric luminosity obtained from the SED fitting (see previous Section) and the intrinsic hard X-ray luminosity by Ricci et al. (2017c) reported in Table 6.2. The source 3C273 has been excluded from the analysis, being its emission affected by Doppler beaming (Punsly and Kharb, 2016). For the X-WISSH sample we used the X-ray luminosities presented in M17. We report in Table 6.1 the bolometric luminosities of the X-WISSH sample, computed following the method used for type 1 sources, as described in the previous Section and in D17. The typical uncertainty for the bolometric luminosity is around 10%, which turns into a 6-8% uncertainty for the bolometric correction.
Finally, for the COSMOS sample we used the data published in L12.

On the upper panel of Figure 6.6, we show K_{BOL} (2-10 keV) as a function of L_{BOL} for all the type 1 sources. Filled black squares represent the average of the bolometric correction computed in bolometric luminosity (not overlapping) bins. The light blue continuous line shows the relation found by L12 for their type 1 COSMOS sample, where the dotted line marks its extrapolation out of the range covered by their data. As clearly visible, the X-WISSH sample covers a range at high luminosities never studied before and, as already pointed out in M17, the data follow the extrapolation of L12 relation at high luminosities. On the contrary, the SWIFT sample data seem to favour a flatter or constant relation at $\log(L_{BOL}/L_{\odot}) < 11$. We have therefore fitted the whole type 1 sample, using a least-square method, with the following relation:

$$K_{BOL}(2-10\,keV) = a\left[1+\left(\frac{log(L_{BOL}/L_{\odot})}{b}\right)^{c}\right]. \tag{6.2}$$

The best-fit relation is shown in Figure 6.6 as a black continuous line and its best-fit parameters, along with the intrinsic spread of the data ($\simeq 0.27$ dex), are listed in Tab. 6.3. Our best-fit relation is almost identical to the L12 relation above $\log(L_{BOL}/L_{\odot}) >$

11, while at lower luminosities the bolometric correction remains constant with a value of K_{BOL} (2-10 keV) $\simeq$ 11.7.

On the lower panel of Figure 6.6, we show K_{BOL} (2-10 keV) as a function of L_{BOL} for the type 2 sources. Filled black circles represent the average of the bolometric correction computed in bolometric luminosity bins, as for the upper panel. The orange continuous line shows the relation found by L12 for their type 2 COSMOS sample, where the dotted line represents its extrapolation out of the range of their data. As expected, the type 2 sources allow to sample the region at the lowest luminosities of the K_{BOL} (2-10 keV) - L_{BOL} plane. The data confirm the trend, already observed at low luminosity for type 1 AGN, that in the range $7.5 < \log(L_{BOL}/L_{\odot}) < 11$ the bolometric correction has a constant value (L_{BOL} (2-10 keV) $\sim$ 12.6). On the contrary, we found that at $\log(L_{BOL}/L_{\odot})$ > 12.5 our solution is systematically higher than the one by L12. This might be due to the new functional form which allows a better representation of the data sample, and to the fact that in L12 the fitting procedure has been carried out on binned data. We list in Tab. 6.3 the values of the best-fit parameters along with the spread ($\sim$ 0.28 dex). The values of the spread for both the type 1 and the type 2 samples are quite similar and in good agreement with those found by L12 ($\sim$0.25 for both populations).

As it is possible to notice in the upper panel of Figure 6.6, where the average values of K_{BOL} (2-10 keV) type 2 sources (open black circles) are compared with those for type 1 sources (filled black squares), type 1 and type 2 AGN seem to share the same, general, bolometric correction relation. Moreover, as already mentioned above, the two samples have very similar values of the spread (0.27 and 0.28 dex). We have thus investigated whether a general bolometric correction relation, for both type 1 and type 2 sources, was consistent with the data. In Figure 6.7 we show the K_{BOL} (2-10 keV) as a function of L_{BOL} for the whole sample of type 1 and type 2 AGN. Black filled hexagons represent the average of the bolometric correction computed in bolometric luminosity bins for the whole sample. Our best fit relation is shown as a black line, while the two black dotted lines correspond to the 1 σ spread of the sample ($\sim$ 0.27 dex). We found that this general K_{BOL} (2-10 keV) relation can be considered statistically representative of the whole AGN population. Indeed, it is not rejected by the χ^2 test if applied on the type 1 and type 2 samples separately (P($>\chi^2$)=0.45 for both cases)[6]. This result was already pointed out by L12, who argued that the bolometric correction relation for the type 2 sources seems to be the natural extension at lower luminosities of the one for the type 1 sources. Thanks to the low and high luminosity samples used in this work, we have then

[6]In order to compute the χ^2-test, being the values of the spread very similar for the type 1, type 2 sources and whole sample, an average spread of $\sim$ 0.27 dex has been assumed.

TABLE 6.3: Best-fit parameters (see Equation 6.2) for the type 1, type 2 and for the general bolometric correction relation.

	a	b	c	spread
Type 1	12.11±0.14	12.05±0.02	17.56±0.12	0.27
Type 2	12.61±0.16	11.98±0.02	25.81±0.62	0.28
General	11.81±0.11	12.00±0.01	17.56±0.12	0.27

been able to derive a universal bolometric correction relation valid for the entire AGN population and over the widest (7 dex) luminosity range ever probed.

In Figure 6.7 the bolometric corrections by L12, for their COSMOS samples of type 1 and type 2 AGN, are shown as cyan and orange lines, respectively. Our result is in good agreement with these relations, if compared within the luminosity range of the COSMOS data used by L12 ($11 < \log(L_{BOL}/L_{\odot}) < 13$). On the contrary, as already found by L12, at $\log(L_{BOL}/L_{\odot}) \sim 11.5$ the Marconi et al. (2004, purple line) and Hopkins et al. (2007, magenta line) bolometric corrections are about 0.20-0.25 dex above ours; it is worth noting that Hopkins et al. (2007) included the IR contribution in the estimate of the bolometric luminosity, being interested in the characterization of an empirical bolometric correction.

The ratio between the bolometric luminosity and the X-ray luminosity (i.e. the K_{BOL}) can be seen as a comparison between the total radiation from the AGN and the relative contribution by the corona plus the accretion disk. The correlation we observe between the X-ray bolometric correction and the bolometric luminosity might support (as already noticed by M17) a scenario in which with the increasing of the bolometric luminosity of the source, the X-ray emitting corona tends to be less powerful, especially if compared to the UV/optical emission. This result seems to be in agreement with the observed "X-ray weakness" which affects the most luminous AGN (Sturm et al., 2011; Cicone et al., 2014) and could be in line with the findings of an anti-correlation between the α_{OX} and the optical luminosity (estimated at 2500 Å), as showed e.g. in the work by Lusso and Risaliti (2016). We have then computed the expected K_{BOL} (2-10 keV) if the relation between the X-ray luminosity and the optical luminosity by Lusso and Risaliti (2016) (in which $L_X \propto L_{UV}^{0.6}$) and a constant $K_{BOL}(4400\ \text{Å}) \sim 5$ (L12) are assumed[7]. As shown in Figure 6.7 as a brown line, the resulting analytical prediction, i.e. K_{BOL} (2-10 keV) $\propto \mathrm{L}_{BOL}^{0.358}$, is in fair agreement with our best-fit relation, sharing the same slope and normalization. This comparison tells us that the bolometric correction relation and the α_{OX} slope are tightly related: the observed correlations are mainly due to the change of the X-ray emission fraction in the bolometric luminosity budget. In this framework,

[7] $L_{4400\text{Å}}$ has been converted into $L_{UV} = L_{2500\text{Å}}$ by assuming a spectral slope of $\lambda^{-1.54}$ (Vanden Berk et al., 2001).

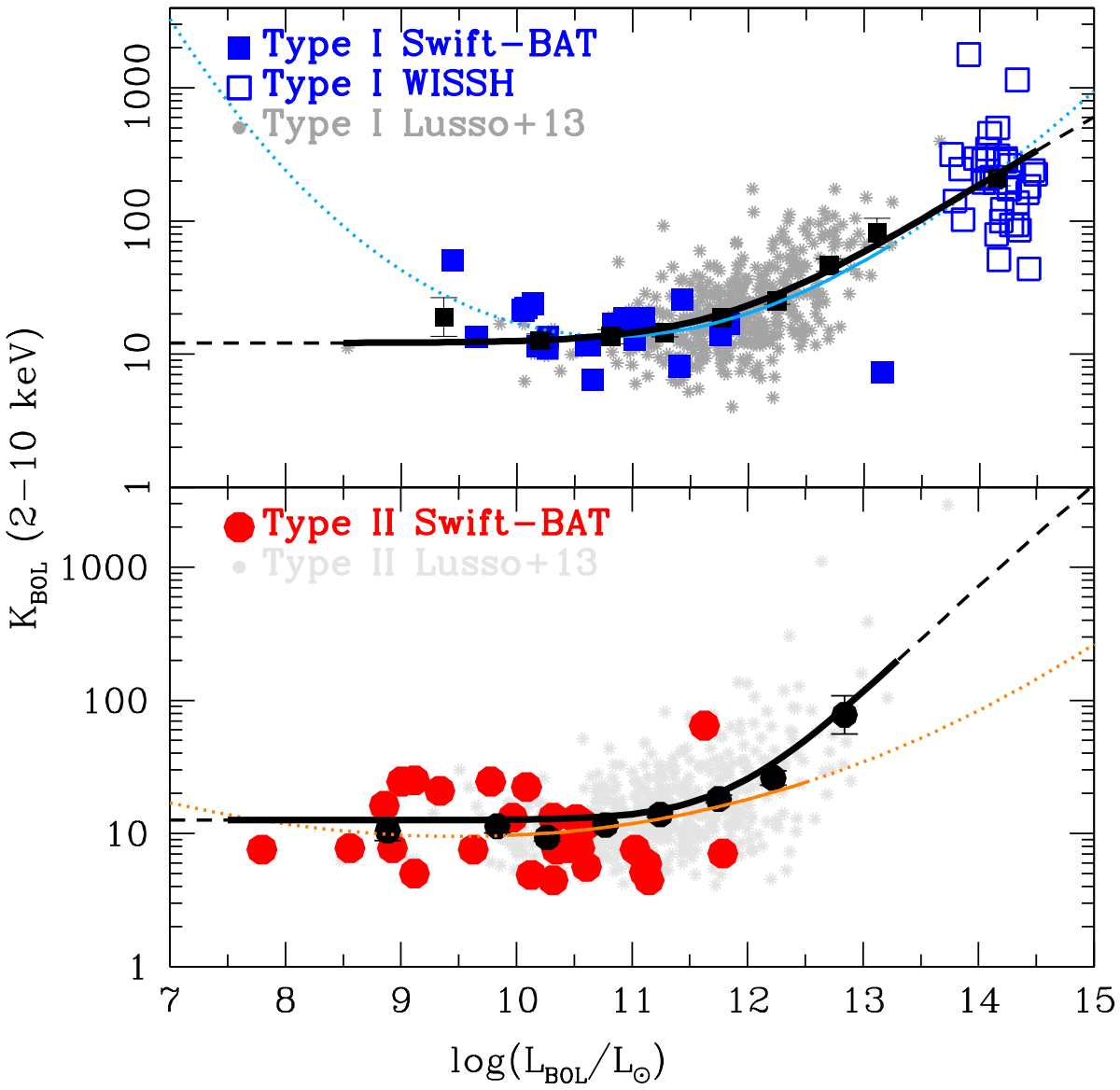

FIGURE 6.6: X-ray bolometric correction in the 2-10 keV band as a function of the bolometric luminosity for the type 1 (upper panel) and type 2 (lower panel) AGN. Symbols of the data as in the legend. Black filled squares and open circles show the average values for type 1 and type 2 sources respectively, in bins of bolometric luminosity. The black solid and dashed lines show our best-fit relations and its extrapolations according to Equation 6.2.

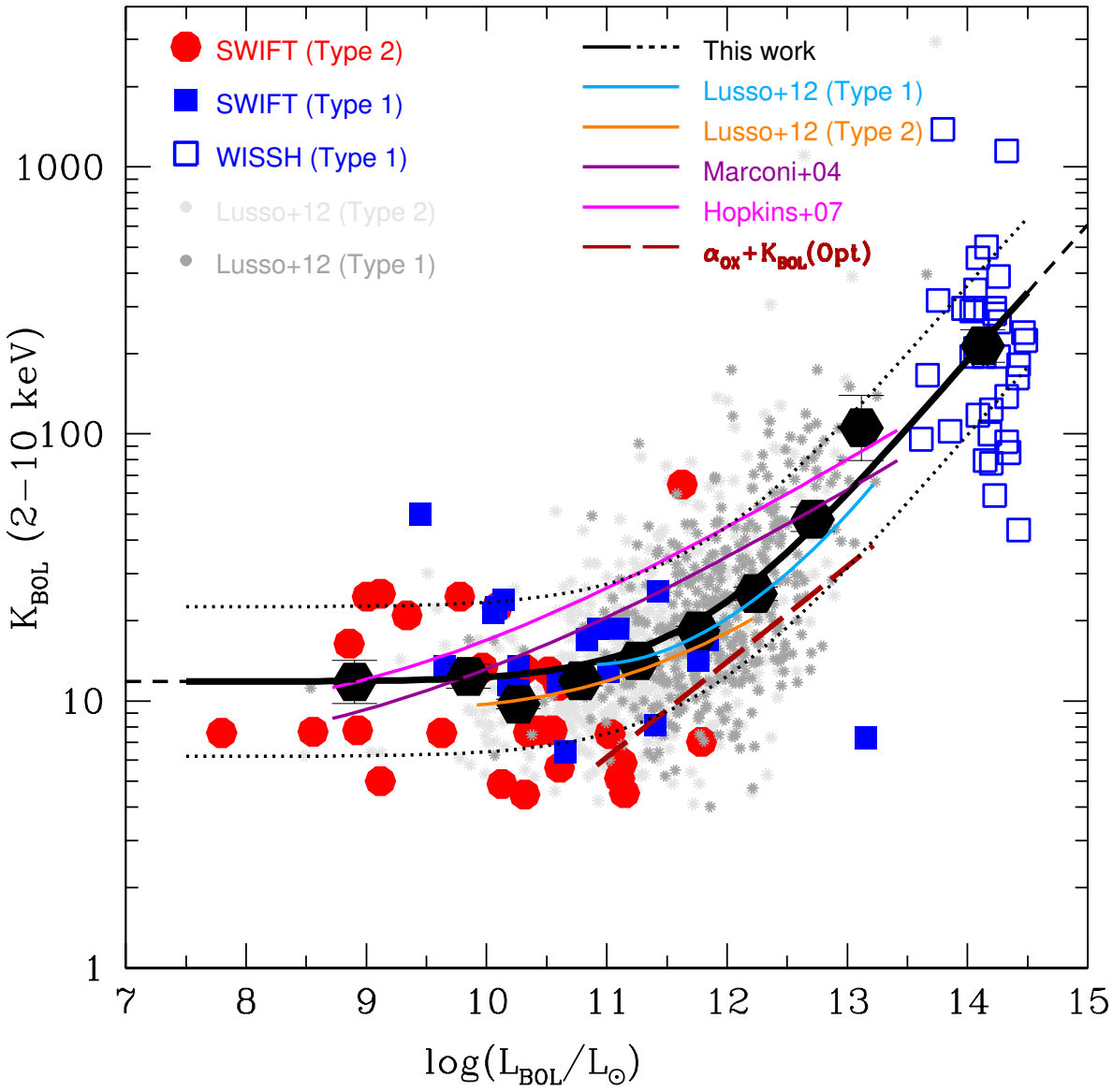

FIGURE 6.7: General X-ray bolometric correction in the 2-10 keV band as a function of the bolometric correction for both type 1 and type 2 AGN. Symbols as in Figure 6.6. Black hexagons are the average bolometric correction values, in bins of bolometric luminosity. The black solid line is our best fit solution and is compared with the relations obtained by L12 for type 1 and type 2 sources (in cyan and orange lines respectively), by Marconi et al. (2004) and by Hopkins et al. (2007); the brown solid line is the analytical prediction obtained by assuming the relation between the X-ray luminosity and the optical luminosity by Lusso and Risaliti (2016) and the optical bolometric correction by L12. See text and Table 6.3 for details.

the X-ray bolometric correction is a better measure of this phenomenon, as it takes into account the whole energetic budget and does not suffer from the obscuration which could affect the UV/optical luminosity (especially in type 2 sources).

6.3.1 Hard X-ray bolometric corrections as a function of the Eddington ratio and of the BH mass

Many authors have found a correlation (but with a huge scatter) between the bolometric correction and either the Eddington ratio ($\lambda_{EDD} = L_{bol}/L_{EDD}$) or the BH mass (e.g., Vasudevan and Fabian, 2007; Vasudevan et al., 2009; Lusso et al., 2010). We have studied these dependencies using the same samples presented in the previous Section but limited only to those objects for which the BH mass measure is available: 21 type 1 and 15 type 2 sources by Onori et al. (2017b) for the SWIFT/BAT sample, 11 WISSH type 1 sources by Vietri et al. (2018) and $\sim$ 650 COSMOS AGN by L12.

In the upper panel of Figure 6.8 the hard X-ray bolometric correction as a function of the Eddington ratio is shown. We computed the ordinary least-squares (OLS) bisector, obtaining the following relation:

$$log(K_{BOL}(2-10keV)) = 0.734 \cdot log(\lambda_{Edd}) + 2.09 \tag{6.3}$$

Our best-fit is compared with the relations published in L12 for their type 1 and type 2 COSMOS AGN.
The same analysis has been performed for the $K_{BOL}(2-10keV)$-M_{BH} relation, whose best-fit relation is shown in the lower panel of Figure 6.8 and has the following form:

$$log(K_{BOL}(2-10keV)) = 0.72 \cdot log(M_{BH}) - 4.58 \tag{6.4}$$

It appears to be steeper than the one found by M17, shown in the same Figure as comparison: this discrepancy might be ascribed to the choice of using the OLS bisector to perform the linear fit. Moreover, while M17 included also the X-WISSH AGN with values of the BH mass estimated from CIV lines (Weedman et al., 2012), we decided to consider only those with more reliable BH masses (from H_β lines by Vietri et al., 2018). It is clearly visible that the distribution of the data in both the $K_{BOL}(2-10keV)$-$_{Edd}$ and the $K_{BOL}(2-10keV)$-M_{BH} relations is quite sparse and similar results are found even if the sample is splitted according to the AGN type classification.

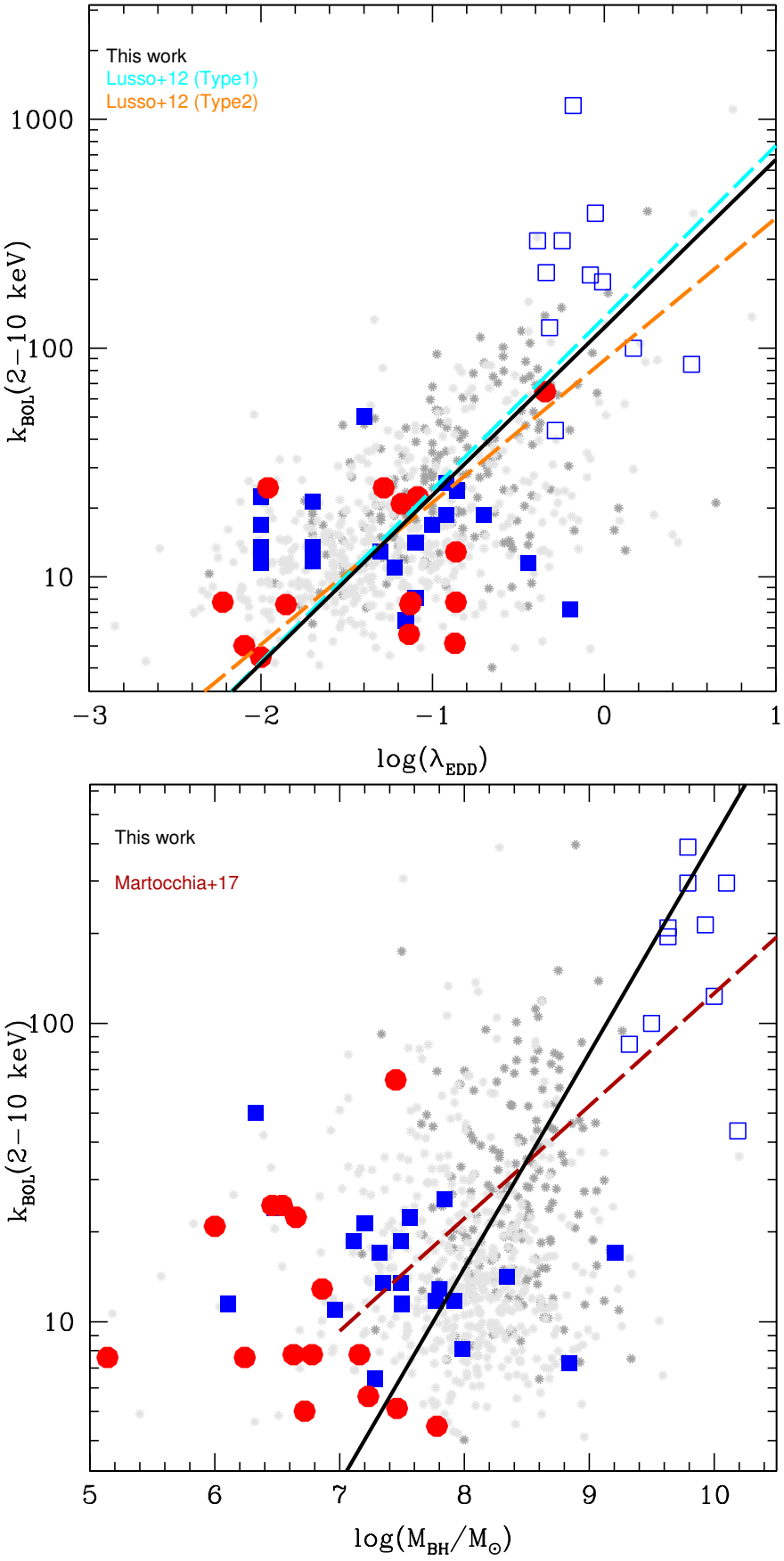

FIGURE 6.8: X-ray bolometric correction in the 2-10 keV band as a function of the Eddington ratio (upper panel) and of the BH mass (lower panel). Black solid lines show our best fit relations. Dotted lines are the linear relations inferred by L12 (for the K_{BOL}-λ_{EDD}) and by M17 (for the K_{BOL}-M_{BH}). Symbols are the same as in Figure 6.7.

6.4 Conclusions

In this Chapter we have combined two AGN samples specifically selected to cover the extremes of the AGN luminosity function, to characterize a new hard X-ray bolometric correction which spans a very wide range ($\sim$ 7 dex) of luminosity. The high-luminosity sample is composed of 41 type 1 AGN belonging to the WISSH AGN sample described in Chapter 4 and for which X-ray observation from XMM and Chandra are available (X-WISSH sample); the low-luminosity sample consists of 21 local type 1 and 27 type 2 sources randomly extracted from the SWIFT/BAT 70-month catalog (SWIFT sample). For the X-WISSH sample we used the X-ray luminosities published in M17 and the bolometric luminosities obtained following the method described in D17. To measure the main physical properties (i.e. L_{BOL}, $M_\star$ and SFR) of the sources in the SWIFT sample, we used a multi-component SED-fitting tool to reproduce both the AGN and the galaxy emission. The procedure is similar to the one adopted in D17, with two main changes: (a) we added a library of galaxy templates because for sources with luminosity lower than the WISSH, the galactic emission can be relevant if compared with the amount of emission coming from the AGN; (b) we used the hard X-ray normalized AGN models by Silva et al. (2004) to compute a virtual photometric pivotal point at 50 μm to be fitted only by the AGN templates.
Our main results are the following:

- We first studied the K_{BOL}(2-10 keV) - L_{BOL} relation for the type 1 and the type 2 samples separately, confirming a positive trend of the relation in both cases. The X-WISSH AGN sample the tail at the high luminosities, while the type 2 SWIFT/BAT sources constrain the low-luminosity region of the plane. The two best-fit relations are in good agreement with the ones found by L12 within the range of COSMOS data. Thanks to the low-luminosity sample, we found that the bolometric correction relation is consistent to be flat at low luminosities.

- The relations found for the type 1 and the type 2 samples present similar intrinsic spreads ($\sim$ 0.27 and $\sim$ 0.28). Moreover, the fact that the average values of K_{BOL} (2-10 keV) for type 2 sources (computed in bins of luminosity) lie on the best fit relation obtained for the type 1 sample, allows us to ask whether the two could share the same bolometric correction relation. We therefore computed a bolometric correction relation combining all the type 1 and type 2 sources, obtaining a universal relation statistically representative of the entire AGN population which spans about 7 decades in luminosity.

- We have then discussed how the positive trend we observe between the X-ray bolometric correction and the bolometric luminosity might be fitted in the "X-ray weakness" scenario, according to which the X-ray emitting corona tends to be less powerful compared with the UV/optical emission with the increasing of the bolometric luminosity.

- We investigated the dependence of the bolometric correction on both the Eddington ratio and BH mass. We found that K_{BOL} (2-10 keV) increases with increasing λ_{EDD} and M_{BH}, although, given the quite sparse distribution of the data points, both relations show larger intrinsic spreads than those found as a function of the bolometric luminosity.

Part of the work presented in this Chapter is going to be included in a paper to be submitted to MNRAS.

CHAPTER 7

Concluding remarks

This Chapter tries to draw some conclusions on the works that have been presented throughout this Thesis. The projects discussed in Chapters 4-6 can be summarized as follows:

- Chapter 4 is devoted to the analysis of a sample of 16 hyper-luminous AGN with FIR data in the *Herschel* SPIRE bands, belonging to the wider WISSH sample, selected by cross-correlating data from the SDSS and the WISE All-Sky Survey. The extreme luminosities they show make them the perfect place to look for feedback phenomena. Thanks to the multi-wavelength coverage, we were able to model the observed fluxes with a multi-component fitting procedure which properly accounts for the quasar and the host-galaxy emission. Moreover, we found that in some cases, our sources show peculiar features in their SED that cannot be described by the standard modelization. Therefore a further warm component, in the form of a pure blackbody, is necessary to reproduce their NIR emission. Along the physical properties we derived via SED-fitting, we focused on the IR properties of the sources. In particular, we analyze the eventual presence of a relation between the galaxy star formation and the black hole activity. By combining our sample with other *Herschel* detected samples, we derive a log-linear relation between the SF and the quasar luminosities, $L_{SF} \propto L_{QSO}^{0.73}$, which seems suggest that the most luminous AGN are hosted in galaxies with the highest star formation activity. Indeed, the

WISSH quasars present extreme values of star formation (up to thousands $M_\odot$/yr), even properly accounting for the AGN contribution to the FIR fluxes, which turned out to be $\sim 50\%$ as predicted by the radiative transfer code by Schneider et al. (2015), applied to our least and most luminous sources.
If compared with other hyper luminous AGN of the plane $\mathrm{L_{SF}} - \mathrm{L_{QSO}}$ with different levels of extinction, the WISSH can be placed in between the heavily dust enshrouded sources and the blue optically selected luminous quasars: it seems that through the WISSH quasars we are therefore witnessing a very peculiar phase in the quasar life, during which the dust in the host has not yet been fully cleared up. This suggests that the typical evolution timescales of the quasar feedback are much shorter than those typical of the host galaxy SF activity. Further high-resolution sub-mm observations are necessary to understand the eventual presence of companions in the vicinity of the AGN which might raise up the SFR estimates (see Bischetti et al. (2018) for the analysis of the source SDSSJ101549.00+002020.0 for which we obtained ALMA data in the last months, and whose companions-corrected SFR is a factor of 6 smaller than the previous one).

- In Chapter 5 we studied the case of the hot DOG W1835, a very luminous and Compton-thick quasar (as indicated by the derived unobscured X-ray luminosity $L_{2-10} \approx 1 - 3 \times 10^{45}$ erg s^{-1}). We modeled NuSTAR spectra using both phenomenological and physically motivated models and accounting treatment for the Compton scattering and the geometry of the obscurer. From the two possible scenarios (an edge-on torus or a sphere isotropically covering the nucleus), a nearly CT ($\log[N_\mathrm{H}/\mathrm{cm}^{-2}] \sim 24$) to heavy CT ($\log[N_\mathrm{H}/\mathrm{cm}^{-2}] \gg 24$) obscuration is required. This makes W1835 the first and most obscured $z > 2$ AGN detected by *NuSTAR* so far. The optical-to-FIR SED modeling gives a bolometric luminosity of $L_\mathrm{bol} \approx 3 - 5 \times 10^{47}$ erg s^{-1}, confirming the hyper-luminous nature of W1835, which exhibits also a powerful star formation activity (with SFR of the order of $\sim$3000 $M_\odot yr^{-1}$), as the previously studied WISSH AGN. The heavy obscuration of the hot DOG, together with its extreme luminosity and SFR, the ratio of X-rays to MIR and its *HST* mildly disturbed morphology, make W1835 as a witness of a late-stage merger in the context of the merger-induced quasar formation scenario. It seems to belong to that evolutionary phase which turns out in the bright blue quasars.

- In Chapter 6 we have combined two AGN samples properly selected to cover the extremes of the AGN luminosity function, to characterize a new hard X-ray bolometric correction which spans the widest range of luminosity ever. The high-luminosity sample (X-WISSH sample) is a sub-sample of the WISSH AGN sample for which X-ray observations are available. On the contrary, the low-luminosity sample (SWIFT

sample) consists of local type 1 and type 2 sources from the SWIFT/BAT 70-month catalog. We adopted a multi-component SED-fitting procedure similar to the one described in Chapter 4. By combining the two samples and a further collection of type 1 and type 2 AGN from the XMM-COSMOS sample by Lusso et al. (2012), we were able to derive new bolometric corrections for the type 1 and the type 2 AGN samples, separately. The high luminosity sample composed by the WISSH AGN constrains the tail at high luminosities, while the type 2 SWIFT/BAT sources constrain the low-luminosity region of the plane, suggesting a flat behavior of the relation at low luminosities. Relying on the fact that the intrinsic spread of these two relations are quite identical and being the average values of the bolometric correction of the type 2 sample lying on the best-fit relation obtained for the type 1 sample, we looked for a universal bolometric correction, finding a new relation which is statistically representative of the whole AGN population and which spans about 7 decades in luminosity.

As a further work, we have just started to study the Black Hole - M_* scaling relation of local type 1 and type 2 AGN using the low luminosity sample presented in Chapter 6. In order to shed light on the growth of SMBHs and its link with the host galaxy evolution over different periods of the cosmic time, it is indeed necessary to build samples of AGN, for which both M_{BH} and M_* and their time derivatives ($\dot{M}_{BH}$ and SFR) are measured, able to span a wide range in luminosity and redshift and including both obscured and unobscured sources. At the moment, such a kind of information is available only for the XMM-COSMOS sample at $z \sim 1.5$ analyzed by Merloni et al. (2010). Thanks to the work on the SWIFT/BAT sample we will cover a complementary L-z (and then M-z) region with respect to the one sampled by the XMM-COSMOS AGN, being also able to get the first information on how low mass local type 1 and type 2 AGN (and their hosts) are growing.

APPENDIX A

Input and Output files of the code

A.1 User Set-Up

The user has to edit a file with the definition of different parameters used along the entire run over the sample of objects:

tmp_dir file path of the temporary file name with ID, z, magnitudes with errors of the objects

prog_dir file path of the file name with ID, z, magnitudes with errors of the objects with the right format

$\mathbf{n_{obj}}$ number of objects

$\mathbf{n_{magn}}$ number of magnitudes

leff_dir file path of the file containing the effective wavelength for each filter

leff_form format of the file with the effective wavelength

$\mathbf{H}_0$ Hubble constant

$\Omega_\mathbf{m}$ real double number corresponding to the ratio between the energy density due to the matter in the universe and the critical density of the universe

Ω_Λ real double number corresponding to the ratio between the energy density due to the cosmological constant in the universe and the critical density of the universe

output_form format of the output file

templ_dir path of the file which contains the templates' names

$\mathbf{n_{Templ}}$ number of templates to use

A.2 Output file

The main output file summarizes the parameters of the best fit model for each objects. A detailed description of the meaning of all the columns with the correspondent label is given below:

ID identifying the name of the object, taken from the input catalogue

n_templ number of the template chosen, corresponding to the row of the input file with the templates'n names

Chi2 χ^2 value

Chi2Red Reduced χ^2_ν value

$\mathbf{A}_i$ normalization parameter for the i-th template

err_$\mathbf{A}_i$ error on the normalization parameter for the i-th template

List of Figures

List of Tables

Bibliography

Aird, J., Alexander, D. M., Ballantyne, D. R., Civano, F., Del-Moro, A., Hickox, R. C., Lansbury, G. B., Mullaney, J. R., Bauer, F. E., Brandt, W. N., Comastri, A., Fabian, A. C., Gandhi, P., Harrison, F. A., Luo, B., Stern, D., Treister, E., Zappacosta, L., Ajello, M., Assef, R., Baloković, M., Boggs, S. E., Brightman, M., Christensen, F. E., Craig, W. W., Elvis, M., Forster, K., Grefenstette, B. W., Hailey, C. J., Koss, M., LaMassa, S. M., Madsen, K. K., Puccetti, S., Saez, C., Urry, C. M., Wik, D. R., and Zhang, W. (2015a). The NuSTAR Extragalactic Survey: First Direct Measurements of the 10 KeV X-Ray Luminosity Function for Active Galactic Nuclei at z0.1. *ApJ*, 815:66.

Aird, J., Coil, A. L., Georgakakis, A., Nandra, K., Barro, G., and Pérez-González, P. G. (2015b). The evolution of the X-ray luminosity functions of unabsorbed and absorbed AGNs out to z
5. *MNRAS*, 451:1892–1927.

Alexander, D. M. and Hickox, R. C. (2012a). What drives the growth of black holes? *NAR*, 56:93–121.

Alexander, D. M. and Hickox, R. C. (2012b). What drives the growth of black holes? , 56:93–121.

Antonucci, R., Barvainis, R., and Alloin, D. (1990). The empirical difference between radio-loud and radio-quiet quasars. *APJ*, 353:416–418.

Assef, R. J., Walton, D. J., Brightman, M., Stern, D., Alexander, D., Bauer, F., Blain, A. W., Diaz-Santos, T., Eisenhardt, P. R. M., Finkelstein, S. L., Hickox, R. C., Tsai, C.-W., and Wu, J. W. (2016). Hot Dust Obscured Galaxies with Excess Blue Light: Dual AGN or Single AGN Under Extreme Conditions? *ApJ*, 819:111.

Avni, Y. (1976). Energy spectra of X-ray clusters of galaxies. *APJ*, 210:642–646.

Azadi, M., Aird, J., Coil, A. L., Moustakas, J., Mendez, A. J., Blanton, M. R., Cool, R. J., Eisenstein, D. J., Wong, K. C., and Zhu, G. (2015). PRIMUS: The Relationship between Star Formation and AGN Accretion. *ApJ*, 806:187.

Bañados, E., Venemans, B. P., Decarli, R., Farina, E. P., Mazzucchelli, C., Walter, F., Fan, X., Stern, D., Schlafly, E., Chambers, K. C., Rix, H.-W., Jiang, L., McGreer, I., Simcoe, R., Wang, F., Yang, J., Morganson, E., De Rosa, G., Greiner, J., Baloković, M., Burgett, W. S., Cooper, T., Draper, P. W., Flewelling, H., Hodapp, K. W., Jun, H. D., Kaiser, N., Kudritzki, R.-P., Magnier, E. A., Metcalfe, N., Miller, D., Schindler, J.-T., Tonry, J. L., Wainscoat, R. J., Waters, C., and Yang, Q. (2016). The Pan-STARRS1 Distant z 5.6 Quasar Survey: More than 100 Quasars within the First Gyr of the Universe. *ApJS*, 227:11.

Baes, M., Gadotti, D., Verstappen, J., De Looze, I., Fritz, J., Vidal Prez, E., and Stalevski, M. (2010). The Complex Interplay of Dust and Star Light in Spiral Galaxy Discs. In Block, D. L., Freeman, K. C., and Puerari, I., editors, *Galaxies and their Masks*, page 187.

Baldry, I. K., Balogh, M. L., Bower, R., Glazebrook, K., and Nichol, R. C. (2004). Color bimodality: Implications for galaxy evolution. In Allen, R. E., Nanopoulos, D. V., and Pope, C. N., editors, *The New Cosmology: Conference on Strings and Cosmology*, volume 743 of *American Institute of Physics Conference Series*, pages 106–119.

Banerji, M., Alaghband-Zadeh, S., Hewett, P. C., and McMahon, R. G. (2015). Heavily reddened type 1 quasars at z 2 - I. Evidence for significant obscured black hole growth at the highest quasar luminosities. *MNRAS*, 447:3368–3389.

Banerji, M., Carilli, C. L., Jones, G., Wagg, J., McMahon, R. G., Hewett, P. C., Alaghband-Zadeh, S., and Feruglio, C. (2017). The discovery of gas-rich, dusty starbursts in luminous reddened quasars at z
2.5 with ALMA. *MNRAS*, 465:4390–4405.

Banerji, M., McMahon, R. G., Hewett, P. C., Alaghband-Zadeh, S., Gonzalez-Solares, E., Venemans, B. P., and Hawthorn, M. J. (2012). Heavily reddened quasars at z 2 in the UKIDSS Large Area Survey: a transitional phase in AGN evolution. *MNRAS*, 427:2275–2291.

Barger, A. J. and Cowie, L. L. (2005). The Number Density of Intermediate- and High-Luminosity Active Galactic Nuclei at z ˜ 2-3. *APJ*, 635:115–122.

Barvainis, R. (1987). Hot dust and the near-infrared bump in the continuum spectra of quasars and active galactic nuclei. *APJ*, 320:537–544.

Barvainis, R., Antonucci, R., and Coleman, P. (1992). Submillimeter observations of radio-quiet quasars and a luminous Seyfert 1 galaxy including the first detections. *APJIL*, 399:L19–L22.

Baumgartner, W. H., Tueller, J., Markwardt, C. B., Skinner, G. K., Barthelmy, S., Mushotzky, R. F., Evans, P. A., and Gehrels, N. (2013). The 70 Month Swift-BAT All-sky Hard X-Ray Survey. *ApJS*, 207:19.

Becker, G., Hewett, P., Worseck, G., and Prochaska, J. (2013). A refined measurement of the mean transmitted flux in the Lyα forest over $2 < z < 5$ using composite quasar spectra. *MNRAS*, 430:2067–2081.

Beelen, A., Cox, P., Benford, D. J., Dowell, C. D., Kovács, A., Bertoldi, F., Omont, A., and Carilli, C. L. (2006). 350 μm Dust Emission from High-Redshift Quasars. *APJ*, 642:694–701.

Behroozi, P. S., Wechsler, R. H., and Conroy, C. (2013). The Average Star Formation Histories of Galaxies in Dark Matter Halos from z = 0-8. *ApJ*, 770:57.

Bell, E. F., Wolf, C., Meisenheimer, K., Rix, H.-W., Borch, A., Dye, S., Kleinheinrich, M., Wisotzki, L., and McIntosh, D. H. (2004). Nearly 5000 Distant Early-Type Galaxies in COMBO-17: A Red Sequence and Its Evolution since z˜1. *APJ*, 608:752–767.

Bendo, G. J., Griffin, M. J., Bock, J. J., Conversi, L., Dowell, C. D., Lim, T., Lu, N., North, C. E., Papageorgiou, A., Pearson, C. P., Pohlen, M., Polehampton, E. T., Schulz, B., Shupe, D. L., Sibthorpe, B., Spencer, L. D., Swinyard, B. M., Valtchanov, I., and Xu, C. K. (2013). Flux calibration of the Herschel-SPIRE photometer. *MNRAS*, 433:3062–3078.

Berta, S., Lutz, D., Genzel, R., Förster-Schreiber, N. M., and Tacconi, L. J. (2016). Measures of galaxy dust and gas mass with Herschel photometry and prospects for ALMA. *AAP*, 587:A73.

Bian, W.-H. and Zhao, Y.-H. (2003). Black Hole-Bulge Relation for Narrow-Line Objects. *PASJ*, 55:143–148.

Bianchi, S. (2008). Dust extinction and emission in a clumpy galactic disk. An application of the radiative transfer code TRADING. *AAP*, 490:461–475.

Bianchi, S., Giovanardi, C., Smith, M. W. L., Fritz, J., Davies, J. I., Haynes, M. P., Giovanelli, R., Baes, M., Bocchio, M., Boissier, S., Boquien, M., Boselli, A., Casasola, V., Clark, C. J. R., De Looze, I., di Serego Alighieri, S., Grossi, M., Jones, A. P., Hughes, T. M., Hunt, L. K., Madden, S., Magrini, L., Pappalardo, C., Ysard, N.,

and Zibetti, S. (2017). The Herschel Virgo Cluster Survey. XX. Dust and gas in the foreground Galactic cirrus. *A&A*, 597:A130.

Bianchi, S., Guainazzi, M., and Chiaberge, M. (2006). The soft X-ray/NLR connection: a single photoionized medium? *A&A*, 448:499–511.

Bianchi, S., Maiolino, R., and Risaliti, G. (2012). AGN Obscuration and the Unified Model. *Advances in Astronomy*, 2012:782030.

Bischetti, M., Piconcelli, E., Feruglio, C., Duras, F., Bongiorno, A., Carniani, S., Marconi, A., Pappalardo, C., Schneider, R., Travascio, A., Valiante, R., Vietri, G., Zappacosta, L., and Fiore, F. (2018). The WISSH quasars project. V. ALMA reveals the assembly of a giant galaxy around a z = 4.4 hyper-luminous QSO. *A&A*, 617:A82.

Bischetti, M., Piconcelli, E., Vietri, G., Bongiorno, A., Fiore, F., Sani, E., Marconi, A., Duras, F., Zappacosta, L., Brusa, M., Comastri, A., Cresci, G., Feruglio, C., Giallongo, E., La Franca, F., Mainieri, V., Mannucci, F., Martocchia, S., Ricci, F., Schneider, R., Testa, V., and Vignali, C. (2017). The WISSH Quasars Project I. Powerful ionised outflows in hyper-luminous quasars. *ArXiv e-prints*.

Blain, A. W., Smail, I., Ivison, R. J., Kneib, J.-P., and Frayer, D. T. (2002). Submillimeter galaxies. *PHYSREP*, 369:111–176.

Blandford, R. D. (1974). The nature of extragalactic double radio sources. *The Observatory*, 94:265–266.

Blandford, R. D. and Begelman, M. C. (1999). On the fate of gas accreting at a low rate on to a black hole. *MNRAS*, 303:L1–L5.

Bongiorno, A., Merloni, A., Brusa, M., Magnelli, B., Salvato, M., Mignoli, M., Zamorani, G., Fiore, F., Rosario, D., Mainieri, V., Hao, H., Comastri, A., Vignali, C., Balestra, I., Bardelli, S., Berta, S., Civano, F., Kampczyk, P., Le Floc'h, E., Lusso, E., Lutz, D., Pozzetti, L., Pozzi, F., Riguccini, L., Shankar, F., and Silverman, J. (2012). Accreting supermassive black holes in the COSMOS field and the connection to their host galaxies. *MNRAS*, 427:3103–3133.

Bongiorno, A., Zamorani, G., Gavignaud, I., Marano, B., Paltani, S., Mathez, G., Møller, P., Picat, J. P., Cirasuolo, M., Lamareille, F., Bottini, D., Garilli, B., Le Brun, V., Le Fèvre, O., Maccagni, D., Scaramella, R., Scodeggio, M., Tresse, L., Vettolani, G., Zanichelli, A., Adami, C., Arnouts, S., Bardelli, S., Bolzonella, M., Cappi, A., Charlot, S., Ciliegi, P., Contini, T., Foucaud, S., Franzetti, P., Guzzo, L., Ilbert, O., Iovino, A., McCracken, H. J., Marinoni, C., Mazure, A., Meneux, B., Merighi, R., Pellò, R., Pollo, A., Pozzetti, L., Radovich, M., Zucca, E., Hatziminaoglou, E., Polletta, M.,

Bondi, M., Brinchmann, J., Cucciati, O., de la Torre, S., Gregorini, L., Mellier, Y., Merluzzi, P., Temporin, S., Vergani, D., and Walcher, C. J. (2007). The VVDS type-1 AGN sample: the faint end of the luminosity function. *A&A*, 472:443–454.

Boyle, B. J. and Terlevich, R. J. (1998). The cosmological evolution of the QSO luminosity density and of the star formation rate. *MNRAS*, 293:L49–L51.

Brightman, M. and Nandra, K. (2011). VizieR Online Data Catalog: XMM survey of 12um selected galaxies (Brightman+, 2011). *VizieR Online Data Catalog*, 741.

Brightman, M., Nandra, K., Salvato, M., Hsu, L.-T., Aird, J., and Rangel, C. (2014). Compton thick active galactic nuclei in Chandra surveys. *MNRAS*, 443:1999–2017.

Brusa, M., Comastri, A., Gilli, R., Hasinger, G., Iwasawa, K., Mainieri, V., Mignoli, M., Salvato, M., Zamorani, G., Bongiorno, A., Cappelluti, N., Civano, F., Fiore, F., Merloni, A., Silverman, J., Trump, J., Vignali, C., Capak, P., Elvis, M., Ilbert, O., Impey, C., and Lilly, S. (2009). High-Redshift Quasars in the COSMOS Survey: The Space Density of z 3 X-Ray Selected QSOs. *ApJ*, 693:8–22.

Bruzual, G. and Charlot, S. (2003). Stellar population synthesis at the resolution of 2003. *MNRAS*, 344:1000–1028.

Buchner, J. and Bauer, F. E. (2017). Galaxy gas as obscurer - II. Separating the galaxy-scale and nuclear obscurers of active galactic nuclei. *MNRAS*, 465:4348–4362.

Buehler, P., Courvoisier, T. J.-L., Staubert, R., Brunner, H., and Lamer, G. (1995). ROSAT spectra of quasars. *AAP*, 295:309–316.

Calistro Rivera, G., Lusso, E., Hennawi, J. F., and Hogg, D. W. (2016). AGNfitter: A Bayesian MCMC Approach to Fitting Spectral Energy Distributions of AGNs. *ApJ*, 833:98.

Calura, F., Pipino, A., and Matteucci, F. (2008). The cycle of interstellar dust in galaxies of different morphological types. *A&A*, 479:669–685.

Calzetti, D., Armus, L., Bohlin, R. C., Kinney, A. L., Koornneef, J., and Storchi-Bergmann, T. (2000). The Dust Content and Opacity of Actively Star-forming Galaxies. *ApJ*, 533:682–695.

Calzetti, D., Kinney, A. L., and Storchi-Bergmann, T. (1994). Dust extinction of the stellar continua in starburst galaxies: The ultraviolet and optical extinction law. *APJ*, 429:582–601.

Cano-Díaz, M., Maiolino, R., Marconi, A., Netzer, H., Shemmer, O., and Cresci, G. (2012). Observational evidence of quasar feedback quenching star formation at high redshift. *A&A*, 537:L8.

Cardelli, J. A., Clayton, G. C., and Mathis, J. S. (1989). The relationship between IR, optical, and UV extinction. In Allamandola, L. J. and Tielens, A. G. G. M., editors, *Interstellar Dust*, volume 135 of *IAU Symposium*, page 5P.

Carniani, S., Marconi, A., Maiolino, R., Balmaverde, B., Brusa, M., Cano-Díaz, M., Cicone, C., Comastri, A., Cresci, G., Fiore, F., Feruglio, C., La Franca, F., Mainieri, V., Mannucci, F., Nagao, T., Netzer, H., Piconcelli, E., Risaliti, G., Schneider, R., and Shemmer, O. (2015). Ionised outflows in z ˜ 2.4 quasar host galaxies. *A&A*, 580:A102.

Cash, W. (1979). Parameter estimation in astronomy through application of the likelihood ratio. *ApJ*, 228:939–947.

Chabrier, G. (2003). Galactic Stellar and Substellar Initial Mass Function. *PASP*, 115:763–795.

Chapman, S. C., Blain, A. W., Smail, I., and Ivison, R. J. (2005). A Redshift Survey of the Submillimeter Galaxy Population. *APJ*, 622:772–796.

Chary, R. and Elbaz, D. (2001). Interpreting the Cosmic Infrared Background: Constraints on the Evolution of the Dust-enshrouded Star Formation Rate. *APJ*, 556:562–581.

Chen, C.-T. J., Hickox, R. C., Goulding, A. D., Stern, D., Assef, R., Kochanek, C. S., Brown, M. J. I., Harrison, C. M., Hainline, K. N., Alberts, S., Alexander, D. M., Brodwin, M., Del Moro, A., Forman, W. R., Gorjian, V., Jones, C., Murray, S. S., Pope, A., and Rovilos, E. (2017). Erratum: The X-Ray and Mid-infrared Luminosities in Luminous Type 1 Quasars (<A href="https://doi.org/10.3847/1538-4357/837/2/145">2017, ApJ, 837, 145</A>). *ApJ*, 847:145.

Chini, R., Kruegel, E., Kreysa, E., and Gemuend, H.-P. (1989). The submillimeter continuum of active galaxies. *AAP*, 216:L5–L7.

Cicone, C., Maiolino, R., Sturm, E., Graciá-Carpio, J., Feruglio, C., Neri, R., Aalto, S., Davies, R., Fiore, F., Fischer, J., García-Burillo, S., González-Alfonso, E., Hailey-Dunsheath, S., Piconcelli, E., and Veilleux, S. (2014). Massive molecular outflows and evidence for AGN feedback from CO observations. *AAP*, 562:A21.

Ciesla, L., Boselli, A., Smith, M. W. L., Bendo, G. J., Cortese, L., Eales, S., Bianchi, S., Boquien, M., Buat, V., Davies, J., Pohlen, M., Zibetti, S., Baes, M., Cooray, A., De Looze, I., di Serego Alighieri, S., Galametz, M., Gomez, H. L., Lebouteiller, V., Madden, S. C., Pappalardo, C., Remy, A., Spinoglio, L., Vaccari, M., Auld, R., and Clements, D. L. (2012). Submillimetre photometry of 323 nearby galaxies from the Herschel Reference Survey. *A&A*, 543:A161.

Civano, F., Brusa, M., Comastri, A., Elvis, M., Salvato, M., Zamorani, G., Capak, P., Fiore, F., Gilli, R., Hao, H., Ikeda, H., Kakazu, Y., Kartaltepe, J. S., Masters, D., Miyaji, T., Mignoli, M., Puccetti, S., Shankar, F., Silverman, J., Vignali, C., Zezas, A., and Koekemoer, A. M. (2011). The Population of High-redshift Active Galactic Nuclei in the Chandra-COSMOS Survey. *ApJ*, 741:91.

Conselice, C. J., Bershady, M. A., Dickinson, M., and Papovich, C. (2003). A Direct Measurement of Major Galaxy Mergers at z˜3. *AJ*, 126:1183–1207.

Courvoisier, T. J.-L. (1989). Long term multi-frequency study of 3C 273. In Hunt, J. and Battrick, B., editors, *Two Topics in X-Ray Astronomy, Volume 1: X Ray Binaries. Volume 2: AGN and the X Ray Background*, volume 296 of *ESA Special Publication*, pages 921–924.

Cresci, G. and Maiolino, R. (2018). Observing positive and negative AGN feedback. *Nature Astronomy*, 2:179–180.

Czerny, B. and Elvis, M. (1987). Constraints on quasar accretion disks from the optical/ultraviolet/soft X-ray big bump. *APJ*, 321:305–320.

Dai, Y. S., Bergeron, J., Elvis, M., Omont, A., Huang, J.-S., Bock, J., Cooray, A., Fazio, G., Hatziminaoglou, E., Ibar, E., Magdis, G. E., Oliver, S. J., Page, M. J., Perez-Fournon, I., Rigopoulou, D., Roseboom, I. G., Scott, D., Symeonidis, M., Trichas, M., Vieira, J. D., Willmer, C. N. A., and Zemcov, M. (2012). A Population of Dust-rich Quasars at z $\Gamma 1.5. APJ, 753 : 33$.

Dai, Y. S., Wilkes, B. J., Bergeron, J., Teplitz, H. I., and Kuraszkiewicz, J. (2016). The relationship between AGN accretion luminosity and host star formation in dusty AGNs. In *American Astronomical Society Meeting Abstracts #227*, volume 227 of *American Astronomical Society Meeting Abstracts*, page 303.03.

Dale, D. A. and Helou, G. (2002). The Infrared Spectral Energy Distribution of Normal Star-Forming Galaxies: Calibration at Far-Infrared and Submillimeter Wavelengths. In *American Astronomical Society Meeting Abstracts* #200, volume 34 of *Bulletin of the American Astronomical Society*, page 710.

Dale, D. A., Helou, G., Magdis, G. E., Armus, L., Díaz-Santos, T., and Shi, Y. (2014). A Two-parameter Model for the Infrared/Submillimeter/Radio Spectral Energy Distributions of Galaxies and Active Galactic Nuclei. *ApJ*, 784:83.

de Vaucouleurs, G., de Vaucouleurs, A., Corwin, Jr., H. G., Buta, R. J., Paturel, G., and Fouqué, P. (1991). *Third Reference Catalogue of Bright Galaxies. Volume I: Explanations and references. Volume II: Data for galaxies between 0^h and 12^h. Volume III: Data for galaxies between 12^h and 24^h.*

Delvecchio, I., Gruppioni, C., Pozzi, F., Berta, S., Zamorani, G., Cimatti, A., Lutz, D., Scott, D., Vignali, C., Cresci, G., Feltre, A., Cooray, A., Vaccari, M., Fritz, J., Le Floc'h, E., Magnelli, B., Popesso, P., Oliver, S., Bock, J., Carollo, M., Contini, T., Le Févre, O., Lilly, S., Mainieri, V., Renzini, A., and Scodeggio, M. (2014). Tracing the cosmic growth of supermassive black holes to z $3 with Herschel. MNRAS, 439 : 2736 - -2754$.

Delvecchio, I., Lutz, D., Berta, S., Rosario, D. J., Zamorani, G., Pozzi, F., Gruppioni, C., Vignali, C., Brusa, M., Cimatti, A., Clements, D. L., Cooray, A., Farrah, D., Lanzuisi, G., Oliver, S., Rodighiero, G., Santini, P., and Symeonidis, M. (2015). Mapping the average AGN accretion rate in the SFR-M_* plane for Herschel-selected galaxies at 0 z $\leq 2.5. MNRAS, 449 : 373 - -389$.

Dey, A., Soifer, B. T., Desai, V., Brand, K., Le Floc'h, E., Brown, M. J. I., Jannuzi, B. T., Armus, L., Bussmann, S., Brodwin, M., Bian, C., Eisenhardt, P., Higdon, S. J., Weedman, D., and Willner, S. P. (2008). A Significant Population of Very Luminous Dust-Obscured Galaxies at Redshift z ˜ 2. *ApJ*, 677:943–956.

Di Matteo, T., Springel, V., and Hernquist, L. (2005). Energy input from quasars regulates the growth and activity of black holes and their host galaxies. *NAT*, 433:604–607.

Draine, B. T. (2003). Scattering by Interstellar Dust Grains. II. X-Rays. *APJ*, 598:1026–1037.

Draine, B. T. and Li, A. (2007). Infrared Emission from Interstellar Dust. IV. The Silicate-Graphite-PAH Model in the Post-Spitzer Era. *APJ*, 657:810–837.

Dressler, A. (1989). Observational Evidence for Supermassive Black Holes. In Osterbrock, D. E. and Miller, J. S., editors, *Active Galactic Nuclei*, volume 134 of *IAU Symposium*, page 217.

Duras, F., Bongiorno, A., Piconcelli, E., Bianchi, S., Pappalardo, C., Valiante, R., Bischetti, M., Feruglio, C., Martocchia, S., Schneider, R., Vietri, G., Vignali, C., Zappacosta, L., La Franca, F., and Fiore, F. (2017). The WISSH quasars project. II. Giant star nurseries in hyper-luminous quasars. *A&A*, 604:A67.

Edelson, R. A. and Malkan, M. A. (1986). Spectral energy distributions of active galactic nuclei between 0.1 and 100 microns. *ApJ*, 308:59–77.

Eisenhardt, P. R. M., Wu, J., Tsai, C.-W., Assef, R., Benford, D., Blain, A., Bridge, C., Condon, J. J., Cushing, M. C., Cutri, R., Evans, II, N. J., Gelino, C., Griffith, R. L., Grillmair, C. J., Jarrett, T., Lonsdale, C. J., Masci, F. J., Mason, B. S., Petty, S.,

Sayers, J., Stanford, S. A., Stern, D., Wright, E. L., and Yan, L. (2012). The First Hyper-luminous Infrared Galaxy Discovered by WISE. *ApJ*, 755:173.

Elvis, M., Wilkes, B., McDowell, J., Green, R., Bechtold, J., Willner, S., Oey, M., Polomski, E., and Cutri, R. (1994). Atlas of quasar energy distributions. *APJs*, 95:1–68.

Esin, A. A., McClintock, J. E., and Narayan, R. (1997). Advection-Dominated Accretion and the Spectral States of Black Hole X-Ray Binaries: Application to Nova Muscae 1991. *APJ*, 489:865–889.

Fabian, A. C. and Iwasawa, K. (1999). The mass density in black holes inferred from the X-ray background. *MNRAS*, 303:L34–L36.

Fabian, A. C., Lohfink, A., Kara, E., Parker, M. L., Vasudevan, R., and Reynolds, C. S. (2015). Properties of AGN coronae in the NuSTAR era. *MNRAS*, 451:4375–4383.

Fan, L., Han, Y., Fang, G., Gao, Y., Zhang, D., Jiang, X., Wu, Q., Yang, J., and Li, Z. (2016a). The Most Luminous Heavily Obscured Quasars Have a High Merger Fraction: Morphological Study of WISE-selected Hot Dust-obscured Galaxies. *ApJ*, 822:L32.

Fan, L., Han, Y., Nikutta, R., Drouart, G., and Knudsen, K. K. (2016b). Infrared Spectral Energy Distribution Decomposition of WISE-selected, Hyperluminous Hot Dust-obscured Galaxies. *ApJ*, 823:107.

Fan, L., Han, Y., Nikutta, R., Drouart, G., and Knudsen, K. K. (2016c). Infrared Spectral Energy Distribution Decomposition of WISE-selected, Hyperluminous Hot Dust-obscured Galaxies. *ApJ*, 823:107.

Fan, X., Narayanan, V. K., Lupton, R. H., Strauss, M. A., Knapp, G. R., Becker, R. H., White, R. L., Pentericci, L., Leggett, S. K., Haiman, Z., Gunn, J. E., Ivezić, Ž., Schneider, D. P., Anderson, S. F., Brinkmann, J., Bahcall, N. A., Connolly, A. J., Csabai, I., Doi, M., Fukugita, M., Geballe, T., Grebel, E. K., Harbeck, D., Hennessy, G., Lamb, D. Q., Miknaitis, G., Munn, J. A., Nichol, R., Okamura, S., Pier, J. R., Prada, F., Richards, G. T., Szalay, A., and York, D. G. (2001). A Survey of z5.8 Quasars in the Sloan Digital Sky Survey. I. Discovery of Three New Quasars and the Spatial Density of Luminous Quasars at z˜6. *AJ*, 122:2833–2849.

Fan, X., Strauss, M. A., Schneider, D. P., Becker, R. H., White, R. L., Haiman, Z., Gregg, M., Pentericci, L., Grebel, E. K., Narayanan, V. K., Loh, Y.-S., Richards, G. T., Gunn, J. E., Lupton, R. H., Knapp, G. R., Ivezić, Ž., Brandt, W. N., Collinge, M., Hao, L., Harbeck, D., Prada, F., Schaye, J., Strateva, I., Zakamska, N., Anderson, S., Brinkmann, J., Bahcall, N. A., Lamb, D. Q., Okamura, S., Szalay, A., and York,

D. G. (2003). A Survey of z5.7 Quasars in the Sloan Digital Sky Survey. II. Discovery of Three Additional Quasars at z6. *AJ*, 125:1649–1659.

Farrah, D., Petty, S., Connolly, B., Blain, A., Efstathiou, A., Lacy, M., Stern, D., Lake, S., Jarrett, T., Bridge, C., Eisenhardt, P., Benford, D., Jones, S., Tsai, C.-W., Assef, R., Wu, J., and Moustakas, L. (2017). The Role of the Most Luminous Obscured AGNs in Galaxy Assembly at z
2. *ApJ*, 844:106.

Feltre, A., Hatziminaoglou, E., Fritz, J., and Franceschini, A. (2012). Smooth and clumpy dust distributions in AGN: a direct comparison of two commonly explored infrared emission models. *MNRAS*, 426:120–127.

Feruglio, C., Bongiorno, A., Fiore, F., Krips, M., Brusa, M., Daddi, E., Gavignaud, I., Maiolino, R., Piconcelli, E., Sargent, M., Vignali, C., and Zappacosta, L. (2014). Gas reservoir of a hyper-luminous quasar at z = 2.6. *A&A*, 565:A91.

Feruglio, C., Fiore, F., Carniani, S., Piconcelli, E., Zappacosta, L., Bongiorno, A., Cicone, C., Maiolino, R., Marconi, A., Menci, N., Puccetti, S., and Veilleux, S. (2015). The multi-phase winds of Markarian 231: from the hot, nuclear, ultra-fast wind to the galaxy-scale, molecular outflow. *A&A*, 583:A99.

Feruglio, C., Fiore, F., Maiolino, R., Piconcelli, E., Aussel, H., Elbaz, D., Le Floc'h, E., Sturm, E., Davies, R., and Cicone, C. (2013). <ASTROBJ>NGC 6240</ASTROBJ>: extended CO structures and their association with shocked gas. *A&A*, 549:A51.

Feruglio, C., Maiolino, R., Piconcelli, E., Menci, N., Aussel, H., Lamastra, A., and Fiore, F. (2010). Quasar feedback revealed by giant molecular outflows. *AAP*, 518:L155.

Fiore, F., Elvis, M., McDowell, J. C., Siemiginowska, A., and Wilkes, B. J. (1994). The complex optical to soft x-ray spectrum of the low-redshift radio-quiet quasars. *APJ*, 431:515–533.

Fiore, F., Feruglio, C., Shankar, F., Bischetti, M., Bongiorno, A., Brusa, M., Carniani, S., Cicone, C., Duras, F., Lamastra, A., Mainieri, V., Marconi, A., Menci, N., Maiolino, R., Piconcelli, E., Vietri, G., and Zappacosta, L. (2017). AGN wind scaling relations and the co-evolution of black holes and galaxies. *ArXiv e-prints*.

Fiore, F., Puccetti, S., Brusa, M., Salvato, M., Zamorani, G., Aldcroft, T., Aussel, H., Brunner, H., Capak, P., Cappelluti, N., Civano, F., Comastri, A., Elvis, M., Feruglio, C., Finoguenov, A., Fruscione, A., Gilli, R., Hasinger, G., Koekemoer, A., Kartaltepe, J., Ilbert, O., Impey, C., Le Floc'h, E., Lilly, S., Mainieri, V., Martinez-Sansigre,

A., McCracken, H. J., Menci, N., Merloni, A., Miyaji, T., Sanders, D. B., Sargent, M., Schinnerer, E., Scoville, N., Silverman, J., Smolcic, V., Steffen, A., Santini, P., Taniguchi, Y., Thompson, D., Trump, J. R., Vignali, C., Urry, M., and Yan, L. (2009). Chasing Highly Obscured QSOs in the COSMOS Field. *ApJ*, 693:447–462.

Fritz, J., Franceschini, A., and Hatziminaoglou, E. (2006). Revisiting the infrared spectra of active galactic nuclei with a new torus emission model. *MNRAS*, 366:767–786.

Gallo, E., Fender, R. P., and Pooley, G. G. (2003). On the correlation between radio and X-ray flux in low/hard state black holes. In Durouchoux, P., Fuchs, Y., and Rodriguez, J., editors, *New Views on Microquasars*, page 209.

Gandhi, P., Horst, H., Smette, A., Hönig, S., Comastri, A., Gilli, R., Vignali, C., and Duschl, W. (2009). Resolving the mid-infrared cores of local Seyferts. *A&A*, 502:457–472.

Gavazzi, G., Fumagalli, M., Cucciati, O., and Boselli, A. (2010). A snapshot on galaxy evolution occurring in the Great Wall: the role of Nurture at z = 0. *AAP*, 517:A73.

Gehrels, N. (1986). Confidence limits for small numbers of events in astrophysical data. *ApJ*, 303:336–346.

Giacconi, R., Gursky, H., Paolini, F. R., and Rossi, B. B. (1962). Evidence for x Rays From Sources Outside the Solar System. *Physical Review Letters*, 9:439–443.

Gil de Paz, A., Boissier, S., Madore, B. F., Seibert, M., Joe, Y. H., Boselli, A., Wyder, T. K., Thilker, D., Bianchi, L., Rey, S.-C., Rich, R. M., Barlow, T. A., Conrow, T., Forster, K., Friedman, P. G., Martin, D. C., Morrissey, P., Neff, S. G., Schiminovich, D., Small, T., Donas, J., Heckman, T. M., Lee, Y.-W., Milliard, B., Szalay, A. S., and Yi, S. (2007). The GALEX Ultraviolet Atlas of Nearby Galaxies. *ApJS*, 173:185–255.

Gilli, R., Comastri, A., and Hasinger, G. (2007). The synthesis of the cosmic X-ray background in the Chandra and XMM-Newton era. *A&A*, 463:79–96.

Gilli, R., Comastri, A., Vignali, C., Ranalli, P., and Iwasawa, K. (2010). The evolution of obscured accretion. *X-ray Astronomy 2009; Present Status, Multi-Wavelength Approach and Future Perspectives*, 1248:359–364.

Glikman, E., Simmons, B., Mailly, M., Schawinski, K., Urry, C. M., and Lacy, M. (2015). Major Mergers Host the Most-luminous Red Quasars at z ˜ 2: A Hubble Space Telescope WFC3/IR Study. *ApJ*, 806:218.

Glikman, E., Urrutia, T., Lacy, M., Djorgovski, S. G., Mahabal, A., Myers, A. D., Ross, N. P., Petitjean, P., Ge, J., Schneider, D. P., and York, D. G. (2012). FIRST-2MASS Red Quasars: Transitional Objects Emerging from the Dust. *ApJ*, 757:51.

Goulding, A. D., Zakamska, N. L., Alexandroff, R. M., Assef, R. J., Banerji, M., Hamann, F., Wylezalek, D., Brandt, W. N., Greene, J. E., Lansbury, G. B., Pâris, I., Richards, G., Stern, D., and Strauss, M. A. (2018). High-redshift Extremely Red Quasars in X-Rays. *ApJ*, 856:4.

Graham, A. W., Onken, C. A., Athanassoula, E., and Combes, F. (2011). An expanded M_{bh}-σ diagram, and a new calibration of active galactic nuclei masses. *MNRAS*, 412:2211–2228.

Granato, G. L. and Danese, L. (1994). Thick Tori around Active Galactic Nuclei - a Comparison of Model Predictions with Observations of the Infrared Continuum and Silicate Features. *MNRAS*, 268:235.

Granato, G. L., De Zotti, G., Silva, L., Bressan, A., and Danese, L. (2004). A Physical Model for the Coevolution of QSOs and Their Spheroidal Hosts. *ApJ*, 600:580–594.

Granato, G. L., Silva, L., Monaco, P., Panuzzo, P., Salucci, P., De Zotti, G., and Danese, L. (2001). Joint formation of QSOs and spheroids: QSOs as clocks of star formation in spheroids. *MNRAS*, 324:757–768.

Grier, C. J., Pancoast, A., Barth, A. J., Fausnaugh, M. M., Brewer, B. J., Treu, T., and Peterson, B. M. (2017). The Structure of the Broad-line Region in Active Galactic Nuclei. II. Dynamical Modeling of Data From the AGN10 Reverberation Mapping Campaign. *ApJ*, 849:146.

Gruppioni, C., Berta, S., Spinoglio, L., Pereira-Santaella, M., Pozzi, F., Andreani, P., Bonato, M., De Zotti, G., Malkan, M., Negrello, M., Vallini, L., and Vignali, C. (2016). Tracing black hole accretion with SED decomposition and IR lines: from local galaxies to the high-z Universe. *MNRAS*, 458:4297–4320.

Guainazzi, M. and Bianchi, S. (2007). On the origin of soft X-rays in obscured AGN: answers from high-resolution spectroscopy with XMM-Newton. *MNRAS*, 374:1290–1302.

Gultekin, K. (2009). Determination of the intrinsic scatter in the M-sigma and M-L relations. *ArXiv e-prints*.

Haas, M., Klaas, U., Müller, S. A. H., Bertoldi, F., Camenzind, M., Chini, R., Krause, O., Lemke, D., Meisenheimer, K., Richards, P. J., and Wilkes, B. J. (2003). The ISO view of Palomar-Green quasars. *AAP*, 402:87–111.

Hao, H., Elvis, M., and Civano, F. (2009). Type 1 AGN SEDs in COSMOS. In Wolk, S., Fruscione, A., and Swartz, D., editors, *Chandra's First Decade of Discovery*, page 115.

Häring, N. and Rix, H.-W. (2004). On the Black Hole Mass-Bulge Mass Relation. *ApJ*, 604:L89–L92.

Harrison, C. M. (2017). Impact of supermassive black hole growth on star formation. *Nature Astronomy*, 1:0165.

Harrison, C. M., Alexander, D. M., Swinbank, A. M., Smail, I., Alaghband-Zadeh, S., Bauer, F. E., Chapman, S. C., Del Moro, A., Hickox, R. C., Ivison, R. J., Menéndez-Delmestre, K., Mullaney, J. R., and Nesvadba, N. P. H. (2012). Energetic galaxy-wide outflows in high-redshift ultraluminous infrared galaxies hosting AGN activity. *MNRAS*, 426:1073–1096.

Harrison, F. A., Craig, W. W., Christensen, F. E., Hailey, C. J., Zhang, W. W., Boggs, S. E., Stern, D., Cook, W. R., Forster, K., Giommi, P., Grefenstette, B. W., Kim, Y., Kitaguchi, T., Koglin, J. E., Madsen, K. K., Mao, P. H., Miyasaka, H., Mori, K., Perri, M., Pivovaroff, M. J., Puccetti, S., Rana, V. R., Westergaard, N. J., Willis, J., Zoglauer, A., An, H., Bachetti, M., Barrière, N. M., Bellm, E. C., Bhalerao, V., Brejnholt, N. F., Fuerst, F., Liebe, C. C., Markwardt, C. B., Nynka, M., Vogel, J. K., Walton, D. J., Wik, D. R., Alexander, D. M., Cominsky, L. R., Hornschemeier, A. E., Hornstrup, A., Kaspi, V. M., Madejski, G. M., Matt, G., Molendi, S., Smith, D. M., Tomsick, J. A., Ajello, M., Ballantyne, D. R., Baloković, M., Barret, D., Bauer, F. E., Blandford, R. D., Brandt, W. N., Brenneman, L. W., Chiang, J., Chakrabarty, D., Chenevez, J., Comastri, A., Dufour, F., Elvis, M., Fabian, A. C., Farrah, D., Fryer, C. L., Gotthelf, E. V., Grindlay, J. E., Helfand, D. J., Krivonos, R., Meier, D. L., Miller, J. M., Natalucci, L., Ogle, P., Ofek, E. O., Ptak, A., Reynolds, S. P., Rigby, J. R., Tagliaferri, G., Thorsett, S. E., Treister, E., and Urry, C. M. (2013). The Nuclear Spectroscopic Telescope Array (NuSTAR) High-energy X-Ray Mission. *ApJ*, 770:103.

Hasinger, G. (2008). Absorption properties and evolution of active galactic nuclei. *A&A*, 490:905–922.

Hasinger, G., Miyaji, T., and Schmidt, M. (2005). Luminosity-dependent evolution of soft X-ray selected AGN. New Chandra and XMM-Newton surveys. *AAP*, 441:417–434.

Hatziminaoglou, E., Omont, A., Stevens, J. A., Amblard, A., Arumugam, V., Auld, R., Aussel, H., Babbedge, T., Blain, A., Bock, J., Boselli, A., Buat, V., Burgarella, D., Castro-Rodríguez, N., Cava, A., Chanial, P., Clements, D. L., Conley, A., Conversi, L., Cooray, A., Dowell, C. D., Dwek, E., Dye, S., Eales, S., Elbaz, D., Farrah, D., Fox, M., Franceschini, A., Gear, W., Glenn, J., González Solares, E. A., Griffin, M., Halpern, M., Ibar, E., Isaak, K., Ivison, R. J., Lagache, G., Levenson, L., Lu, N., Madden, S., Maffei, B., Mainetti, G., Marchetti, L., Mortier, A. M. J., Nguyen, H. T.,

O'Halloran, B., Oliver, S. J., Page, M. J., Panuzzo, P., Papageorgiou, A., Pearson, C. P., Pérez-Fournon, I., Pohlen, M., Rawlings, J. I., Rigopoulou, D., Rizzo, D., Roseboom, I. G., Rowan-Robinson, M., Sanchez Portal, M., Schulz, B., Scott, D., Seymour, N., Shupe, D. L., Smith, A. J., Symeonidis, M., Trichas, M., Tugwell, K. E., Vaccari, M., Valtchanov, I., Vigroux, L., Wang, L., Ward, R., Wright, G., Xu, C. K., and Zemcov, M. (2010). HerMES: Far infrared properties of known AGN in the HerMES fields. *AAP*, 518:L33.

Heckman, T. M. (1980). An optical and radio survey of the nuclei of bright galaxies - Activity in normal galactic nuclei. *A&A*, 87:152–164.

Heckman, T. M. and Best, P. N. (2014). The Coevolution of Galaxies and Supermassive Black Holes: Insights from Surveys of the Contemporary Universe. *Annual Review of Astronomy and Astrophysics*, 52:589–660.

Hernán-Caballero, A., Hatziminaoglou, E., Alonso-Herrero, A., and Mateos, S. (2016). The near-to-mid infrared spectrum of quasars. *MNRAS*, 463:2064–2078.

Hildebrand, R. H. (1983). The Determination of Cloud Masses and Dust Characteristics from Submillimetre Thermal Emission. *QJRAS*, 24:267.

Ho, L. C., Filippenko, A. V., and Sargent, W. L. W. (1994). The Palomar Observatory dwarf Seyfert survey. In Courvoisier, T. and Blecha, A., editors, *Multi-Wavelength Continuum Emission of AGN*, volume 159 of *IAU Symposium*, pages 275–278.

Ho, L. C. and Kim, M. (2014). The Black Hole Mass Scale of Classical and Pseudo Bulges in Active Galaxies. *ApJ*, 789:17.

Hönig, S. F. and Kishimoto, M. (2010). The dusty heart of nearby active galaxies. II. From clumpy torus models to physical properties of dust around AGN. *A&A*, 523:A27.

Hopkins, A. M. and Beacom, J. F. (2006). On the Normalization of the Cosmic Star Formation History. *APJ*, 651:142–154.

Hopkins, P. F., Hernquist, L., Cox, T. J., Di Matteo, T., Robertson, B., and Springel, V. (2005). Luminosity-dependent Quasar Lifetimes: Reconciling the Optical and X-Ray Quasar Luminosity Functions. *APJ*, 632:81–91.

Hopkins, P. F., Hernquist, L., Cox, T. J., and Kereš, D. (2008). A Cosmological Framework for the Co-Evolution of Quasars, Supermassive Black Holes, and Elliptical Galaxies. I. Galaxy Mergers and Quasar Activity. *ApJS*, 175:356–389.

Hopkins, P. F., Quataert, E., and Murray, N. (2012). Stellar feedback in galaxies and the origin of galaxy-scale winds. *MNRAS*, 421:3522–3537.

Hopkins, P. F., Richards, G. T., and Hernquist, L. (2007). An Observational Determination of the Bolometric Quasar Luminosity Function. *APJ*, 654:731–753.

Hopkins, P. F., Torrey, P., Faucher-Giguère, C.-A., Quataert, E., and Murray, N. (2016). Stellar and quasar feedback in concert: effects on AGN accretion, obscuration, and outflows. *MNRAS*, 458:816–831.

Huang, J.-S., Rigopoulou, D., Magdis, G., Rowan-Robinson, M., Dai, Y., Bock, J. J., Burgarella, D., Chapman, S., Clements, D. L., Cooray, A., Farrah, D., Glenn, J., Oliver, S., Smith, A. J., Wang, L., Page, M., Riechers, D., Roseboom, I., Symeonidis, M., Fazio, G. G., Yun, M., Webb, T. M. A., and Efstathiou, A. (2014). HerMES: Spectral Energy Distributions of Submillimeter Galaxies at z 4. *ApJ*, 784:52.

Hughes, D. H., Dunlop, J. S., and Rawlings, S. (1997). High-redshift radio galaxies and quasars at submillimetre wavelengths: assessing their evolutionary status. *MNRAS*, 289:766–782.

Hughes, D. H., Robson, E. I., Dunlop, J. S., and Gear, W. K. (1993). Thermal Dust Emission from Quasars - Part One - Submillimetre Spectral Indices of Radio Quiet Quasars. *MNRAS*, 263:607.

Inoue, A., Shimizu, I., Iwata, I., and Tanaka, M. (2014). An updated analytic model for attenuation by the intergalactic medium. *MNRAS*, 442:1805–1820.

Jia, J., Ptak, A., Heckman, T. M., Braito, V., and Reeves, J. (2012). A Chandra Observation of the Ultraluminous Infrared Galaxy IRAS 19254-7245 (the Superantennae): X-Ray Emission from the Compton-thick Active Galactic Nucleus and the Diffuse Starburst. *ApJ*, 759:41.

Jiang, L., Fan, X., Hines, D. C., Shi, Y., Vestergaard, M., Bertoldi, F., Brandt, W. N., Carilli, C. L., Cox, P., Le Floc'h, E., Pentericci, L., Richards, G. T., Rieke, G. H., Schneider, D. P., Strauss, M. A., Walter, F., and Brinkmann, J. (2006). Probing the Evolution of Infrared Properties of z ˜ 6 Quasars: Spitzer Observations. *AJ*, 132:2127–2134.

Jones, S. F., Blain, A. W., Stern, D., Assef, R. J., Bridge, C. R., Eisenhardt, P., Petty, S., Wu, J., Tsai, C.-W., Cutri, R., Wright, E. L., and Yan, L. (2014). Submillimetre observations of WISE-selected high-redshift, luminous, dusty galaxies. *MNRAS*, 443:146–157.

Jorge, Z. (2006). Black Hole Physics. In *Proceedings of the School on Particle Physics, Gravity and Cosmology*, page 13.

Just, D. W., Brandt, W. N., Shemmer, O., Steffen, A. T., Schneider, D. P., Chartas, G., and Garmire, G. P. (2007). The X-Ray Properties of the Most Luminous Quasars from the Sloan Digital Sky Survey. *APJ*, 665:1004–1022.

Kalfountzou, E., Civano, F., Elvis, M., Trichas, M., and Green, P. (2014). The largest X-ray-selected sample of z3 AGNs: C-COSMOS and ChaMP. *MNRAS*, 445:1430–1448.

Kelly, B. C., Bechtold, J., Trump, J. R., Vestergaard, M., and Siemiginowska, A. (2008). Observational Constraints on the Dependence of Radio-Quiet Quasar X-Ray Emission on Black Hole Mass and Accretion Rate. *ApJS*, 176:355–373.

Kennicutt, R. C. and Evans, N. J. (2012). Star Formation in the Milky Way and Nearby Galaxies. *Annual Review of Astronomy and Astrophysics*, 50:531–608.

Kennicutt, Jr., R. C. (1998). Star Formation in Galaxies Along the Hubble Sequence. *ARAA*, 36:189–232.

Khachikian, E. Y. and Weedman, D. W. (1974). An atlas of Seyfert galaxies. *apj*, 192:581–589.

King, A. R. and Pounds, K. A. (2003). Black hole winds. *MNRAS*, 345:657–659.

Kormendy, J. and Ho, L. C. (2013). Coevolution (Or Not) of Supermassive Black Holes and Host Galaxies. *Annual Review of Astronomy and Astrophysics*, 51:511–653.

Kormendy, J. and Richstone, D. (1995). Inward Bound—The Search For Supermassive Black Holes In Galactic Nuclei. *Annual Review of Astronomy and Astrophysics*, 33:581.

Krawczyk, C. M., Richards, G. T., Mehta, S. S., Vogeley, M. S., Gallagher, S. C., Leighly, K. M., Ross, N. P., and Schneider, D. P. (2013). Mean Spectral Energy Distributions and Bolometric Corrections for Luminous Quasars. *APJS*, 206:4.

Krolik, J. H. and Begelman, M. C. (1988). Molecular tori in Seyfert galaxies - Feeding the monster and hiding it. *APJ*, 329:702–711.

Kylafis, N. D. and Bahcall, J. N. (1987). Dust distribution in spiral galaxies. *APJ*, 317:637–645.

La Franca, F., Fiore, F., Comastri, A., Perola, G. C., Sacchi, N., Brusa, M., Cocchia, F., Feruglio, C., Matt, G., Vignali, C., Carangelo, N., Ciliegi, P., Lamastra, A., Maiolino, R., Mignoli, M., Molendi, S., and Puccetti, S. (2005). The HELLAS2XMM Survey. VII. The Hard X-Ray Luminosity Function of AGNs up to z = 4: More Absorbed AGNs at Low Luminosities and High Redshifts. *ApJ*, 635:864–879.

Lagache, G., Dole, H., Puget, J.-L., Prez-Gonzlez, P. G., Le Floc'h, E., Rieke, G. H., Papovich, C., Egami, E., Alonso-Herrero, A., Engelbracht, C. W., Gordon, K. D., Misselt, K. A., and Morrison, J. E. (2004). Polycyclic Aromatic Hydrocarbon Contribution to the Infrared Output Energy of the Universe at z $\sim=$ 2. *APJS*, 154:112–117.

LaMassa, S. M., Ricarte, A., Glikman, E., Urry, C. M., Stern, D., Yaqoob, T., Lansbury, G. B., Civano, F., Boggs, S. E., Brandt, W. N., Chen, C.-T. J., Christensen, F. E., Craig, W. W., Hailey, C. J., Harrison, F., Hickox, R. C., Koss, M., Ricci, C., Treister, E., and Zhang, W. (2016). Peering Through the Dust: NuSTAR Observations of Two FIRST-2MASS Red Quasars. *ApJ*, 820:70.

Lani, C., Netzer, H., and Lutz, D. (2017). Intrinsic AGN SED black hole growth in the Palomar-Green quasars. *MNRAS*, 471:59–79.

Lanzuisi, G., Piconcelli, E., Fiore, F., Feruglio, C., Vignali, C., Salvato, M., and Gruppioni, C. (2009). Revealing X-ray obscured quasars in SWIRE sources with extreme mid-IR/optical flux ratios. *A&A*, 498:67–81.

Lanzuisi, G., Ranalli, P., Georgantopoulos, I., Georgakakis, A., Delvecchio, I., Akylas, T., Berta, S., Bongiorno, A., Brusa, M., Cappelluti, N., Civano, F., Comastri, A., Gilli, R., Gruppioni, C., Hasinger, G., Iwasawa, K., Koekemoer, A., Lusso, E., Marchesi, S., Mainieri, V., Merloni, A., Mignoli, M., Piconcelli, E., Pozzi, F., Rosario, D. J., Salvato, M., Silverman, J., Trakhtenbrot, B., Vignali, C., and Zamorani, G. (2015). Compton thick AGN in the XMM-COSMOS survey. *A&A*, 573:A137.

Laor, A. (2001). On the Linearity of the Black Hole-Bulge Mass Relation in Active and in Nearby Galaxies. *ApJ*, 553:677–682.

Laor, A. and Draine, B. T. (1993). Spectroscopic constraints on the properties of dust in active galactic nuclei. *APJ*, 402:441–468.

Laor, A., Fiore, F., Elvis, M., Wilkes, B. J., and McDowell, J. C. (1997). The Soft X-Ray Properties of a Complete Sample of Optically Selected Quasars. II. Final Results. *APJ*, 477:93–113.

Lawrence, A. and Elvis, M. (1982). Obscuration and the various kinds of Seyfert galaxies. *ApJ*, 256:410–426.

Leipski, C., Meisenheimer, K., Walter, F., Besel, M.-A., Dannerbauer, H., Fan, X., Haas, M., Klaas, U., Krause, O., and Rix, H.-W. (2013). Complete Infrared Spectral Energy Distributions of Millimeter Detected Quasars at z 5. *APJ*, 772:103.

Leipski, C., Meisenheimer, K., Walter, F., Klaas, U., Dannerbauer, H., De Rosa, G., Fan, X., Haas, M., Krause, O., and Rix, H.-W. (2014). Spectral Energy Distributions of

QSOs at z 5: Common Active Galactic Nucleus-heated Dust and Occasionally Strong Star-formation. *ApJ*, 785:154.

Leitherer, C. and Heckman, T. M. (1995). Synthetic properties of starburst galaxies. *ApJS*, 96:9–38.

Li, A. and Draine, B. T. (2001). Infrared Emission from Interstellar Dust. II. The Diffuse Interstellar Medium. *APJ*, 554:778–802.

Lotz, J. M., Davis, M., Faber, S. M., Guhathakurta, P., Gwyn, S., Huang, J., Koo, D. C., Le Floc'h, E., Lin, L., Newman, J., Noeske, K., Papovich, C., Willmer, C. N. A., Coil, A., Conselice, C. J., Cooper, M., Hopkins, A. M., Metevier, A., Primack, J., Rieke, G., and Weiner, B. J. (2008). The Evolution of Galaxy Mergers and Morphology at z 1.2 in the Extended Groth Strip. *ApJ*, 672:177–197.

Lotz, J. M., Primack, J., and Madau, P. (2004). A New Nonparametric Approach to Galaxy Morphological Classification. *AJ*, 128:163–182.

Lusso, E., Comastri, A., Simmons, B. D., Mignoli, M., Zamorani, G., Vignali, C., Brusa, M., Shankar, F., Lutz, D., Trump, J. R., Maiolino, R., Gilli, R., Bolzonella, M., Puccetti, S., Salvato, M., Impey, C. D., Civano, F., Elvis, M., Mainieri, V., Silverman, J. D., Koekemoer, A. M., Bongiorno, A., Merloni, A., Berta, S., Le Floc'h, E., Magnelli, B., Pozzi, F., and Riguccini, L. (2012). Bolometric luminosities and Eddington ratios of X-ray selected active galactic nuclei in the XMM-COSMOS survey. *MNRAS*, 425:623–640.

Lusso, E., Comastri, A., Vignali, C., Zamorani, G., Brusa, M., Gilli, R., Iwasawa, K., Salvato, M., Civano, F., Elvis, M., Merloni, A., Bongiorno, A., Trump, J. R., Koekemoer, A. M., Schinnerer, E., Le Floc'h, E., Cappelluti, N., Jahnke, K., Sargent, M., Silverman, J., Mainieri, V., Fiore, F., Bolzonella, M., Le Fèvre, O., Garilli, B., Iovino, A., Kneib, J. P., Lamareille, F., Lilly, S., Mignoli, M., Scodeggio, M., and Vergani, D. (2010). The X-ray to optical-UV luminosity ratio of X-ray selected type 1 AGN in XMM-COSMOS. *aap*, 512:A34.

Lusso, E. and Risaliti, G. (2016). The Tight Relation between X-Ray and Ultraviolet Luminosity of Quasars. *ApJ*, 819:154.

Lusso, E. and Risaliti, G. (2017). Quasars as standard candles. I. The physical relation between disc and coronal emission. *A&A*, 602:A79.

Ma, Z. and Yan, H. (2015). Co-evolution of Extreme Star Formation and Quasars: Hints from Herschel and the Sloan Digital Sky Survey. *ApJ*, 811:58.

Madau, P., Ferguson, H. C., Dickinson, M. E., Giavalisco, M., Steidel, C. C., and Fruchter, A. (1996). High-redshift galaxies in the Hubble Deep Field: colour selection and star formation history to z˜4. *MNRAS*, 283:1388–1404.

Madau, P., Ferrara, A., and Rees, M. (2001). Early Metal Enrichment of the Intergalactic Medium by Pregalactic Outflows. *APJ*, 555:92–105.

Madsen, K. K., Harrison, F. A., Markwardt, C. B., An, H., Grefenstette, B. W., Bachetti, M., Miyasaka, H., Kitaguchi, T., Bhalerao, V., Boggs, S., Christensen, F. E., Craig, W. W., Forster, K., Fuerst, F., Hailey, C. J., Perri, M., Puccetti, S., Rana, V., Stern, D., Walton, D. J., Jørgen Westergaard, N., and Zhang, W. W. (2015). Calibration of the NuSTAR High-energy Focusing X-ray Telescope. *ApJS*, 220:8.

Magdis, G. E., Daddi, E., Béthermin, M., Sargent, M., Elbaz, D., Pannella, M., Dickinson, M., Dannerbauer, H., da Cunha, E., Walter, F., Rigopoulou, D., Charmandaris, V., Hwang, H. S., and Kartaltepe, J. (2012). The Evolving Interstellar Medium of Star-forming Galaxies since z = 2 as Probed by Their Infrared Spectral Energy Distributions. *APJ*, 760:6.

Magnelli, B., Lutz, D., Saintonge, A., Berta, S., Santini, P., Symeonidis, M., Altieri, B., Andreani, P., Aussel, H., Béthermin, M., Bock, J., Bongiovanni, A., Cepa, J., Cimatti, A., Conley, A., Daddi, E., Elbaz, D., Förster Schreiber, N. M., Genzel, R., Ivison, R. J., Le Floc'h, E., Magdis, G., Maiolino, R., Nordon, R., Oliver, S. J., Page, M., Pérez García, A., Poglitsch, A., Popesso, P., Pozzi, F., Riguccini, L., Rodighiero, G., Rosario, D., Roseboom, I., Sanchez-Portal, M., Scott, D., Sturm, E., Tacconi, L. J., Valtchanov, I., Wang, L., and Wuyts, S. (2014). The evolution of the dust temperatures of galaxies in the SFR-$M_?$ plane up to z $\sim 2. AAP, 561 : A86$.

Magnelli, B., Lutz, D., Santini, P., Saintonge, A., Berta, S., Albrecht, M., Altieri, B., Andreani, P., Aussel, H., Bertoldi, F., Béthermin, M., Bongiovanni, A., Capak, P., Chapman, S., Cepa, J., Cimatti, A., Cooray, A., Daddi, E., Danielson, A. L. R., Dannerbauer, H., Dunlop, J. S., Elbaz, D., Farrah, D., Förster Schreiber, N. M., Genzel, R., Hwang, H. S., Ibar, E., Ivison, R. J., Le Floc'h, E., Magdis, G., Maiolino, R., Nordon, R., Oliver, S. J., Pérez García, A., Poglitsch, A., Popesso, P., Pozzi, F., Riguccini, L., Rodighiero, G., Rosario, D., Roseboom, I., Salvato, M., Sanchez-Portal, M., Scott, D., Smail, I., Sturm, E., Swinbank, A. M., Tacconi, L. J., Valtchanov, I., Wang, L., and Wuyts, S. (2012). A Herschel view of the far-infrared properties of submillimetre galaxies. *A&A*, 539:A155.

Magorrian, J., Tremaine, S., Richstone, D., Bender, R., Bower, G., Dressler, A., Faber, S. M., Gebhardt, K., Green, R., Grillmair, C., Kormendy, J., and Lauer, T. (1998). The Demography of Massive Dark Objects in Galaxy Centers. *AJ*, 115:2285–2305.

Maiolino, R., Shemmer, O., Imanishi, M., Netzer, H., Oliva, E., Lutz, D., and Sturm, E. (2007). Dust covering factor, silicate emission, and star formation in luminous QSOs. *A&A*, 468:979–992.

Marchese, E., Della Ceca, R., Caccianiga, A., Severgnini, P., Corral, A., and Fanali, R. (2012). The optical-UV spectral energy distribution of the unabsorbed AGN population in the XMM-Newton Bright Serendipitous Survey. *A&A*, 539:A48.

Marconi, A. and Hunt, L. K. (2003). The Relation between Black Hole Mass, Bulge Mass, and Near-Infrared Luminosity. *APJ*, 589:L21–L24.

Marconi, A., Risaliti, G., Gilli, R., Hunt, L. K., Maiolino, R., and Salvati, M. (2004). Local supermassive black holes and relics of active galactic nuclei. In Storchi-Bergmann, T., Ho, L. C., and Schmitt, H. R., editors, *The Interplay Among Black Holes, Stars and ISM in Galactic Nuclei*, volume 222 of *IAU Symposium*, pages 49–52.

Martocchia, S., Piconcelli, E., Zappacosta, L., Duras, F., Vietri, G., Vignali, C., Bianchi, S., Bischetti, M., Bongiorno, A., Brusa, M., Lanzuisi, G., Marconi, A., Mathur, S., Miniutti, G., Nicastro, F., Bruni, G., and Fiore, F. (2017). The WISSH quasars project. III. X-ray properties of hyper-luminous quasars. *aap*, 608:A51.

Masnou, J. L., Wilkes, B. J., Elvis, M., McDowell, J. C., and Arnaud, K. A. (1992). The soft X-ray excess in Einstein quasar spectra. *AAP*, 253:35–48.

Mateos, S., Carrera, F. J., Alonso-Herrero, A., Rovilos, E., Hernán-Caballero, A., Barcons, X., Blain, A., Caccianiga, A., Della Ceca, R., and Severgnini, P. (2015). Revisiting the relationship between 6 μm and 2-10 keV continuum luminosities of AGN. *MNRAS*, 449:1422–1440.

Mathez, G. (1976). Evolution of the luminosity function of quasars - A model with constant density and luminosity evolution. *Aap*, 53:15–21.

Mathis, J. S., Rumpl, W., and Nordsieck, K. H. (1977). The size distribution of interstellar grains. *APJ*, 217:425–433.

McConnell, N. J. and Ma, C.-P. (2013). Revisiting the Scaling Relations of Black Hole Masses and Host Galaxy Properties. *apj*, 764:184.

Melbourne, J., Soifer, B. T., Desai, V., Pope, A., Armus, L., Dey, A., Bussmann, R. S., Jannuzi, B. T., and Alberts, S. (2012). The Spectral Energy Distributions and Infrared Luminosities of z 2 Dust-obscured Galaxies from Herschel and Spitzer. *AJ*, 143:125.

Menci, N., Fiore, F., Puccetti, S., and Cavaliere, A. (2008). The Blast Wave Model for AGN Feedback: Effects on AGN Obscuration. *APJ*, 686:219–229.

Menci, N., Fontana, A., Giallongo, E., and Salimbeni, S. (2005). Bimodal Color Distribution in Hierarchical Galaxy Formation. *ApJ*, 632:49–57.

Merloni, A. (2004). The anti-hierarchical growth of supermassive black holes. *MNRAS*, 353:1035–1047.

Merloni, A., Bongiorno, A., Bolzonella, M., Brusa, M., Civano, F., Comastri, A., Elvis, M., Fiore, F., Gilli, R., Hao, H., Jahnke, K., Koekemoer, A. M., Lusso, E., Mainieri, V., Mignoli, M., Miyaji, T., Renzini, A., Salvato, M., Silverman, J., Trump, J., Vignali, C., Zamorani, G., Capak, P., Lilly, S. J., Sanders, D., Taniguchi, Y., Bardelli, S., Carollo, C. M., Caputi, K., Contini, T., Coppa, G., Cucciati, O., de la Torre, S., de Ravel, L., Franzetti, P., Garilli, B., Hasinger, G., Impey, C., Iovino, A., Iwasawa, K., Kampczyk, P., Kneib, J.-P., Knobel, C., Kovač, K., Lamareille, F., Le Borgne, J.-F., Le Brun, V., Le Fèvre, O., Maier, C., Pello, R., Peng, Y., Perez Montero, E., Ricciardelli, E., Scodeggio, M., Tanaka, M., Tasca, L. A. M., Tresse, L., Vergani, D., and Zucca, E. (2010). On the Cosmic Evolution of the Scaling Relations Between Black Holes and Their Host Galaxies: Broad-Line Active Galactic Nuclei in the zCOSMOS Survey. *APJ*, 708:137–157.

Merloni, A. and Heinz, S. (2008). A synthesis model for AGN evolution: supermassive black holes growth and feedback modes. *MNRAS*, 388:1011–1030.

Merloni, A. and Heinz, S. (2013). *Evolution of Active Galactic Nuclei*, page 503.

Miettinen, O., Novak, M., Smolčić, V., Schinnerer, E., Sargent, M., Murphy, E. J., Aravena, M., Bondi, M., Carilli, C. L., Karim, A., Salvato, M., and Zamorani, G. (2015). (Sub)millimetre interferometric imaging of a sample of COSMOS/AzTEC submillimetre galaxies. II. The spatial extent of the radio-emitting regions. *AAP*, 584:A32.

Minezaki, T., Yoshii, Y., Kobayashi, Y., Enya, K., Suganuma, M., Tomita, H., Aoki, T., and Peterson, B. A. (2004). Inner Size of a Dust Torus in the Seyfert 1 Galaxy NGC 4151. *APJIL*, 600:L35–L38.

Mor, R. and Netzer, H. (2012). Hot graphite dust and the infrared spectral energy distribution of active galactic nuclei. *MNRAS*, 420:526–541.

Mor, R., Netzer, H., and Elitzur, M. (2009). Dusty Structure Around Type-I Active Galactic Nuclei: Clumpy Torus Narrow-line Region and Near-nucleus Hot Dust. *APJ*, 705:298–313.

Mullaney, J. R., Alexander, D. M., Aird, J., Bernhard, E., Daddi, E., Del Moro, A., Dickinson, M., Elbaz, D., Harrison, C. M., Juneau, S., Liu, D., Pannella, M., Rosario,

D., Santini, P., Sargent, M., Schreiber, C., Simpson, J., and Stanley, F. (2015). ALMA and Herschel reveal that X-ray-selected AGN and main-sequence galaxies have different star formation rate distributions. *MNRAS*, 453:L83–L87.

Mullaney, J. R., Daddi, E., Béthermin, M., Elbaz, D., Juneau, S., Pannella, M., Sargent, M. T., Alexander, D. M., and Hickox, R. C. (2012a). The Hidden "AGN Main Sequence": Evidence for a Universal Black Hole Accretion to Star Formation Rate Ratio since z ˜ 2 Producing an M $_{BH}$-M $_{*}$ Relation. *ApJ*, 753:L30.

Mullaney, J. R., Pannella, M., Daddi, E., Alexander, D. M., Elbaz, D., Hickox, R. C., Bournaud, F., Altieri, B., Aussel, H., Coia, D., Dannerbauer, H., Dasyra, K., Dickinson, M., Hwang, H. S., Kartaltepe, J., Leiton, R., Magdis, G., Magnelli, B., Popesso, P., Valtchanov, I., Bauer, F. E., Brandt, W. N., Del Moro, A., Hanish, D. J., Ivison, R. J., Juneau, S., Luo, B., Lutz, D., Sargent, M. T., Scott, D., and Xue, Y. Q. (2012b). GOODS-Herschel: the far-infrared view of star formation in active galactic nucleus host galaxies since z 3. *MNRAS*, 419:95–115.

Murphy, K. D. and Yaqoob, T. (2009). An X-ray spectral model for Compton-thick toroidal reprocessors. *MNRAS*, 397:1549–1562.

Nandra, K., O'Neill, P. M., George, I. M., and Reeves, J. N. (2007). An XMM-Newton survey of broad iron lines in Seyfert galaxies. *MNRAS*, 382:194–228.

Narayan, R. and Yi, I. (1994). Advection-dominated accretion: A self-similar solution. *APJ*, 428:L13–L16.

Narayanan, D., Dey, A., Hayward, C. C., Cox, T. J., Bussmann, R. S., Brodwin, M., Jonsson, P., Hopkins, P. F., Groves, B., Younger, J. D., and Hernquist, L. (2010). A physical model for z ˜ 2 dust-obscured galaxies. *MNRAS*, 407:1701–1720.

Nenkova, M., Ivezić, Ž., and Elitzur, M. (2002). Dust Emission from Active Galactic Nuclei. *ApJ*, 570:L9–L12.

Nenkova, M., Sirocky, M. M., Nikutta, R., Ivezić, Ž., and Elitzur, M. (2008). AGN Dusty Tori. II. Observational Implications of Clumpiness. *APJ*, 685:160–180.

Netzer, H. (2009). Accretion and star formation rates in low-redshift type II active galactic nuclei. *MNRAS*, 399:1907–1920.

Netzer, H., Lani, C., Nordon, R., Trakhtenbrot, B., Lira, P., and Shemmer, O. (2016). Star Formation Black Hole Growth and Dusty Tori in the Most Luminous AGNs at z=2-3.5. *APJ*, 819:123.

Netzer, H., Lutz, D., Schweitzer, M., Contursi, A., Sturm, E., Tacconi, L. J., Veilleux, S., Kim, D.-C., Rupke, D., Baker, A. J., Dasyra, K., Mazzarella, J., and Lord, S. (2007). Spitzer Quasar and ULIRG Evolution Study (QUEST). II. The Spectral Energy Distributions of Palomar-Green Quasars. *Apj*, 666:806–816.

Netzer, H. and Maoz, D. (1990). On the emission-line response to continuum variations in the Seyfert galaxy NGC 5548. *ApJ*, 365:L5–L7.

Netzer, H., Mor, R., Trakhtenbrot, B., Shemmer, O., and Lira, P. (2014). Star Formation and Black Hole Growth at z ˜= 4.8. *APJ*, 791:34.

Netzer, H., Shemmer, O., Maiolino, R., Oliva, E., Croom, S., Corbett, E., and di Fabrizio, L. (2004). Near-Infrared Spectroscopy of High-Redshift Active Galactic Nuclei. II. Disappearing Narrow-Line Regions and the Role of Accretion. *ApJ*, 614:558–567.

Onori, F., La Franca, F., Ricci, F., Brusa, M., Sani, E., Maiolino, R., Bianchi, S., Bongiorno, A., Fiore, F., Marconi, A., and Vignali, C. (2017a). Detection of faint broad emission lines in type 2 AGN - I. Near-infrared observations and spectral fitting. *MNRAS*, 464:1783–1832.

Onori, F., Ricci, F., La Franca, F., Bianchi, S., Bongiorno, A., Brusa, M., Fiore, F., Maiolino, R., Marconi, A., Sani, E., and Vignali, C. (2017b). Detection of faint broad emission lines in type 2 AGN - II. On the measurement of the black hole mass of type 2 AGN and the unified model. *MNRAS*, 468:L97–L102.

Ott, S. (2010). The Herschel Data Processing System HIPE and Pipelines Up and Running Since the Start of the Mission. In Mizumoto, Y., Morita, K.-I., and Ohishi, M., editors, *Astronomical Data Analysis Software and Systems XIX*, volume 434 of *Astronomical Society of the Pacific Conference Series*, page 139.

Padovani, P., Alexander, D. M., Assef, R. J., De Marco, B., Giommi, P., Hickox, R. C., Richards, G. T., Smolčić, V., Hatziminaoglou, E., Mainieri, V., and Salvato, M. (2017). Active galactic nuclei: what's in a name? *aapr*, 25:2.

Pancoast, A., Brewer, B. J., and Treu, T. (2014). Modelling reverberation mapping data - I. Improved geometric and dynamical models and comparison with cross-correlation results. *MNRAS*, 445:3055–3072.

Pappalardo, C., Bendo, G. J., Bianchi, S., Hunt, L., Zibetti, S., Corbelli, E., di Serego Alighieri, S., Grossi, M., Davies, J., Baes, M., De Looze, I., Fritz, J., Pohlen, M., Smith, M. W. L., Verstappen, J., Boquien, M., Boselli, A., Cortese, L., Hughes, T., Viaene, S., Bizzocchi, L., and Clemens, M. (2015). The Herschel Virgo Cluster Survey. XVII. SPIRE point-source catalogs and number counts. *A&A*, 573:A129.

Pappalardo, C., Bizzocchi, L., Fritz, J., Boselli, A., Boquien, M., Boissier, S., Baes, M., Ciesla, L., Bianchi, S., Clemens, M., Viaene, S., Bendo, G. J., De Looze, I., Smith, M. W. L., and Davies, J. (2016). The Herschel Virgo Cluster Survey. XIX. Physical properties of low luminosity FIR sources at z 0.5. *A&A*, 589:A11.

Peng, Y., Maiolino, R., and Cochrane, R. (2015). Strangulation as the primary mechanism for shutting down star formation in galaxies. *Nature*, 521:192–195.

Peterson, B. M. (1997). *An Introduction to Active Galactic Nuclei.*

Petric, A. O., Ho, L. C., Flagey, N. J. M., and Scoville, N. Z. (2015). Herschel Survey of the Palomar-Green QSOs at Low Redshift. *APJS*, 219:22.

Phinney, E. S. (1989). Dusty Disks and the Infrared Emission from AGN. In Meyer, F., editor, *NATO Advanced Science Institutes (ASI) Series C*, volume 290 of *NATO Advanced Science Institutes (ASI) Series C*, page 457.

Piconcelli, E., Bianchi, S., Miniutti, G., Fiore, F., Guainazzi, M., Jimenez-Bailon, E., and Matt, G. (2008). Heavy absorption and soft X-ray emission lines in the XMM-Newton spectrum of the type 2 radio-loud quasar 3C 234. *A&A*, 480:671–676.

Piconcelli, E., Vignali, C., Bianchi, S., Zappacosta, L., Fritz, J., Lanzuisi, G., Miniutti, G., Bongiorno, A., Feruglio, C., Fiore, F., and Maiolino, R. (2015). The hidden quasar nucleus of a WISE-selected, hyperluminous, dust-obscured galaxy at z ˜ 2.3. *A&A*, 574:L9.

Pilbratt, G. L., Riedinger, J. R., Passvogel, T., Crone, G., Doyle, D., Gageur, U., Heras, A. M., Jewell, C., Metcalfe, L., Ott, S., and Schmidt, M. (2010). Herschel Space Observatory. An ESA facility for far-infrared and submillimetre astronomy. *A&A*, 518:L1.

Planck Collaboration, Abergel, A., Ade, P. A. R., Aghanim, N., Alves, M. I. R., Aniano, G., Armitage-Caplan, C., Arnaud, M., Ashdown, M., Atrio-Barandela, F., and et al. (2014). Planck 2013 results. XI. All-sky model of thermal dust emission. *A&A*, 571:A11.

Planck Collaboration, Ade, P. A. R., Aghanim, N., Arnaud, M., Ashdown, M., Aumont, J., Baccigalupi, C., Banday, A. J., Barreiro, R. B., Bartlett, J. G., and et al. (2016). Planck 2015 results. XIII. Cosmological parameters. *A&A*, 594:A13.

Pounds, K. A., King, A. R., Page, K. L., and O'Brien, P. T. (2003). Evidence of a high-velocity ionized outflow in a second narrow-line quasar PG 0844+349. *MNRAS*, 346:1025–1030.

Pozzi, F., Vignali, C., Comastri, A., Pozzetti, L., Mignoli, M., Gruppioni, C., Zamorani, G., Lari, C., Civano, F., Brusa, M., Fiore, F., Maiolino, R., and La Franca, F. (2007). The HELLAS2XMM survey. X. The bolometric output of luminous obscured quasars: The Spitzer perspective. *A&A*, 468:603–612.

Puchnarewicz, E. M., Mason, K. O., Romero-Colmenero, E., Carrera, F. J., Hasinger, G., McMahon, R., Mittaz, J. P. D., Page, M. J., and Carballo, R. (1996). Optical and X-ray properties of the RIXOS active galactic nuclei - I. The continua. *MNRAS*, 281:1243–1266.

Punsly, B. and Kharb, P. (2016). The Detection of Diffuse Extended Structure in 3C 273: Implications for Jet Power. *ApJ*, 833:57.

Ranalli, P., Comastri, A., and Setti, G. (2003). The 2-10 keV luminosity as a Star Formation Rate indicator. *A&A*, 399:39–50.

Reeves, J. N., Turner, M. J. L., Ohashi, T., and Kii, T. (1997). An X-ray survey of quasars using ASCA. *MNRAS*, 292:468.

Ricci, C., Assef, R. J., Stern, D., Nikutta, R., Alexander, D. M., Asmus, D., Ballantyne, D. R., Bauer, F. E., Blain, A. W., Boggs, S., Boorman, P. G., Brandt, W. N., Brightman, M., Chang, C. S., Chen, C.-T. J., Christensen, F. E., Comastri, A., Craig, W. W., Díaz-Santos, T., Eisenhardt, P. R., Farrah, D., Gandhi, P., Hailey, C. J., Harrison, F. A., Jun, H. D., Koss, M. J., LaMassa, S., Lansbury, G. B., Markwardt, C. B., Stalevski, M., Stanley, F., Treister, E., Tsai, C.-W., Walton, D. J., Wu, J. W., Zappacosta, L., and Zhang, W. W. (2017a). NuSTAR Observations of WISE J1036+0449, a Galaxy at z˜1 Obscured by Hot Dust. *ApJ*, 835:105.

Ricci, C., Bauer, F. E., Treister, E., Schawinski, K., Privon, G. C., Blecha, L., Arevalo, P., Armus, L., Harrison, F., Ho, L. C., Iwasawa, K., Sanders, D. B., and Stern, D. (2017b). Growing supermassive black holes in the late stages of galaxy mergers are heavily obscured. *MNRAS*, 468:1273–1299.

Ricci, C., Trakhtenbrot, B., Koss, M. J., Ueda, Y., Del Vecchio, I., Treister, E., Schawinski, K., Paltani, S., Oh, K., Lamperti, I., Berney, S., Gandhi, P., Ichikawa, K., Bauer, F. E., Ho, L. C., Asmus, D., Beckmann, V., Soldi, S., Baloković, M., Gehrels, N., and Markwardt, C. B. (2017c). BAT AGN Spectroscopic Survey. V. X-Ray Properties of the Swift/BAT 70-month AGN Catalog. *ApJS*, 233:17.

Ricci, F., La Franca, F., Marconi, A., Onori, F., Shankar, F., Schneider, R., Sani, E., Bianchi, S., Bongiorno, A., Brusa, M., Fiore, F., Maiolino, R., and Vignali, C. (2017d). Detection of faint broad emission lines in type 2 AGNs - III. On the M_{BH}-σ relation of type 2 AGNs. *MNRAS*, 471:L41–L46.

Ricci, F., La Franca, F., Onori, F., and Bianchi, S. (2017e). Novel calibrations of virial black hole mass estimators in active galaxies based on X-ray luminosity and optical/near-infrared emission lines. *A&A*, 598:A51.

Richards, G., Lacy, M., Storrie-Lombardi, L., Hall, P., Gallagher, S., Hines, D., Fan, X., Papovich, C., Vanden Berk, D., Trammell, G., Schneider, D., Vestergaard, M., York, D., Jester, S., Anderson, S., Budavári, T., and Szalay, A. (2006). Spectral Energy Distributions and Multiwavelength Selection of Type 1 Quasars. *APJs*, 166:470–497.

Rieke, G. H., Alonso-Herrero, A., Weiner, B. J., Prez-Gonzlez, P. G., Blaylock, M., Donley, J. L., and Marcillac, D. (2009). Determining Star Formation Rates for Infrared Galaxies. *APJ*, 692:556–573.

Roche, P. F., Aitken, D. K., Phillips, M. M., and Whitmore, B. (1984). 8-13 micron spectrophotometry of galaxies. II - 10 Seyferts and 3C 273. *MNRAS*, 207:35–45.

Rosario, D. J., Santini, P., Lutz, D., Netzer, H., Bauer, F. E., Berta, S., Magnelli, B., Popesso, P., Alexander, D. M., Brandt, W. N., Genzel, R., Maiolino, R., Mullaney, J. R., Nordon, R., Saintonge, A., Tacconi, L., and Wuyts, S. (2013). Nuclear Activity is More Prevalent in Star-forming Galaxies. *ApJ*, 771:63.

Rosario, D. J., Santini, P., Lutz, D., Shao, L., Maiolino, R., Alexander, D. M., Altieri, B., Andreani, P., Aussel, H., Bauer, F. E., Berta, S., Bongiovanni, A., Brandt, W. N., Brusa, M., Cepa, J., Cimatti, A., Cox, T. J., Daddi, E., Elbaz, D., Fontana, A., Förster Schreiber, N. M., Genzel, R., Grazian, A., Le Floch, E., Magnelli, B., Mainieri, V., Netzer, H., Nordon, R., Pérez Garcia, I., Poglitsch, A., Popesso, P., Pozzi, F., Riguccini, L., Rodighiero, G., Salvato, M., Sanchez-Portal, M., Sturm, E., Tacconi, L. J., Valtchanov, I., and Wuyts, S. (2012). The mean star formation rate of X-ray selected active galaxies and its evolution from z ˜ 2.5: results from PEP-Herschel. *A&A*, 545:A45.

Runnoe, J. C., Brotherton, M. S., and Shang, Z. (2012a). Updating quasar bolometric luminosity corrections. *MNRAS*, 422:478–493.

Runnoe, J. C., Brotherton, M. S., and Shang, Z. (2012b). Updating quasar bolometric luminosity corrections - II. Infrared bolometric corrections. *MNRAS*, 426:2677–2688.

Rupke, D. S. N. and Veilleux, S. (2011). Integral Field Spectroscopy of Massive, Kiloparsec-scale Outflows in the Infrared-luminous QSO Mrk 231. *APJIL*, 729:L27.

Rybicki, G. B. and Lightman, A. P. (1979). Book-Review - Radiative Processes in Astrophysics. *Astronomy Quarterly*, 3:199.

Sanders, D. B., Mazzarella, J. M., Kim, D.-C., Surace, J. A., and Soifer, B. T. (2003). The IRAS Revised Bright Galaxy Sample. *AJ*, 126:1607–1664.

Sanders, D. B., Phinney, E. S., Neugebauer, G., Soifer, B. T., and Matthews, K. (1989). Continuum energy distribution of quasars - Shapes and origins. *APJ*, 347:29–51.

Sanders, D. B., Soifer, B. T., Elias, J. H., Madore, B. F., Matthews, K., Neugebauer, G., and Scoville, N. Z. (1988). Ultraluminous infrared galaxies and the origin of quasars. *ApJ*, 325:74–91.

Santini, P., Maiolino, R., Magnelli, B., Lutz, D., Lamastra, A., Li Causi, G., Eales, S., Andreani, P., Berta, S., Buat, V., Cooray, A., Cresci, G., Daddi, E., Farrah, D., Fontana, A., Franceschini, A., Genzel, R., Granato, G., Grazian, A., Le Floc'h, E., Magdis, G., Magliocchetti, M., Mannucci, F., Menci, N., Nordon, R., Oliver, S., Popesso, P., Pozzi, F., Riguccini, L., Rodighiero, G., Rosario, D. J., Salvato, M., Scott, D., Silva, L., Tacconi, L., Viero, M., Wang, L., Wuyts, S., and Xu, K. (2014). The evolution of the dust and gas content in galaxies. *AAP*, 562:A30.

Santini, P., Rosario, D. J., Shao, L., Lutz, D., Maiolino, R., Alexander, D. M., Altieri, B., Andreani, P., Aussel, H., Bauer, F. E., Berta, S., Bongiovanni, A., Brandt, W. N., Brusa, M., Cepa, J., Cimatti, A., Daddi, E., Elbaz, D., Fontana, A., Förster Schreiber, N. M., Genzel, R., Grazian, A., Le Floc'h, E., Magnelli, B., Mainieri, V., Nordon, R., Pérez Garcia, A. M., Poglitsch, A., Popesso, P., Pozzi, F., Riguccini, L., Rodighiero, G., Salvato, M., Sanchez-Portal, M., Sturm, E., Tacconi, L. J., Valtchanov, I., and Wuyts, S. (2012). Enhanced star formation rates in AGN hosts with respect to inactive galaxies from PEP-Herschel observations. *A&A*, 540:A109.

Savage, B. D. and Mathis, J. S. (1979). Observed properties of interstellar dust. *ARAA*, 17:73–111.

Sazonov, S., Churazov, E., and Krivonos, R. (2015). Does the obscured AGN fraction really depend on luminosity? *MNRAS*, 454:1202–1220.

Schartmann, M., Meisenheimer, K., Camenzind, M., Wolf, S., and Henning, T. (2005). Towards a physical model of dust tori in Active Galactic Nuclei. Radiative transfer calculations for a hydrostatic torus model. *AAP*, 437:861–881.

Schawinski, K. (2009). The Role of AGN in the Migration of Early-Type Galaxies from the Blue Cloud to the Red Sequence. In Heinz, S. and Wilcots, E., editors, *American Institute of Physics Conference Series*, volume 1201 of *American Institute of Physics Conference Series*, pages 17–20.

Schawinski, K., Koss, M., Berney, S., and Sartori, L. F. (2015). Active galactic nuclei flicker: an observational estimate of the duration of black hole growth phases of

10^5 yr. *MNRAS*, 451:2517–2523.

Schawinski, K., Simmons, B. D., Urry, C. M., Treister, E., and Glikman, E. (2012). Heavily obscured quasar host galaxies at z $\sim 2 arediscs, notmajormergers. MNRAS, 425 : L61 - -L65$.

Schlegel, D. J., Finkbeiner, D. P., and Davis, M. (1998). Maps of Dust Infrared Emission for Use in Estimation of Reddening and Cosmic Microwave Background Radiation Foregrounds. *apj*, 500:525–553.

Schmidt, M. (1963). 3C 273 : A Star-Like Object with Large Red-Shift. *nat*, 197:1040.

Schmidt, M. (1968). Space Distribution and Luminosity Functions of Quasi-Stellar Radio Sources. *Apj*, 151:393.

Schneider, R., Bianchi, S., Valiante, R., Risaliti, G., and Salvadori, S. (2015). The origin of the far-infrared continuum of zΛ6 quasars. A radiative transfer model for SDSS J1148+5251. *AAP*, 579:A60.

Seyfert, C. K. (1943). The Distribution of Luminosity in the Planetary Nebula NGC 6572. *PASP*, 55:32–34.

Shakura, N. I. and Sunyaev, R. A. (1973). Black holes in binary systems. Observational appearance. *AAP*, 24:337–355.

Shankar, F., Bernardi, M., Sheth, R. K., Ferrarese, L., Graham, A. W., Savorgnan, G., Allevato, V., Marconi, A., Läsker, R., and Lapi, A. (2016). Selection bias in dynamically measured supermassive black hole samples: its consequences and the quest for the most fundamental relation. *MNRAS*, 460:3119–3142.

Shankar, F., Salucci, P., Granato, G. L., De Zotti, G., and Danese, L. (2004). Supermassive black hole demography: the match between the local and accreted mass functions. *MNRAS*, 354:1020–1030.

Shankar, F., Weinberg, D. H., and Miralda-Escudé, J. (2009). Self-Consistent Models of the AGN and Black Hole Populations: Duty Cycles, Accretion Rates, and the Mean Radiative Efficiency. *APJ*, 690:20–41.

Shao, L., Lutz, D., Nordon, R., Maiolino, R., Alexander, D. M., Altieri, B., Andreani, P., Aussel, H., Bauer, F. E., Berta, S., Bongiovanni, A., Brandt, W. N., Brusa, M., Cava, A., Cepa, J., Cimatti, A., Daddi, E., Dominguez-Sanchez, H., Elbaz, D., Förster Schreiber, N. M., Geis, N., Genzel, R., Grazian, A., Gruppioni, C., Magdis, G., Magnelli, B., Mainieri, V., Pérez García, A. M., Poglitsch, A., Popesso, P., Pozzi, F.,

Riguccini, L., Rodighiero, G., Rovilos, E., Saintonge, A., Salvato, M., Sanchez Portal, M., Santini, P., Sturm, E., Tacconi, L. J., Valtchanov, I., Wetzstein, M., and Wieprecht, E. (2010). Star formation in AGN hosts in GOODS-N. *A&A*, 518:L26.

Shen, Y. and Ho, L. C. (2014). The diversity of quasars unified by accretion and orientation. *Nature*, 513:210–213.

Shimizu, T. T., Meléndez, M., Mushotzky, R. F., Koss, M. J., Barger, A. J., and Cowie, L. L. (2016). Herschel far-infrared photometry of the Swift Burst Alert Telescope active galactic nuclei sample of the local universe - II. SPIRE observations. *MNRAS*, 456:3335–3353.

Shuder, J. M. and Osterbrock, D. E. (1981). Empirical results from a study of active galactic nuclei. *ApJ*, 250:55–65.

Silk, J. and Rees, M. J. (1998). Quasars and galaxy formation. *A&A*, 331:L1–L4.

Silva, L., Granato, G. L., Bressan, A., and Danese, L. (1998). Modeling the Effects of Dust on Galactic Spectral Energy Distributions from the Ultraviolet to the Millimeter Band. *APJ*, 509:103–117.

Silva, L., Maiolino, R., and Granato, G. L. (2004). Connecting the cosmic infrared background to the X-ray background. *MNRAS*, 355:973–985.

Singh, K. P. (2013). An X-ray view of quasars. *Bulletin of the Astronomical Society of India*, 41:137.

Soltan, A. (1982). Masses of quasars. *MNRAS*, 200:115–122.

Spinoglio, L., Andreani, P., and Malkan, M. A. (2002). The Far-Infrared Energy Distributions of Seyfert and Starburst Galaxies in the Local Universe: Infrared Space Observatory Photometry of the 12 Micron Active Galaxy Sample. *ApJ*, 572:105–123.

Springel, V., White, S. D. M., Jenkins, A., Frenk, C. S., Yoshida, N., Gao, L., Navarro, J., Thacker, R., Croton, D., Helly, J., Peacock, J. A., Cole, S., Thomas, P., Couchman, H., Evrard, A., Colberg, J., and Pearce, F. (2005). Simulations of the formation, evolution and clustering of galaxies and quasars. *Nature*, 435:629–636.

Stalevski, M., Fritz, J., Baes, M., Nakos, T., and Popović, L. Č. (2012). 3D radiative transfer modelling of the dusty tori around active galactic nuclei as a clumpy two-phase medium. *MNRAS*, 420:2756–2772.

Stalevski, M., Ricci, C., Ueda, Y., Lira, P., Fritz, J., and Baes, M. (2016). The dust covering factor in active galactic nuclei. *MNRAS*, 458:2288–2302.

Stanley, F., Harrison, C. M., Alexander, D. M., Swinbank, A. M., Aird, J. A., Del Moro, A., Hickox, R. C., and Mullaney, J. R. (2015). A remarkably flat relationship between the average star formation rate and AGN luminosity for distant X-ray AGN. *MNRAS*, 453:591–604.

Stern, D. (2015). The X-Ray to Mid-infrared Relation of AGNs at High Luminosity. *ApJ*, 807:129.

Stern, D., Lansbury, G. B., Assef, R. J., Brandt, W. N., Alexander, D. M., Ballantyne, D. R., Baloković, M., Bauer, F. E., Benford, D., Blain, A., Boggs, S. E., Bridge, C., Brightman, M., Christensen, F. E., Comastri, A., Craig, W. W., Del Moro, A., Eisenhardt, P. R. M., Gandhi, P., Griffith, R. L., Hailey, C. J., Harrison, F. A., Hickox, R. C., Jarrett, T. H., Koss, M., Lake, S., LaMassa, S. M., Luo, B., Tsai, C.-W., Urry, C. M., Walton, D. J., Wright, E. L., Wu, J., Yan, L., and Zhang, W. W. (2014). NuSTAR and XMM-Newton Observations of Luminous, Heavily Obscured, WISE-selected Quasars at z ˜ 2. *ApJ*, 794:102.

Stevans, M. L., Shull, J. M., Danforth, C. W., and Tilton, E. M. (2014). HST-COS Observations of AGNs. II. Extended Survey of Ultraviolet Composite Spectra from 159 Active Galactic Nuclei. *APJ*, 794:75.

Sturm, E., González-Alfonso, E., Veilleux, S., Fischer, J., Graciá-Carpio, J., Hailey-Dunsheath, S., Contursi, A., Poglitsch, A., Sternberg, A., Davies, R., Genzel, R., Lutz, D., Tacconi, L., Verma, A., Maiolino, R., and de Jong, J. A. (2011). Massive Molecular Outflows and Negative Feedback in ULIRGs Observed by Herschel-PACS. *ApJ*, 733:L16.

Suganuma, M., Yoshii, Y., Kobayashi, Y., Minezaki, T., Enya, K., Tomita, H., Aoki, T., Koshida, S., and Peterson, B. A. (2006). Reverberation Measurements of the Inner Radius of the Dust Torus in Nearby Seyfert 1 Galaxies. *APJ*, 639:46–63.

Symeonidis, M. (2017). What produces the far-infrared/submillimetre emission in the most luminous QSOs? *MNRAS*, 465:1401–1408.

Symeonidis, M., Giblin, B. M., Page, M. J., Pearson, C., Bendo, G., Seymour, N., and Oliver, S. J. (2016). AGN are cooler than you think: the intrinsic far-IR emission from QSOs. *MNRAS*, 459:257–276.

Tazaki, F., Ueda, Y., Terashima, Y., Mushotzky, R. F., and Tombesi, F. (2013). Suzaku View of the Swift/BAT Active Galactic Nuclei. V. Torus Structure of Two Luminous Radio-loud Active Galactic Nuclei (3C 206 and PKS 0707-35). *ApJ*, 772:38.

Telfer, R. C., Zheng, W., Kriss, G. A., and Davidsen, A. F. (2002). The Rest-Frame Extreme-Ultraviolet Spectral Properties of Quasi-stellar Objects. *APJ*, 565:773–785.

Teng, S. H., Rigby, J. R., Stern, D., Ptak, A., Alexander, D. M., Bauer, F. E., Boggs, S. E., Brandt, W. N., Christensen, F. E., Comastri, A., Craig, W. W., Farrah, D., Gandhi, P., Hailey, C. J., Harrison, F. A., Hickox, R. C., Koss, M., Luo, B., Treister, E., and Zhang, W. W. (2015). A NuSTAR Survey of Nearby Ultraluminous Infrared Galaxies. *ApJ*, 814:56.

Teng, S. H. and Veilleux, S. (2010). X-QUEST: A Comprehensive X-ray Study of Local ULIRGS and QSOs. *ApJ*, 725:1848–1876.

Treister, E., Schawinski, K., Urry, C. M., and Simmons, B. D. (2012). Major Galaxy Mergers Only Trigger the Most Luminous Active Galactic Nuclei. *ApJ*, 758:L39.

Treister, E. and Urry, C. M. (2006). The Evolution of Obscuration in Active Galactic Nuclei. *ApJ*, 652:L79–L82.

Treister, E., Urry, C. M., and Lira, P. (2005). AGN Unification and the X-ray and Infrared Backgrounds. In *American Astronomical Society Meeting Abstracts*, volume 37 of *Bulletin of the American Astronomical Society*, page 1223.

Treister, E., Urry, C. M., and Virani, S. (2009). The Space Density of Compton-Thick Active Galactic Nucleus and the X-Ray Background. *ApJ*, 696:110–120.

Tremaine, S., Gebhardt, K., Bender, R., Bower, G., Dressler, A., Faber, S. M., Filippenko, A. V., Green, R., Grillmair, C., Ho, L. C., Kormendy, J., Lauer, T. R., Magorrian, J., Pinkney, J., and Richstone, D. (2002). The Slope of the Black Hole Mass versus Velocity Dispersion Correlation. *APJ*, 574:740–753.

Trumpler, R. J. (1930). Absorption of Light in the Galactic System. *PASP*, 42:214.

Tsai, C.-W., Eisenhardt, P. R. M., Wu, J., Stern, D., Assef, R. J., Blain, A. W., Bridge, C. R., Benford, D. J., Cutri, R. M., Griffith, R. L., Jarrett, T. H., Lonsdale, C. J., Masci, F. J., Moustakas, L. A., Petty, S. M., Sayers, J., Stanford, S. A., Wright, E. L., Yan, L., Leisawitz, D. T., Liu, F., Mainzer, A. K., McLean, I. S., Padgett, D. L., Skrutskie, M. F., Gelino, C. R., Beichman, C. A., and Juneau, S. (2015). The Most Luminous Galaxies Discovered by WISE. *APJ*, 805:90.

Tuffs, R. J., Popescu, C. C., Völk, H. J., Kylafis, N. D., and Dopita, M. A. (2004). Modelling the spectral energy distribution of galaxies. III. Attenuation of stellar light in spiral galaxies. *AAP*, 419:821–835.

Ueda, Y., Akiyama, M., Hasinger, G., Miyaji, T., and Watson, M. G. (2014). Toward the Standard Population Synthesis Model of the X-Ray Background: Evolution of X-Ray Luminosity and Absorption Functions of Active Galactic Nuclei Including Compton-thick Populations. *ApJ*, 786:104.

Ueda, Y., Akiyama, M., Ohta, K., and Miyaji, T. (2003). Cosmological Evolution of the Hard X-Ray Active Galactic Nucleus Luminosity Function and the Origin of the Hard X-Ray Background. *ApJ*, 598:886–908.

Urrutia, T., Lacy, M., and Becker, R. H. (2008). Evidence for Quasar Activity Triggered by Galaxy Mergers in HST Observations of Dust-reddened Quasars. *ApJ*, 674:80–96.

Urry, C. M. and Padovani, P. (1995). Unified Schemes for Radio-Loud Active Galactic Nuclei. *PASP*, 107:803.

Valiante, R., Schneider, R., Salvadori, S., and Bianchi, S. (2011). The origin of the dust in high-redshift quasars: the case of SDSS J1148+5251. *MNRAS*, 416:1916–1935.

Valiante, R., Schneider, R., Salvadori, S., and Gallerani, S. (2014). High-redshift quasars host galaxies: is there a stellar mass crisis? *MNRAS*, 444:2442–2455.

Vanden Berk, D. E., Richards, G. T., Bauer, A., Strauss, M. A., Schneider, D. P., Heckman, T. M., York, D. G., Hall, P. B., Fan, X., Knapp, G. R., Anderson, S. F., Annis, J., Bahcall, N. A., Bernardi, M., Briggs, J. W., Brinkmann, J., Brunner, R., Burles, S., Carey, L., Castander, F. J., Connolly, A. J., Crocker, J. H., Csabai, I., Doi, M., Finkbeiner, D., Friedman, S., Frieman, J. A., Fukugita, M., Gunn, J. E., Hennessy, G. S., Ivezić, Ž., Kent, S., Kunszt, P. Z., Lamb, D. Q., Leger, R. F., Long, D. C., Loveday, J., Lupton, R. H., Meiksin, A., Merelli, A., Munn, J. A., Newberg, H. J., Newcomb, M., Nichol, R. C., Owen, R., Pier, J. R., Pope, A., Rockosi, C. M., Schlegel, D. J., Siegmund, W. A., Smee, S., Snir, Y., Stoughton, C., Stubbs, C., SubbaRao, M., Szalay, A. S., Szokoly, G. P., Tremonti, C., Uomoto, A., Waddell, P., Yanny, B., and Zheng, W. (2001). Composite Quasar Spectra from the Sloan Digital Sky Survey. *AJ*, 122:549–564.

Vasudevan, R. V. and Fabian, A. C. (2007). Piecing together the X-ray background: bolometric corrections for active galactic nuclei. *MNRAS*, 381:1235–1251.

Vasudevan, R. V., Mushotzky, R. F., Winter, L. M., and Fabian, A. C. (2009). Optical-to-X-ray emission in low-absorption AGN: results from the Swift-BAT 9-month catalogue. *MNRAS*, 399:1553–1575.

Veilleux, S., Rupke, D. S. N., Kim, D.-C., Genzel, R., Sturm, E., Lutz, D., Contursi, A., Schweitzer, M., Tacconi, L. J., Netzer, H., Sternberg, A., Mihos, J. C., Baker, A. J., Mazzarella, J. M., Lord, S., Sanders, D. B., Stockton, A., Joseph, R. D., and Barnes, J. E. (2009). Spitzer Quasar and Ulirg Evolution Study (QUEST). IV. Comparison of 1 Jy Ultraluminous Infrared Galaxies with Palomar-Green Quasars. *ApJS*, 182:628–666.

Veilleux, S., Teng, S. H., Rupke, D. S. N., Maiolino, R., and Sturm, E. (2014). Half-megasecond Chandra Spectral Imaging of the Hot Circumgalactic Nebula around Quasar Mrk 231. *ApJ*, 790:116.

Vietri, G., Piconcelli, E., Bischetti, M., Duras, F., Martocchia, S., Bongiorno, A., Marconi, A., Zappacosta, L., Bisogni, S., Bruni, G., Brusa, M., Comastri, A., Cresci, G., Feruglio, C., Giallongo, E., La Franca, F., Mainieri, V., Mannucci, F., Ricci, F., Sani, E., Testa, V., Tombesi, F., Vignali, C., and Fiore, F. (2018). The WISSH quasars project. IV. Broad line region versus kiloparsec-scale winds. *aap*, 617:A81.

Vito, F., Brandt, W. N., Stern, D., Assef, R. J., Chen, C.-T. J., Brightman, M., Comastri, A., Eisenhardt, P., Garmire, G. P., Hickox, R., Lansbury, G., Tsai, C.-W., Walton, D. J., and Wu, J. W. (2018). Heavy X-ray obscuration in the most luminous galaxies discovered by WISE. *MNRAS*, 474:4528–4540.

Vito, F., Gilli, R., Vignali, C., Comastri, A., Brusa, M., Cappelluti, N., and Iwasawa, K. (2014). The hard X-ray luminosity function of high-redshift (3 z 5) active galactic nuclei. *MNRAS*, 445:3557–3574.

Vittorini, V., Shankar, F., and Cavaliere, A. (2005). The impact of energy feedback on quasar evolution and black hole demographics. *MNRAS*, 363:1376–1388.

Volonteri, M., Haardt, F., and Madau, P. (2003). The Assembly and Merging History of Supermassive Black Holes in Hierarchical Models of Galaxy Formation. *ApJ*, 582:559–573.

Volonteri, M., Salvaterra, R., and Haardt, F. (2006). Constraints on the accretion history of massive black holes from faint X-ray counts. *MNRAS*, 373:121–127.

Wachter, K., Leach, R., and Kellogg, E. (1979). Parameter estimation in X-ray astronomy using maximum likelihood. *ApJ*, 230:274–287.

Walcher, J., Groves, B., Budavári, T., and Dale, D. (2011). Fitting the integrated spectral energy distributions of galaxies. *APSS*, 331:1–52.

Wang, R., Carilli, C. L., Wagg, J., Bertoldi, F., Walter, F., Menten, K. M., Omont, A., Cox, P., Strauss, M. A., Fan, X., Jiang, L., and Schneider, D. P. (2008). Thermal Emission from Warm Dust in the Most Distant Quasars. *APJ*, 687:848–858.

Weedman, D., Sargsyan, L., Lebouteiller, V., Houck, J., and Barry, D. (2012). Infrared Classification and Luminosities for Dusty Active Galactic Nuclei and the Most Luminous Quasars. *APJ*, 761:184.

Welty, D. E. and Fowler, J. R. (1992). Ultraviolet, optical, and infrared observations of the high-latitude molecular cloud toward HD 210121. *APJ*, 393:193–205.

Whitaker, E. J. (2013). Congruence and Noncongruence Subgroups of Gamma(2) via Graphs on Surfaces. *ArXiv e-prints*.

Wiebe, D. V., Ade, P. A. R., Bock, J. J., Chapin, E. L., Devlin, M. J., Dicker, S., Griffin, M., Gundersen, J. O., Halpern, M., Hargrave, P. C., Hughes, D. H., Klein, J., Marsden, G., Martin, P. G., Mauskopf, P., Netterfield, C. B., Olmi, L., Pascale, E., Patanchon, G., Rex, M., Scott, D., Semisch, C., Thomas, N., Truch, M. D. P., Tucker, C., Tucker, G. S., and Viero, M. P. (2009). BLAST Observations of Resolved Galaxies: Temperature Profiles and the Effect of Active Galactic Nuclei on FIR to Submillimeter Emission. *ApJ*, 707:1809–1823.

Wik, D. R., Hornstrup, A., Molendi, S., Madejski, G., Harrison, F. A., Zoglauer, A., Grefenstette, B. W., Gastaldello, F., Madsen, K. K., Westergaard, N. J., Ferreira, D. D. M., Kitaguchi, T., Pedersen, K., Boggs, S. E., Christensen, F. E., Craig, W. W., Hailey, C. J., Stern, D., and Zhang, W. W. (2014). NuSTAR Observations of the Bullet Cluster: Constraints on Inverse Compton Emission. *ApJ*, 792:48.

Wilkes, B. J. and Elvis, M. (1987). Quasar energy distributions. I - Soft X-ray spectra of quasars. *APJ*, 323:243–262.

Williams, P. R., Pancoast, A., Treu, T., Brewer, B. J., Barth, A. J., Bennert, V. N., Buehler, T., Canalizo, G., Cenko, S. B., Clubb, K. I., Cooper, M. C., Filippenko, A. V., Gates, E., Hoenig, S. F., Joner, M. D., Kandrashoff, M. T., Laney, C. D., Lazarova, M. S., Li, W., Malkan, M. A., Rex, J., Silverman, J. M., Tollerud, E., Walsh, J. L., and Woo, J.-H. (2018). The Lick AGN Monitoring Project 2011: Dynamical Modeling of the Broad-line Region. *ApJ*, 866:75.

Willott, C. J., Delorme, P., Reylé, C., Albert, L., Bergeron, J., Crampton, D., Delfosse, X., Forveille, T., Hutchings, J. B., McLure, R. J., Omont, A., and Schade, D. (2010). The Canada-France High-z Quasar Survey: Nine New Quasars and the Luminosity Function at Redshift 6. *AJ*, 139:906–918.

Witt, A. N. and Gordon, K. D. (1996). Radiative transfer in cloudy galaxies: evolution of far-IR luminosity. In Dwek, E., editor, *American Institute of Physics Conference Series*, volume 348 of *American Institute of Physics Conference Series*, pages 230–236.

Wright, E. L., Eisenhardt, P. R. M., Mainzer, A. K., Ressler, M. E., Cutri, R. M., Jarrett, T., Kirkpatrick, J. D., Padgett, D., McMillan, R. S., Skrutskie, M., Stanford, S. A., Cohen, M., Walker, R. G., Mather, J. C., Leisawitz, D., Gautier, III, T. N., McLean, I., Benford, D., Lonsdale, C. J., Blain, A., Mendez, B., Irace, W. R., Duval, V., Liu, F., Royer, D., Heinrichsen, I., Howard, J., Shannon, M., Kendall, M., Walsh, A. L., Larsen, M., Cardon, J. G., Schick, S., Schwalm, M., Abid, M., Fabinsky, B., Naes, L.,

and Tsai, C.-W. (2010). The Wide-field Infrared Survey Explorer (WISE): Mission Description and Initial On-orbit Performance. *AJ*, 140:1868–1881.

Wu, J., Tsai, C.-W., Sayers, J., Benford, D., Bridge, C., Blain, A., Eisenhardt, P. R. M., Stern, D., Petty, S., Assef, R., Bussmann, S., Comerford, J. M., Cutri, R., Evans, II, N. J., Griffith, R., Jarrett, T., Lake, S., Lonsdale, C., Rho, J., Stanford, S. A., Weiner, B., Wright, E. L., and Yan, L. (2012). Submillimeter Follow-up of WISE-selected Hyperluminous Galaxies. *ApJ*, 756:96.

Xilouris, E. M., Alton, P. B., Davies, J. I., Kylafis, N. D., Papamastorakis, J., and Trewhella, M. (1998). Optical and NIR modelling of NGC 891. *AAP*, 331:894–900.

Yaqoob, T. (2012). The nature of the Compton-thick X-ray reprocessor in NGC 4945. *MNRAS*, 423:3360–3396.

Yu, Q. and Tremaine, S. (2002). Observational constraints on growth of massive black holes. *MNRAS*, 335:965–976.

Zamorani, G. (1981). X-Ray Properties of Quasars. In Philip, A. G. D., editor, *X-ray Symposium 1981 (1981)*, page 61.

Zappacosta, L., Comastri, A., Civano, F., Puccetti, S., Fiore, F., Aird, J., Del Moro, A., Lansbury, G. B., Lanzuisi, G., Goulding, A., Mullaney, J. R., Stern, D., Ajello, M., Alexander, D. M., Ballantyne, D. R., Bauer, F. E., Brandt, W. N., Chen, C.-T. J., Farrah, D., Harrison, F. A., Gandhi, P., Lanz, L., Masini, A., Marchesi, S., Ricci, C., and Treister, E. (2018). The NuSTAR Extragalactic Surveys: X-Ray Spectroscopic Analysis of the Bright Hard-band Selected Sample. *ApJ*, 854:33.

Zubovas, K. and King, A. (2012). Clearing Out a Galaxy. *APJ*, 745:L34.